Voltammetry of Adsorbed Monolayers: Computer Simulation and Experiment

J. Paul Loughman B.A. MOD., M.A., M.Sc.

Submitted for the Award of: Ph.D.

Supervisor: Prof. R. J. Forster

Dublin City University

School of Chemical Sciences

Submitted August 2001

I hereby certify that this material, which I now submit for assessment on the programme of study leading to the award of Ph.D. is entirely my own work and has not been taken from the work of others save and to the extent that such work has been cited and acknowledged within the text of my work.

Signed: Paul Loughnane ID No. :98970801

Date: 3 September 2001

Acknowledgement

For his insightful guidance and motivating influence, I sincerely thank my supervisor, Prof. R. J. Forster.

Index

Appendices

Abstract

Title: **Voltammetry of Adsorbed Monolayers: Computer Simulation and Experiment**

Author: **J. Paul Loughman B.A. MOD., M.A., M.Sc.**

Facile and accurate determination of both kinetic and thermodynamic electrochemical parameters from simple cyclic voltammograms of adsorbed species has been achieved using a new computer based theoretical model. This removes, for the most part, a major deficiency in cyclic voltammetric analysis. This model incorporates an integrated approach to simulation in cyclic voltammetry involving a combination of Marcus electron transfer theory and a simplex fitting algorithm. The model uses a modern electron transfer theory in a unique way and is demonstrated to be an important and useful diagnostic tool for the electrochemist. With this model, the effect of the electrode material on the electrochemical response of adsorbed osmium complexes has been investigated and it has been found that the non-adiabatic rate of heterogeneous electron transfer does not depend simply on the density of states within the electrode. In contrast, it is found that the non-adiabatic rate of heterogeneous electron transfer depends on the density of states modulated by the square of the coupling. Studies on the effect of bond conjugation within bridging ligands in adsorbed monolayers using the electron transfer model have been carried out. Surprisingly, the presence of bond conjugation gives a lower rate constant. Analogous experiments were carried out on complexes in solution. The model has been comprehensively tested using both theoretical and experimental data and has proven to be highly sensitive to the heterogeneous electron transfer rate constant, k^{o}, and to a lesser extent, the reorganisation energy, λ. This electron transfer model will enable future studies of adsorbed monolayers where distributions of formal potentials and / or distributions of heterogeneous electron transfer rate constants exist.

CHAPTER 1

Literature Survey

1.1. Introduction

Chemistry never ceases to amaze me. For example, take an element, an extremely reactive metal and chemically combine it with another element, a toxic gas, a salt is produced. What is so amazing about that? Well, if the metal is sodium and the gas is chlorine, then sodium chloride or "common salt" has been made. Of course, sodium chloride is an essential part of the mammalian diet and is therefore a compound with fundamentally different properties to those of the starting elements! Is that not amazing? Furthermore, take another type of salt, a piece of wire and a computer and apply some simple but careful manipulation, it is possible to study, understand and model a process which is of fundamental importance in science and technology! In fact, this is the primary objective in this work and the process which will be investigated is called the *heterogeneous electron transfer process*.

Understanding the dynamics of the heterogeneous electron transfer is central to a range of scientific advances from the development of the latest molecular electronic devices to the study of catalysis and corrosion. With the advent of microelectrodes and high performance instrumentation, the electrochemist now has at his disposal the tools to study heterogeneous electron transfer reactions. Measurement of the rate of electron transfer and the associated thermodynamic properties has now become almost a routine procedure. Furthermore, the use of adsorbed monolayers has allowed the electrochemist to vary in a controlled manner the microenvironment within which the electron transfer occurs. This has revolutionised the understanding of the effects of distance, molecular structure and solvent reorganisation on the dynamics of the electron transfer process.

Cyclic voltammetry is an electrochemical technique which is of paramount importance in the study of the electron transfer process. The major advantage of this technique is the relative ease and speed at which cyclic voltammetric experiments can be carried out. However, the major deficiency is that the extraction of electron transfer rate constants and thermodynamic parameters can be quite difficult. To address and remove this deficiency is one of the primary objectives of this work.

The advantages of microelectrodes in electrochemistry have been well explored and documented.[1,2,3,4] Various models for electron transfer across the electrode / monolayer interface have been developed.[5,6,7,8] By combining these theoretical models with experimental cyclic voltammetric data and computer based minimisation algorithms, it ought to be possible for the electrochemist to quickly elicit valuable information about the system under study. This first chapter reviews the current knowledge in these areas and in subsequent chapters a new approach will be described for simulating cyclic voltammetric responses.

As the microelectrode and the computer are the instruments that are central to this work, to begin with, descriptions of microelectrode properties and fabrication techniques are given. Then, electron transfer theory is outlined from the Butler-Volmer model to the "state of the art" Marcus theory. Next, descriptions of electron transfer dynamics of both solution phase reactants and adsorbed monolayers are outlined. Finally, in this chapter, the main principles of computer simulation and the properties of the chosen fitting algorithm will be discussed.

1.2. Microelectrodes

Microelectrodes have made a very significant impact in electrochemistry over the last 15 years. There was an explosion of interest in microelectrodes (also known as ultramicroelectrodes) in the literature in the mid 1980s and this interest has been sustained right through to the present day.

Microelectrodes can be defined as electrodes with at least one dimension small enough that their properties, e.g., mass transport regime, are a function of size.[1,2] Forster[3] more recently defined microelectrodes as "*miniature electrodes where the critical electrode dimension is less than 10 μm yet remains much greater than the thickness of the electrical double layer, which is typically 10 to 100 Å.*" Indeed, disk-shaped electrodes with 1 μm diameters are now routine, and a number of reports[4,9] have described much smaller electrodes with dimensions of the order of nanometers. Microelectrodes were first used as probes for *in vivo* measurements of neurotransmitters.[2,10] Their very small area generates extremely small currents, simultaneously minimising damage to tissue and causing a minimum amount of

electrolysis. Many other applications of these small electrodes have been reported including the measurement of the rates of fast chemical reactions,[3,11,12,13] performance of voltammetric measurements inside single cells,[14] observation of changes in the conductivity of single ion channels,[15] detection of analytes eluted from a capillary zone electrophoresis column,[16] and performance of small-scale etching and lithography.[17] As will be discussed in more detail later, the performance of the electrode with respect to speed and spatial resolution scales with the electrode radius.

Several different types of microelectrode exist, including spherical, hemispherical, disk and ring microelectrodes. The simplest type is the microsphere. Spherical microelectrodes are fundamentally different to the other types in that all points on their surface are equivalent and hence the rate of diffusion is not a function of position on the surface. However, microspheres are difficult to fabricate and for this reason the other types of microelectrode, particularly the microdisk are more commonly used. Microdisks are readily fabricated by sealing very fine wires (e.g., platinum and gold) into glass and cutting perpendicular to the axis of the wire and polishing the front face of the disk which is created. As illustrated in Figure 1.1, the diffusion field around the microdisk electrode is hemispherical and a uniform flux of electroactive species, and therefore current density, cannot be obtained over the surface of the disk. The rate of diffusion to the edge of the disk will always be higher than to the centre. As a result, the rate of diffusion to the disk and hence the current density are usually estimated as space averaged quantities. This can complicate the understanding of some reactions at microdisk electrodes, e.g., coupled chemical reactions where the concentrations of intermediates will not be uniform over the disk.

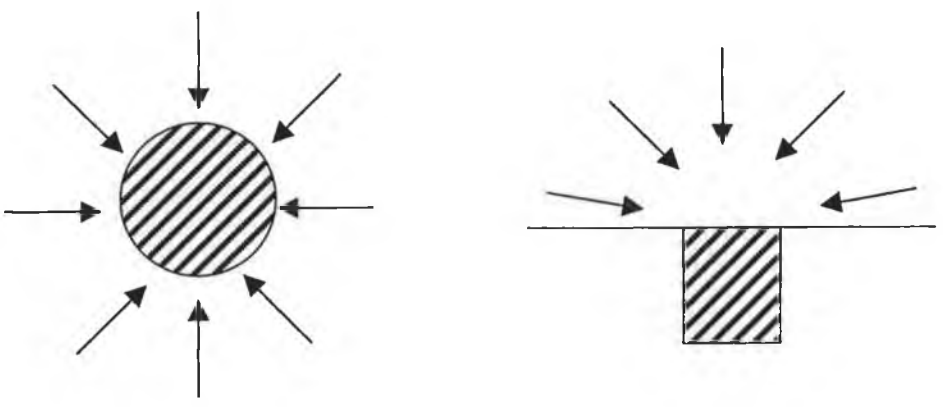

Figure 1.1. Illustrations of the spherical and disk type microelectrodes and their diffusion fields.

While much of the experimental work presented in this thesis deals with spontaneously adsorbed monolayers, microelectrodes have several advantages over macroelectrodes for analysing solution phase reactants and these advantages are discussed first.

1.3. Properties and Advantages of Microelectrodes

It is simpler to derive expressions for the microsphere electrode whose properties approximate to the other types including the microdisk.

1.3.1. Mass Transport

Consider an experiment where a potential step is applied to an inert microsphere electrode in a solution containing only the electroactive species, concentration c^{∞}, and an electrolyte. This potential step is such that the electroactive species is oxidised/reduced at a diffusion-controlled rate. Diffusion of electroactive species to any spherical electrode may be described by Fick's second law in spherical co-ordinates, i.e.,

$$\frac{\partial c}{\partial t} = D\frac{\partial^2 c}{\partial r^2} + \frac{2D}{r}\frac{\partial c}{\partial r} \qquad (1)$$

So, the initial condition is at t = 0 and r $\geq r_0$

$$c = c^{\infty}$$

and the boundary conditions are for t > 0, at

$$r = \infty, c = c^{\infty}$$

and at

$$r = r_0, c = 0$$

where r is the distance from the centre of the sphere, r_0 the radius of the sphere, D the diffusion coefficient for the electroactive species, c its concentration is a function of r and time t.

The solution to this set of equations may be found by Laplace transform techniques and it may be shown that the current density, i_d, is given by

$$i_d = \frac{nFDc^{\infty}}{r_0} + \frac{nFD^{1/2}c^{\infty}}{\pi^{1/2}t^{1/2}} \tag{2}$$

At a conventional electrode with radius 0.1 cm, the transient term is always dominant for timescales where natural convection can be ignored. At a microsphere the situation is different in that the response is the sum of a steady state and a transient component, both of which can be significant. Indeed for a microelectrode, it is possible to identify three types of diffusional regimes depending on the timescale.

(a) Short Times

At short times, the second term in Equation 2 will be much larger than the first and the current density is given by the Cottrell equation

$$i_d = \frac{nFD^{1/2}c^{\infty}}{\pi^{1/2}t^{1/2}} \tag{3}$$

In this case, a transient current with the same shape as that occurring with a conventional or large electrode is obtained, i.e., a plot of i(t) vs. $t^{-1/2}$ is linear.

(b) Long Times

As t increases, the transient current density will decrease and the current density will eventually be given by the first term in Equation 2. This is a steady state value given by

$$i_d = \frac{nFDc^{\infty}}{r_0} \tag{4}$$

From this it is clear that the steady state rate of diffusion and hence the steady state current density varies according to the radius of the electrode. Electrochemists use this ability to vary the steady state rate of diffusion by changing the size of the microelectrode to study the kinetics of electrode reactions.

The steady state rate of diffusion to microelectrodes and hence the steady state current is very high for microelectrodes. This property of microelectrodes promotes their use in the study of rapid electron transfer and fast-coupled chemical reactions. For example, the steady state mass transfer coefficient, k_m, at a 10 μm diameter microsphere is 10^{-5} m^2s^{-1} which is comparable to that at (a) a rapidly rotating disk (ca 4000 rpm) or (b) a planar electrode 10 ms after the imposition of a potential step. There are at least two other applications, which this high rate of steady state diffusion to microelectrodes allows, namely

1. The current should be independent of convection (e.g., microelectrodes can be used for analysis in flowing streams without complications from flow rate effects).
2. When a mass transport controlled reaction and a reaction controlled by surface kinetics are occurring simultaneously (e.g., the oxidation of the surface of solid electrodes), microelectrode size can be used to discriminate against the surface reaction (i_d is proportional to r_0, while i_k varies with r_0^2, where i_k is the current density associated with the reaction controlled by surface kinetics).[1]

(c) Intermediate Times

At intermediate times, the current density is described by the sum of the transient and steady state terms as per Equation 2.

$$i_d = \frac{nFDc^{\infty}}{r_0} + \frac{nFD^{1/2}c^{\infty}}{\pi^{1/2}t^{1/2}} \qquad (2)$$

Because of the predominance of the microdisk electrode in the laboratory, it is important to modify the equation for the microsphere to apply to the microdisk. This can be done simply by using the relation

$$r_0 = \frac{\pi a}{4} \qquad (5)$$

where a is the radius of the disk.

Therefore, the response to the potential step described above for a microdisk is given by:

$$i_d = \frac{4nFDc^{\infty}}{\pi a} + \frac{nFD^{1/2}c^{\infty}}{\pi^{1/2}t^{1/2}} \tag{6}$$

The steady state current is readily calculated by multiplying the steady state term by the disk area, i.e.

$$\pi a^2 \tag{7}$$

giving the following

$$i_d = 4nFDc^{\infty}a \tag{8}$$

As illustrated in Figure 1.2, at short times, the diffusion field at a microdisk electrode is linear (Cottrell behaviour) while at longer times this field becomes spherical.

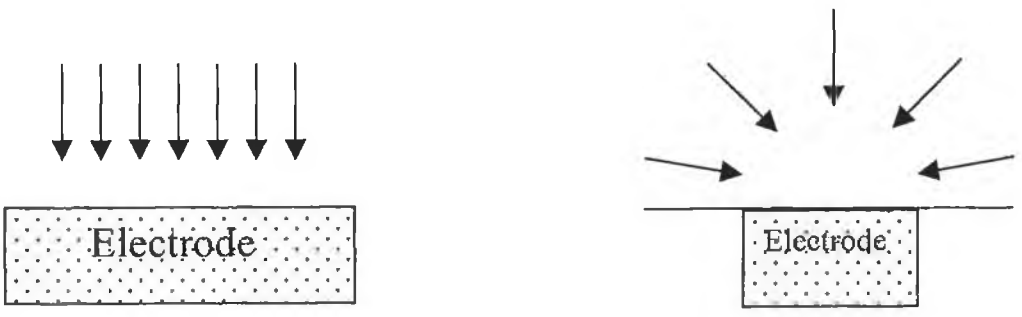

(a) (b)

Figure 1.2. Representations of the (a) linear or planar diffusion and (b) spherical or convergent diffusion field at a microdisk electrode at short and long times, respectively.

This transformation in the diffusion field may be understood as follows:

In a timescale of seconds, the depletion layer for molecules in solution attains dimensions much larger than the dimensions of the microelectrode. The result is a deviation from planar diffusion. Enhanced mass transport due to non-planar diffusion sets in and a sigmoidal shape, steady state response is obtained. This enhanced mass transport becomes useful in the study of electrochemical kinetics. At short times the dimension of the diffusion layer is smaller than that of the electrode and planar diffusion dominates. The response obtained is then identical to that of a conventional sized electrode.

From an experimental point of view, interpretation of results is always more straightforward when the timescale is such that one type diffusion field predominates significantly over the other, i.e., experiments carried out at intermediate times give results which are difficult to interpret.

1.3.2. Discrimination against Charging Currents

For an electrode placed in an electrolyte, there is, at each potential, a characteristic surface charge. Whenever the potential of an electrode is changed, the charge on the metal side of the interface will change and some reorganisation of the ions and dipoles in the double layer on the solution side will occur. This results in a flow of electrons into or out of the surface giving rise to a current known as the charging or capacitive current. This current adds to the Faradaic response and distorts the experimental data for the electron transfer process. Since the charging current may be of similar or even greater magnitude than the Faradaic current under certain conditions, e.g., at short times or with low concentrations of electroactive species, electrochemists usually want to increase the ratio of the Faradaic to charging current and reduce this distortion. Microelectrodes facilitate this discrimination against charging currents.

Considering a spherical microelectrode under pseudo - steady state conditions, the diffusion controlled or Faradaic current, i_f is proportional to the radius of the sphere,

r_0, whereas the charging current, i_c, is an extensive property and is proportional to the area. Hence,

$$\frac{i_f}{i_c} \propto \frac{r_0}{r_0^2} \propto \frac{1}{r_0} \tag{9}$$

Equation 9 shows that the ratio (i_f / i_c) improves as the electrode size decreases which explains how microelectrodes discriminate against charging currents. The same conclusion can be drawn for microdisks.

1.3.3. RC Cell Time Constants

The experimental response time of an electrochemical cell is given by the product of the resistance, R, and the capacitance, C. The RC cell time constant dictates the lower timescale limit for every electrochemical measurement and determines the shortest time at which electrochemical measurements are not distorted. Therefore, valid electrochemical data can only be obtained at timescales that are longer than the cell time constant by a factor of five or ten times.[18] Obviously the RC cell time constant is of fundamental importance when measuring fast electrochemical processes.

How is the RC cell time constants determined?

For a potential step the charging current is,

$$i_c(t) = \frac{\Delta E}{R} \exp(-t / RC) \tag{10}$$

where ΔE is the step amplitude and t is the time measured from the application of the step, which gives,

$$Ln(i_c) = Ln(\frac{\Delta E}{R}) + (-\frac{1}{RC})t \tag{11}$$

Therefore a plot of Ln(i_c) against t should be linear with slope = -1/RC and intercept = Ln(ΔE/R) allowing determination of the RC constant.

If the potential applied is a triangular wave as in cyclic voltammetry, the charging current rises from zero to an approximately constant value and is given by,

$$i_c = \nu C + (\frac{E_i}{R} - \nu C)\exp(-t / R\ C) \tag{12}$$

where ν is the scan rate and E_i is the initial potential. The plateau height of i_c is proportional to ν whereas i_f is proportional to $\nu^{1/2}$. As the scan rate is increased, the potential difference between the cathodic and anodic peaks in the cyclic voltammogram also increases as a result of both electron transfer kinetics and "iR" drop. On the other hand, the charging current increases proportionally to ν and causes increasing interference with the Faradaic current. Thus, an increase in the scan rate with the purpose of achieving larger diffusion rates renders the extraction of accurate kinetic information more difficult.[19]

Since the capacitance of a microelectrode is proportional to its area and R is inversely proportional to the radius, then for a spherical electrode,

$$RC \propto r_0^2 \frac{1}{r_0} \propto r_0 \tag{13}$$

Hence, the time constant decreases as the electrode is made smaller and the charging current will be less at all times. This gives a faster response time for the cell. When the electrode radius decreases from 0.5 mm to 5 μm, the cell response time decreases by a factor of 100. The need to minimise RC is obvious when one considers high speed transient measurements given that meaningful electrochemical data can only be extracted at timescales that are typically 5 to 10 times longer than the RC cell time constant.[3]

The decrease in the relative importance of the charging current at microelectrodes can be advantageous in many types of experiment. In potential step experiments, data free from distortion by charging current can be obtained at earlier times. As stated above, this allows the study of faster electron transfer processes and coupled chemical reactions as well as lowering the detection limit of pulse voltammetry (i_f / c^{∞} is larger

at short times). In cyclic voltammetry, it is possible to use faster potential scan rates and therefore, again to investigate more rapid kinetics.

1.3.4. Decreased Distortion From iR Drop

Solution resistance is often a cause of distortion in electrochemical data and precludes experimental measurements in many solvents. Ohmic or iR drop results from the fact that any current, i, flowing through a cell must be carried through a volume of solution of electrical resistance, R. Hence, throughout experimental electrochemistry, it is necessary to minimise distortion of the data by uncorrected iR drops. It is particularly a problem in experiments where the current varies since, then, the iR drop will necessarily change through the experiment. In experiments with larger electrodes, the iR drop is usually minimised by electronic compensation or by using a 3-electrode cell and a Luggin capillary.[20] Neither method is free from problems and in extreme conditions (e.g., at high potential scan rates or using poorly conducting media) the distortion makes the data unfit for interpretation.

Microelectrodes offer a way to solve these problems. Take the case of non-steady state conditions where linear diffusion is dominant, the current is proportional to the electrode area giving,

$$iR \propto r_0^2 \frac{1}{r_0} \propto r_0 \tag{14}$$

and it can be seen from this that the iR drop will decrease with the radius of the microelectrode. However, in steady state conditions, i_d is proportional to r_0 and the iR drop appears to be independent of the size of the electrode. But the microelectrode is still advantageous as the following scenario shows.

The resistance of a cell is given by

$$R = \frac{1}{4\pi\kappa r_0} \tag{15}$$

where κ is the specific conductance.

Take a cell with a 10 μm diameter electrode in a solution of electrolyte in an organic solvent. With κ = 0.01 ohm^{-1} cm^{-1}, the resistance of this cell is 16000 ohms. The steady state diffusion controlled current for a 10 mM solution of electroactive species may be calculated from the steady state current density given by the relation

$$i_d = \frac{nFDc^{\infty}}{r_0} \tag{4}$$

to be 5nA. Hence, the iR drop = 0.08 mV which is negligible. So, the absolute currents with these electrodes are very small, usually in the pA-nA range. Thus, even with highly resistive solvents, the uncompensated resistive drop (iR) that perturbs accurate potential measurements is small.[4]

There are many experiments where the current density is high or the medium has a large resistance, which would lead to very distorted data with a normal electrode. The great reduction in iR drop, which results from the use of microelectrodes, opens many possibilities. A high current density can arise in a number of circumstances:

(i) When a high concentration of electroactive species (e.g., >1 M) is present in solution. This is the case in many industrial processes, e.g., electrosyntheses, electroplating etc. The use of microelectrodes can allow the study of kinetics and mechanism in the exact conditions used in the technological application.

(ii) When cyclic voltammograms are recorded at high scan rates. For diffusion controlled reactions, the peak current will increase with the square root of the potential scan rate and this inevitably leads to large current densities. However, microelectrodes allow experimentation with high scan rates to provide meaningful electrochemical data because of the advantages with respect both charging current and iR drop.

(iii) In the study of very high-speed processes[3] e.g., electron transfer across the electrode/monolayer interface. Here, the large current density arises because of the rapid kinetics and absence of diffusion in the processes.

(iv) During measurements at very short times after a potential step or during ac studies at high frequency. Such studies again allow investigation of very fast reactions.

Microelectrodes may also be used to record meaningful data in media such as

(a) Solutions with little or no added electrolyte.[21] This can be of interest, for example, to understand the role of electrolytes in electron transfer and coupled chemical reactions and also makes possible the electroanalysis of process streams and natural waters without the need to add electrolyte.

(b) In non-polar solvents,[22] e.g., toluene or benzene. For example, the work on the electrochemistry of the fullerenes in solvents such as benzene, employed microelectrodes.[4]

(c) In supercritical water[4] and high-resistance solid electrolytes.

(d) The very small size of such electrodes allows them to be employed as high-resolution probes in the scanning electrochemical microscope (SECM).[4,23,24,25,26]

(e) Other unusual media. This would include ice and other frozen solvents, glasses,[27] gases[28] and polymer electrolytes.[29]

So, microelectrodes have very specific and well-understood advantages over macroelectrodes in electrochemistry. By using microelectrodes, the electrochemist can study electron transfer processes in a unique manner. These advantages will be used effectively in the experimental work in this thesis. Next, the principal methods used for microelectrode fabrication are comprehensively reviewed.

1.4. Fabrication of Microelectrodes

The increased interest in conducting research using microelectrodes has been partially due to the onset of availability of a range of suitable materials (e.g., microscopic wires) for construction and their relative ease of fabrication. The principal materials for microelectrode fabrication have been platinum and gold micro-wires, mercury deposited onto platinum, and carbon fibres.

The procedure for fabricating platinum[30] and gold microelectrodes involves sealing the microscopic wire (diameter 1 to 50 μm) in soft glass. A copper wire (e.g., tinned annealed copper 0.2 kg 18 swg) of approximate length 4 cm is joined to an aluminium "hook up" wire by wrapping the aluminium wire around the copper wire and soldering the two. These joined wires are then connected to the chosen microscopic wire by means of soldering (for larger diameters of ~ 25 μm) or by means of a conductive paint (diameters of ~ 5 μm). The microwires have to be sealed in the glass by heating in a flame before (in the case of the smaller diameter) or after (in the case of the larger diameter) connecting to the hook up wire.

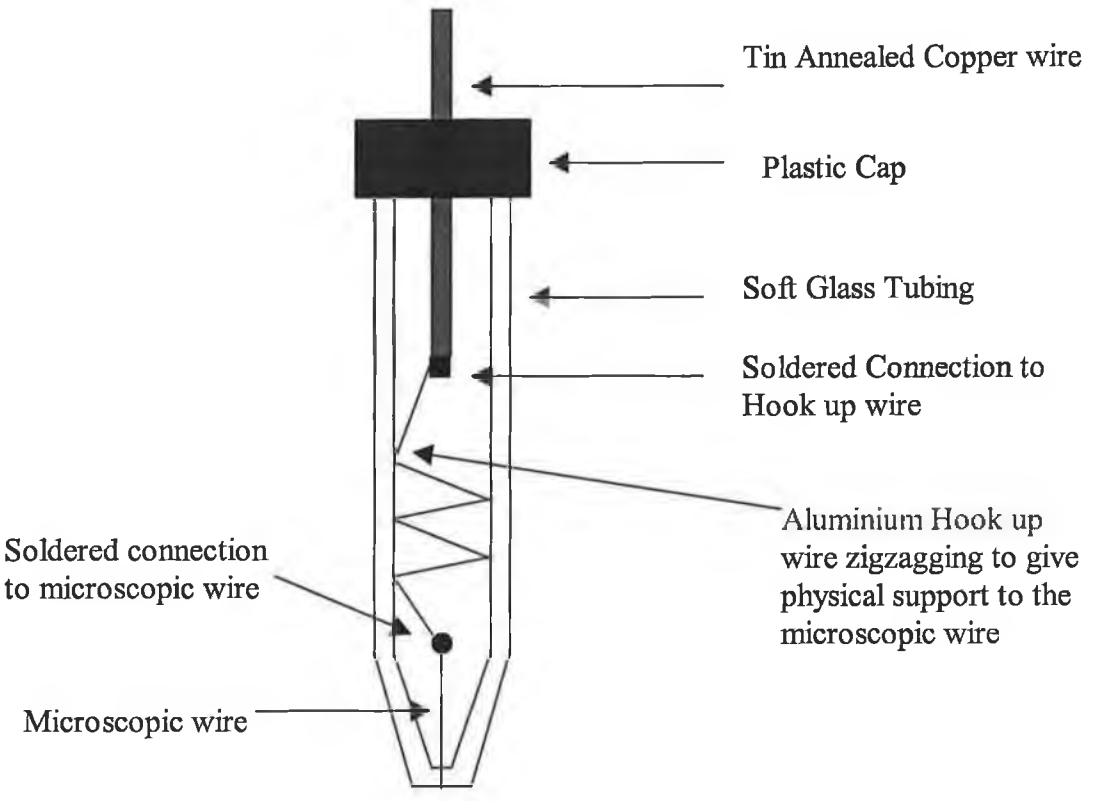

Figure 1.4. Modern Design of an Au or Pt Microelectrode

Exposure of the microdisk electrode is usually carried out by removing excess glass using emery paper followed by successive polishing with 12.5, 5, 1, 0.3, and 0.05 μm alumina.[6]

1.4.1. Polishing and Pre-treatment of Microelectrodes

Solid electrodes always require pre-treatment to clean and activate the surface prior to an electrochemical measurement. Such a procedure has to be reproducibly repeated since the performance of the electrode depends greatly on the physico-chemical state of its surface. Non uniform surface energy, caused by unsaturated valences at the edge atoms of crystal lattices, is heterogeneously distributed across the electrode surface, mainly because of faults present in the crystal plane.[31] Electrode activity depends on this surface energy and also on the occurrence of passivating layers which may block the active electrode sites.[32] Removal of passivating layers, contaminants, chemisorbed or physically adsorbed particles to produce an active electrode is one of the main goals of a pre-treatment procedure. Heterogeneous electron-transfer kinetics (and the associated wave/peak analysis, slopes, half-wave potentials, peak potentials, etc.) as well as electrode capacitance depend significantly on the state of the electrode surface.[33] Pre-treatment conditions remain empirical to a considerable extent despite the fact that their effect on electrochemical characteristics of various types of working electrodes has been extensively studied in the past two decades.

1.4.2. Other Types of Microelectrode

1.4.2.1. Mercury Microelectrodes

The unique properties of mercury have attracted interest in the microelectrode fabrication area. A large portion of the papers reporting on the use of mercury microelectrodes is devoted to anodic stripping. Other papers demonstrate the application of these electrodes in voltammetry and as amperometric detectors. Stationary mercury microelectrodes were prepared on a variety of substrates. First, exposed carbon fibres[34] and small graphite epoxy disks[35] were employed. It was followed by deposition of mercury on platinum[36] and carbon microdisks.[37] Iridium[38] and gold microdisks[39] were also used as substrates.

1.4.3.2. Carbon Fibre Microelectrodes

Carbon fibres are characterised by a unique combination of properties that are favourable for the fabrication of microelectrodes:

1. Carbon fibres have strength usually exceeding that of steel.
2. They have a broad range of surface properties from inert to various kinds of activated and chemically modified surfaces.

There are many types of carbon fibres commercially available, but most of them have been exclusively designed for the main technical application, i.e., for reinforcement of synthetic resins. Mechanical properties as well as chemical reactivity of carbon fibres depend very much on the kind and orientation of precursor material (usually PAN, i.e., polyacrylonitrile, or pitch) and on the details of the heat treatment procedure. Therefore, the choice of the right carbon fibre is an important first step in the fabrication of microelectrodes.

Anisotropic mesophase pitch fibres are high performance fibres characterised by high Young's moduli (HM), i.e., high stiffness. The common ex-PAN fibres belong to one of the two main categories, high tensile strength (HT) or HM. There are also some intermediate modulus (IM) PAN fibres, characterised by the tensile strengths of HT types but improved moduli.

The arrangement of graphitic ribbons and lamellae in PAN or pitch-based fibres, respectively, differs very much. Highly oriented ex-PAN fibres have an "onion peel" orientation of the graphitic ribbons, at least at their outside. HM pitch fibres usually have a "radial" texture of the graphitic lamellae.

Other facts which need to be considered when selecting carbon fibres for electrochemical applications are:

1. Many carbon fibres have non-circular cross sections.

2. They may have been subject to chemical or electrochemical surface oxidation.
3. They may be coated with a hard-to-remove finish of organic substances.

Fabrication

The preparation and general aspects of carbon fibre electrodes have been reviewed elsewhere.[40] Besenhard et al[41] describe the various methods of preparing conically shaped carbon fibres, the simplest one being burning of carbon fibres in a flame.[42]

Ponchon et al[43] were first to use carbon fibres for microelectrodes. Their electrodes have approximately 500 μm of the fibre protruding from the glass capillary, resulting in a cylindrical electrode. This design results in a large Faradaic current, but the voltammograms exhibit non-steady state behaviour at 300 mV s^{-1}.

Wightman[44] has employed carbon fibres in the fabrication of microelectrodes. These fibres have diameters in the range of 6-12 μm.[45] This method of construction is relatively simple with the fibre being sealed with epoxy in a glass capillary. Approximately 50% of the electrodes constructed by this method were useful for electroanalysis.

Electrochemical etching has been performed in acidic[46] as well as in basic[42,47] electrolytes. Etching in basic electrolytes has the advantage that there will be no intercalation damage of HM fibre.

Poorly oriented, i.e., poorly graphitised HT carbon fibres, usually do not form perfect cones after flaming or electrochemical etching. Moreover, they show much more pitting corrosion than HM fibres.

The radial arrangement of carbon lamellae in mesophase pitch fibres is still reflected in the topography of their cones after flaming or etching.

The relatively crude method of carbon fibre pointing by flaming, preferably in H_2/O_2, has two important disadvantages:

1. There is a much less uniform attack of the fibres, leading to pits in ex-PAN fibres and to splintering in the case of mesophase pitch fibres.
2. Flaming produces very long and fragile cones. This is true for ex-PAN as well as for pitch fibres. After electrochemical etching the length of typical cones is about 5 times the fibre diameter, whereas after flaming the length is about 10-20 times the diameter.

Encapsulation of the upper parts of conically shaped microelectrodes can be a problem. Well-adherent and highly resistive films on carbon fibres can be obtained by anodic electrodeposition of allyl-substituted poly(oxyphenylene) and a subsequent thermal treatment of the deposit.[48] This was proposed earlier for the insulation of metallic substrates.[49] Other methods of encapsulation, namely, by sticking the tip of the fibre in a thin protective layer of silicone rubber during the electrodeposition process have been investigated.[50]

1.4.4. Improvements to the Basic Microelectrode Design

1.4.4.1. Necessity for Improvements

As discussed in Section 1.3.2, the capacitance decreases with decreasing electrode area. However for some systems, the capacitive current *increases* with *decreasing* electrode radii.

Stray capacitance is responsible for this undesirable effect. This capacitance is caused by the counter and reference electrodes, on the one hand, and the working electrode, on the other.

1.4.4.2. Shieldings to Reduce Stray Capacitance

In order to work with small concentrations, very small microelectrodes, and fast scan rates at the same time, improvements to the basic design of microelectrodes such as shieldings[51,52,] have been proposed. A significant source of capacitance can arise

from the dielectric properties of the insulator body. In effect, the inner conductor, the electrode insulator, and the electrolyte solution create a capacitance in parallel with the interfacial electrode-solution capacitance.

When working with sub-micron electrodes, Wipf et al[53] carried out calculations and measurements of electrode capacitance. Differences in capacitance between 0.32 μm radius electrode and that of a 0.95 μm radius electrode were investigated and reported. The difference is due to different construction methods used in the fabrication of the two microelectrodes rather than the difference in electrode radius. The large capacitance observed at the 0.95 μm radius electrode arises from the use of silver epoxy injected inside the electrode for electrical connection of the hook-up wire to the micro-wire. The silver epoxy coats the interior walls of the glass tube and provides a large inner-conductor surface area and, thus, a large capacitance. The capacitance of the 0.32 μm radius electrode is considerably reduced by connecting the electrode wire directly to a coaxial cable. The outer conductor (or shielding) was grounded, further reducing the capacitance at the smaller electrode. The capacitance of the insulator was greatly reduced by using aluminium foil wrapped around the electrode body up to the electrode tip and slipping a glass tube around the foil/electrode. The tube was sealed in place with epoxy to prevent solution access to the foil. The foil was connected to electrical ground which has the effect of shorting the electrode body capacitance.

Working with somewhat larger (2 μm and 5 μm radius) electrodes, Tschuncky and Heinze[54] also used coaxial cable as a hook-up wire and made the connection to the micro-wire with a small amount of solder rather than the silver epoxy. They then went on to describe a completely new variant of electrode construction. This involved placing a second wire in the glass tube, identical to the hook-up wire, which has no microwire attached to it and hence no connection to the solution. This wire was placed parallel to the microelectrode hook-up wire and a special current follower allowed one to measure and subtract the signal at both the microelectrode hook-up wire and this second capacitance wire simultaneously. A pure capacitive signal can then be obtained from this second wire giving the stray capacitance, which is a capacitance of the working electrode versus the reference and counter electrodes.

The voltammograms obtained show the Faradaic signal and the difference of the capacitive currents measured at the microelectrode hook-up wire and the second unconnected wire and are known as subtractive scan voltammograms.

Also in this work, a novel method was used for connecting Wollaston wires to hook-up wires without the aid of silver epoxy or solder. The hook-up wire and the Wollaston wire are fixed in position and joined together by using a Bunsen flame to seal them in the glass tubing.

The success of these microelectrode improvements is demonstrated by cyclic voltammograms at scan rate = 20,000 V/s which show the progressive reduction in the capacitive current with each alteration.

1.4.5. Other Microelectrode Design Variants

1.4.5.1. Platinum Electrodes

Abruña and Pendley[55] designed a method for platinum microelectrode fabrication which had the following properties.

1. Extremely quick and easy.
2. Allowed for the construction of very small microelectrodes (typically with total outer diameters between 1 and 5 μm).
3. Gave a smooth taper and excellent metal to glass seal.

This method involved pulling annealed platinum wire (75 μm) placed inside a borosilicate pipette to give microelectrodes of 1-5 μm in total tip diameter. It was noted that it was essential that the platinum wire be annealed and not hard drawn. Hard-drawn platinum wire can be used to make microelectrodes, but there is no reduction in the wire's diameter upon pulling.

Using the Abruña / Pendley method, platinum disk electrodes of extraordinarily small diameters can be prepared. From the magnitude of the limiting current, they

estimated the diameter of a platinum disk to be about 27 angstroms, which they believed was the smallest ever reported in 1990.

Lewis et al[9] developed a method that allowed routine fabrication of electrodes with electrochemical radii as small as 10 angstroms. This fabrication procedure was a two-step method with the first step being an electrochemical etching of a 0.5 mm diameter Pt or Pt-Ir (70:30) wire. The etched wires were then translated at 0.10 mm/s through an electrically heated molten glass bead. The size of the aperture in the resultant glass coating was related to the translation velocity and to the temperature of the molten glass. At a constant wire translation velocity, the effective aperture radius increased with increasing glass melt temperature. Precise control over the temperature and translation velocity was required in order to fabricate the smallest aperture structures. So by controlling the size of the apertures giving the exposed metal area, microelectrodes with radii as low as 10 angstroms could be fabricated.

However, it is important to note that these "nanodes" do not comply with the definition of a microelectrode[3] given in Section 1.2, Page 3 which states that the critical dimension of a microelectrode should be much greater than the thickness of the electrical double layer, which is typically 10 to 100 Å. Where the electrode radius is smaller than the double layer thickness, non-ideal responses may be observed and the data cannot be analysed using conventional models based on linear or radial diffusion. To understand the impact of the electrochemical double layer, its structure must be considered.

The solution side of the double layer is made up of several layers. The layer closest to the electrode, the inner layer, contains solvent molecules and sometimes other specifically adsorbed species, e.g., ions or molecules.[18] This inner layer is also called the compact, Helmholtz, or Stern layer. The locus of the electrical centres of the specifically adsorbed ions is called the inner Helmholtz plane. Solvated ions can only approach the metal to a distance further out than the inner Helmholtz plane, the locus of centres of these nearest solvated ions is called the outer Helmholtz plane. The interaction of the solvated ions with the charged metal of the electrode involves only long range electrostatic forces, so that their interaction is essentially independent of the chemical properties of the ions. These ions are said to be non-specifically

adsorbed. Because of thermal agitation in the solution, the non-specifically adsorbed ions are distributed in a three-dimensional region, called the diffuse layer, which extends from the outer Helmholtz plane into the bulk of the solution. There is a potential profile across this double-layer region and the structure of the layer can affect the rates of electrode processes. Because a non-specifically adsorbed electroactive species can only approach the electrode to the outer Helmholtz plane, the total potential it experiences is less than the potential between the electrode and the solution by an amount equal to the potential drop across the diffuse layer. Obviously, the electrochemical response of electrodes whose critical dimension is close to or less than the thickness of the double layer will be affected by the structure of this layer.

1.4.5.2. Gold Microelectrodes.

The use of gold wires presents some difficulties with respect to the choice of glass tubing for microelectrode fabrication. For most purposes, glass is the best choice as an insulator because of its inertness, low cost, availability, and the fact that it is easily machined and polished. Nevertheless, the reproducible construction of well-sealed metal electrodes is not an easy task. The main difficulty for reproducing such electrodes stems from the relatively big difference between the thermal expansion coefficients of the metal and the glass. In order to fabricate well-sealed platinum electrodes a "soft", i.e., borosilicate, glass is required.

Malem and Mandler[56] have addressed this fabrication problem for gold microelectrodes by centering a gold wire in a Pasteur pipette, which was previously cut and sealed by flame. Special glass powder (used for glass soldering) with a similar thermal expansion coefficient to gold is then added until most of the wire is covered. After tapping, the pipette is heated slowly to 420° C (10°C/min) and left at this temperature for one hour. After slow cooling, electrical connection to the exposed end of the gold wire is achieved using silver epoxy. Exposure of the gold microdisk is carried out in the usual way. The effectiveness of this powdered glass technique is demonstrated by comparing the cyclic voltammograms for gold electrodes in 1 M H_2SO_4, one of which was imbedded in standard borosilicate glass, the other sealed in this special soldering glass. The imperfect sealing of the gold

electrode in borosilicate glass is shown by the characteristic tilting of the current-voltage curve which is due to a decrease of the cell resistance. The perfect sealing of the soldering glass is shown by the lack of tilting of the current- voltage curve.

Evidently, there is a wide range of materials and techniques currently available for microelectrode fabrication. Depending on their experimental objectives, electrochemists may select a particular material and fabrication method which will define the performance of the microelectrode.

As much of this thesis is based on current electron transfer theory, it is essential now to describe, as concisely as possible, the origins of this theory. An understanding of electron transfer theory is a prerequisite to assembling the electron transfer model developed here. The construction of a cyclic voltammogram simulation model based on electron transfer theory is a primary goal of this thesis.

1.5. Electron Transfer Theory

1.5.1. Introduction

A great deal of work has gone into theoretical efforts to describe the effects of molecular structure and environment on electron transfer kinetics. The goal of most workers in the theoretical area of research is to make predictions that can be tested by experiments, so that an understanding of the fundamental structural and environmental factors that cause reactions to be kinetically fast or slow[18] can be obtained. Having gained this theoretical understanding, it is possible to design superior new systems (e.g., electron transfer rate controlling monolayers, molecular switches or diodes, etc.) for many scientific and technological purposes.

Major contributions were made in this area in the 1950s and 1960s by Marcus,[57,58,59,60] and these theoretical approaches still form the basis for modern electron transfer models.[5-8]

Electron transfer reactions, whether homogeneous or heterogeneous, are radiationless electronic rearrangements of a reacting complex. There are, accordingly, many common elements between theories of electron transfer and treatments of

radiationless deactivation in excited molecules. Since the transfer is radiationless, the electron must move from an initial state (on an electrode or a reductant) to a receiving state (on another solvated species or an electrode) of the same energy. This demand for isoenergetic electron transfer is a fundamental aspect with important consequences throughout chemistry.

For example, an activation overpotential for reduction can sometimes be ascribed to a need to adjust the electrode potential so that the energies of the available electrons on the electrode match the energies where the densities of possible receiving states is high. Reduction would be allowed energetically at the potential corresponding to the lowest empty states, but it would be much faster at more negative potentials where many more receiving states are available. After the transfer, the electron could drop down into lower states on the solute, so that the final state is reached by either route.

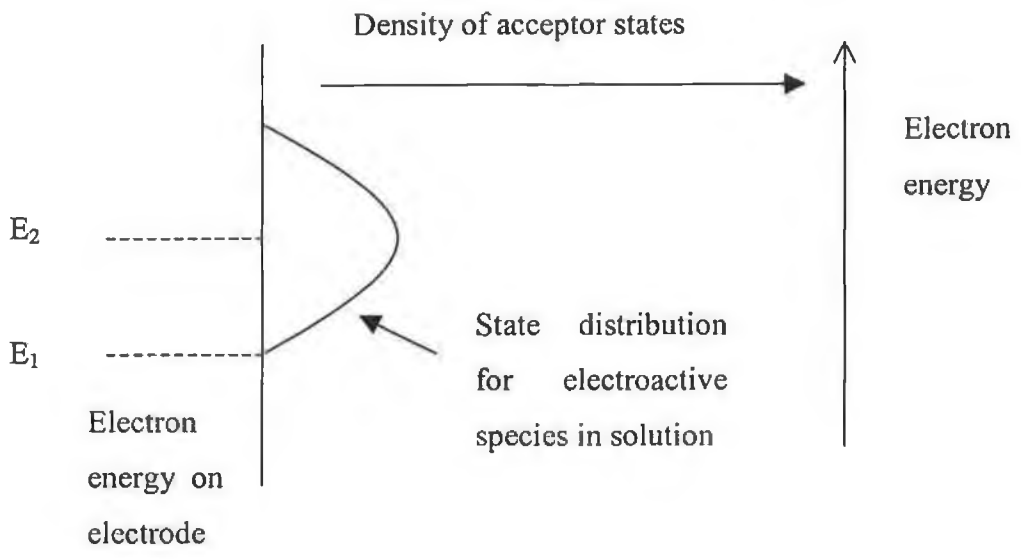

Figure 1.3. The effect of acceptor state density on the rate of electron-transfer. The horizontal axis on the solution side shows the density of states. Reduction is possible at the potential E_1, but it may occur more rapidly at the more negative value E_2, where a higher density of acceptor state exists. From Bard and Faulkner.[18]

Another important aspect of most theories, is an assumption that the reactants and products do not change their configurations during the actual act of transfer. This is based on the Franck-Condon principle,[61] which says, in part, that nuclear momenta and positions do not change on the time scale of electronic transitions. Where this applies, the condition that the reactants and products share a common nuclear configuration at the moment of electron transfer also applies. Thus, the rate constant for electron transfer has to include a factor accounting for the frequency with which a reactant molecule becomes distorted into a configuration that lies also on the energy surface describing the product. This configuration may be difficult to achieve if the reactant and product are structurally very different, and the rate of electron transfer may be correspondingly slow. A similar concept is the basis for the rationale for the very fast charge transfer rates observed for couples involving aromatic hydrocarbons and their radical ions.[62] In those cases, very small structural changes arise upon oxidation and reduction. Accounting quantitatively for structural effects is complex, and differences in the approach to this aspect comprise some of the most important distinctions among the various electron transfer theories.

1.5.2. Butler-Volmer Model.

The Butler-Volmer formulation of electrode kinetics[63,64] is the oldest and least complicated model constructed to describe heterogeneous electron transfer. However, it is a macroscopic model that does not explicitly consider the individual steps in the electron-transfer event. Consider the following reaction in which an oxidised species, Ox, e.g., $[Ru(2,2'\text{-bipyridyl})_3]^{3+}$, is converted to the reduced form, Red, e.g., $[Ru(2,2'\text{-bipyridyl})_3]^{2+}$, by adding a single electron.

$$Ox + e \underset{k_f}{\overset{k_b}{\rightleftarrows}} Red$$

As a starting point, consider the situation for a chemical, as opposed to an electrochemical, reaction. Simplified activated complex theory assumes an Arrhenius type dependence of the forward rate constant, k'_f, on the chemical free energy of activation, $\Delta G^{\neq}$:

$$k_f = \frac{kT}{h}\exp\left(\frac{-\Delta G^{\neq}}{RT}\right) \tag{16}$$

where k, h and R are the Boltzmann, Planck and gas constants, respectively, and T is the absolute temperature. However, electrochemistry has the significant advantage that the driving force for the reaction can be controlled instrumentally. This capability contrasts sharply with homogeneous redox reactions where one must change the temperature, or the chemical structure of a reactant, if the driving force is to be altered. Therefore, for a heterogeneous electron transfer reaction, the free energy of the reaction depends on the electrical driving force, i.e., the applied potential relative to the formal potential, $E^{o\prime}$, and $\Delta G^{\neq}$ must be replaced by the electrochemical free energy, $\Delta\overline{G}^{\neq}$.

The electrochemical rate constant for the forward reaction, i.e., reduction, is given by:

$$k_f = \frac{kT}{h}\exp\left(\frac{-\Delta\overline{G}_f^{\neq}}{RT}\right) \tag{17}$$

As illustrated in Figure 1.4, both "chemical" and "electrical" components contribute to the electrochemical free energies of activation. The dashed line of Figure 1.4 shows that a shift in the potential of the electrode to a value E, changes the energy of electrons within the electrode by –nFE. Under these circumstances, the barrier for the oxidation process, $\Delta\overline{G}_b^{\neq}$, is now less than $\Delta G_b^{\neq}$ by a fraction of the total energy change. This fraction is designated as $(1-\alpha)$ where α is the transfer coefficient. It takes on values between zero and unity depending on the shape of the free energy curves in the intersection region. Thus, the free energies of activation can be separated as described by Equations 18 and 19.

$$\Delta\overline{G}_f^{\neq} = \Delta G_f^{\neq} + \alpha nFE \tag{18}$$

$$\Delta\overline{G}_b^{\neq} = \Delta G_b^{\neq} - (1-\alpha)nFE \tag{19}$$

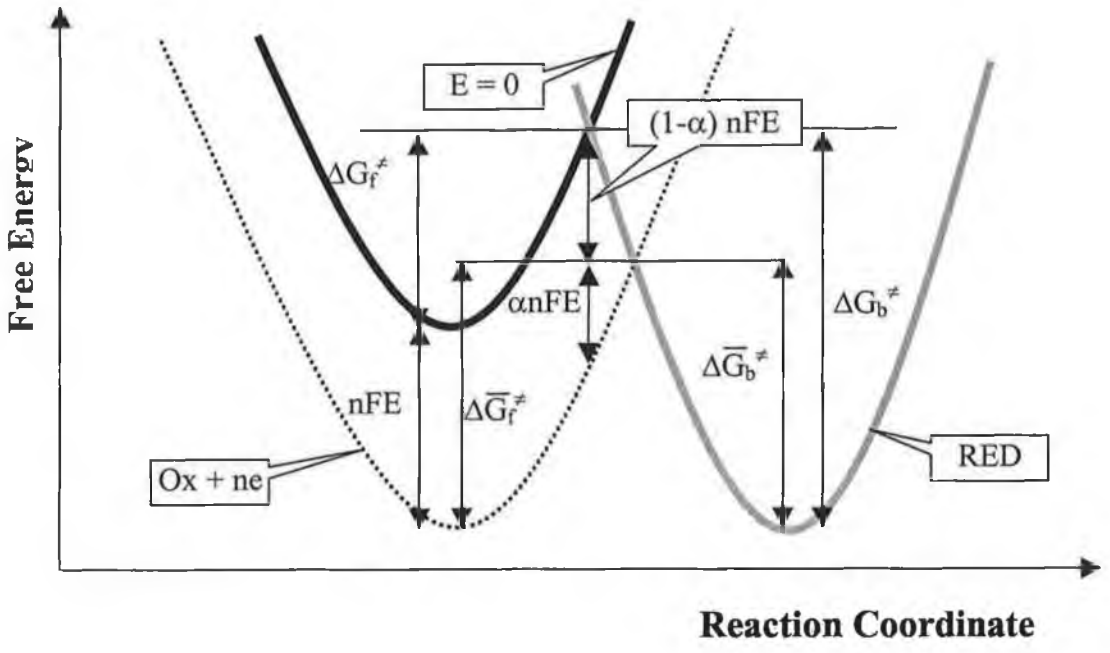

Figure 1.4. Detailed illustration of the effects of potential on the free energies of activation for oxidation and reduction according to the Butler-Volmer formulation of electrode kinetics.

Substitution into Equation 17 yields the following expressions describing the potential dependence of the reduction and oxidation reactions, respectively.

$$k_f = \frac{kT}{h}\exp\left(\frac{-\Delta G_f^{\neq}}{RT}\right)\exp\left(\frac{-\alpha nFE}{RT}\right) \tag{20}$$

$$k_b = \frac{kT}{h}\exp\left(\frac{-\Delta G_b^{\neq}}{RT}\right)\exp\left(\frac{(1-\alpha)nFE}{RT}\right) \tag{21}$$

The first exponential term in both equations is independent of the applied potential and is designated as $k_f°$ and $k°_b$, for the forward and backward processes, respectively. They represent the rate constants for the reaction at equilibrium, i.e., for a solution containing equal concentrations of both oxidised and reduced forms. However, the system is at equilibrium at E°′ and the product of the rate constant and the bulk concentration are equal for the forward and backward reactions, i.e., $k_f°$ must equal $k_b°$. Therefore, the standard heterogeneous electron transfer rate constant is designated simply as k°. Substitution into Equations 20 and 21 yields the Butler-Volmer equations.

$$k_f = k^{\circ}\exp\left(\frac{-\alpha nF(E-E^{\circ'})}{RT}\right) \tag{22}$$

$$k_b = k^{\circ}\exp\left(\frac{(1-\alpha)nF(E-E^{\circ'})}{RT}\right) \tag{23}$$

The dynamics of the system are described by k° and its units are cm s^{-1} and s^{-1} for solution phase and adsorbed reactants, respectively. A redox couple with a large k° will establish the equilibrium concentrations given by the Nernst equation on a short timescale. Kinetically facile systems of this type require high speed electrochemical techniques to successfully probe the electrode dynamics. The largest k° values that have been reliably measured are of the order of 10 cm s^{-1} and are associated with mechanistically simple reactions, i.e., there are no coupled chemical kinetics or significant structural differences between oxidised and reduced forms.

The empirical Butler-Volmer formulation of electrode kinetics provides an experimentally accessible theoretical description of electrode kinetics. From a plot of the ln(k) vs. overpotential ($\eta = E - E^{\circ\prime}$) α and k° can be obtained from the slope and intercept, respectively.

However, the Butler-Volmer formulation is deficient in a number of respects. First, the prediction that the rate constants for simple outer sphere electron transfer reactions will increase exponentially with increasing electrical driving force agrees with experiment only over a limited range of overpotentials. The advent of microelectrodes allows heterogeneous electron transfer rates to be measured over very wide ranges of η. Experimentally, one finds that k initially depends exponentially on η but then becomes independent of the driving force for sufficiently large values. Second, the Butler-Volmer formulation fails to account for the known distance dependence of heterogeneous electron transfer rate constants. Third, it cannot predict how changes in the redox centre's structure or the solvent affect k°.

The Marcus theory directly addresses these issues and is widely accepted as the most powerful and complete description of both heterogeneous and homogeneous electron transfer reactions. The Marcus theory is therefore chosen as the preferred basis for the theoretical electron-transfer models constructed in this thesis and described in detail in Chapter 3.

1.5.3. Marcus Theory

Concentrate first on the standard heterogeneous electron transfer rate constant, k°, i.e., when the electrochemical driving force is zero. The transition state theory focuses on the intersection or crossover point of the free energy curves for the oxidised and reduced forms illustrated in Figure 1.5. In this formulation, the rate of reaction depends on the product of the number of molecules with sufficient energy to reach the transition state at a particular instant in time and the probability at which they cross over the transition state. The number of molecules at the transition state

depends on the free energy of activation, $\Delta G°$. Thus, the heterogeneous electron transfer rate constant is given by:

$$k^{\circ} = \upsilon \sigma \exp\left(\frac{-\Delta G^{\circ}}{RT}\right) \tag{24}$$

where υ is a frequency factor (s^{-1}) that describes the rate of reactive crossings of the transition state and σ is an equivalent reaction-layer thickness (cm).

The power of Marcus theory is that it provides a theoretical basis for these parameters and that it is amenable to testing through experiment. As illustrated in Figure 1.5, the Marcus theory assumes that the dependence of the free energy of activation on the reaction coordinate can be described as a simple parabola. This approximation assumes that each vibration involved in the activation of the redox centre behaves as a harmonic oscillator and that the solvent energy depends quadratically on the charge density of the molecule. Thus, the free energies of both outer sphere solvent reorganisation, ΔG_{os}, and inner-sphere vibrations, ΔG_{is}, contribute to the total free energy of activation, ΔG_{Total}, as described by Equation 25.

$$\Delta G_{Total} = \Delta G_{is} + \Delta G_{os} \tag{25}$$

The inner sphere free energy of activation represents the minimum energy required to change the internal structure of the redox centre to its nuclear transition state configuration.

Figure 1.5 also illustrates the Marcus reorganisation energies for oxidation, i.e., λ_{Ox}, and reduction, i.e., λ_{Red}. λ_{Ox} is defined as the vertical difference between the reduced and oxidised forms' free energies at the equilibrium nuclear configuration of the oxidised form for a reaction with zero driving force. λ_{Red} is defined as the vertical difference between the reduced and oxidised forms' free energies at the equilibrium nuclear configuration of the reduced form for a reaction with zero driving force.

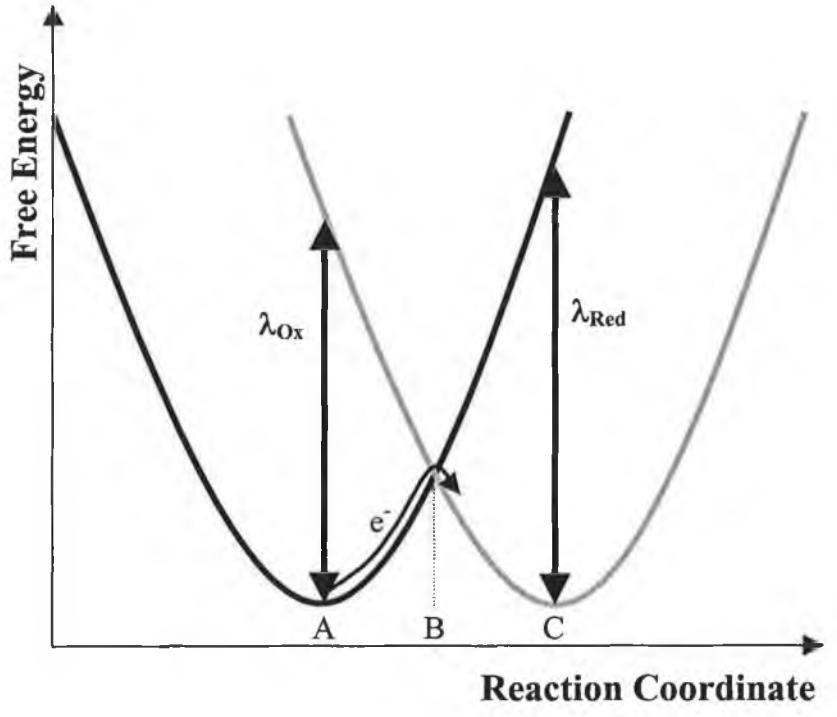

Figure 1.5. Plot of the free energy of the oxidised and reduced forms as a function of the normalised reaction coordinate. The Marcus reorganisation energies for oxidation and reduction are denoted by the double headed arrows. A and C denote the equilibrium nuclear configurations of Ox and Red, respectively, B denotes the configuration of the transition state. The diagram represents the situation in which the equilibrium potential energies of Ox and Red are identical.

The outer sphere, or solvent, component of the free energy of activation arises because the charge on the redox centre typically changes significantly during the electron transfer event. The free energy of activation for outer sphere reorganisation depends on both the static and optical dielectric constants of the solvent as described by Equation 26:

$$\Delta G_{os} = \frac{n^2 e^2}{32\pi\varepsilon_o r}\left(\frac{1}{\varepsilon_{op}} - \frac{1}{\varepsilon_s}\right) \qquad (26)$$

where n is the number of electrons transferred, e is the electronic charge, ε_o is the permittivity of free space, r is the molecular radius, ε_{op} and ε_s are the optical and static dielectric constants, respectively. Therefore, unlike the empirical Butler-Volmer theory, in the Marcus formulation, the heterogeneous electron transfer rate constant is sensitive to both the structure of the redox centre and the nature of the solvent.

The frequency factor, υ, of Equation 24 describes the rate of reactive crossings of the transition state. Thus, as described by Equation 27, υ is the product of the rate of motion along the reaction coordinate, υ_n, and the probability of crossing over from the reactant to product hypersurfaces once the transition state has been reached, κ_{el}.

$$\upsilon = \upsilon_n \kappa_{el} \qquad (27)$$

For reactions in which electron transfer significantly distorts the bond lengths and angles of the molecule, i.e., $\Delta G_{is} >> \Delta G_{os}$, the frequency factor is typically in the range 10^{13} to 10^{14} s^{-1}. In contrast, if the molecular structure is largely unperturbed by redox switching, then υ_n is dictated by the dynamics of solvent reorganisation and for typical electrochemical solvents is in the range of 10^{11} to 10^{12} s^{-1}.

The magnitude of κ_{el} varies from zero to unity depending on whether the electronic coupling between the reactant and the electrode is weak or strong. In the case of strong electronic coupling, as shown in Figure 1.6 there is significant flattening of the reaction hypersurface close to the transition state.

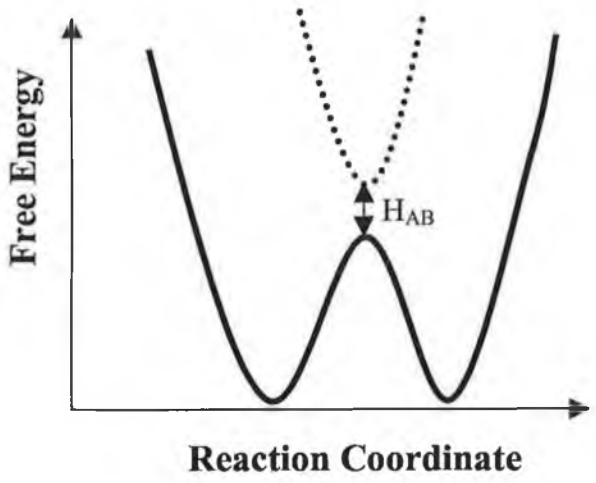

Figure 1.6. Reaction coordinate diagram for an adiabatic heterogeneous electron transfer showing flattening of the reaction hypersurface.

Under these circumstances, the rate of crossing the barrier region is reduced but the probability of electron transfer actually occurring once the transition state has been achieved, is close to unity. Reactions involving strong electronic coupling are termed adiabatic and the reaction rates are sensitive to the dynamics of solvent relaxation. Heterogeneous electron transfers are often assumed to be adiabatic because it simplifies the kinetic analysis. However, this assumption is often not justified and invalidates much of the subsequent analysis. In contrast, non-adiabatic reactions involve weak coupling and the transition state appears as a sharp cusp similar to that illustrated in Figure 1.5 and $\kappa_{el} \rightarrow 0$.

1.5.4. Potential Dependence of the Rate Constant

The standard heterogeneous electron transfer rate constant, k°, depends on both a frequency factor and a Franck-Condon barrier:[65,66,67,68]

$$k^{\circ} = A_{et} \exp(-\Delta G^{\neq} / RT) \tag{28}$$

where A_{et} is the pre-exponential and $\Delta G^{\neq}$ is the electrochemical free energy of activation.[69] For an adiabatic reaction, the pre-exponential factor is given by the product of κ_{el}, the electronic transmission coefficient and υ_n, a frequency factor dictated either by nuclear or solvent motion. In contrast, for a nonadiabatic reaction, $\kappa_{el} << 1$ and the pre-exponential factor is dictated by the electron hopping frequency in the activated complex, υ_{el}.

One approach to decoupling these two contributions from electronic coupling effects (A_{et}) and free energies of activation ($\Delta G^{\neq}$) is to use classical temperature-resolved measurements of k° to measure the free energy of activation, $\Delta G^{\neq}$, allowing A_{et} to be determined. In this way, information about the strength of electronic coupling can be obtained.[70,71] A second method involves measuring electron-transfer rate constants at a single temperature over a broad range of reaction driving forces. For example, Finklea and Hanshew,[5] have assembled a model describing through-space electron tunnelling which provides a good description of electron tunnelling in monolayers. In this model, the cathodic rate constant is given by integral over energy (ϵ) of three

functions: (a) the Fermi function for the metal n(ϵ), (b) a Gaussian distribution of energy levels for acceptor states in the monolayer $D_{Ox}(\epsilon)$, and (c) a probability factor describing electron tunnelling at a given energy, P(ϵ).

$$k_{Ox}(\eta) = \mathrm{A} \int_{-\infty}^{\infty} D_{Ox}(\varepsilon)\ n(\varepsilon)\ \mathrm{P}(\varepsilon)\ d\varepsilon \tag{29}$$

The zero point of energy is taken as the Fermi level of the metal at the particular overpotential of interest. The Fermi function describes the distribution of occupied states within the metal and is defined by:

$$n(\varepsilon) = \left(\frac{1}{1 + \exp[(\varepsilon - \varepsilon_F)/k_B T]} \right) \tag{30}$$

where k_B is the Boltzmann constant. The density of acceptor states is derived from the Marcus theory,[57,72] and can be represented by Equation 31.

$$D_{Ox}(\varepsilon) = \exp\left[-\frac{(\varepsilon + \eta - \lambda)^2}{4k\lambda T} \right] \tag{31}$$

where λ is the reorganisation energy. The probability of direct elastic tunnelling[73,74] through a trapezoidal energy barrier of height E_B can be approximated by Equation 32.

$$P(\varepsilon) = (E_B - \varepsilon + e\eta/2)\exp(-\beta d) \tag{32}$$

where E_B is the average barrier height at zero overpotential and d is the electron transfer distance. β is the tunnelling constant and is given by

$$\beta = (2(2m)^{1/2}/\hbar)(E_B - \varepsilon + e\eta/2)^{1/2} \tag{33}$$

where m is the mass of the electron.

Chidsey,[75] Creager,[7] and Murray,[76] have modelled non-adiabatic heterogeneous electron transfer for long-chain alkane-thiol monolayers using an expression similar to Equation 29 except that the energy dependent prefactor in the tunnelling probability expression is excluded.

The current for the reaction of an immobilised redox centre following first order kinetics is:[40]

$$i_F = nFA(k_{Ox}(\eta)\,\Gamma_{Red,\,\eta} - k_{Red}(\eta)\,\Gamma_{Ox,\,\eta}) \qquad (34)$$

where $\Gamma_{Red,\,\eta}$ and $\Gamma_{Ox,\,\eta}$ are the instantaneous surface coverages of the oxidised and reduced species and $k_{Ox}(\eta)$ and $k_{Red}(\eta)$ are the reaction rate constants given by Equation 29 or its complement in which $n(\epsilon)$ is replaced $(1-n(\epsilon))$ and $-\lambda$ is replaced by $+\lambda$ in Equation 31 with or without a tunnelling probability function.

The sensitivity of the heterogeneous electron transfer rate constant to the overpotential depends on the extent of electronic coupling between the reactant and the electrode.[77] For a strongly coupled electron transfer reactions, i.e., an adiabatic process, electron transfer occurs predominantly through states near the Fermi level of the electrode. For non-adiabatic systems, electrons with energies below the Fermi level may be transferred and one must sum over all electron energies rather that just at the Fermi level, E_f.

The effects of the strength of the electronic coupling on the rate constant only become apparent at high driving forces, i.e., when the overpotential is more than half the reorganisation energy. As discussed in a later section, perhaps the most significant consequence of Equations 28 and 29 is that, unlike the Butler-Volmer theory, they both predict curvature in plots of ln k vs. η. For extremely large driving forces, k no longer depends on the overpotential reaching a maximum value when η is approximately equal to λ - this is the "*Marcus inverted region*" for a heterogeneous electron transfer reaction.

1.5.5. Evidence for Marcus Inverted Region

There have been many attempts to detect the inverted region predicted by Marcus theory, but until 1984 almost all failed to observe a significant decrease in rate constants at high overpotentials. However, Creutz and Sutin[78] did observe a few bimolecular examples showing a slight decrease in rate constant for $-\Delta G^0 > 1.5$ eV. The first indication that the inverted region might exist came from a study by Beitz and Miller[79] of the reactions of electrons trapped in a glassy matrix. The first definitive observations were made in 1984 by Miller et al[80] on intermolecular charge-shift reactions between the biphenyl radical anion and various acceptors in a rigid low-temperature glass.

Weber and Creager[7] while working with voltammetric data acquired over a wide range of scan rates for ferrocene oxidation/reduction in self-assembled monolayers of N-(15-mercaptopentadecyl) ferrocenecarboxamide coadsorbed with 16-mercaptohexadecanol unto gold electrodes, have shown the electrochemical analogue of the Marcus inverted region. This is where the rate of electron-transfer does not decrease with increasing driving force, as in molecular donor-acceptor electron transfer, rather it becomes independent of driving force. They present a series of calculated log ($k_{red} + k_{ox}$) vs. overpotential curves for a specific value of k^o and for several values of the reorganisation energy. The curves are similar to those reported by Chidsey[75] and also by Finklea et al[5,81] on different systems. The curves show that if the reorganisation energy is made extremely large, then the calculated rate constant sum does indeed increase almost exactly logarithmically with overpotential, as in the simple Butler-Volmer model. This can be understood by noting that the parabolic reaction co-ordinate assumed in the Marcus treatment is closely approximated by a linear function when the applied potential is much less than the reorganisation energy. However, as the reorganisation energy decreases, the calculated curves begin to level off at high overpotential, until a pair of plateau regions is predicted for which the sum of the reductive and oxidative rate constants is nearly independent of potential. This occurs when the overpotential is much larger than the reorganisation energy and reflects the fact that the entire distribution of redox-active molecules with states available to transfer electrons (unoccupied states for reduction, occupied for oxidation) is matched by states in the electrode that are also available to transfer

electrons (occupied states for reduction, unoccupied for oxidation). At this point, increasing the driving force by applying a greater overpotential does not make any new states available for electron transfer between any two states and therefore the rate does not change.

1.5.6. Electron Transfer Dynamics of Solution Phase Reactants

Heterogeneous electron transfer rate constants can be conveniently measured using transient electrochemical techniques such as cyclic voltammetry and chronoamperometry. As illustrated previously, research in this area is dominated by the use of microelectrodes. As described in Section 1.3. and illustrated in Figure 1.2, at short times the diffusion layer thickness is much smaller than the microelectrode radius and the dominant mass transport mechanism is planar diffusion. Under these conditions, the classical theories, e.g., that of Nicholson and Shain,[82] can be used to extract kinetic parameters from the scan rate dependence of the separation between the anodic and cathodic peak potentials. Rate constants for solution phase species using this theory will be calculated in Chapter 4. However, there are several possible difficulties to extracting accurate heterogeneous electron transfer rate constants using transient electrochemical techniques. First, the Faradaic and charging currents must be separated. For example, in cyclic voltammetry, the charging current increases proportionally to the scan rate, while the Faradaic current for a diffusive species is proportional to the square root of the scan rate. These dependencies cause the ratio of the Faradaic to charging current ratio to *decrease* with *increasing* scan rate. One strategy for dealing with this problem is to measure the double layer charging current in blank electrolyte and then to subtract this signal from the total current observed in the presence of the analyte of interest. The second difficulty is the problem associated with ohmic drop. Determining heterogeneous electron transfer rate constants often relies on measuring the scan rate dependence of the peak-to-peak separation, ΔE_P. Ohmic effects represent a serious problem, not only because they will cause a significant ΔE_P to be observed even when heterogeneous electron transfer is fast, but also because the magnitude of the ohmic effect depends on the experimental timescale. Several strategies have been used to decrease ohmic effects. First, the Faradaic information is extracted by means of convolution of the voltammograms with the diffusion operator $(\pi t)^{-1/2}$. Second, the experimental

voltammogram is simulated using a model that incorporates ohmic and capacitive factors. Third, ohmic drop is corrected for on-line using positive feedback circuitry.

As shown in Table 1.1, the heterogeneous electron transfer dynamics of a diverse range of organic and inorganic species have been investigated using transient techniques including, anthracene,[83] anthraquinone, benzoquinone,[84] ferrocene,[12] ferrocyanide,[85] 9-fluorenone,[86] and $[Ru(bpy)_3]^{2+}$. The magnitudes of k° vary significantly, for example, large poly-aromatic hydrocarbons that can be reduced with very little change in bond lengths or angles exhibit very large standard heterogeneous electron transfer rate constants, e.g., k° for anthracene[87] is 3.3 cm s^{-1}. In contrast, where the structure of the molecule is significantly distorted by the redox reaction, or where the reaction involves multiple steps, k° values as small as 10^{-9} cm s^{-1} can be observed, i.e., electrode kinetics span ten orders of magnitude!

Table 1.1. Rate constants for heterogeneous electron transfer as determined using transient methods.

Analyte	**Electrode**[a]	**k^o / cm s^{-1}**
Anthracene	Au, 6.5 μm	3.46(0.55)
Anthraquinone	Pt cylinder, r = 25.4 μm, l < 0.25 cm	1.78(0.35)
Benzoquinone	Au, 6.5 μm	0.39(0.1)
Ferrocene	Au, 5 μm	3.1(1.1)
Ferrocyanide	C cylinder, r = 15 μm, l = 500 μm	0.0114(0.0022)
9-fluorenone	Pt, 6 μm	3
$[Ru(bpy)_3]^{2+}$	Au, 5 μm	2.5

[a] Dimension given is the radius of a microdisk electrode unless otherwise stated.

A useful strategy in trying to extend the upper limit of measurable electron transfer rate constants is to perform measurements at lower temperatures. This strategy is successful because even for heterogeneous electron transfers with negligible inner sphere reorganisation energies, activation barriers of the order of 20-25 kJ mol^{-1} are expected. Therefore, considerably slower rates of heterogeneous electron transfer are observed even by decreasing the temperature of the electrochemical cell by a few tens of degrees. Measurements of this type are greatly facilitated by microelectrodes since solvents, such as alcohols or nitriles, that remain liquid over a wide temperature range can be used without catastrophic ohmic effects. For example, Weaver and co-workers[88] investigated the ferrocene, *o*-nitrotoluene and nitrometisylene systems in acetonitrile, propionitrile, and butyronitrile at a gold microdisk using scan rates up to 10^4 V s^{-1} between 200 and 300 K. The experimental voltammograms were interpreted with the aid of simulated responses that accounted for the activation enthalpy, temperature-dependent diffusion coefficients, and double layer capacitance. For ferrocene, the standard heterogeneous electron transfer rate constants ranged from 0.083 cm s^{-1} at 198 K to approximately 5.5 cm s^{-1} at 298 K yielding an activation enthalpy of 20 kJ mol^{-1}.

1.6. Adsorbed Monolayers.

It is important to outline the current state of knowledge with respect to research on self-assembled and spontaneously adsorbed monolayers as it is a primary goal of this work to simulate the cyclic voltammetric responses of adsorbed species.

While experiments involving solution phase reactants have provided deep insights into the dynamics of heterogeneous electron transfer, the magnitude of the diffusion controlled current at short times ultimately limits the maximum rate constant that can be measured. For diffusive species, the thickness of the diffusion layer, δ, is defined as $\delta = (\pi Dt)^{1/2}$ and is therefore proportional to the square root of the polarisation time, t; D is the diffusion coefficient. One can estimate that the diffusion layer thickness is approximately 50 Å if the diffusion coefficient is $1x10^{-5}$ cm^2s^{-1} and the polarisation time is 10 ns. Given a typical bulk concentration of the electroactive species of 1 mM, this analysis reveals that only 10,000 molecules would be oxidised or reduced at a 1 μm radius microdisk under these conditions. The average current for this

experiment is only 170 nA, which is too small to be detected with nanosecond time resolution.

One successful approach to eliminating this diffusion limitation is to use self-assembled or spontaneously adsorbed monolayers. When immobilised on an electrode surface the electroactive species no longer needs to diffuse to the electrode to undergo electron transfer. Moreover, the electroactive species is preconcentrated on the electrode surface. For example, in the situation considered above, there would be approximately 1.7×10^{-20} mol of electroactive material within the diffusion layer. Given that the area of a 1 μm disk is approximately 3.1×10^{-8} cm^2, this translates into an "equivalent surface coverage" of about 5.4×10^{-13} mol cm^{-2}. In contrast, the surface coverage, Γ, observed for dense monolayers of adsorbates is typically more than two orders of magnitude larger with coverages of the order of 10^{-10} mol cm^{-2} being observed. This higher concentration gives rise to much larger currents that are easier to detect at short timescales.

1.6.1. Electron-Transfer Kinetics in Organised Monolayers

Many research papers have been written on the general subject of electron-transfer kinetics in organised monolayers. That this is an area of intense study is primarily due to the well-defined structural character of self-assembled monolayers which provides molecular surfaces of great potential for practical applications. Also, the idea of placing a redox centre (in the controlled chemical environment of an adsorbate) at a fixed distance from the surface of a microelectrode (set by the length of the bridging ligand) is particularly attractive to electrochemical researchers. Important questions that can be addressed using this approach include: how is the rate of electron transfer affected by the groups surrounding the redox centre? how is the rate of electron-transfer affected by the length of the bridging ligand (i.e., the distance from the electrode or microelectrode surface)? what about the level of aromaticity of the bridging ligand? how does the electron transfer actually occur? are through space or through-bond tunnelling mechanisms important? These are just a sample of the type of questions which researchers hope to answer by studying the electrochemistry of monolayers.

There are many different types of compounds used to construct monolayers for research purposes. However, it is possible to identify two main families of compounds which have attracted considerable interest in the electrochemical literature, namely, the alkanethiols (with attached redox centres of ferrocene or ruthenium complexes) and complexes of osmium with attached groups such as bpy (i.e., 2,2′-bipyridyl), p0p (i.e., 4,4′ –bipyridyl), p2p (i.e., 1,2-bis(4-pyridyl)-ethane), and p3p (i.e., 4,4′-trimethylenedipyridine).

1.6.2. Monolayers Based on AlkaneThiols

Finklea and Hanshew's[5] work on organised thiol monolayers with attached pentaammine(pyridine) ruthenium redox centres is a prime example of the type of electrochemical studies which have been carried out on monolayer coated electrodes. In this work, the ability to control spacing with accuracy and high resolution is used to design experiments (both cyclic voltammetry and chronoamperometry) which carefully test both the Marcus model of electron transfer and tunnelling theory. Marcus theory alone (tunnelling not included) predicts that Tafel plots will be curved, with the absolute slope decreasing as the absolute overpotential increases. At sufficiently large overpotentials the rate constant becomes independent of overpotential (the equivalent of the Marcus "inverted" region in homogeneous electron transfer). If through-space tunnelling is included, then the Tafel plot becomes asymmetrical. The Tafel plots for the ferrocenethiol monolayers used by Finklea and Hanshew did not exhibit the predicted asymmetry of through-space tunnelling. They used this evidence along with the results of other electrochemical tests on the monolayers to hypothesise that the mechanism of electron transfer from the redox centre to the electrode and vice versa was through-bond tunnelling.

The physical conformation of the monolayer itself was also investigated. Studies of the reversible (i.e., slow scan rate) cyclic voltammograms of the HS-C_n-Ru monolayers[5] reveal that the redox centres are fully solvated by the aqueous electrolyte. The formal potentials are identical for all of the redox centres, which implies that the local environment around each redox centre is remarkably uniform. All of the redox centres are rapidly exchanging electrons with the electrode on the

time scale of the experiment. The reversible CV data point to an ordered structure with all of the redox centres outside of the hydrocarbon portion of the monolayer.

Murray et al[8] also studied the electron transfer kinetics of monolayers based on ferrocene alkanethiols. In this case, low temperatures (125 K to 175 K) were used in the experiments. In this study, all ferrocene alkanethiol monolayers in the low temperature solvent exhibited substantial broadening of cyclic voltammograms and non-linear Ln(i) vs. time plots in potential step experiments. The peak broadening is attributed to kinetic dispersion caused by intercalation of the organic solvent into the monolayer. Reorganisation energies are calculated from the CV data and are deemed to be unreliable due to the presence of the peak broadening.

Potential step measurements show that the rate constants do not follow the exponential increase with overpotential classically expected from Butler-Volmer theory, but instead fold over at higher overpotential as anticipated by Marcus theory when overpotential is not negligible with respect to reorganisation energy. Murray[8] makes the point that for kinetically uniform ferrocene monolayers in aqueous acid, the variation in rate constant with overpotential is symmetrical about overpotential=0. As per Finklea,[5] through bond tunnelling is hypothesised to be the electron transfer mechanism.

1.6.3. Monolayers Based on Osmium Complexes

Forster and co-workers[6,70,89,90,91] and Abruña and co-workers[92,93,94] have led research into the electrochemistry of spontaneously adsorbed monolayers based on osmium compounds with attached groups such as bpy, p0p, p2p and p3p and in some cases have looked at ruthenium analogues.

The redox properties of electroactive centres within organised monolayers of these compounds have attracted interest for, primarily, the following reason. These adsorbed monolayers enable both the nature of the chemical functional groups and their topology to be controlled, thus allowing the effects of both chemical and geometric properties on the overall transfer rate to be explored.

Forster and Faulkner[6,79] have studied the equilibrium properties and fundamental electron-transfer characteristics and the effects of solvent, potential, and temperature on electron-transfer dynamics of spontaneously adsorbed monolayers of $[Os(bpy)_2Cl(pNp)]^+$, where bpy is 2,2′-bipyridyl and pNp is 4,4′-bipyridyl, 1,2-bis(4-pyridyl)ethane, or 4,4′-trimethylenepyridine (see Figure 1.7)

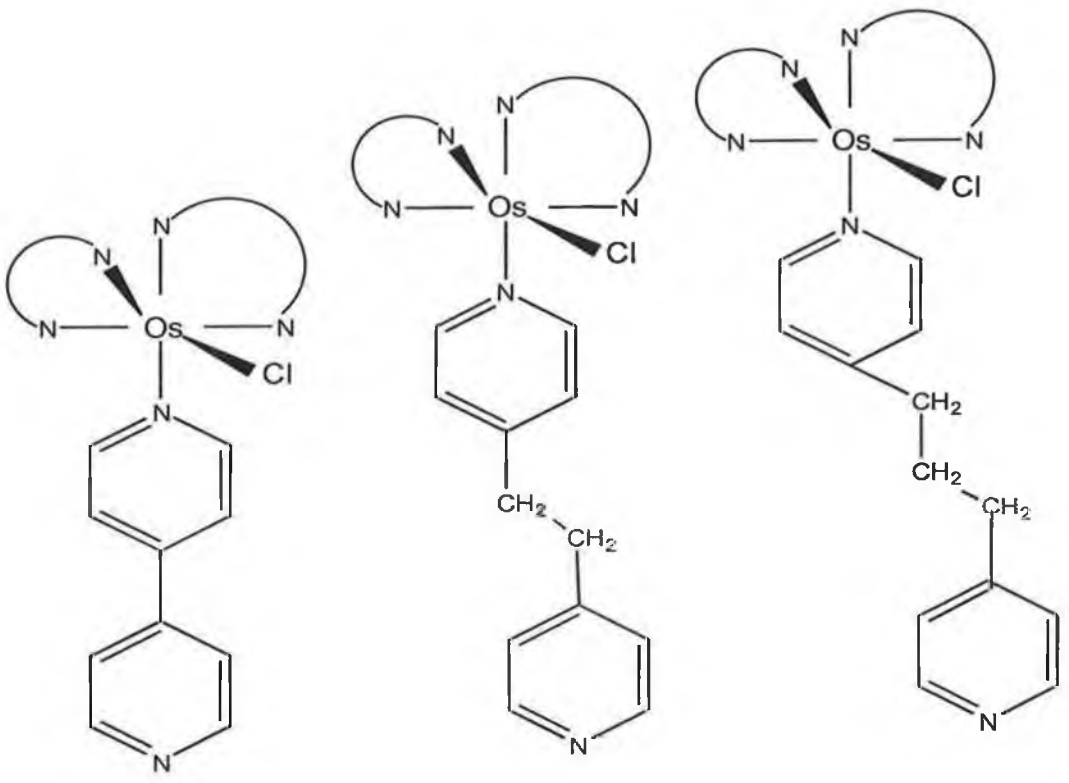

Figure 1.7. Structure of $[Os(bpy)_2Cl(pNp)]^+$, where bpy is 2,2′-bipyridyl and pNp is 4,4′-bipyridyl, 1,2-bis(4-pyridyl)ethane, or 4,4′-trimethylenepyridine.

One of the most important conclusions arrived at in this study[6] was that the electron-transfer mechanism was through-space rather than, as in the case of the alkanethiol monolayers, through-bond. This was determined mainly from the estimate of β^{o}, the tunnelling parameter, which was determined from the distance dependence of the standard rate constant, k^{o}. The value of β^{o} reported was consistent with the value expected for through-space tunnelling (1.3-1.8 $Å^{-1}$) and was considerably larger than values associated with through-bond tunnelling. Through-space electron tunnelling implied electron tunnelling through the surrounding medium rather than through the bonds of the bridging ligand. Further research by Forster and Faulkner[89] on these monolayers showed that electron-transfer rates were strongly linked to solvent dynamics.

Abruña and co-workers have carried out studies on related monolayers. The effects of solvent type on the formal potential of $[Os(bpy)_2(dipy)Cl]^{+}$ (dipy, 4,4′ trimethylenedipyridine) have been studied and reported.[92] In a later study,[93] the formation and structure of this same osmium complex adsorbed onto Pt(111) substrate was investigated using scanning tunnelling microscopy (STM) and electrochemical scanning tunnelling microscopy (ECSTM). Abruña et al[93] report that these microscopic techniques with the ability to provide electronic and structural information with sub-angstrom resolution are invaluable tools in the study of formation, structure, and behaviour of a wide variety of self-assembling molecules on the atomic scale. Abruña and co-workers have also carried out one of the few studies on mixed monolayers[94] comprised of osmium and ruthenium complexes.

As exemplified by the work of Chidsey,[75] Abrûna,[92] and Finklea,[5] electroactive adsorbed monolayers have been developed that exhibit close to ideal reversible electrochemical behaviour under a wide variety of experimental conditions of timescale, temperature, solvent and electrolyte. These studies have elucidated the effects of electron transfer distance, tunnelling medium, molecular structure, electric fields and ion pairing on heterogeneous electron transfer dynamics. Moreover, they have provided the detailed experimental data necessary to comprehensively test contemporary models such as the Marcus theory. First, as shown in Figure 1.8, a plot of ln k^{o} vs. the number of repeating units in the bridging ligand (typically the number

of methylene units in an alkane chain) is linear.[95,96,97,98] This result indicates that tunnelling rates decay exponentially with distance. The slope of this plot yields the tunnelling parameter, β, which for alkane-thiol systems is 1.0-1.1 $Å^{-1}$. Second, as illustrated in Figure 1.9, unlike the predictions of the Butler-Volmer theory, ln k Vs η is not linear for all driving forces. As predicted by the Marcus theory, when the overpotential becomes comparable to the reorganisation energy of the redox couple, curvature is observed and k eventually becomes independent of the driving force. Third, by using temperature dependent measurements of k and E°′, the activation enthalpy and reaction entropy can be obtained. These values can then be used to calculate the free energy of activation and provided k° is known the pre-exponential factor can be determined.

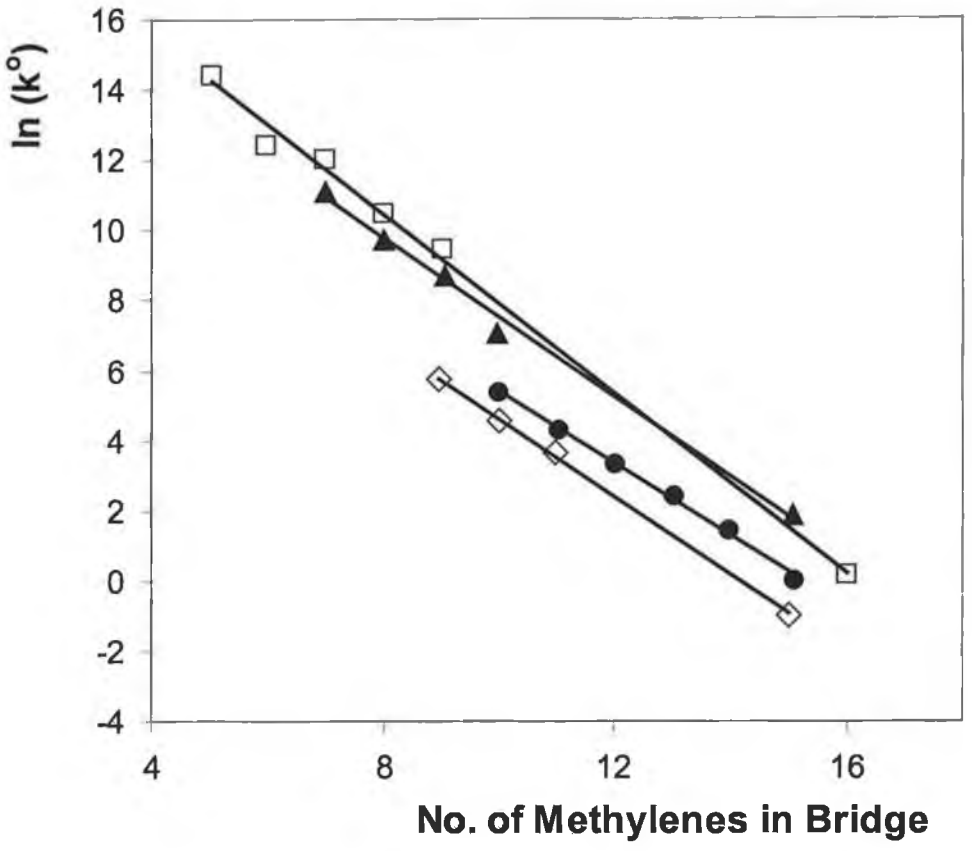

Figure 1.8. Semi-log plots of the standard heterogeneous electron transfer rate constant, k°, versus the number of methylene units in the alkane-thiol bridge. The symbols ●, ▲, □, and ◇ denote $HS(CH_2)_nCONHCH_2py\text{-}Ru(NH_3)_5^{2+}$, $HS(CH_2)_nNHCO$-Ferrocene, $HS(CH_2)_nOOC$-Ferrocene and Cytochrome C electrostatically adsorbed on $HS(CH_2)_nCOOH$.

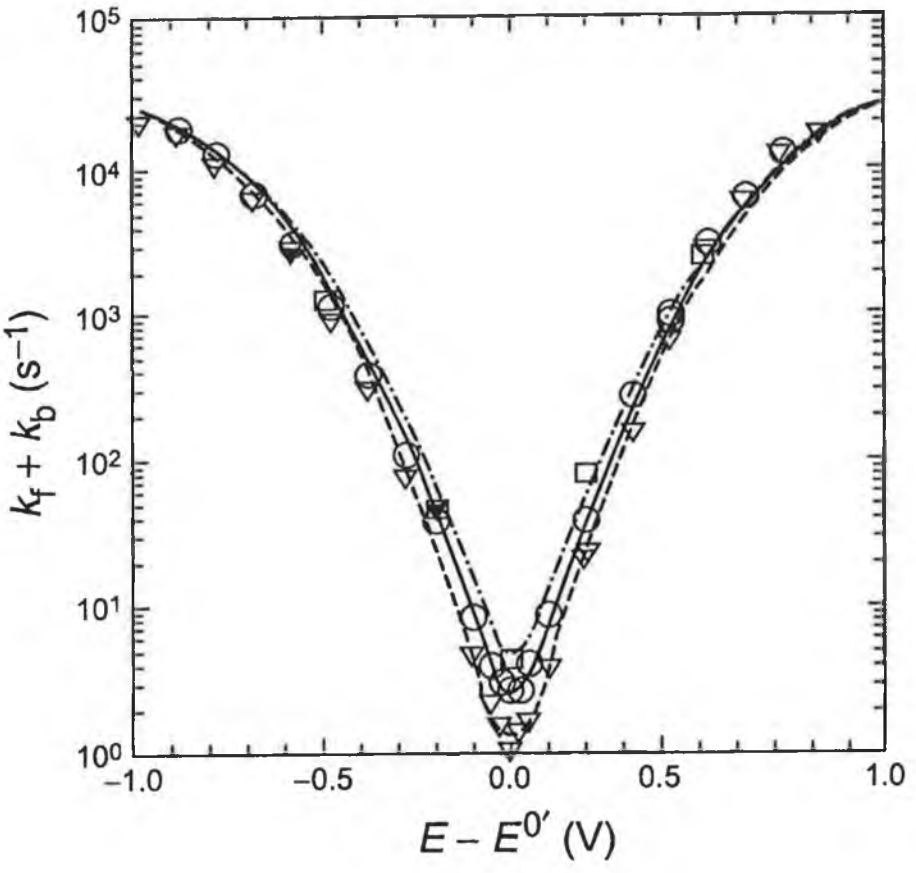

Figure 1.9. Tafel plots of Ln(k) vs. Overpotential for a mixed self-assembled monolayer containing $HS(CH_2)_{16}OOC$-Ferrocene and $HS(CH_2)_{15}CH_3$ in 1.0 M $HClO_4$ at three temperatures. The symbols, ▽, ○, and □ denote data obtained at 1, 25 and 47 °C. The solid lines are the predictions of the Marcus theory for a standard heterogeneous electron transfer rate constant of 1.25 s^{-1} at 25 °C and a reorganisation energy of 0.85 eV (≡54.8 kJ mol^{-1}).

Abruña and co-workers formed spontaneously adsorbed monolayers of the complex $[Os(bpy)_2$ Cl (4,4'-trimethylene-dipyridine)$]^+$, and investigated the dynamics and energetics of heterogeneous electron transfer.[92] The voltammetric responses observed for the $Os^{2+/3+}$ redox reaction at scan rates over 8000 V s^{-1} were close to the behaviour expected for an ideal, reversible, one-electron transfer reaction involving a surface confined species. They used Laviron's formalism[99] describing the variation of the peak potential with scan rate to estimate the rate of heterogeneous electron transfer as $2x10^5$ s^{-1}. Studies on metal centred oxidation and ligand based reduction processes reveal that matching the energy of states within the redox centre and the bridge can significantly increase k°.[90] Relatively few systems exist that allow orientational effects on heterogeneous electron transfer to be probed. To address this issue, Forster and co-workers[100] compared the rates of heterogeneous electron transfer for spontaneously adsorbed and Langmuir monolayers of $[Os(dpp)_2$ Qbpy$](ClO_4)_2$ where dpp is 4,7-diphenyl-1,10-phenanthroline and Qbpy is 2,2′:4′,4″:4″4″-quarterpyridyl. In the spontaneously adsorbed monolayers the quarterpyridyl ligand acts as a bridge between the redox centre and the surface of the microelectrode. In contrast, in the horizontal touch experiments on Langmuir films, the quarterpyridyl ligand was in the aqueous sub-phase and electrical contact occurred through the diphenyl-phenanthroline ligands. The heterogeneous electron transfer rate constants as measured at an overpotential of 50 mV were $1.20 \pm 0.3\times10^6$ and $1.7 \pm 0.2\times10^5$ s^{-1} for the spontaneously adsorbed and Langmuir monolayers, respectively. Given that the reorganisation energies are indistinguishable for the two systems, this result suggests that molecular orientation can significantly affect k.

Having reviewed modern electron transfer theory and the work of the principal researchers in the field of electrochemical studies on adsorbed monolayers, it is necessary at this point to describe the chosen algorithm which will be incorporated in the cyclic voltammogram simulation. This algorithm known as the simplex will be used in the model which will be described in detail in Chapter 3.

1.7 Modelling of Cyclic Voltammograms using the Simplex Method

1.7.1. General Description

As mentioned earlier, a primary objective is to build a theoretical model based on current electron-transfer theory that will produce theoretical cyclic voltammograms which can be compared with experimental data. Furthermore, by matching the theoretical and experimental responses, it should be possible to extract useful kinetic information. For this work, the simplex algorithm has been chosen as the basis for the computer-based fitting procedure. The simplex algorithm is commonly used as a method of fitting experimental data to theoretical models by minimising the differences between the experimental and theoretical curves. The simplex algorithm allows more than one parameter (inputs to the model) to be changed at one time and gives a much more efficient method of searching for the optimum than simply changing the parameters one at a time. The downhill simplex method is attributed to Nelder and Mead (1965)[101] and requires only function evaluations, not derivatives. As this thesis will show, the simplex method can find "the best fit" for the electron-transfer models considered here.

A simplex is the geometrical figure consisting, in N dimensions, of N+1 points (or vertices) and all their interconnecting line segments, polygonal faces, etc. In two dimensions, a simplex is a triangle. In three dimensions it is tetrahedron, not necessarily the regular tetrahedron.

This algorithm is designed for multidimensional minimisation or optimisation where the algorithm is given a starting guess or N-vector of independent variables as the first estimate. This guess can be generated by a function that gives random numbers so that consecutive runs of the simplex can be started from different points. The algorithm can then make its own way downhill through the complexity of an N-dimensional topography, until it encounters a minimum. To check if this is just a local minimum, the simplex can be started again or "re-exploded" from this minimum. If it once again finds this same minimum, then this is strong evidence that this minimum is the absolute minimum.

The downhill simplex method must be started not just with a single point, but with N+1 points, defining an initial simplex (Hence, in two dimensions i.e., two independent variables, the simplex is a triangle). The algorithm now takes a series of steps, most steps just moving the point of the simplex where the function is largest ("highest point") through the opposite face of the simplex to a lower point. These steps are called reflections, and they are constructed to conserve the volume of the simplex. The simplex is nondegenerate when it encloses a finite inner N – dimensional volume. If any point of a nondegenerate simplex is taken as the origin, then the N other points define vector directions that span the N – dimensional vector space. When it can do so, the method expands the simplex in one or another direction to take larger steps. When it reaches a "valley floor ", the method contracts itself in the transverse direction and tries to move down the valley. If there is a situation where the simplex is trying to "pass through the eye of a needle", it contracts itself in all directions, pulling itself around its lowest (best) point.

Termination criteria have to be carefully chosen. The termination conditions have to be such that the simplex knows when it has reached a minimum so that it can restart from this minimum, and re-find the minimum in reasonable time. Computation time becomes an important factor when using simplexes with complex functions including integration steps such as those in the electron transfer models included in this thesis. With more than one independent variable, the option of requiring a certain tolerance for a single independent variable will not be suitable. It is possible to identify one "cycle" or step of the multidimensional algorithm. It is then possible to terminate when the vector distance moved in that step is fractionally smaller in magnitude than some tolerance. Alternatively, another option is to choose that the decrease in the function value in the terminating step be fractionally smaller than some tolerance. Both of these methods are used for termination conditions in this work and a preference is shown for the former. Also note that either of the above criteria might be fooled by a single anomalous step that, for one reason or another, failed to get anywhere. Because of this, all results obtained in this work have been obtained after several restarts of the multidimensional minimisation routine at a point where it claims to have found a minimum.

1.7.2 The Use of the Simplex Algorithm in Cyclic Voltammetry

The simplex method was used by Creager[7] as a means of fitting the peak potential vs. log (scan rate) data to predictions from theory as a means of analysing cyclic voltammetric data. The independent variables used by Creager were the heterogeneous electron-transfer self-exchange rate constant, k^o, and the reorganisation energy, λ. These parameters are also used in this work but the simplex will be used to match the full theoretical cyclic voltammetric curve to the experimental cyclic voltammogram as opposed to the peak potential vs. log (scan rate). Using the full curve should allow the shape of the experimental curve to influence the result of the simplex and therefore give a more accurate analysis of the cyclic voltammetric data.

1.8. Computer Simulation

By building the theoretical electron-transfer model and translating the mathematics of the theory into code (in this case, the Visual Basic language), a computer simulator for the relevant electron-transfer theory is, in fact, being created. For this reason, it is important to understand the key elements of computer simulation.

1.8.1. The Elements of Computer Simulation

Five elements comprise a computer simulation.[102]

1. Assumptions upon which the simulation is built.
2. Parameters, or fixed values,
3. Inputs, or independent variables.
4. Algorithms, or process decision rules
5. Outputs, or dependent variables

Ideally, theoretical principles provide the underlying assumptions and algorithms. Computer simulations are similar to standard inductive research designs in that both employ independent, dependent and control variables. They differ in that in simulations the dependent variable values are determined by the algorithms driving the simulation rather than by observation and measurement. In this work, the simulation of cyclic voltammograms is carried out using all the above and will be

compared to experimental data and the simulation will be forced to match the experimental data by changing the inputs to the simulation model.

1.9. Conclusions

A wide-ranging review of microelectrode properties and fabrication techniques has been given which illustrates the continuing fundamental importance of the microelectrode in electrochemistry. The relevance of the organised structure of adsorbed monolayers to an understanding of the dynamics of heterogeneous electron transfer has been demonstrated. The main categories of adsorbed monolayers attracting research interest have been described. Electron-transfer theory has been reviewed from the Butler-Volmer to the Marcus theory. A computer-fitting algorithm has been selected and described.

The groundwork has now been completed for the next stages in this thesis. The following chapters will describe the laboratory work carried out and will demonstrate a new approach to cyclic voltammetry simulation, namely the construction and testing of an electron-transfer model incorporating a fitting algorithm. The function of this model will be to rapidly provide the electrochemist with accurate kinetic and thermodynamic data on adsorbed monolayers using cyclic voltammograms. This model will be described in Chapter 3.

1.10. References

1 Montenegro, M. I.; "*Microelectrodes: Theory and Applications.*" Queiros, M.; Daschbach, J. L. (eds.), NATO ASI Series,© **1991** Kluwer Academic Publishers.

2 Montenegro, M. I.; "*Applications of Microelectrodes in Kinetics*", Research in Chemical Kinetics., Compton, R. G.; Hancock, G. (eds,), **1994**, *2*.

3 Forster, R. J. *"Ultrafast Electrochemical Techniques"*, Encyclopedia of Analytical Chemistry", Meyers, R. (ed.), Wiley, New York, **2000**, 10142.

4 Bard, A. J.; Abruña, H. D.; Chidsey, C. E.; Faulkner, L. R.; Feldberg, S. E.; Itaya, K.; Majda, M.; Melroy, O.; Murray, R. W.; Porter, M. D.; Soriaga, M. P.; White, H. S.; *"The Electrode/Electrolyte Interface-A Status Report", J. Phys. Chem.* **1993**, *97*, 7147.

5 Finklea, O. H.; Hanshew, D. D. *J. Am. Chem. Soc.* **1992**, *114*, 3173.

6 Forster, R. J.; Faulkner, L. R. *J. Am. Chem. Soc.* **1994**, *116*, 5444.

7 Weber, K.; Creager, S. E. *Anal. Chem.* **1994**, *66*, 3164.

8 Richardson, J. N.; Rowe, G. K.; Carter, M. T.; Tender, L. M.; Curtin, L. S.; Peck, S. R.; Murray, R. W. *Electrochimica Acta*. **1995**, *40*, 1331.

9 Penner, R. M.; Heben, M. J.; Longin, T. L.; Lewis, N. S. *Science*, **1990**, *250*, 1118.

10 Kissinger, P. T.; Hart, J. B.; Adams, R. N. *Brain Res.* **1973**, *55*, 209.; Conti, J. C.; Strope, E.; Adams, R. N.; Marsden, C. A. *Life Sci.* **1978,** *23*, 2705; Ewing, A. G.; Wightman, R. M.; Dayton, M. A. *Brain Res.*. **1982**, *249*, 361.

11 Fitch, A.; Evans, D. H. *J. Electroanal. Chem.* **1986,** *202*, 83.; Bower, W. J.; Engelman, E. E.;Evans, D. H. *J. Electroanal. Chem.* **1989** *262*,67.; Andrieux, C. P.; Hapiot, P.; Saveant, J. M. *J. Phys. Chem.* **1988**, *92*, 5987.

12 Wipf, D. O.; Kristensen, E. W.; Deakin, M. R.; Wightman, R. M. *Anal. Chem.* **1988**, *60*, 306.

13 Wipf, D. O.; Wightman, R. M. *Anal. Chem.* **1988**, *60*, 2460; Andreiux, C. P.; Garreau, D.; Happiot, P.; Pinson, J.; Savient, J. M. *J. Electroanal. Chem.* **1988**, *243*, 321.

14 Tanaka, K.; Kashiwagi, N.; *Bioelectrochem. Bioenerg.* **1987**, *17*, 519.

15 Neher, E.; Sackman, B. *Nature*. **1976**, *260*, 779.

16 Wallingford, R. A.; Ewing, A. G. *Anal. Chem*. **1988**, *60*, 1972.

17 Lin, C. W.; Fan, F. R.; Bard, A. J. *J. Electrochem. Soc*. **1987**, *134*, 1038.

18 A. J. Bard, L. R. Faulkner, "*Electrochemical Methods-Fundamentals and Applications*", John Wiley & Sons, **1980.**

19 Andrieux, C. P.; Hapiot, P.; Saveant, J. M. *Chem. Rev*. **1990**, *90* 723.

20 Heinze, J. *J. Electroanal. Chem*. **1981**, *1*, 124.

21 Bond, A. M.; Fleischmann, M.; Robinson, J. *J. Electroanal. Chem*. **1984**, *168*, 299.

22 Pena, M. J.; Fleischmann, N.; Garrard, *J. Electroanal. Chem. **1987***, 220, 31.

23 Tsionsky, M.; Bard, A. J.; Mirkin, M. V. *J. Am. Chem. Soc*. **1997**, *119*, 10785.

24 Fan, F. F.; Mirkin, M. V.; Bard, A. J. *J. Phys. Chem*. **1994**, *98*, 1475.

25 Horrocks, B. R.; Mirkin, M. V.; Bard, A. J. *J. Phys. Chem*. **1994**, *98*, 9106.

26 Wei, C.; Bard, A. J. *J.Electrochem. Soc*. **1995**, *142*, 8, 2523.

27 Bond, A. M.; Fleischmann, M.; Robinson, J. *J. Electroanal. Chem*. **1984**, *180*, 257.

28 Ghoroghchian, J.; Sarfarazi, F.; Dibble, T.; Cassidy, J.; Smith, J. J.; Russel, A.; Fleischmann, M.; Pons, S. *Anal. Chem*. **1986**, *58*, 2278.

29 Jernigan, J. C.; Chidsey, C. E.;Murray, R. W. *J. Am. Chem. Soc*. **1985**, *107*, 2824.

30 (a) Faulkner, L. R.; Walsh, M. R..; Xu, C. Contemporary Electroanalytical Chemistry; Ivaska, A.; Ed.; Plenum Press: New York, **1990**; p 5. (b) Xu, C. Ph.D. Thesis, University of Illinois at Urbana-Champaign, **1992**.

31 Stulik, K. *Electroanalysis*, **1992**, *4*, 829.

32 McDermott, M. T.; McDermott, A.; McCreery, R. L. *Anal. Chem*. **1993**, *65*, 937.

33 McCreery, R. L.; *Electroanal. Chem.; ed*, Bard, A. J.; Dekker, M.; New York, **1991**, *17*, 221.

34 Cushman, M. R.; Bennett, B. G.; Anderson, C. W. *Anal.Chim.Acta*, **1981**, *130*, 323.

35 Wang, J. *Anal. Chem*. **1982**, *54*, 221.

36 Wehmeyer, K. R.; Wightman, R. M. *Anal. Chem.* **1985**, *57*, 1989.

37 Ciszkowska, M.; Stojek, Z. *J. Electroanal. Chem., Interfacial Electrochem.*, **1985**, *191*, 101.

38 Golas, J.; Galus, Z.; Osteryoung, J. *Anal. Chem.* **1987**, *59*,389.

39 O' Shea, T.; Lunte, S. M. *Anal. Chem.* **1993**, *65*, 247.

40 Tender, L.; Carter, M. T.; Murray, R. W. *Anal. Chem.* **1994**, *66*, 3173.

41 Besenhard, J. O.; Mohwald, H.; Nickl, J. J. *Rev. Chim. Min.* **1982**, *19*,588.

42 Besenhard, J. O.; Kurtze, A.; Sauter, R.; Josowicz, M.;; Lieb, H. D.; Potje, K. *Carbon '86, Deutsche Keramische Gesellschaft, Bad Honnef.* **1986**, 417.

43 Ponchon, J. L.; Cespuglio, K.; Gonon, F.; Jouvet, M.; Pujol, J. F. *Anal. Chem.* **1979**, *51*,1483.

44 Wightman, R. M.; *Anal. Chem.* **1981**, *53*, 1125.

45 Dayton, M. A.; Ewing, A. G.; Wightman, R. M. *Anal. Chem.* **1980**,*52*,2393.

46 Besenhard, J. O.; *International meeting on Ion-Selective Electrodes, Shanghai,* **1985**.

47 Abe, T.; Itaya, K.; Uchida, I. *Chem.Lett.* **1988**, *8*, 399.

48 Potje-Kamloth, K.; Janata, J.; Josowicz, M. *Ber. Bunsenges. Phys. Chem.* **1989**, *3*, 1480.

49 Mengoli, G.; Bianco, P.; Daolio, S.; Munari, M. T. *J. Electrochem. Soc.* **1981**, *128*, 2276.

50 Besenhard, J. O.; Gausmann, H. P.; Schulte, A.; Schur, K.; Jannakoudakis, P. D. *NATO ASI: Microelectrodes: Theory and Applications*. **1992**

51 Besenhard, J. O.; Schulte, A.; Jannakoudakis, P. D.; Heinze, J.; Tschuncky, P.; *Tagungsband Dechema Symp. Mikroelektrochemie, Friedrichoda*. **1992**

52 Baer, C. D.; Stone, N. J.; Sweigart, D. A. *Anal. Chem.* **1988**,*60*,168.

53 Wipf, D. O.; Michael, A. C.; Wightman, R. M. *J. Electroanal. Chem.* **1989**, *269*,25.

54 Tschuncky, P.; Heinze, J. *Anal. Chem.* **1995**, *67*, 4020.

55 Pendley, B. D.; Abruña, H. A. *Anal. Chem.* **1990**, *62*,782.

56 Malem, F.; Mandler, D. *J. Electrochem. Soc.***1992**, *139*, L65.

57 Marcus, R. A. *J. Chem. Phys.* **1956**, *24*, 4966.

58 Marcus, R. A. *J. Chem. Phys.* **1965**, *43*, 679.

59 Marcus, R. A. *Ann. Rev. Phys. Chem.* **1964**, *15*, 155.

60 Marcus, R. A. *Electrochim. Acta.* **1968**, *13*, 955.

61 Kauzmann, W.; *"Quantum Chemistry"*, Acad. Press, New York, **1957**.

62 Peover, M. E. *Electroanal. Chem.* **1967**, *2*, 1.

63 Butler, J. A. V. *Trans. Faraday Soc.* **1924**, *19*, 729.

64 Erdey-Gruz, T.; Volmer, M. *Z. Physik. Chem.* **1930** *150A*, 203.

65 Bagchi, G. *Ann. Rev. Chem.* **1989**, *40*, 115.

66 Sutin, N. *Acc. Chem. Res.* **1982**, *15*, 275.

67 Barr, S. W.; Guyer, K. L.; Li, T. T.-T.; Liu, H. Y.; Weaver, M. J. *J. Electrochem. Soc.* **1984**, *131*, 1626.

68 Weaver, M. J. *Chem. Rev.* **1992**, *92*, 463.

69 Sutin, N. Brunschwig, B. S. *ACS Symp. Ser.* **1982**, *198*, 105.

70 Forster, R. J.; Vos, J. G. and Keyes, T. E. *The Analyst.*, **1998**, *123*, 1905.

71 Forster, R. J.; O'Kelly, J. P. *J. Phys. Chem.* **1996**, *100*, 3695.

72 Marcus, R. A. *J. Phys. Chem.* **1963**, *67*, 853.

73 Schmickler, W. *J. Electroanal. Chem.* **1977**, *82*, 65.

74 Bockris, J. O'M.; Khan, S. U. M. *Quantum Electrochemistry,* Plenum Press, New York, 1979, Chap. 8

75 Chidsey, C. E. D. *Science* **1991**, *251*, 919.

76 Tender, L.; Carter, M. T.; Murray, R. W. *Anal. Chem.* **1994**, *66*, 3173.

77 Miller, C. J.; "*Physical Electrochemistry: Principles, Methods, and Applications*", Ed. I. Rubinstein, Dekker, New York, **1995**.

78 Creutz, Sutin, *J. Am. Chem. Soc.* **1977**, *99*, 241.

79 Beitz, Miller, *J. Chem. Phys.* **1979**, *71*, 4579.

80 Miller, Calcaterra, Closs, *J. Am. Chem. Soc.* **1984**, *106*, 3047.

81 Finklea, H. O.; Liu, L.; Ravenscroft, M. S.; Punturi, S. *J. Phys. Chem.* ***1996***, *100*, 18852.

82 Nicholson, R. S.; Shain, I. *Anal. Chem.* **1964**, *36*, 706.

83 Howell, J. O.; Wightman, R. M. *Anal. Chem.* **1984**, 56, 524.

84 Montenegro, M. I.; Pletcher, D. *J. Electroanal. Chem.* **1986**, *200*, 371.

85 Neudeck, A.; Dittrich, J.; *J. Electroanal. Chem.* **1991**, *313*, 37.

86 Wipf, D. O.; Wightman, M. R *Anal. Chem.* **1988**, *60*, 2460.

87 Andrieux, C. P.; Garreau, D.; Hapiot, P.; Pinson, J.; Savéant, J. M. *J. Electroanal. Chem.* **1988,** *243*, 321.

88 Safford, L. K.; Weaver, M. J. *J. Electroanal. Chem.* **1992,** *331*, 857.

89 Forster, R. J.; Faulkner, L. R. *J. Am. Chem. Soc.*, **1994**, *116*, 5453.

90 Forster, R. J.; Vos, J. G.; Keyes, T. E. *Analyst.* **1998**, *123*, 1905.

91 Forster, R. J. *Inorg. Chem.* **1996**, *35*, 3394.

92 Acevedo, D.; Abruña, H. D. *J. Phys. Chem.* **1991**, *95*, 9590.

93 Hudson, J. E.; Abruña, H. D. *J. Phys. Chem.* **1996**, *100*, 4556.

94 Tirado, J. D.; Abruña, H. D. *J. Phys. Chem.* **1996**, *100*, 1036.

95 Weber, K.; Hockett, L.; Creager, S. *J. Phys. Chem. B.* **1997,** *101*, 8286.

96 Smalley, J. F.; Feldberg, S. W.; Chidsey, C. E. D.; Linford, M. R.; Newton, M. R.; Liu, Y.-P. *J. Phys. Chem.* **1995**, *99*, 13141.

97 Feng, Z. Q.; Imabayashi, S.; Kakiuichi, T.; Niki, K. *J. Chem. Soc., Faraday Trans.* **1997,** *93*, 1367.

98 Song, S.; Clark, R. A.; Bowden, E. F.; Tarlov, M. J. *J. Phys. Chem.* **1993**, *97*, 6564.

99 Laviron, E. *J. Electroanal. Chem.* **1979**, *101*, 19.

100 Forster, R. J.; Keyes, T. E.; Majda, M. *J. Phys. Chem. B,* **2000,** *104*, 4425.

101 Nelder; Mead, *Computer. J.* **1965**, *79*, 308.

102 Whicker, M. L.; Sigelman, L. *"Computer Simulation Applications"*, Sage Publications Ltd, **1991**.

CHAPTER 2

Synthesis and Characterisation of Surface Active Osmium and Ruthenium Complexes

2.1. Introduction

Chapter 1 included a comprehensive review of the main principles of solution phase electrochemistry. This chapter reports the synthesis and characterisation of a series of surface active osmium and ruthenium complexes. Moreover, it presents the fabrication and properties of microelectrodes. Finally, it provides details regarding the general electrochemical properties of the complexes, their diffusion coefficients in solution and examines the cyclic voltammograms of some of these complexes in solution using a number of different electrode materials.

2.2. Experimental Section

2.2.1. Apparatus Used

All potentials are quoted with respect to a Ag/AgCl reference electrode. Cyclic voltammetry was performed using a CH Instruments Model 660 Electrochemical Workstation and a conventional three-electrode cell. All solutions were degassed using nitrogen, and a blanket of nitrogen was maintained over the solution during all experiments.

All cyclic voltammograms were measured at 298 K.

Ohmic drop was measured during each experiment and limited in all cases to < 8 mV which corresponds to less than 3% of the measured peak to peak separation.

All absorption spectra were measured on a Varian Carey 50 Scan UV-Visible spectrophotometer.

2.2.2. Chronoamperometry

In high speed chronoamperometry,[1] a custom built function generator-potentiostat, with a rise time of less than 10 ns, was used to apply potential steps of variable pulsewidth and amplitude directly to a two-electrode cell. A Pt foil and an Ag/AgCl reference electrode were combined to form a counter electrode. The foil lowered the resistance and provided a high frequency path.

2.2.3. Adsorption Experiments (Chapters 4 and 5)

Spontaneously adsorbed monolayers were formed *in-situ* using a 10 μM solution of the metal complex in the electrolyte solution of interest. A low concentration of the surface active complex in solution improved the stability of the monolayers, yet minimised the diffusional contribution to the overall current in chronoamperometry or cyclic voltammetry. For example, at a 5 μm radius microelectrode the solution phase component will contribute less than 5 % to the overall Faradaic current at 5 V s^{-1}.

2.3. Microelectrodes: Fabrication and Characterisation

Platinum and gold microelectrodes were fabricated in accordance with previously described techniques.[2] The procedure for fabrication involved sealing the microscopic wires (radii 5 and 25 μm) in soft glass. A copper wire (i.e., tinned annealed copper 0.2 kg 18 swg) of approximate length 4 cm was joined to an aluminium "hook up" wire by wrapping the aluminium wire around the copper wire and soldering the two. These joined wires were then connected to the chosen microscopic wire by means of soldering (for larger diameters of ~ 25 μm) or by means of a conductive paint (diameters of ~ 5 μm). The microwires were sealed in the glass by heating in a flame before (in the case of the smaller diameter) or after (in the case of the larger diameter) connecting to the hook up wire.

The microdisk electrode was exposed by removing excess glass using emery paper followed by successive polishing with 12.5, 5, 1, 0.3 and 0.05 μm alumina for 10 minutes each.

After rinsing (milli -Q water) and sonication for 5 minutes to remove any adhering polishing material, the electrodes were electrochemically cleaned in 0.1 M H_2SO_4.

In the case of the platinum microelectrodes, the success rate of fabrication was 90%, with the electrodes being tested using ferrocene dissolved in CH_3CN as a solution phase electrochemical probe with 0.1 M $LiClO_4$ as supporting electrolyte.

It is unlikely that the polished disk of the microwire is always positioned precisely in the centre of the glass insulator. However, for solution phase reactants, what is important is that the distance from the wire to the edge of the glass is always much greater than the thickness of the depletion layer. If this is not the case, the diffusion field will be distorted complicating the interpretation of the voltammetric responses. For the timescales used in this work, the depletion layer thickness is never more than 10 radii in thickness[3], i.e., 250 μm.

Figure 2.1 shows an optical micrograph of a typical 25 μm radius platinum microelectrode and while it cannot be concluded that the microwire is centred in the glass, it is obvious that the wire is surrounded by a layer of glass that is significantly more than 10 radii in thickness.

Figure 2.1. An optical micrograph of a typical 25 μm radius platinum microelectrode. This is a side view of the electrode surface through the glass insulator. The tip of the microwire along with its shadow are visible at the top of the lower, left quadrant. The magnification used is 200x.

2.4. Syntheses

2.4.1. Synthesis of $[Os(bpy)_2Cl(p2p)]^+$

The synthesis of $[Os(bpy)_2Cl(p2p)]^+$, where bpy is 2,2′-bipyridyl and p2p is 1,2-bis(4-pyridyl)ethane, was previously described by Forster and Faulkner.[4] $[Os(bpy)_2Cl_2]$ was prepared by a modification of the procedure described by Buckingham et al.[5] using $OsCl_3$ as the starting material instead of $K_2[OsCl_6]$. The 1,2-bis(4-pyridyl)ethane, (p2p), osmium complex was synthesised by refluxing $[Os(bpy)_2Cl_2]$ with a 2 - to 3 - fold excess of the 1,2-bis(4-pyridyl)ethane, (p2p), bridging ligand in methanol for several hours. In a typical synthesis, 200 mg of $[Os(bpy)_2Cl_2]$ (3.5×10^{-4} mol) was placed in methanol and refluxed for 10-20 min to ensure complete dissolution of the complex. A solution of 130 mg of 1,2-bis(4-pyridyl)ethane (Aldrich) (7.0×10^{-4} mol) in 10 cm^3 of methanol was added, after which time refluxing was continued for an additional 8 h. Excess solvent was removed by rotary evaporation and, following cooling to room temperature, a 3 fold molar excess of NH_4PF_6 dissolved in 5 cm^3 of H_2O was added to precipitate $[Os(bpy)_2Cl(p2p)]PF_6$. The product was filtered and washed with ice water and ether. The complex was recrystallised from aqueous methanol to give red-brown crystals, yield 260 mg, 86%.

$[Os(bpy)_2Cl(p2p)]^+$, 1H-n.m.r. (400 MHz) d (CH_3CN): 2.50 - 3.00 (4H, m,), 6.9 - 7.80 (H, m), 8.30 - 8.50 (H, m).

Elemental analysis: $[Os(bpy)_2Cl(p2p)]^+$ Calculated for C 44.28%, H 3.25%, N 9.69 %. Found C 43.77%; H 3.81% N 8.63%.

2.4.2. Synthesis of $[Os(bpy)_2Cl(bpe)]^+$

$[Os(bpy)_2Cl(bpe)]^+$, where bpy is 2,2′-bipyridyl and bpe is *trans*-1,2-bis(4-pyridyl)ethylene, was synthesised[6] using methods similar to those published previously.[7] $[Os(bpy)_2Cl_2]$ (0.22 g, 3.5×10^{-4} mol) was first refluxed in dry methanol (10 cm^3) until completely dissolved. Trans-1,2-bis(4-pyridyl)ethylene) (0.07 g, 3.8×10^{-4} mol) was added over 1 hour and the resulting solution was refluxed for a further

12 hours. After this period the reaction mixture was cooled and added dropwise to a concentrated aqueous solution of NH_4PF_6. Elemental analysis, NMR, HPLC and UV/VIS spectroscopy all indicate that the compound is obtained in the form $[Os(bpy)_2Cl(bpeH)](PF_6)_3$, where the free pyridine group is protonated. That the unbound pyridine moiety of the 1,2-bis(4-pyridyl)ethylene ligand is protonated is not unexpected since the synthesis was carried out in dry methanol. This protonation does not persist in aqueous media and the complex is capable of forming spontaneously adsorbed monolayers. Yield 263 mg, 65%.

Elemental analysis: $[Os(bpy)_2Cl(bpeH)](PF_6)_3$ Calculated for $C_{32}N_6H_{26}OsClP_3F_{18}$ C 33.25%, H 2.25%,N 7.27%. Found C 32.98%, H 2.43%, N 7.34%

2.4.3. Synthesis of $[Os(OMe\text{-}bpy)_2Cl(p3p)]^+$

The surface active complex, $[Os(OMe\text{-}bpy)_2Cl(p3p)]PF_6$, where bpy is 2,2′-bipyridyl, OMe is 4,4′-dimethoxy-2,2′-bipyridyl and p3p is 1,4-trimethylene dipyridine was prepared from $[Os(OMe\text{-}bpy)_2\ Cl_2]$ which was synthesised by Dr. R. J. Forster using a procedure described by Heller and co-workers.[8] 138 mg (2.0×10^{-4} mol) of $[Os(OMe\text{-}bpy)_2\ Cl_2]$ was placed in 40 cm^3 of methanol and refluxed for 10 minutes to ensure complete dissolution. A solution of 40 mg (2.0×10^{-4} mol) of 1,4-trimethylene dipyridine dissolved in 10 cm^3 of methanol was added, and the solution was refluxed for 15 hr. The progress of the reaction was monitored using HPLC and cyclic voltammetry. After the reaction was complete, the volume was reduced to 5 cm^3 by rotary evaporation. Ammonium hexafluorophosphate (95+%, Aldrich) was then added, and the dark purple product was collected by filtration and washed with diethylether. The product was recrystallised from aqueous methanol to give dark green-black crystals, yield 160 mg, 82%.

Elemental analysis: Calculated for $C_{37}H_{38}O_4N_6OsClPF_6$, C:44.37%, H:3.79%, N:8.39%. Found C:44.8%, H:3.3%, N:8.2%. The complex was further characterised using IR, UV-Vis, NMR and cyclic voltammetry.

2.4.4. Synthesis of $[Ru(bpy)_2Cl(4\text{-}tet)]^+$

3,6-Bis(4-pyridyl)-1,2,4,5-tetrazine,(4-tet), was synthesised by Dr. R. J. Forster using the following method.

3,6-Bis(4-pyridyl)-1,2,4,5-tetrazine,(4-tet). 4-Cyanopyridine (52 g, 0.5 mol) and hydrazine monohydrate (25g, 0.5 mol) were combined and heated to 100 °C for 5 h. The resulting yellow solid was collected after cooling and recrystallised from hot ethanol/water, 2:1, v/v. This was then stirred for 2 h in ethanol with a slight excess of 2,3-dichloro-5,6-dicyano-1,4-benzoquinone at room temperature. The resulting bright pink solid was then collected and recrystallised as described.

Yield, 10 g, (8%). Mp 244-246 °C, CHN, (Calculated for $C_{12}H_8N_6$; C: 61.02%; H: 3.39%; N: 35.59%. Found C: 60.69%; H: 3.28%, N: 35.01%, (200 MHz) ^{1}H NMR data [CD_3CN]: H^2, H^6, $H^{2'}$, $H^{6'}$, 8.92 ppm (m) (4H), H^3, H^5, $H^{3'}$, $H^{5'}$, 8.48 ppm (m).

$[Ru(bpy)_2Cl(4\text{-}tet)]ClO_4$. 4-tet (0.12 g, 5.1 x 10^{-4} mol) was dissolved in 20 cm^3 of ethylene glycol and heated to reflux. cis-$Ru(bpy)_2Cl_2$ (0.2 g, 4.2 x 10^{-4} mol) was dissolved in ethylene glycol and added to the refluxing solution over 20 min. The reaction mixture was allowed to reflux for a further 4 h. This solution was analysed for completion by HPLC and UV-Vis Spectroscopy. To avoid photochemical decomposition, this solution was wrapped in aluminium foil. After cooling, a solution of concentrated aqueous $NaClO_4$ was added. The resulting solid (yield 0.281 g, 85%) was collected by filtration and recrystallised from acetone/water (1/1 v/v). The purity of the complex was confirmed by CHN.

Elemental analysis: Calculated for $C_{32}H_{24}O_4N_{10}RuCl_2$; C:48.99%, H:3.06%, N:17.86%. Found C:47.32%, H:2.94%, N:17.41%. The complex was further characterised using HPLC, UV-Vis, NMR and cyclic voltammetry.

2.4.5. Synthesis of $[Os(bpy)_2Cl(4\text{-}bpt)]^+$

$[Os(bpy)_2Cl(4\text{-}bpt)]^+$ where 4-bpt is 3,5-bis(2-pyridyl)1,2,4- triazole was synthesised by Forster, Vos and Keyes[9] according to the following procedure.

3,5-Bis(pyridin-4-yl)-1,2,4,-triazole (4-bpt). 4-Cyanopyridine (52 g, 0.5 mol) and hydrazine monohydrate (25g, 0.5 mol) were combined and heated to 100 °C for 5 h. The resulting yellow solid was collected after cooling and refluxed in 2 M HCl for 20 min. This solution was neutralised with ammonia and the resulting tan coloured solid was recrystallised from ethanol. This product was then refluxed in 500 cm^3 of 5 M HNO_3 for 30 min. After cooling to 0 °C, sodium nitrite (90 g) was slowly added. The solution was stirred at room temperature for 30 min and then heated at boiling for 5 min. Addition of ammonia precipitated the 4-bpt product which was then recrystallised from ethanol. Yield, 20g (18%), ^{1}H NMR data [$(CD_3)_2SO$]: H^2, H^6, $H^{2'}$, $H^{6'}$, 8.75 ppm (d) (4H); H^3, H^5, $H^{3'}$, $H^{5'}$, 7.99 ppm (d) (4H); NH, 7.15 ppm (s. broadened). Mp: 216-220 °C.

[Os(bpy)$_2$Cl(4-bpt)]PF$_6$. 4-bpt (0.15 g, 4.3 x 10^{-4} mol) was dissolved in ethylene glycol (40 cm^3) and heated to reflux, $Os(bpy)_2Cl_2$ (0.22 g, 3.5 x 10^{-4} mol) dissolved in ethylene glycol (10 cm^3) was added to the solution over 1 h and the reagents were refluxed together for a further 2 h. After this period, the reaction mixture was cooled and added dropwise to a concentrated aqueous solution of NH_4PF_6. The resulting brown precipitate was collected by filtration, yield 315 mg, 92%.

^{1}H NMR data [CD_3CN]: bipyridyl, H^3, 8.47-8.52 (d); H^4 (t), 7.84-7.86; H^6 (d), 7.62-7.64; H^5 (t), 7.28-7.32; 4-bpt, H^2, 8.73 (d); H^3, 7.95-7.92 (dd); H^5, 7.96-7.92 (dd); H^6, 8.73; $H^{2''}$, 7.54-7.57 (dd); $H^{3''}$, 8.23 (d); $H^{5''}$, 8.23 (d); $H^{6''}$, 7.54-7.57.

Elemental analysis: Calculated for $OsC_{32}H_{25}N_9ClNH_4PF_6.3H_2O$, C 39.26, H 3.58, N 14.3%; Found, C 38.70, H 3.62, N 14.21%

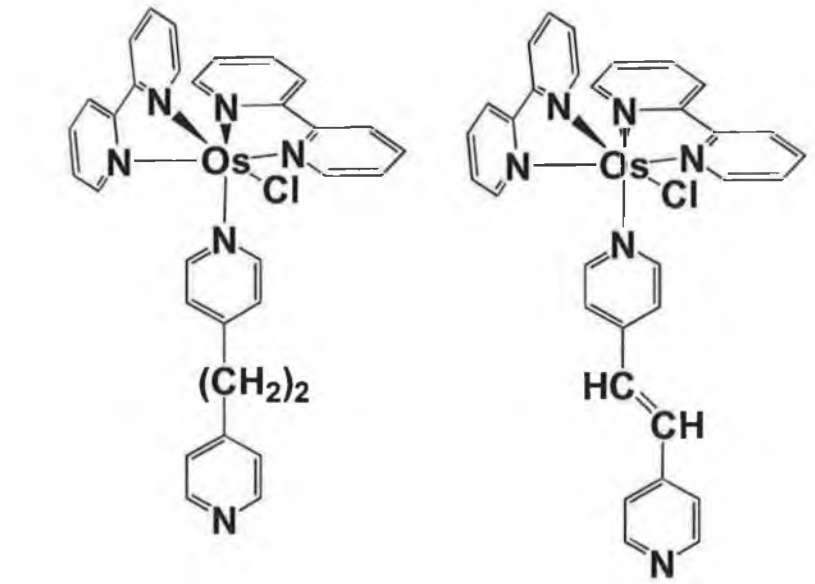

(I) (II)

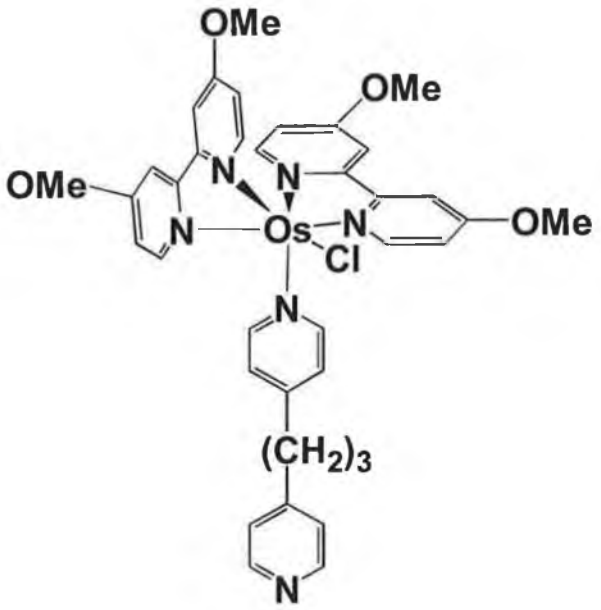

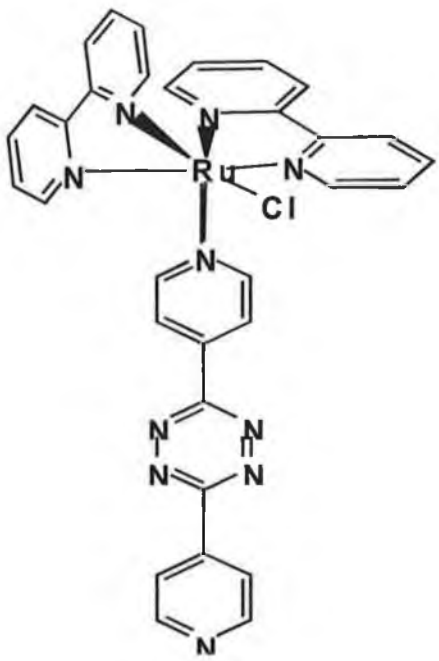

(III) (IV)

Figure 2.2. Structure of (I) $[Os(bpy)_2Cl(p2p)]^+$, (II) $[Os(bpy)_2Cl(bpe)]^+$, (III) $[Os(OMe\text{-}bpy)_2Cl(p3p)]^+$, and (IV) $[Ru(bpy)_2Cl(4\text{-}tet)]^+$ where bpy is 2,2′-bipyridyl, p2p is 1,2-bis(4-pyridyl)ethane, bpe is *trans*-1,2-bis(4-pyridyl)ethylene, OMe is 4,4′-dimethoxy-2,2′-bipyridyl and p3p is 1,4-trimethylene dipyridine, 4-tet is 3,6-bis(4-pyridyl)-1,2,4,5-tetrazine.

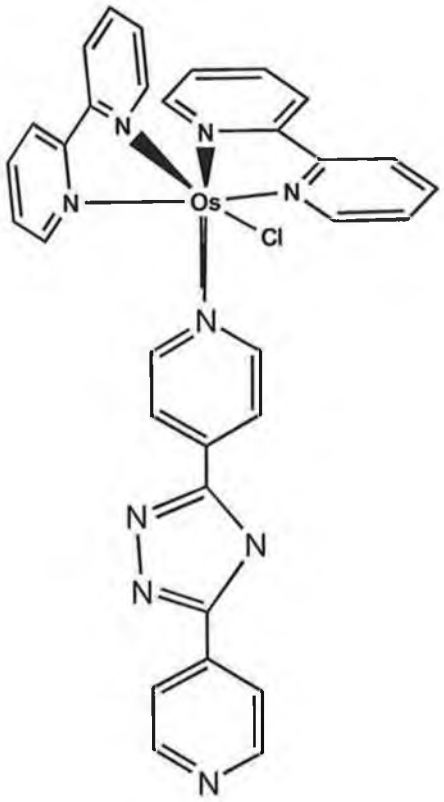

Figure 2.3. Structure of $[Os(bpy)_2Cl(4\text{-bpt})]^+$ where 4-bpt is 3,5-bis(2-pyridyl)1,2,4-triazole.

2.5. Absorption Spectra of $[Os(bpy)_2Cl(p2p)]^+$ and $[Os(bpy)_2Cl(bpe)]^+$

In Chapter 4, the electrochemical properties of adsorbed monolayers of $[Os(bpy)_2Cl(p2p)]^+$ and $[Os(bpy)_2Cl(bpe)]^+$ concentrating mainly on the influence of the conjugated bond in the bridging ligand will be investigated In this section, the absorption spectra of both these complexes in solution at pH 7 and pH 1 are measured. By measuring absorption spectra at low pH, the effect of protonation of both the non-conjugated and conjugated bridging ligands on their absorption spectra is observed. This should give a qualitative indication of the level of electronic coupling between the metal and the protonated bridging ligand.

The very intense absorption bands in the ultra-violet region are due to π to π^* ligand centred transitions at the bipyridyl head groups. The intense bands in the visible region are due to metal to ligand charge transfer (MLCT) transitions.[10] A reduction in absorption of these MLCT bands for the complex on protonation of the bridging ligand would indicate a reduction in electron density around the redox centre. This reduction in absorption in the visible region would indicate electronic coupling between the metal and the bridging ligand.

The pH was adjusted using concentrated perchloric acid. Using concentrated acid reduces the pH without changing the solution concentration appreciably.

Figure 2.4 shows the ultra-violet absorption spectra for the $[Os(bpy)_2Cl(p2p)]^+$ solution at both pHs. This figure shows that there is no real change in the absorption spectrum of this complex on protonation of the bridging ligand. In this case the electron density around the metal does not appear to be affected by the protonation of the ligand. This suggests that there is no, or very little, electronic coupling present between the p2p ligand and the metal.

However, Figure 2.5 illustrates a significant decrease in the absorption properties of the $[Os(bpy)_2Cl(bpe)]^+$ solution at 400 nm approx. indicating the greater reduction in the electron density around the metal on protonation due to the presence of the double

bond in the bridging ligand. So protonation of the nitrogen in the pyridine ring at the end of the bridging ligand reduces the electron density around the metal when conjugation is present due to electronic coupling. While these effects are minor and difficult to quantify, the influence of the double bond in the bridging ligand is still shown in these experiments.

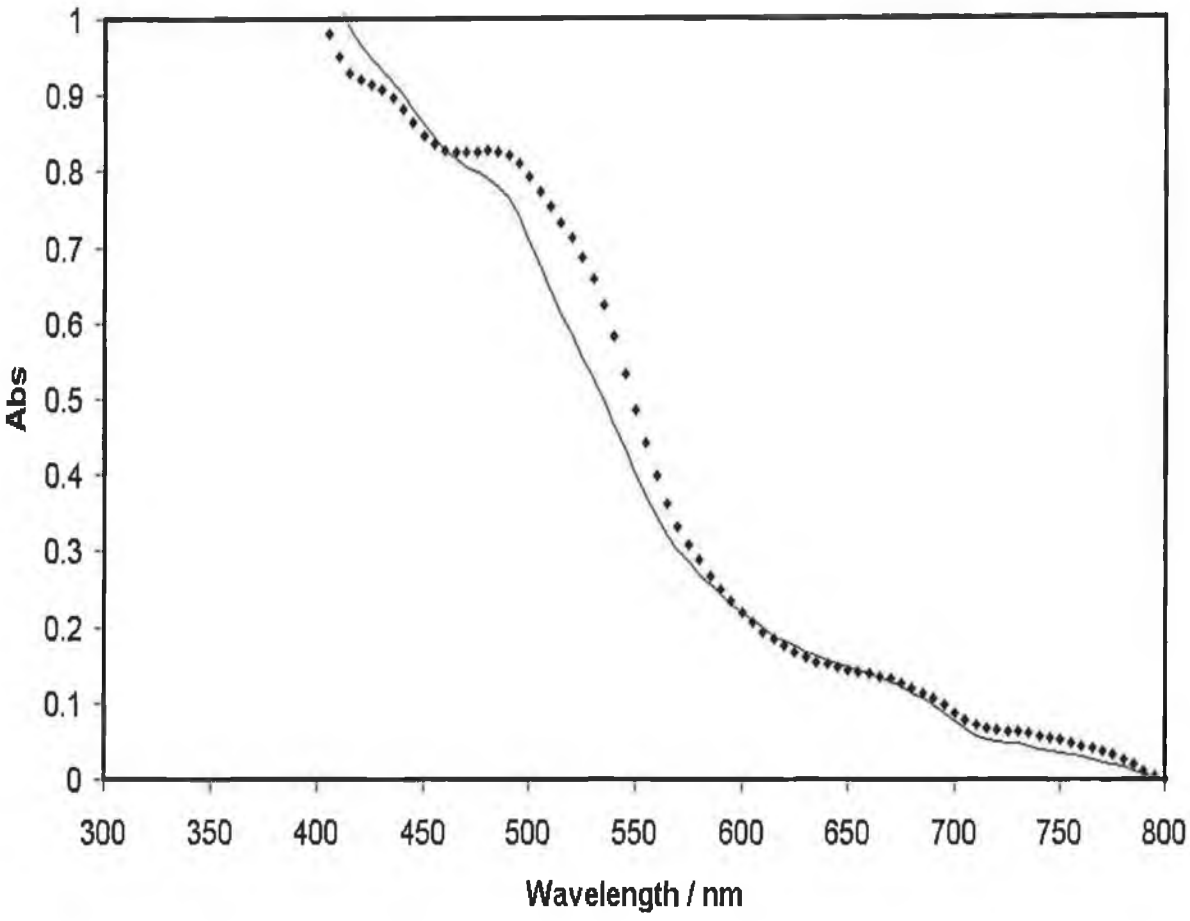

Figure 2.4. Ultra violet-visible absorption spectra for the $[Os(bpy)_2Cl(p2p)]^+$ solution at pH 7 (broken line) and pH 1(solid line). The absorption spectra were run on a Varian Carey 50 Scan UV-Visible spectrophotometer. The pH was adjusted using concentrated perchloric acid.

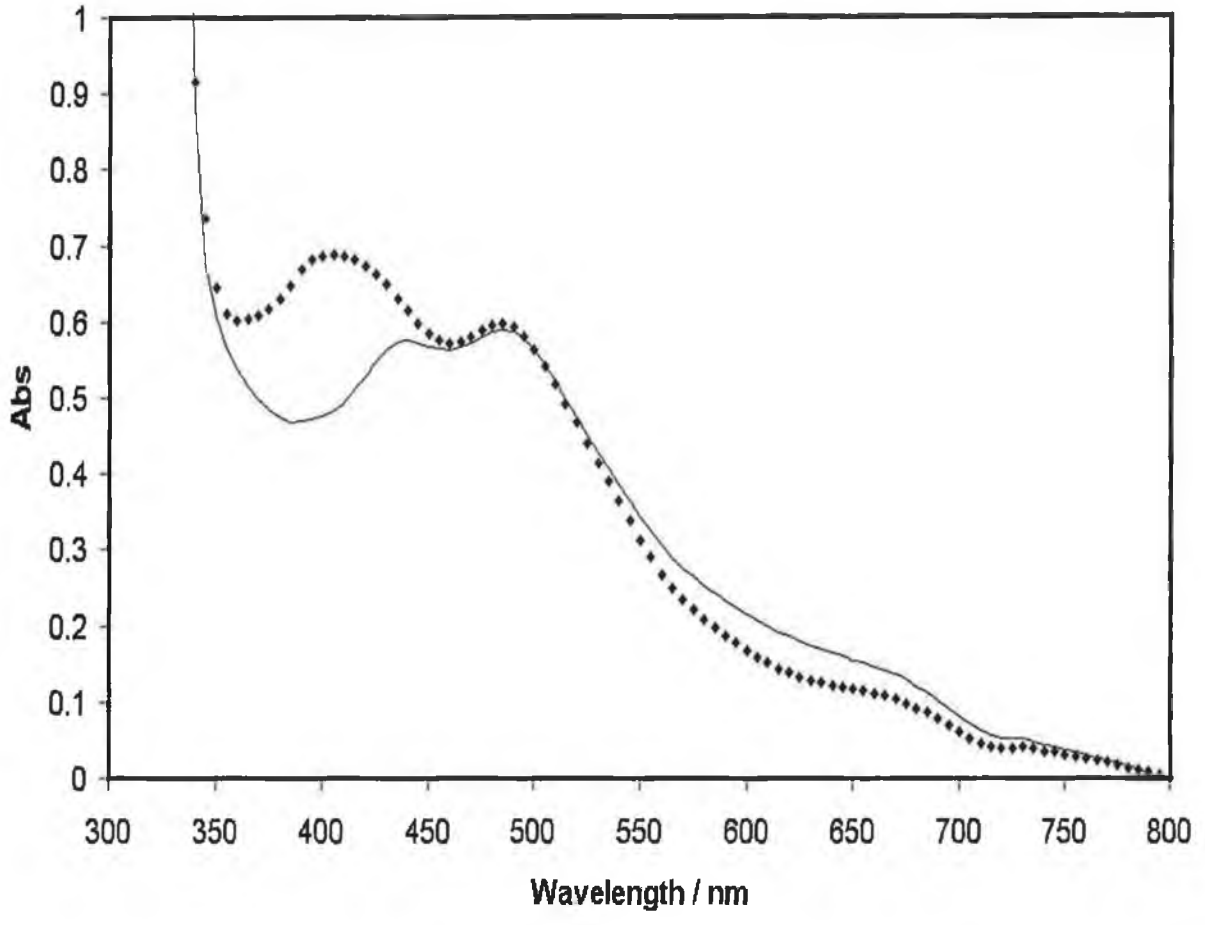

Figure 2.5. Ultra violet absorption spectra for the $[Os(bpy)_2Cl(bpe)]^+$ solution at pH 7 (broken line) and pH 1(solid line). The absorption spectra were run on a Varian Carey 50 Scan UV-Visible spectrophotometer. The pH was adjusted using concentrated perchloric acid.

2.6. Determination of Microscopic Surface Areas of Microelectrodes

There are number of experimental techniques for measuring the "real" or microscopic surface area in electrochemistry. The determination of microscopic surface area is fundamentally important because it allows the accurate determination of the area occupied per molecule in adsorption experiments. Also, the microscopic surface area when divided by the geometric area, gives a value for electrode surface roughness which can influence the response of a microelectrode. Amongst the available methods are the following:

The capacitance ratio is a method normally used with solid electrodes, but it is also applicable to liquid metals. It is widely adopted for the estimation of the surface area ratio for different samples of the same electrode material.[11] The experimental differential capacitance of the electrode under investigation in aqueous solutions is divided by 15-17 μF cm^{-2}, the empirically established range of capacitance per unit area measured with a Hg electrode at moderately negative charges.

Hydrogen adsorption from solution is a method used for transition metals showing hydrogen adsorption in potential regions prior to massive H_2 evolution. The experimental technique may be cyclic voltammetry or chronoamperometry.[12] The method has been established mainly with platinum electrodes[13] but it has been extended to rhodium, iridium, and nickel. The principle of this method is that the charge under the voltammetric peaks for hydrogen adsorption or desorption is assumed to correspond to adsorption of one hydrogen atom on each metal atom of the surface. The charge associated with a one-to-one hydrogen-metal correspondence per unit surface area is calculated on the basis of the distribution of metal atoms on the surface. It is important to note that the hydrogen adsorption approach cannot be applied to gold electrodes since hydrogen does not adsorb.

2.6.1. Oxide Formation

The method used in this work for determining the microscopic surface area is oxide formation. This method is applicable to metals showing well-developed regions for oxide monolayer formation and reduction. As oxide monolayer formation readily takes place with both gold and platinum, it can be applied to both electrode materials.

Oxygen is assumed to be chemisorbed in a monoatomic layer prior to O_2 evolution with a one-to-one relationship with surface metal atoms. This implies that the charge associated with the formation or reduction of the layer is related to the real area of the microelectrode. Factors for conversion of the charge into area are derived in different ways depending on whether the surface is deemed to be polycrystalline or of single crystal face type. The distribution of metal atoms is well defined for a perfect single crystal face,[14] whereas it is taken as an average value between the main low-index faces for polycrystalline surfaces. The resulting value is generally very close to that pertaining to the (100) face.[15]

The relationship between charge of formation or reduction of the layer Q_o and area is based on the following equations:[16]

$$Q_o = 2eN_A\Gamma_o A \qquad (1)$$

where N_A is the Avogadro constant, Γ_0 the surface concentration of atomic oxygen assumed to be equal to N_A, the surface density of metal atoms. From the value of N_A per unit surface area, the value of Q_o^S, the reference charge, is calculated so that:

$$A = \frac{Q_o}{Q_o^S} \qquad (2)$$

The reduction peak at 0.8 V approx. is characteristic for gold oxide reduction and it is the area under this peak that is used for calculating the electrochemical area. A similar reduction peak, albeit at a different potential, is used for platinum electrodes. The electrochemical area of the electrode is obtained by dividing the area under the reduction peak by a factor (420 $\mu C\ cm^{-2}$, 390 $\mu C\ cm^{-2}$ for polycrystalline platinum and gold, respectively).[17,18,19]

However, there are some difficulties with this method. Oxygen adsorption usually results in oxide formation by a place-exchange mechanism. This leads to the charge associated with the formation of the layer being a function of time. Thick oxide phase layers can sometimes form as the potential, where the monolayer is completed, is difficult to assess.

Therefore, it is essential that the areas determined by the gold oxide method are independently verified. The real surface area of the electrode is independently verified when the limiting surface coverages for the complexes in the adsorption studies (in Chapters 4 and 5) are measured by integrating the Faradaic charge under the $Os^{2+/3+}$ wave. The surface coverage is directly related to the microscopic surface area of the electrode by the following equation:

$$\Gamma = \frac{Q}{nFA} \tag{3}$$

where Γ is the surface coverage of the complex, Q is the charge under the $Os^{2+/3+}$ wave, n is the number of electrons involved, F is the Faraday constant and A is the microscopic or real surface area of the microelectrode.

For example, the limiting surface coverage measured for $[Os(bpy)_2Cl(bpe)]^+$, at high bulk concentrations, i.e., > 200 μM is (7.0 ± 0.5) x 10^{-11} mol cm$^-$2, bpy is 2,2′-bipyridyl and bpe is trans-1,2-bis(4-pyridyl)ethylene. The corresponding area per molecule calculated using Equation 4 is (237 ± 17) Å^2.

$$A_M = \frac{1}{\Gamma \times N_A} \tag{4}$$

where A_M is the area per molecule, Γ is the surface coverage of the complex and N_A is the Avogadro constant. This analysis suggests that the effective radius of the complex is approximately 8.7 Å.

Crystallographic data for related osmium polypyridyl complexes[20] suggest that the radii for these complexes are approximately 7.5 Å. When additional volume

contributions from solvent and charge compensating counterions are taken into account, the experimental radius of 8.7 Å compares favourably with that predicted on the basis of the crystallographic data. This close agreement between theory and experiment suggests that the microscopic areas of the gold microelectrodes determined using the oxide formation method are accurate. Similar agreement is observed for $[Os(OMe\text{-}bpy)_2Cl(p3p)]^+$ monolayers where OMe is 4,4′-dimethoxy-2,2′-bipyridyl and p3p is 1,4-trimethylene dipyridine.

Figure 2.6 is an example of a cyclic voltammogram obtained for a 25 μm radius gold microelectrode in 0.2 M H_2SO_4 using scan rate of 0.1 Vs^{-1} and potential limits of 0.0 to 1.5 V. The reference electrode used was Ag/AgCl. The well defined peak at approximately 0.8 Volts is characteristic of gold oxide reduction and the area under this peak is used for the calculation of the electrochemical area of the microelectrode.

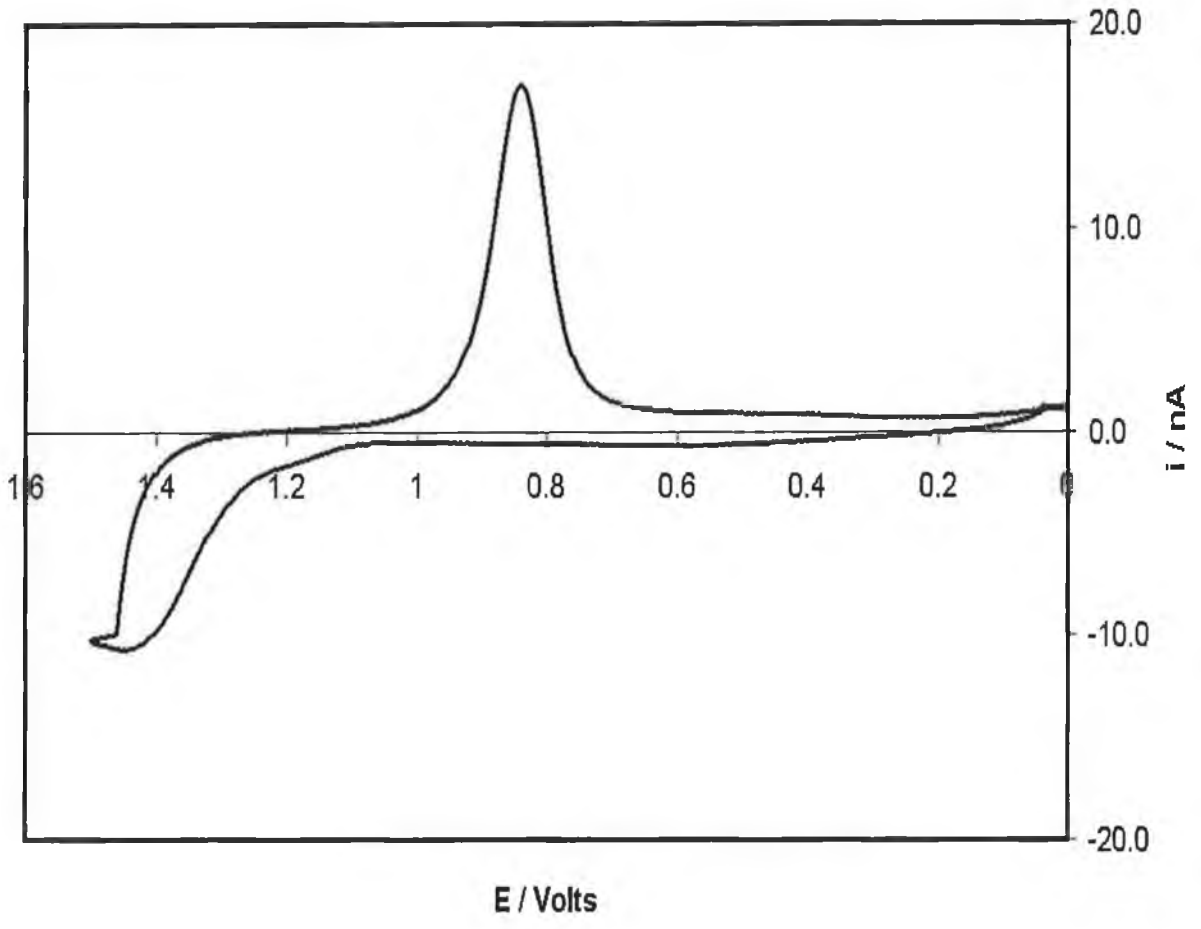

Figure 2.6. Cyclic voltammogram for a 25 μm radius gold microelectrode in 0.2 M H_2SO_4 using scan rate of 0.1 Vs^{-1} and potential limits of 0.0 to 1.5 V. The reference electrode used was Ag/AgCl. The peak at approximately 0.8 Volts is characteristic of gold oxide reduction and the area under this peak is used for the calculation of the electrochemical area of the microelectrode.

2.7. Determination of Geometric Surface Areas

When dealing with disk microelectrodes, the simplest method of estimating the geometric surface area is to use the geometric formula for the area of a disk, i.e., πr^2, r being the radius of the microwire used in the fabrication of the microelectrode. However, a perfect geometrically shaped disk is not always exposed when fabricating microelectrodes. While forming an elliptical instead of a disk electrode does not affect any experimental data, as the electrochemical area is determined before individual experiments, it is important in determining a true surface roughness of a microelectrode. A true surface roughness of a microelectrode is of fundamental importance when comparing theoretical and experimental data.

2.7.1. Redox–Active Probe Method

A commonly used method for determining the geometric surface area of a microelectrode is to conduct a series of solution phase experiments using a redox active compound in solution.

A species of known diffusion coefficient[21], $[Os(bpy)_3]^{2+}$ ($D = 1.16 \times 10^{-5}$ cm^2 s^{-1}), was dissolved at known concentration in DMF with 0.1 M $LiClO_4$ as electrolyte. Steady state (slow scan rate) cyclic voltammograms were run for each microelectrode. From the characteristic sigmoidal shaped response, the limiting current i_d. was obtained The radius of each electrode was obtained from the well known relation[22,23,24,25]

$$i_d = 4nFrcD \tag{5}$$

where n is the number of electrons transferred, F is the Faraday constant, and D is the diffusion coefficient of the redox active species.

The surface roughness was calculated by dividing the "real" microscopic surface area, determined by the oxide formation method, by the geometric area determined using the redox active probe. Table 2.1 gives the surface roughness calculated in this way for the platinum microelectrodes used in this work.

Table 2.1. Surface roughness for platinum microelectrodes. The geometric area was determined by steady state cyclic voltammetry using a redox-active probe, $[Os(bpy)_3]^{2+}$. The "real" microscopic surface area was determined by the oxide formation method. The surface roughness is calculated by dividing the real area by the geometric area. The radius listed here is the nominal radius of the micro-wire used in the fabrication of the microelectrode.

Type of Microelectrode	Radius Microns	Surface Roughness
Pt disk	1	1.9
Pt disk	1	2.2
Pt disk	1	1.5
Pt disk	5	1.8
Pt disk	5	1.3
Pt disk	5	1.4
Pt disk	10	1.4
Pt disk	10	1.6
Pt disk	10	1.8
Pt-disk	12.5	1.6
Pt disk	12.5	2.2
Pt-disk	25	1.4
Pt-disk	25	1.5
Pt-disk	25	1.6

2.8. RC Time Constants

In this and the following chapters, measurements were made using microelectrodes fabricated with different materials. As explained in 1.3.3, the RC cell time constant is of fundamental importance when measuring fast electrochemical processes. At this point, the measured RC cell time constants for the microelectrodes used in this thesis are given.

RC cell time constants, measured in blank electrolyte solution, were between 0.01 and 0.5 μs depending on the electrode material and radius as well as the supporting electrolyte concentration. The interfacial kinetics were measured only at times greater than about 5 to 10 RC. This condition was satisfied by selecting a microelectrode of appropriate radius.

In Chapter 5, the electrochemical properties of $[Os(OMe\text{-}bpy)_2Cl(p3p)]^{2+}$ monolayers assembled on various electrode materials will be examined. Table 2.2 gives the electrode response times, total cell resistances, R, and area normalised interfacial capacitances for $[Os(OMe\text{-}bpy)_2Cl(p3p)]^{2+}$ monolayers assembled on various electrode materials.

Table 2.2. Electrode Response Times, Total Cell Resistances, R, and Area Normalised Interfacial Capacitances for $[Os(OMe\text{-}bpy)_2Cl(p3p)]^{2+}$ Monolayers Assembled on Various Electrode Materials.[a]

Electrode Material	RC / ns[b]	R / kΩ	C / μF cm^{-2}
Platinum	171(30)	8.4(0.3)	26(4)
Mercury	135(20)	7.8(0.1)	22(3)
Gold	162(26)	8.2(0.3)	25(3)
Silver	180(46)	8.1(0.4)	28(6)
Carbon	440(90)	3.3(0.1)	27(5)

[a] Measured using potential step chronoamperometry from –0.15 to –0.1 V. The monolayer is in the 1+ oxidation state. The supporting electrolyte is aqueous 1.0 M $NaClO_4$.

[b] The electrode radius is 5 μm except for carbon where it is 12.5 μm.

2.9. Determination of Diffusion Coefficients

2.9.1. $[Os(bpy)_2Cl(p2p)]^+$

$[Os(bpy)_2Cl(p2p)]PF_6$ (0.0117 g) was placed in a volumetric flask (10 cm^3) and $LiClO_4$ (0.1060 g) was added. The solids were then dissolved in CH_3CN by swirling and the solution was made up to the mark. This gave a 1.3 mM solution of the osmium complex in 0.1 M $LiClO_4$ supporting electrolyte.

Using a 1 mm radius platinum macroelectrode with a Ag/AgCl reference electrode, cyclic voltammograms were run over scan rates ranging from 1 mV s^{-1} to 3 V s^{-1} with a potential window of 0 to 0.6 Volts. Figures 2.7 and 2.8 illustrate the cyclic voltammograms for scan rates of 10 and 200 mV s^{-1}, respectively.

From this series of cyclic voltammograms, the anodic and cathodic peak currents and the peak to peak separation were determined. The scan rates from 2 to 200 mV s^{-1} had a peak to peak separation of less than 83 mV and plots of $\nu^{1/2}$ vs. $-i_{pa}$ and $\nu^{1/2}$ vs. i_{pc} were linear with a correlation coefficient of 0.9997 and 0.9981, respectively. The absolute value of the ratio i_{pc}/i_{pa} was found to be 0.82 ± 0.07. Between these scan rates, the process should be under diffusion control and these data were selected for calculation of the diffusion coefficient for the complex.

2.9.2. Modes of Mass Transfer

Mass transfer, i.e., the movement of material from one location in solution to another, arises either from differences in electrical or chemical potential at the two locations, or from movement of a volume element of solution. The modes of mass transfer are:[26]

1. *Migration.* Movement of a charged body under the influence of an electric field (a gradient of electrical potential).
2. *Diffusion.* Movement of a species under the influence of a gradient of chemical potential (i.e., a concentration gradient).
3. *Convection.* Stirring or hydrodynamic transport.

In these cyclic voltammetric experiments, the operating conditions of so-called semi-infinite linear diffusion. This means that the electrode dimensions are larger than the thickness of the diffusion layer and that there is a bulk solution far enough from the electrode that the concentrations of all species remain unchanged throughout the experiment.

The process under study is a single, reversible, electron transfer. There are several theoretical criteria to confirm this.[27] The difference in cathodic and anodic peak potentials, ΔE_p, should be 57 mV. In actual experiments, a ΔE_p of 57 mV is rarely observed because of small distortions due to solution resistance effects. In practice, ΔE_p is usually significantly larger than 57 mV. The ratio of i_{pc}/i_{pa} in theory for a diffusion controlled process should be equal to 1. Again, deviations from this often occur in practice and this deviation for some osmium and ruthenium complexes has been measured. The major criterion to distinguish diffusion controlled processes from processes featuring the adsorption of the electroactive species is that the peak current should scale linearly with the square root of the scan rate.[28,29,30] As will be shown, this is clearly evident in the solution phase experiments described here.

The slopes of the best fit lines through the data points on the plots of $\nu^{1/2}$ vs. i_{pa} and $\nu^{1/2}$ vs. i_{pc} are then used with the Randles-Sevçik relation[31,32,33] (Equation 6) to determine the diffusion coefficient. Figure 2.9 illustrates the plots of $\nu^{1/2}$ vs.-i_{pa} and $\nu^{1/2}$ vs. i_{pc}.

$$i_P = 2.69x10^5 D^{1/2} C\nu^{1/2} An^{3/2} \qquad (6)$$

where i_p is peak current, D is the diffusion coefficient, ν is the scan rate, A is the geometric area of the macroelectrode and C is the concentration of the redox active species, n is the number of electrons involved.

Thus, a plot of peak current obtained under these conditions (cathodic or anodic) versus $\nu^{1/2}$ will be linear having slope of $2.69x10^5An^{3/2}CD^{1/2}$. Knowing A, n, and C, the diffusion coefficient for the complex can be determined.

The diffusion coefficient for $[Os(bpy)_2Cl(p2p)]^+$ was calculated to be $(1.62\pm0.02) \times 10^{-7}$ cm^2 s^{-1}.

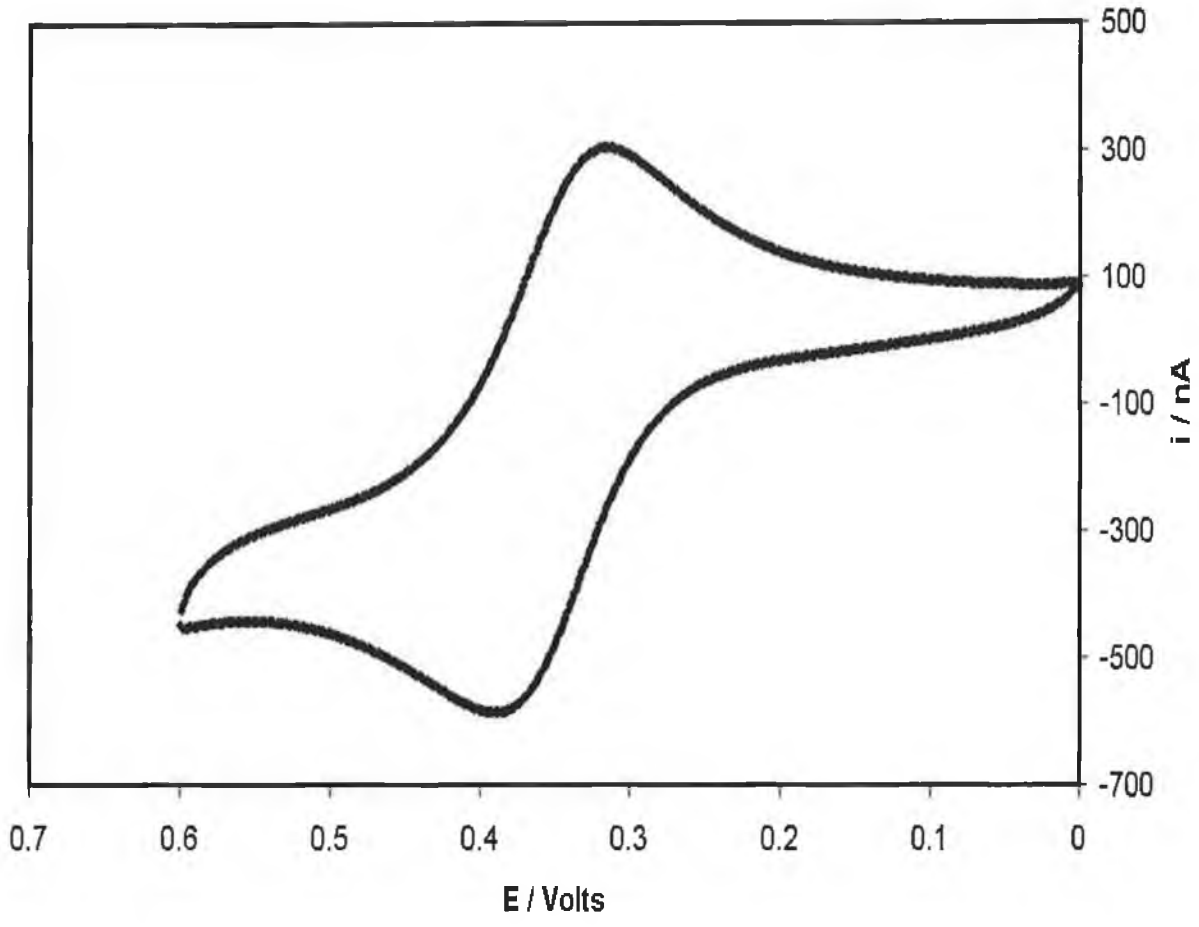

Figure 2.7. Cyclic voltammogram for 1.3 mM solution of $[Os(bpy)_2Cl(p2p)]PF_6$ in CH_3CN with 0.1 M $LiClO_4$ as supporting electrolyte; bpy is 2,2′–bipyridyl, p2p is 1,2-bis(4-pyridyl)ethane. The cyclic voltammogram was recorded using a 1 mm radius platinum macroelectrode with a Ag/AgCl reference electrode. The scan rate used was 10 mV s^{-1} with potential limits of 0.0 to 0.6 V.

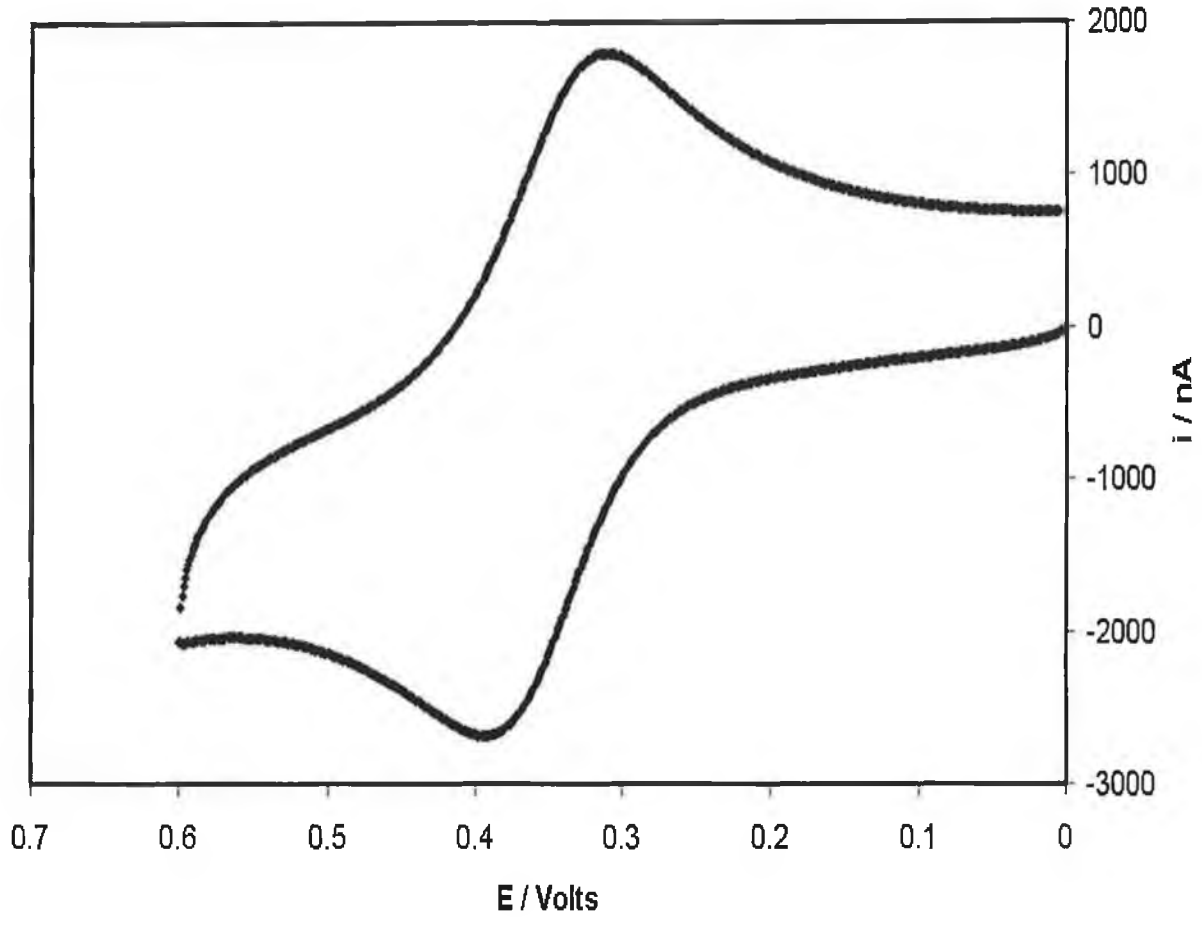

Figure 2.8. Cyclic voltammogram for 1.3 mM solution of $[Os(bpy)_2Cl(p2p)]PF_6$ in CH_3CN with 0.1 M $LiClO_4$ as supporting electrolyte; bpy is 2,2′ – bipyridyl, p2p is 1,2-bis(4-pyridyl)ethane. The cyclic voltammogram was recorded using a 1 mm radius platinum macroelectrode with a Ag/AgCl reference electrode. The scan rate used was 200 mV s^{-1} with potential limits of 0.0 to 0.6 V.

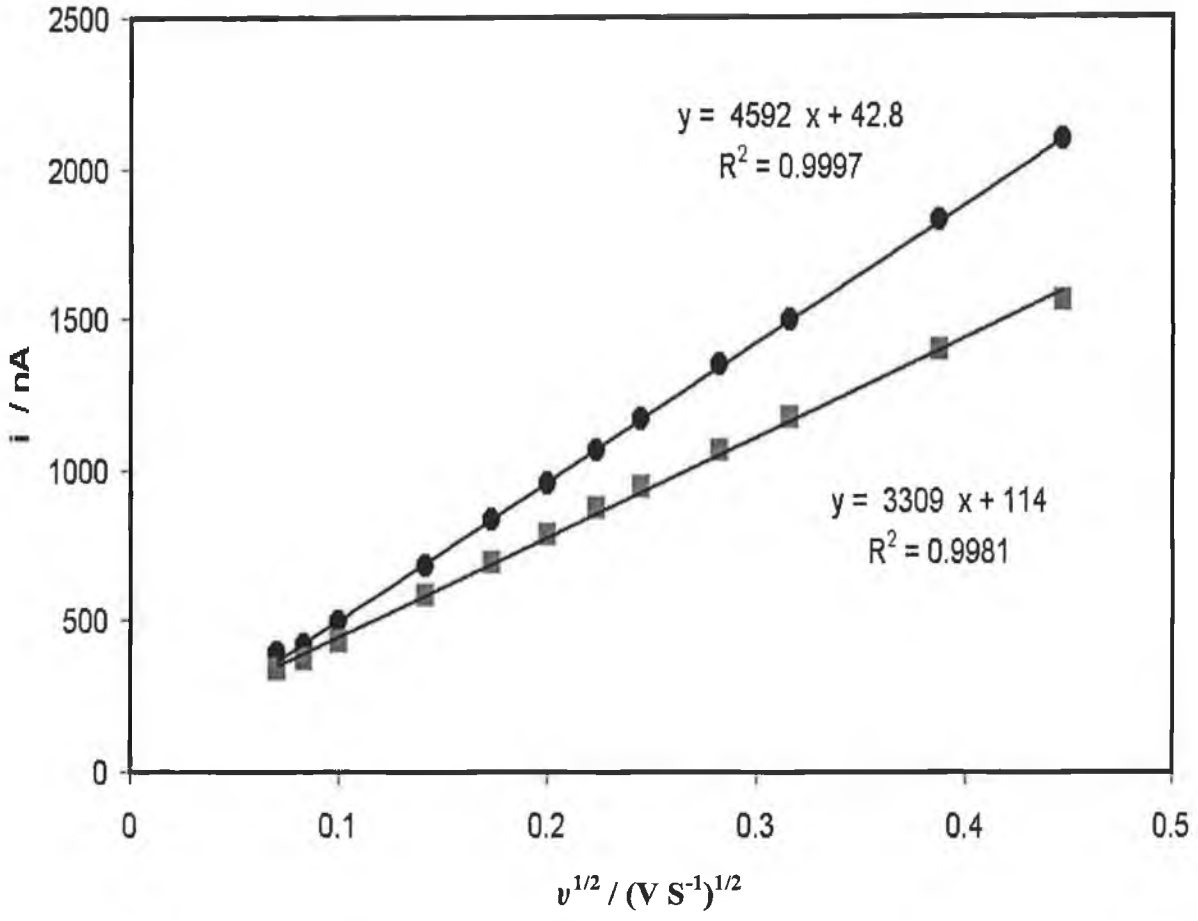

Figure 2.9. Plots of $v^{1/2}$ vs. $-i_{pa}$ and $v^{1/2}$ vs. i_{pc} for the cyclic voltammograms for 1.3 mM solution of $[Os(bpy)_2Cl(p2p)]PF_6$ in CH_3CN with 0.1 M $LiClO_4$ as supporting electrolyte; bpy is 2,2′–bipyridyl, p2p is 1,2-bis(4-pyridyl)ethane. The cyclic voltammograms were recorded using a 1 mm radius platinum macroelectrode and an Ag/AgCl reference electrode. The $-i_{pa}$ data are represented by ●. The i_{pc} data are represented by ■.

2.9.3. $[Os(bpy)_2Cl(bpe)]^+$

$[Os(bpy)_2Cl(bpeH)](PF_6)_3$ (0.0086 g) was placed in a volumetric flask (10 cm^3) and $LiClO_4$ (0.1060 g) was added. The solids were then dissolved in CH_3CN by swirling and the solution was made up to the mark. This gave a 0.74 mM solution of the osmium complex in 0.1 M $LiClO_4$ supporting electrolyte.

Using a 1 mm radius platinum macroelectrode and a Ag/AgCl reference electrode, cyclic voltammograms were run over scan rates ranging from 1 mV s^{-1} to 20 V s^{-1} with a potential window of 0 to 0.6 Volts. Figures 2.10 and 2.11 illustrate the cyclic voltammograms for scan rates of 10 mV s^{-1} and 200 mV s^{-1}, respectively.

From this series of cyclic voltammograms, the anodic and cathodic peak currents and the peak to peak separation were determined. The scan rates from 2 to 200 mV s^{-1} had a peak to peak separation of less than 76 mV and plots of $\nu^{1/2}$ vs. $-i_{pa}$ and $\nu^{1/2}$ vs. i_{pc} were linear with a correlation coefficient of 0.9999 and 0.9998, respectively. The absolute value of the ratio i_{pc}/i_{pa} was found to be 0.93±0.09. Between these scan rates, the process should be under semi-infinite diffusion control and these data were selected for calculation of the diffusion coefficient for the complex.

The slopes of the best fit lines through the data points on the plots of $\nu^{1/2}$ vs. i_{pa} and $\nu^{1/2}$ vs. i_{pc} are then used with the Randles-Sevçik relation (i.e., Equation 7) to determine the diffusion coefficient. Figure 2.12 illustrates this.

The diffusion coefficient for $[Os(bpy)_2Cl(bpe)]^+$ was calculated to be (1.38±0.01) x 10^{-6} cm^2 s^{-1}.

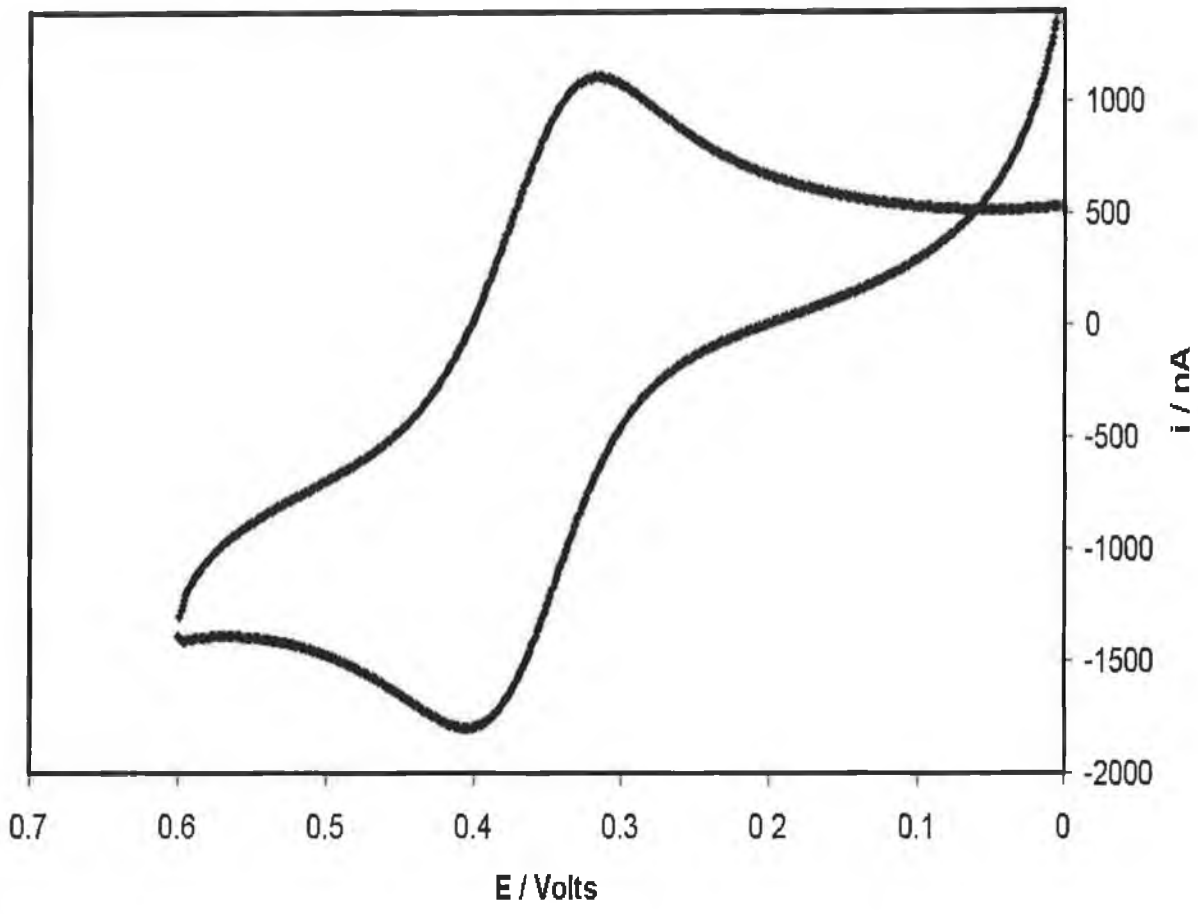

Figure 2.10. Cyclic voltammogram for 0.74 mM solution of $[Os(bpy)_2Cl(bpeH)](PF_6)_3$ in CH_3CN with 0.1 M $LiClO_4$ as supporting electrolyte; bpy is 2,2′-bipyridyl, p2p is 1,2-bis(4-pyridyl)ethane, bpe is *trans*-1,2-bis(4-pyridyl)ethylene. The cyclic voltammogram was recorded using a 1 mm radius platinum macroelectrode with a Ag/AgCl reference electrode. The scan rate used was 10 mV s^{-1} with potential limits of 0.0 to 0.6 V.

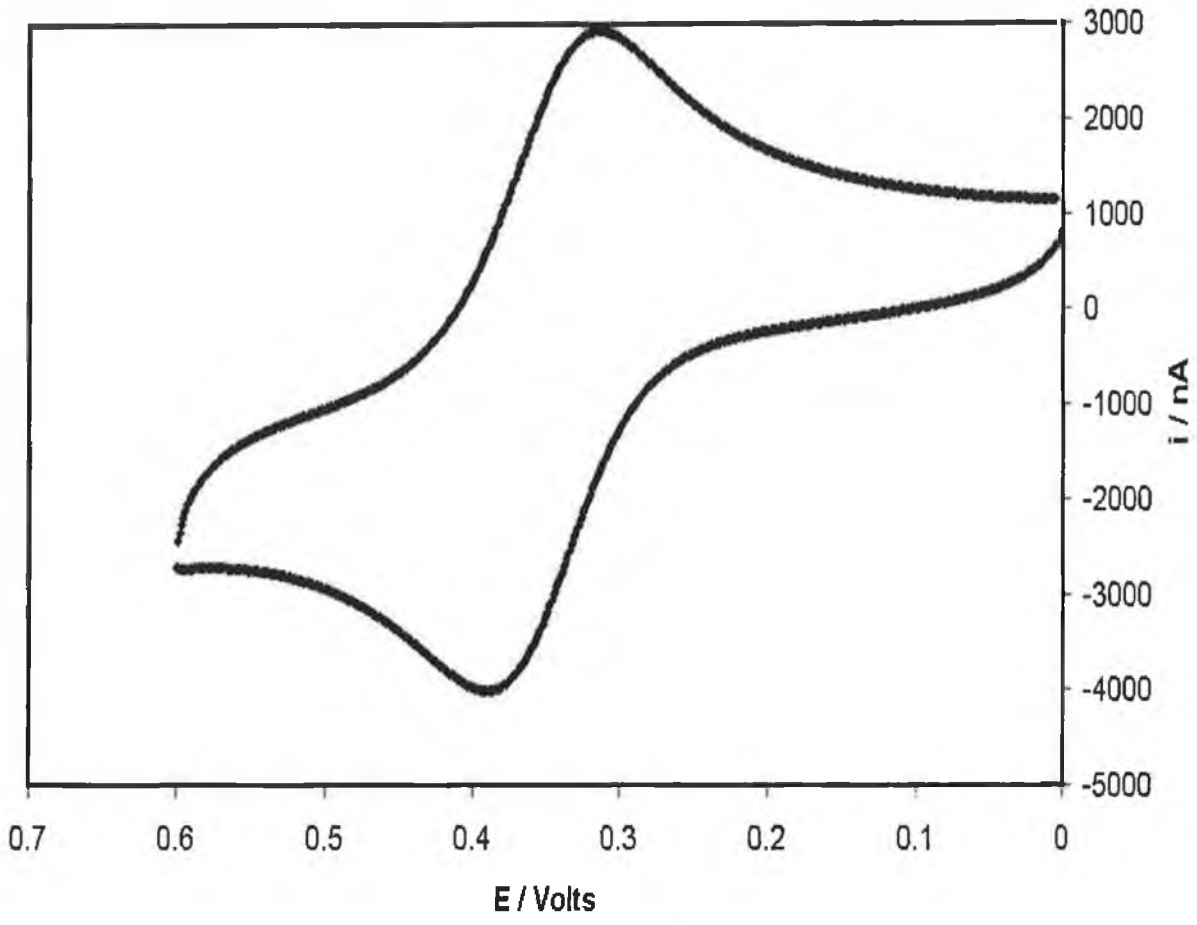

Figure 2.11. Cyclic voltammogram for 0.74 mM solution of $[Os(bpy)_2Cl(bpeH)](PF_6)_3$ in CH_3CN with 0.1 M $LiClO_4$ as supporting electrolyte; bpy is 2,2′-bipyridyl, p2p is 1,2-bis(4-pyridyl)ethane, bpe is *trans*-1,2-bis(4-pyridyl)ethylene. The cyclic voltammogram was recorded using a 1 mm radius platinum macroelectrode with a Ag/AgCl reference electrode. The scan rate used was 200 mV s^{-1} with potential limits of 0.0 to 0.6 V.

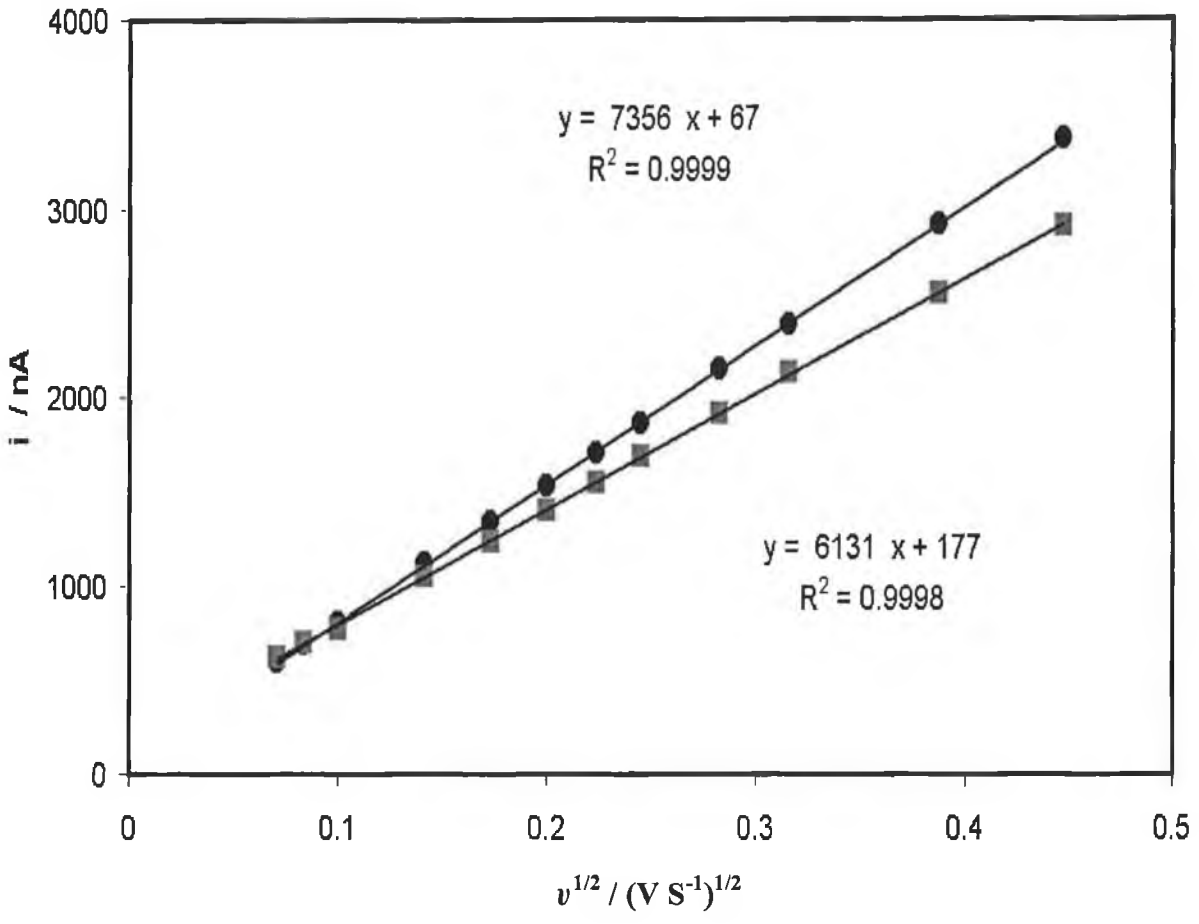

Figure 2.12. Plots of $v^{1/2}$ vs. $-i_{pa}$ and $v^{1/2}$ vs. i_{pc} for cyclic voltammograms of 0.74 mM solution of $[Os(bpy)_2Cl(bpeH)](PF_6)_3$ in CH_3CN with 0.1 M $LiClO_4$ as supporting electrolyte; bpy is 2,2′-bipyridyl, p2p is 1,2-bis(4-pyridyl)ethane, bpe is *trans*-1,2-bis(4-pyridyl)ethylene. The cyclic voltammograms were recorded using a 1 mm radius platinum macroelectrode with a Ag/AgCl reference electrode. The $-i_{pa}$ data are represented by ●. The i_{pc} data are represented by ■.

2.9.4. $[Ru(bpy)_2Cl(4\text{-}tet)]^+$

A 1.0 mM solution of $[Ru(bpy)_2Cl(4\text{-}tet)]^+$ where bpy is 2,2′-bipyridyl., 4-tet is 3,6-bis(4-pyridyl)-1,2,4,5-tetrazine, was made up in CH_3CN with 0.1 M $[CH_3(CH_2)_3]_4NBF_4$ as supporting electrolyte.

Using a freshly polished, sonicated, washed and acid cleaned 25 μm gold microelectrode, cyclic voltammograms were run over various scan rates in order to establish the solution phase properties of the complex. The scan rates used range from very slow (20 mV s^{-1}) to fast (800 Vs^{-1}). The steady state response is observed at the slow scan rate while a semi-infinite diffusion response at fast scan rates is observed.

From this series of cyclic voltammograms, the anodic and cathodic peak currents and the peak to peak separation were determined. The scan rates from 0.1 to 20 V s^{-1} had a peak to peak separation of less than 72 mV and plots of $\nu^{1/2}$ vs. $-i_{pa}$ and $\nu^{1/2}$ vs. i_{pc} were linear with a correlation coefficient of 0.993 and 0.999, respectively. The absolute value of the ratio i_{pc}/i_{pa} was found to be 0.85±0.14. Between these scan rates, the process should be under diffusion control and these data were selected for calculation of the diffusion coefficient for the complex.

The slopes of the best fit lines through the data points on the plots of $\nu^{1/2}$ vs. i_{pa} and $\nu^{1/2}$ vs. i_{pc} are then used with the Randles-Sevçik relation (Equation 6) to determine the diffusion coefficient. Figure 2.13 illustrates this.

The diffusion coefficient for $[Ru(bpy)_2Cl(4\text{-}tet)]^+$ was calculated to be $(3.9\pm0.2) \times 10^{-5}$ cm^2 s^{-1}.

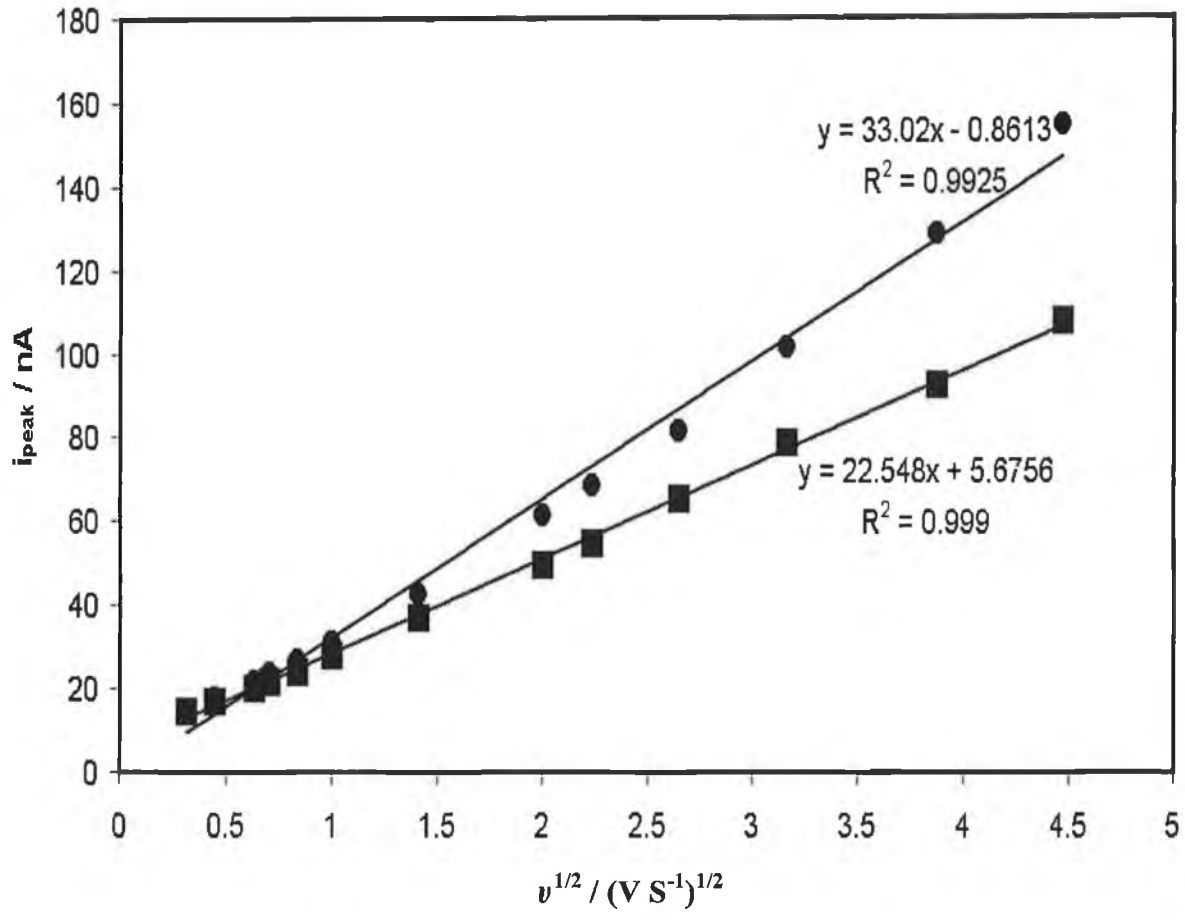

Figure 2.13. Plots of $\nu^{1/2}$ vs. $-i_{pa}$ and $\nu^{1/2}$ vs. i_{pc} for cyclic voltammograms of 0.1 mM solution of $[Ru(bpy)_2Cl(4\text{-tet})]^+$ in CH_3CN with 0.1 M $[CH_3(CH_2)_3]_4NBF_4$ as supporting electrolyte; bpy is 2,2′-bipyridyl, 4-tet is 3,6-bis(4-pyridyl)-1,2,4,5-tetrazine. The cyclic voltammograms were recorded using 25 μm radius gold microelectrode with a Ag/AgCl reference electrode. The $-i_{pa}$ data are represented by ●. The i_{pc} data are represented by ■.

2.9.5. $[Os(bpy)_2Cl(4bpt)]^+$

Solution phase experiments were carried out on $[Os(bpy)_2Cl(4bpt)].PF_6$ in a similar way as for the ruthenium complex using a 0.1 mM solution of the complex and the electrolyte 1.0 M, tetrabutyl ammonium tetrafluoroborate $[CH_3(CH_2)_3]_4NBF_4$ in acetonitrile.

Using a freshly polished, sonicated, washed and acid cleaned 25 μm gold microelectrode, cyclic voltammograms were run over various scan rates in order to establish the solution phase properties of the complex. The scan rates used range from 1 to 29 Vs^{-1}.

From this series of cyclic voltammograms, the anodic and cathodic peak currents and the peak to peak separation were determined. The scan rates from 2 to 10 V s^{-1} had a large peak to peak separation of up to 162 mV while plots of $\nu^{1/2}$ vs. $-i_{pa}$ and $\nu^{1/2}$ vs. i_{pc} were still linear with a correlation coefficient of 0.998. The absolute value of the ratio i_{pc}/i_{pa} was found to be 1.21±0.05. This high ratio and the large ΔE_p at relatively low scan rates indicate that the electron transfer process may not be exclusively under diffusion control despite the clear linearity of the plots. Therefore, the subsequently calculated diffusion coefficient must be regarded as merely an approximation of the true value.

The diffusion coefficient for $[Os(bpy)_2Cl(4bpt)].PF_6$ was calculated to be $(1.61\pm0.08) \times 10^{-6}$ cm^2 s^{-1}.

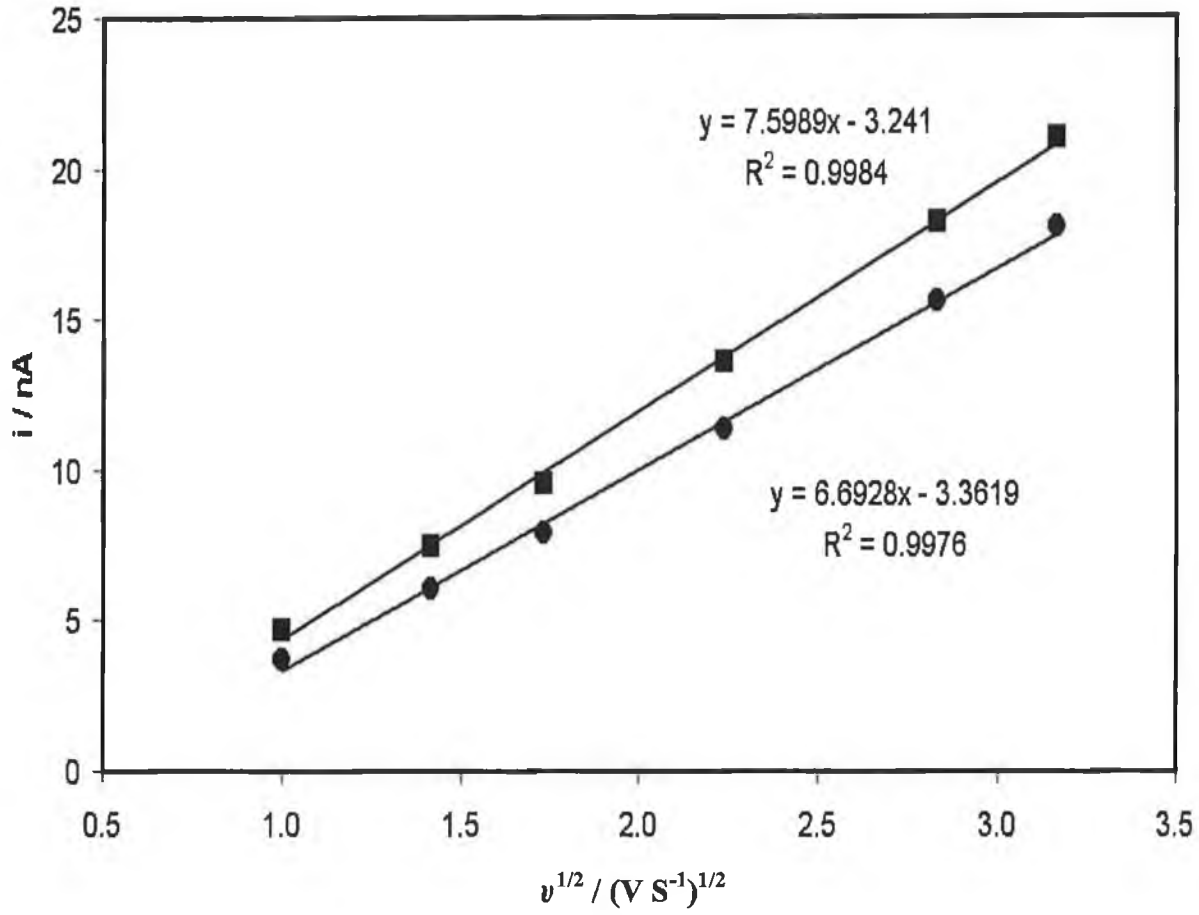

Figure 2.14. Plots of $\nu^{1/2}$ vs. $-i_{pa}$ and $\nu^{1/2}$ vs. i_{pc} for cyclic voltammograms of 0.1 mM solution of $[Os(bpy)_2Cl(4\text{-}bpt)]^+$ in CH_3CN with 0.1 M $[CH_3(CH_2)_3]_4NBF_4$ as supporting electrolyte; bpy is 2,2′-bipyridyl. The cyclic voltammograms were recorded using 25 μm radius gold microelectrode with a Ag/AgCl reference electrode. The $-i_{pa}$ data are represented by ●. The i_{pc} data are represented by ■.

2.9.6. Discussion of Diffusion Coefficients

Table 2.3 gives the diffusion coefficients measured for the osmium and ruthenium complexes under investigation here. Table 2.4 lists a range of different compounds with their diffusion coefficients taken from the literature for comparison purposes. There are a number of features apparent in the diffusion study.

The diffusion coefficients measured are in the range 10^{-7} to 10^{-5} cm^2 s^{-1} with the ruthenium complex having the highest diffusion coefficient. These values are not unreasonable when compared to the values in Table 2.4. Physical size can often be the dominant effect with respect to diffusion. However, this interpretation cannot be applied here to explain the range in diffusion coefficients, as the complexes are all of similar size.

The plots of (scan rate)$^{1/2}$ vs. peak currents all showed the expected linearity for a freely diffusing species. However, the slopes for the anodic peak current vs. (scan rate)$^{1/2}$ were significantly different to the slopes for the cathodic peak current vs. (scan rate)$^{1/2}$. The range in the measured diffusion coefficients was disturbingly large for complexes of similar size with the highest value (i.e., the value for the complex with the 4-tet bridging ligand) being 240 times the lowest value (i.e., the value for the complex with the p2p bridging ligand). Perhaps most importantly, the plots of (scan rate)$^{1/2}$ vs. peak currents do not go through zero, as they should, for an exclusively diffusion based process. This observation suggests that even in acetonitrile the complexes adsorb to some extent causing inaccurate diffusion coefficients to be extracted. It is perhaps important to note that these results were used only for the characterisation of the complexes and were not used elsewhere in the thesis. In order to accurately probe the impact of the different bridging ligands on diffusion of the complexes, the surface active pyridine nitrogen would have to be blocked, e.g., by methylation.

Table 2.3. The diffusion coefficients for $[Os(bpy)_2Cl(p2p)]^+$, $[Os(bpy)_2Cl(bpe)]^+$, $[Os(bpy)_2Cl(4bpt)]^+$, $[Ru(bpy)_2Cl(4\text{-}tet)]^+$, bpy is 2,2′-bipyridyl, p2p is 1,2-bis(4-pyridyl)ethane, bpe is *trans*-1,2-bis(4-pyridyl)ethylene, 4-bpt is 3,5-bis(2-pyridyl)1,2,4- triazole, 4-tet is 3,6-bis(4-pyridyl)-1,2,4,5-tetrazine.

Complex	**10^6 D cm^2 s^{-1}**
$[Os(bpy)_2Cl(p2p)]^+$	0.162(0.002)
$[Os(bpy)_2Cl(bpe)]^+$	1.38(0.01)
$[Os(bpy)_2Cl(4bpt)]^+$	1.61(0.01)
$[Ru(bpy)_2Cl(4\text{-}tet)]^+$	39.0(2.0)

Table 2.4. Diffusion coefficients for a number different species taken from the literature for comparison purposes. bpy is 2,2'-bipyridyl and 2,3-dpp is 2,3-bis(2-pyridyl)pyrazine.

Species	10^6 D / cm^2 s^{-1}
Bis(biphenyl)chromium(I)[34]	3.78 – 5.19
$Fe(CN)_6^{4-}$[35]	5.19-7.05
$Fe(CN)_6^{3-}$[36]	7.17(0.18)
Ferrocene[32,37]	21.7(0.5)
$Ru(NH_3)_6^{3+}$[32]	5.48(0.22)
$\{[(bpy)_2Ru(\mu\text{-}2,3\text{-}dpp)]_2Ru(\mu\text{-}2,3\text{-}dpp)Ru[\mu\text{-}2,3\text{-}dpp)Ru(bpy)_2]_2\}^{12+}$[38]	4.7
Benzoquinone[39]	21.3(0.7)
Naphthoquinone[35]	18.6(0.5)
Anthraquinone[35]	19.8(1.0)
Anthracene[35]	20.0(0.5)

2.10. Effect of Electrode Material on Electrochemical Properties

In Chapter 5, the effect of the electrode material on the electrochemical properties of adsorbed monolayers of $[Os(OMe\text{-}bpy)_2Cl(p3p)]^+$ using microelectrodes will be studied. In this section, the response of osmium complexes in solution in the absence of adsorption using macroelectrodes of various types will be investigated. The solutions are the same ones used in the determination of the diffusion coefficients of $[Os(bpy)_2Cl(p2p)]^+$ and $[Os(bpy)_2Cl(bpe)]^+$. The electrodes used are platinum, radius 1 mm, gold, radius 1 mm, and glassy carbon, radius 1.5 mm.

A selection of the cyclic voltammograms recorded is shown in Figures 2.15 to 2.20. The influence of the type of electrode material is striking in that the effect of changing the electrode material on the voltammetric response is significantly greater than changing the identity of the metal complex itself.

Figures 2.15 and 2.16 show the response of the complexes using the platinum macroelectrode. The responses are similar having clearly defined peaks, with slowly increasing ΔE_p with increasing scan rate and relatively low capacitive background currents. Diffusion control is clearly evident for the data measured at slow scan rate (i.e., < 200 mV s^{-1}) with the platinum macroelectrode. This is why the data from the platinum macroelectrode was chosen to calculate the diffusion coefficients for these complexes. The cyclic voltammograms are stable and as the wave is repeatedly cycled, there is no change in peak heights or peak shapes and no following chemical reaction.

Figures 2.17 and 2.18 show the response of the complexes using the gold macroelectrode. The responses are similar to each other but substantially different to the responses obtained with the platinum electrode. The peak to peak separation is higher than with platinum at equivalent scan rates and ΔE_p increases more quickly with increasing scan rate. There is a high capacitive background current which interferes with the detection of the peak potential as the scan rate is increased.

Figures 2.19 and 2.20 show the response of the complexes using the glassy carbon macroelectrode. Unlike for platinum and gold, the responses are different to each other and substantially different to the responses obtained with the platinum and gold electrodes. The peak to peak separation is much higher than with platinum and gold at equivalent scan rates and increases more quickly with increasing scan rate. These differences are most likely due to the difficulty in preparing electrodes of different materials in an identical way. The carbon electrode is also different in that it cannot be electrochemically cleaned like the metal electrodes. In Chapter 5, a similar finding with the electrochemical response of adsorbed monolayers on carbon fibre and platinum microelectrodes is reported.

There is a high capacitive background current which interferes with the detection of the peak potential as the scan rate is increased.

Figures 2.21 and 2.22 show the ΔE_p changing with scan rate for the three different electrodes and, in fact, give a concise summary of the performance of each electrode.

Evidently, the platinum macroelectrode is superior to the gold and the gold macroelectrode is superior to the glassy carbon macroelectrode for the study of these osmium complexes in solution phase.

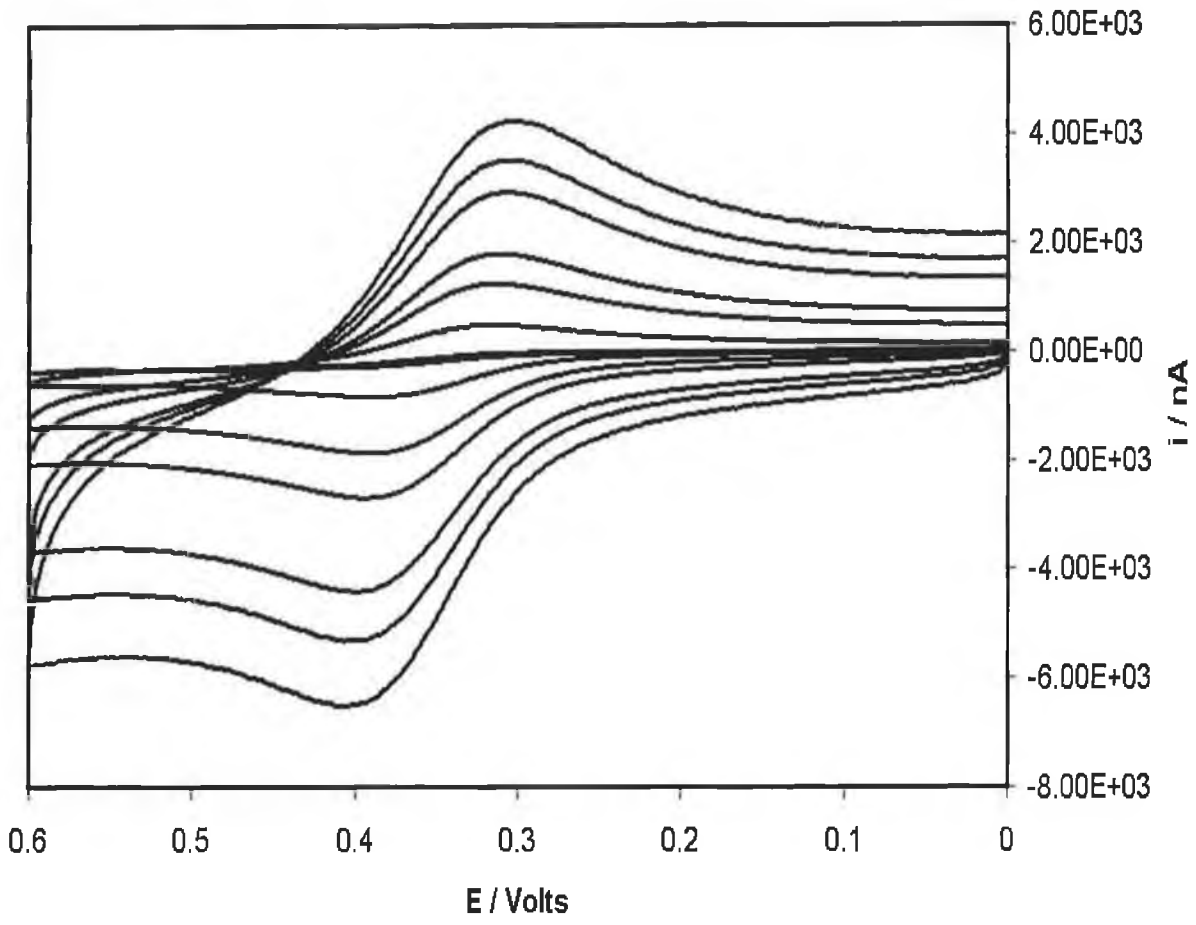

Figure 2.15. Cyclic voltammograms for 1.3 mM solution of $[Os(bpy)_2Cl(p2p)]PF_6$ in CH_3CN with 0.1 M $LiClO_4$ as supporting electrolyte; bpy is 2,2′-bipyridyl, p2p is 1,2-bis(4-pyridyl)ethane. The series was recorded using a 1 mm radius platinum macroelectrode with a Ag/AgCl reference electrode. The scan rates are (top to bottom) 1000, 700, 500, 200, 100, 20, and 1 mV s^{-1}. The cathodic currents are up, and the anodic currents are down. The lower scan rate cyclic voltammograms (i.e., 1-200 mV s^{-1}) show the process under diffusional control. The higher scan rate cyclic voltammograms (i.e., 500-1000 mV s^{-1}) show the process under kinetic control.

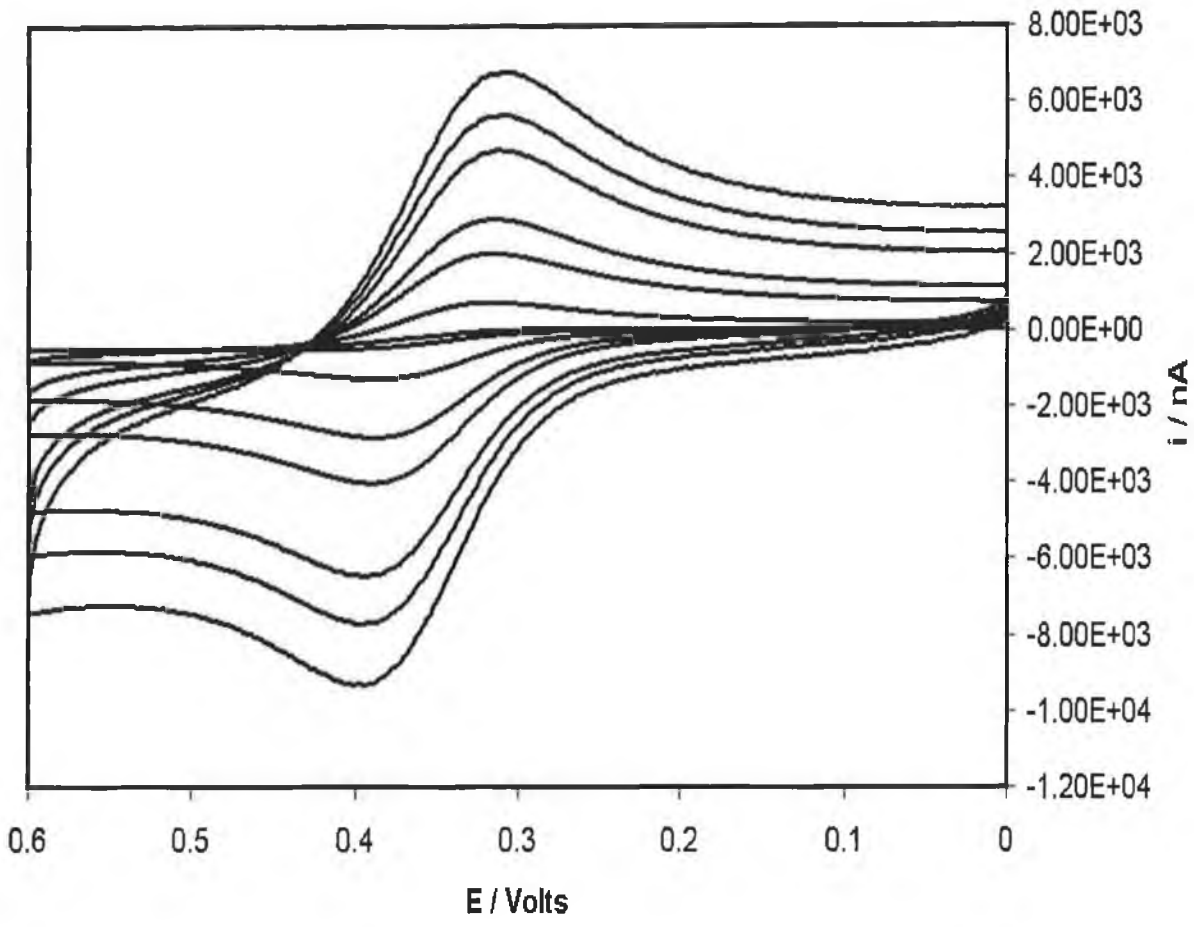

Figure 2.16. Cyclic voltammograms for 0.74 mM solution of $[Os(bpy)_2Cl(bpeH)](PF_6)_3$ in CH_3CN with 0.1 M $LiClO_4$ as supporting electrolyte; bpy is 2,2′–bipyridyl, p2p is 1,2-bis(4-pyridyl)ethane, bpe is *trans*-1,2-bis(4-pyridyl)ethylene. The series was recorded using a 1 mm radius platinum macroelectrode with a Ag/AgCl reference electrode. The scan rates are (top to bottom) 1000, 700, 500, 200, 100, 20, and 1 mV s^{-1}. The cathodic currents are up, and the anodic currents are down. The lower scan rate cyclic voltammograms (i.e., 1-200 mV s^{-1}) show the process under diffusional control. The higher scan rate cyclic voltammograms (i.e., 500-1000 mV s^{-1}) show the process under kinetic control.

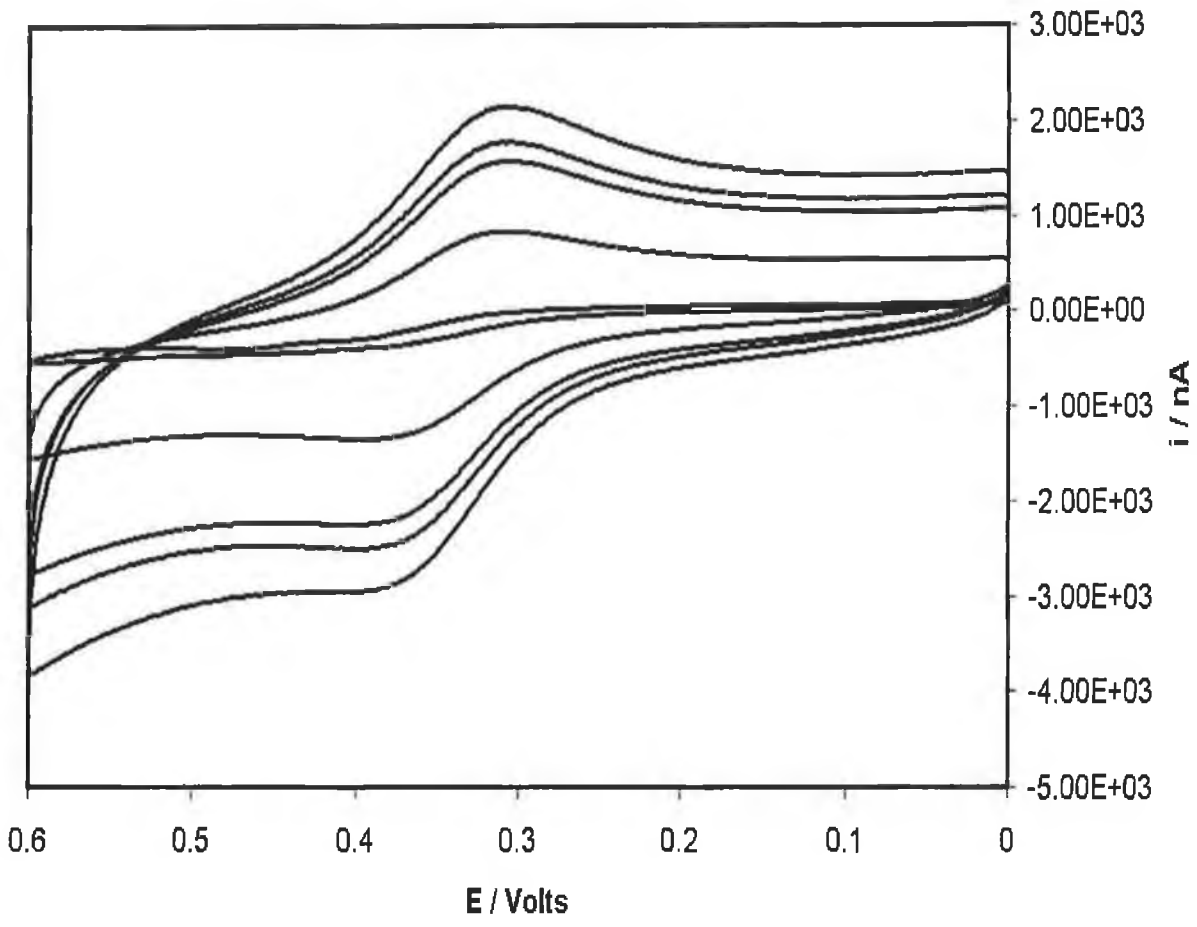

Figure 2.17. Cyclic voltammograms for 1.3 mM solution of $[Os(bpy)_2Cl(p2p)]PF_6$ in CH_3CN with 0.1 M $LiClO_4$ as supporting electrolyte; bpy is 2,2′-bipyridyl, p2p is 1,2-bis(4-pyridyl)ethane. The series was recorded using a 1 mm radius gold macroelectrode with a Ag/AgCl reference electrode. The scan rates are (top to bottom) 80, 60, 50, 20, and 1 mV s^{-1}. The cathodic currents are up, and the anodic currents are down. The process is already under kinetic control at scan rates of 50 mV s^{-1} and higher.

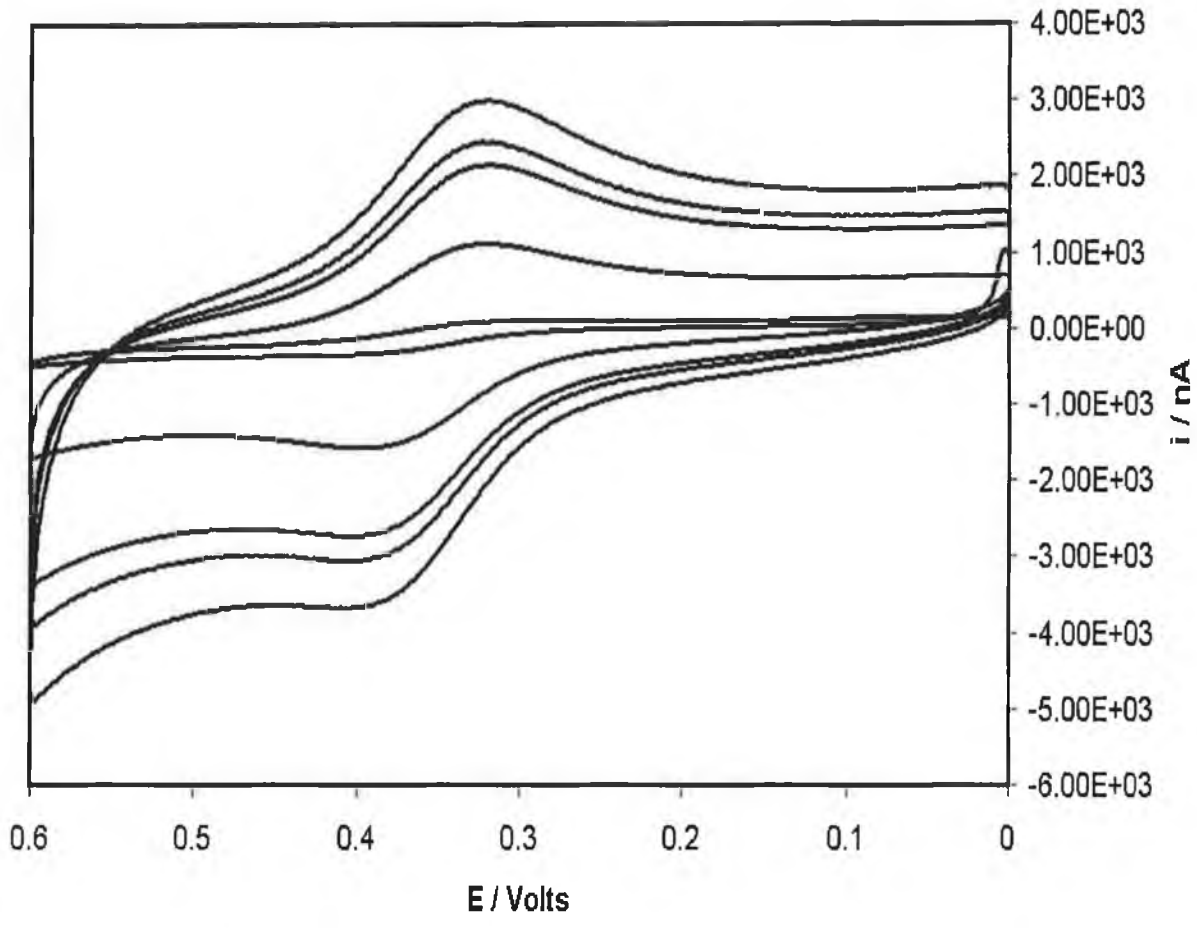

Figure 2.18. Cyclic voltammograms for 0.74 mM solution of $[Os(bpy)_2Cl(bpeH)](PF_6)_3$ in CH_3CN with 0.1 M $LiClO_4$ as supporting electrolyte; bpy is 2,2′-bipyridyl, bpe is *trans*-1,2-bis(4-pyridyl)ethylene. The series was recorded using a 1 mm radius gold macroelectrode with a Ag/AgCl reference electrode. The scan rates are (top to bottom) 80, 60, 50, 20, and 1 mV s^{-1}. The cathodic currents are up, and the anodic currents are down. The process is already under kinetic control at scan rates of 50 mV s^{-1} and higher.

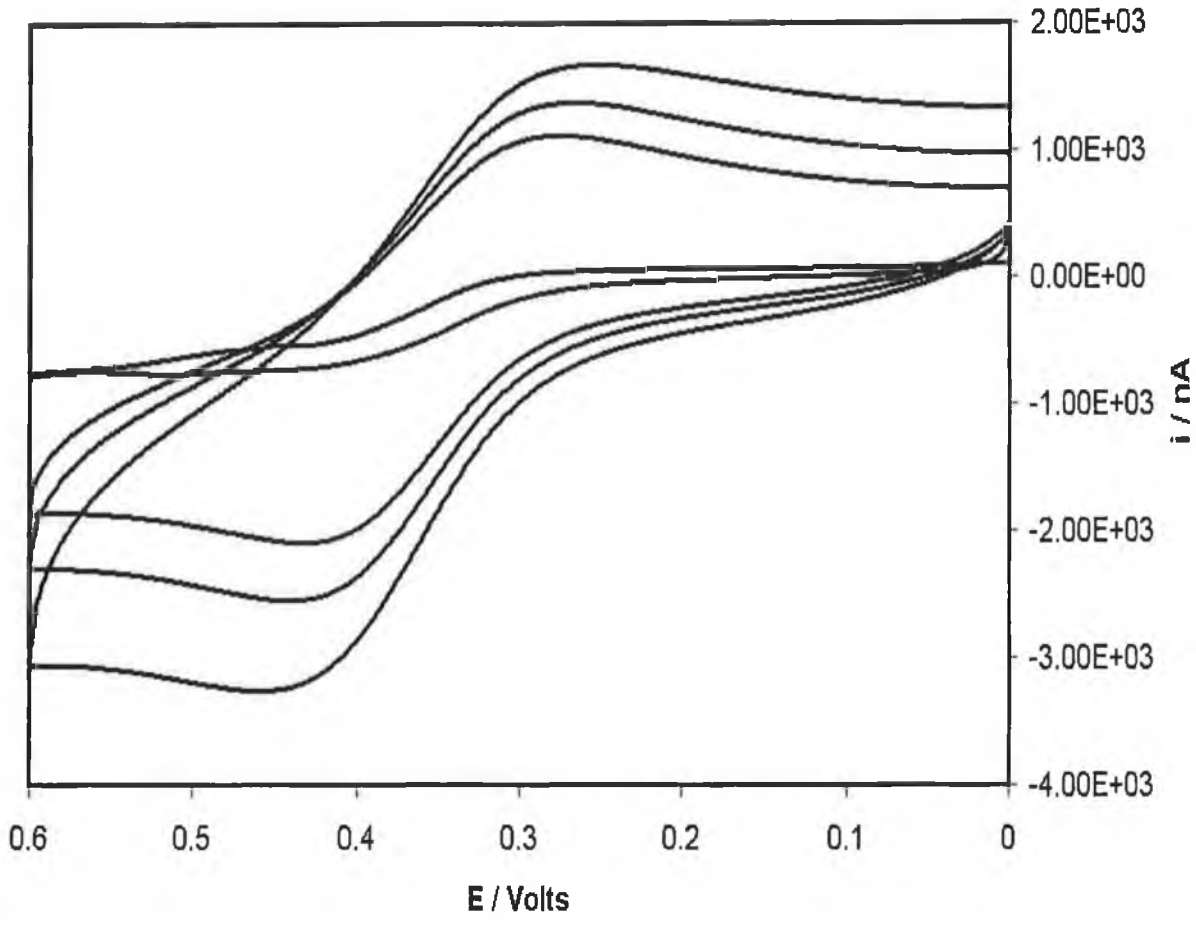

Figure 2.19. Cyclic voltammograms for 1.3 mM solution of $[Os(bpy)_2Cl(p2p)]PF_6$ in CH_3CN with 0.1 M $LiClO_4$ as supporting electrolyte; bpy is 2,2′-bipyridyl, p2p is 1,2-bis(4-pyridyl)ethane. The series was recorded using a 1.5 mm radius glassy carbon macroelectrode with a Ag/AgCl reference electrode. The scan rates are (top to bottom) 50, 30, 20, and 1 mV s^{-1}. The cathodic currents are up, and the anodic currents are down. The process is already under kinetic control at scan rates of 50 mV s^{-1} and higher.

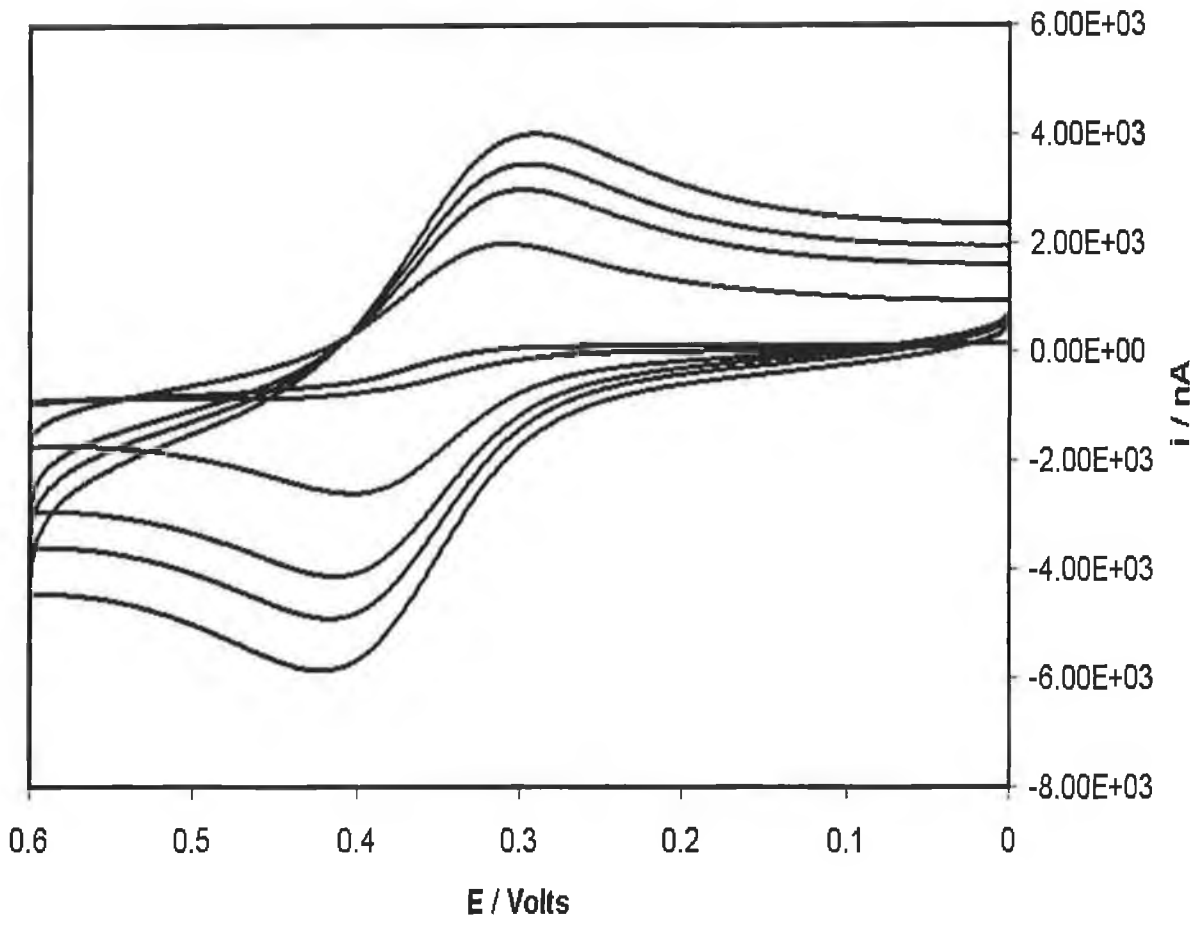

Figure 2.20. Cyclic voltammograms for 0.74 mM solution of $[Os(bpy)_2Cl(bpeH)](PF_6)_3$ in CH_3CN with 0.1 M $LiClO_4$ as supporting electrolyte; bpy is 2,2′-bipyridyl, bpe is *trans*-1,2-bis(4-pyridyl)ethylene. The series was recorded using a 1.5 mm radius glassy carbon macroelectrode with a Ag/AgCl reference electrode. The scan rates are (top to bottom) 100, 70, 50, 20, and 1 mV s^{-1}. The cathodic currents are up, and the anodic currents are down. The process is already under kinetic control at scan rates of 50 mV s^{-1} and higher.

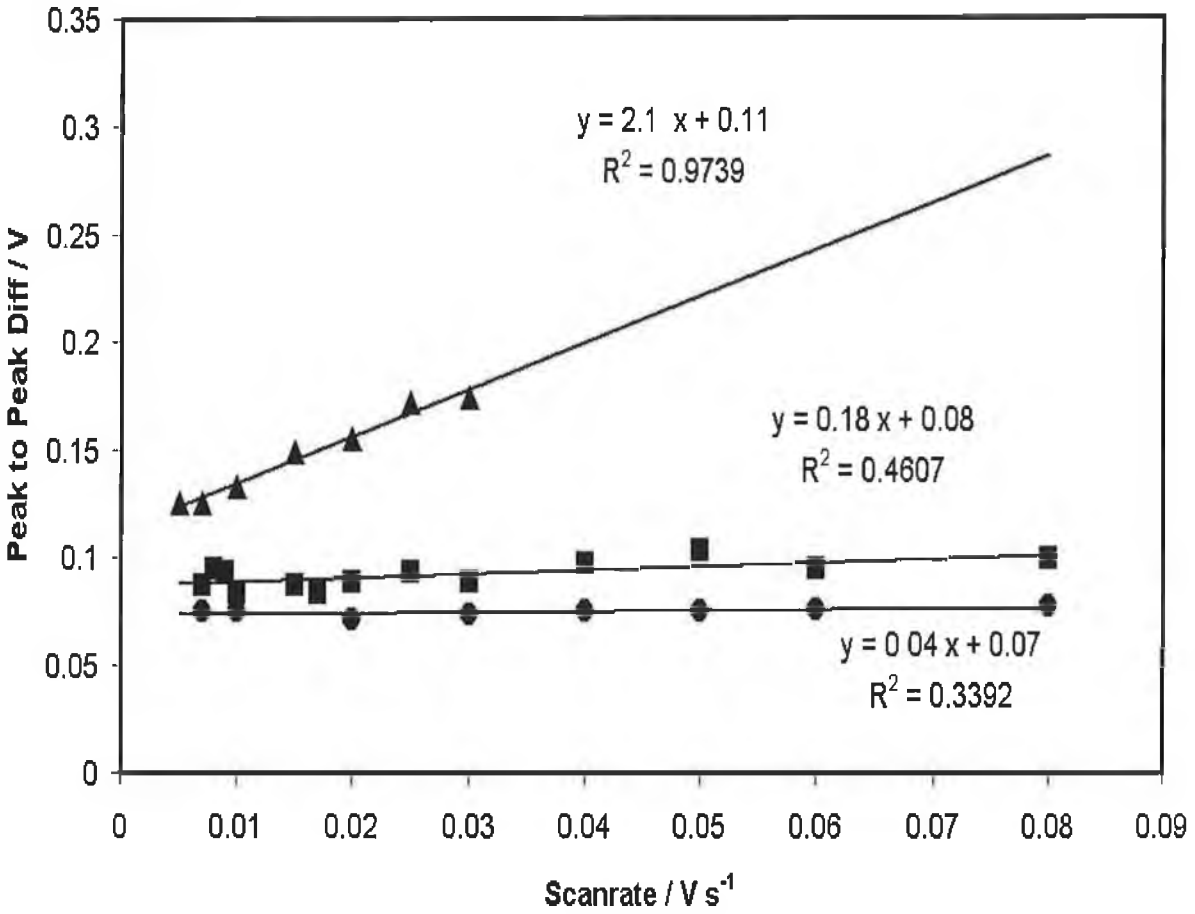

Figure 2.21. The difference between the anodic and cathodic peak potentials plotted against the scan rate for 1.3 mM solution of $[Os(bpy)_2Cl(p2p)]PF_6$ in CH_3CN with 0.1 M $LiClO_4$ as supporting electrolyte; bpy is 2,2′-bipyridyl, p2p is 1,2-bis(4-pyridyl)ethane. The data collected using the 1 mm radius platinum macroelectrode is denoted by (●). The data collected using the 1 mm radius gold macroelectrode is denoted by (■). The data collected using the 1.5 mm radius glassy carbon macroelectrode is denoted by (▲).

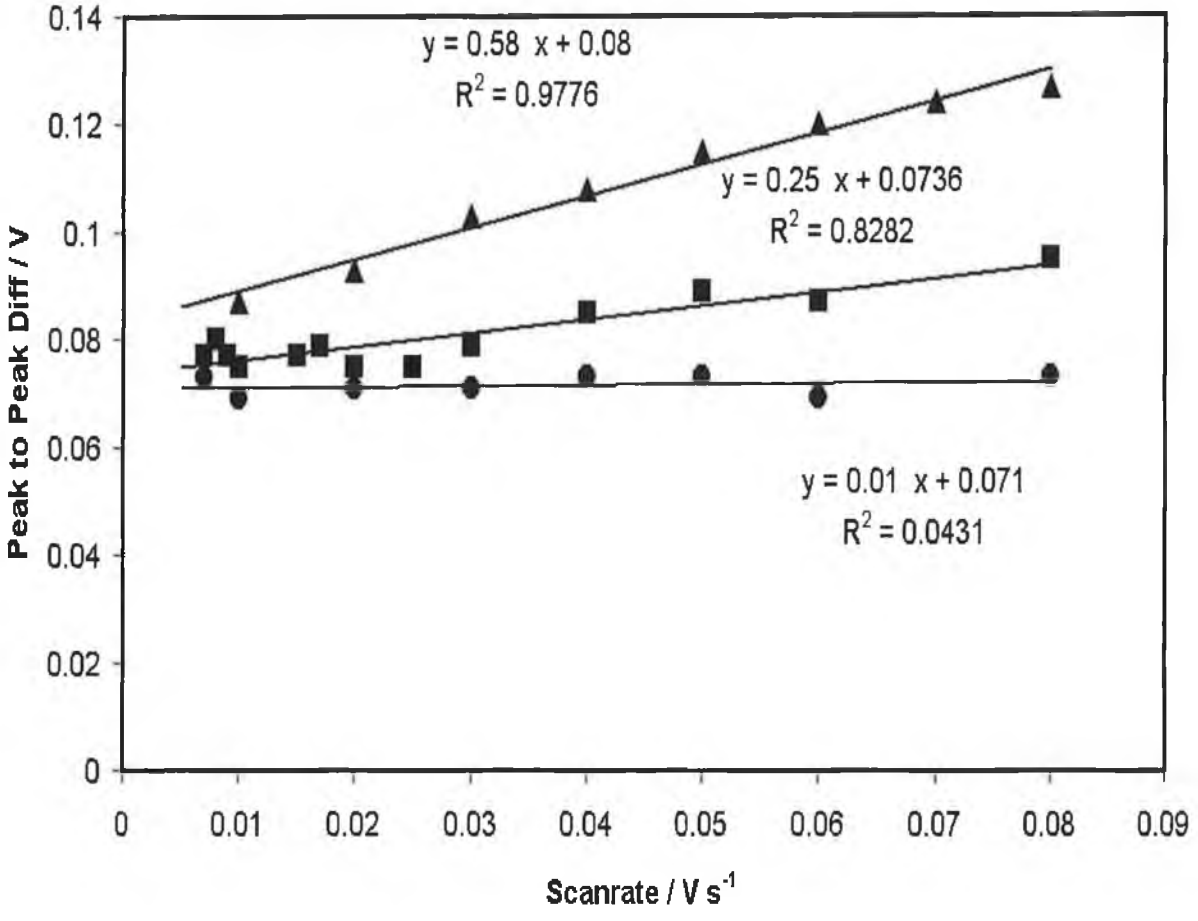

Figure 2.22. The difference between the anodic and cathodic peak potentials plotted against the scan rate for 0.74 mM solution of $[Os(bpy)_2Cl(bpeH)](PF_6)_3$ in CH_3CN with 0.1 M $LiClO_4$ as supporting electrolyte; p2p is 1,2-bis(4-pyridyl)ethane, bpe is *trans*-1,2-bis(4-pyridyl)ethylene. The data collected using the 1 mm radius platinum macroelectrode is denoted by (●). The data collected using the 1 mm radius gold macroelectrode is denoted by (■). The data collected using the 1.5 mm radius glassy carbon macroelectrode is denoted by (▲).

2.11. Conclusions

A comprehensive study on the solution phase electrochemical properties of a series of osmium and ruthenium complexes has been carried out. The effect of conjugation of the bridging ligand has been explored in terms of its influence on the UV-VIS absorption spectra of osmium complexes in solution in acid media. By demonstrating the decrease in the absorption at 400 nm due to the protonation of the conjugated bridging ligand, the reduction in electron density at the metal and head groups allowed by the conjugation in the bridge has been shown qualitatively. This is evidence of electronic coupling between the metal and the bridging ligand containing the double bond. This is a significant finding. This investigation in Chapter 4 will be extended when the electrochemical properties of these osmium complexes in adsorption studies are explored. The diffusion coefficients have been measured and discussed. No particular significance was attributed to the different bridging ligands. The effect of the electrode material has been investigated and platinum, in this case, has been shown be the optimum electrode for solution phase studies. In Chapter 5, the effect of the electrode material in adsorption studies using similar complexes will be shown.

2.12. References

1 Xu, C. Ph.D. Thesis, University of Illinois at Urbana-Champaign, **1992**.

2 (a) Faulkner, L. R.; Walsh, M. R.; Xu, C. Contemporary Electroanalytical Chemistry; Ivaska, A., Ed.; Plenum Press: New York, **1990**; p 5. (b) Xu, C. Ph.D. Thesis, University of Illinois at Urbana-Champaign, **1992**.

3 Forster, R. J. *"Ultrafast Electrochemical Techniques"*, Encyclopedia of Analytical Chemistry", Meyers, R. (ed.), Wiley, New York, **2000**, 10142.

4 Forster, R. J.; Faulkner, L. R. *J. Am. Chem. Soc.* **1994**, *116*, 12, 5444.

5 Buckingham, D. A.; Dwyer, F. P.; Goodwin, H. A.; Sargeson, A. M. Aust. *J. Chem.* **1964**, *17*, 325.

6 Forster, R. J.; Figgemeier, E.; Loughman, P.; Lees, A.; Hjelm, J.; Vos, J. G. *Langmuir*, **2000,** *16*, 7871.

7 Forster, R. *J. Inorg. Chem.* **1996**, *35*, 3394.

8 Taylor, C; Kenaussis, G.; Katakis, I.; Heller, A. *J. Electroanal. Chem.* **1995**, *396*, 511.

9 Forster, R. J.; Vos, J. G.; Keyes, T. E. *Analyst,* **1998**, *123*, 1905.

10 Kochanski, E. (ed), Photoprocesses in Transition Metal Complexes, Biosystems and Other Molecules. Experiment and Theory, **1992**, 233.

11 Breiter, M. *J. Electroanal. Chem.*, **1977**, *81*, 275.

12 Will, F. G.; Knorr, C. A.; *Z. Elektrochem.* **1960**, *64*, 258.

13 Gilman, S. *J. Phys. Chem.* **1963**, *67*, 78.

14 Motoo, S.; Furuya, N. *J. Electroanal. Chem.* **1984**, *167,* 309.

15 Hayes, M.; Kuhn, A. T. *Appl. Surf. Sci.* **1980**, *6,* 1.

16 Commission on Electrochemistry, *J. Electroanal. Chem.* **1992**, *327*, 354.

17 Michri, A.; Pshchenichnikov, A. G.; Burshtein, R. Kh.; *Elektrokhimiya*, **1972**, *8*, 364.

18 Burshtein, K. *Elektrokhimiya*, **1967**, *3*, 349.

19 Woods, R., Bard, A. J.(Ed.); *Electroanal. Chem., Chemisorption at Electrodes*, Marcel Dekker, New York, **1976**, *9*, 1.

20 (a) Goodwin, H. A.; Kepert, D. L.; Patrck, J. M.; Skelton, B. W.; White, A. H. *Aust. J. Chem.* **1984**, *37*,1817. (b) Ferguson, J. E.; Love, J. L.; Robinson, W. T. *Inorg. Chem.* **1972**, *11*, 1662. (c) Rillema, D. P.; Jones, D. S.; Levy, H. A. J. *Chem. Soc., Chem. Commun.* **1979**, 849.

21 O' Hanlon, D.; Ph.D. Thesis, Dublin City University, **1999**.

22 Penner, R. M.; Heben, M. J.; Longin, T. L.; Lewis, N. S. *Science*, **1990**, *250*, 1118.

23 Ciszkowska, M.; Donten, M.; Stojek, Z.; *Anal. Chem.*, **1994**, *66*, 4112.

24 Yang, Bard, A. J.; *J. Electroanal. Chem.* **1991**, *306*,87.

25 Baur, Wightman, R. M. *J. Electroanal. Chem.* **1991**, *305*,73.

26 Bard, A. J.; Faulkner, L. R.; "Electrochemical Methods", John Wiley & Sons, **1980**

27 Gosser, D. K. Cyclic Voltammetry: Simulation and Analysis of Reaction Mechanisms, **1993**,VCH Publishers Inc.

28 Ciszkowska, M.; Donten, Z.; Stojek, *Anal. Chem.* **1994**, *66*, 4112.

29 Yang, Bard, A. J. *J. Electroanal. Chem.* **1991**, *306*,87.

30 Baur, Wightman, R. M. *J. Electroanal. Chem.* **1991**, *305*,73.

31 Randles, J. E. B. *Trans. Faraday Soc.* **1948**, *44*, 327

32 Sevçik, A.; *Collect. Czech. Chem. Commun.* **1948**, *13*, 349.

33 Nicholson, R. S.; Shain, *Anal. Chem.* **1964**, *36*, 706.

34 Orlik, M. *J. Electroanal. Chem.* **1997**, *434*,139.

35 Denault, G.; Mirken, M. V.; Bard, A. J. *J. Electroanal. Chem.* **1991**, *308*, 27.

36 Baur, J. E.; Wightman, R. M.; *J. Electroanal. Chem.* **1991**, *305*, 73.

37 Wipf, D. O.; Michael, A. C.; Wightman, R. M.; *J. Electroanal. Chem.* **1989**, *269*, 15.

38 Ceroni, P.; Paolucci, F.; Paradisi, C.; Juris, A.; Roffia, S.; Serroni, S.; Campagna, S.; Bard, A. J. *J. Am. Chem. Soc.* **1998**, *120*, 5480.

39 Howell, J. O.; Wightman, R. M.; *Anal. Chem.* **1984**, *56*, 524.

CHAPTER 3

Construction and Testing of the Electron Transfer Computer Model

3.1. Introduction

In Chapter 1, microelectrode technology, the electrochemistry of adsorbed monolayers, current electron transfer theory, computer "best fit" algorithms and the principles for computer simulation have been comprehensively reviewed. Using this review as the starting point, a new approach to cyclic voltammogram simulation can now be described.

The primary objective of this third chapter is to describe the construction and testing of a model which can be used by the electrochemist studying redox active adsorbed monolayers to quickly extract both kinetic and thermodynamic information from cyclic voltammograms. As will be discussed later, redox active monolayers can provide a detailed understanding of electron transfer across interfaces and across molecular species. This understanding is essential in the design of ultra small scale electronic devices using molecular and solid-state components. This understanding is also a prerequisite for the production of "molecular wires" that promote fast heterogeneous electron transfer between a remote redox centre and a metal surface. These "molecular wires" are important for high speed molecular electronics applications, e.g., molecule-based computing. So the main aim is to provide a new tool for the study of adsorbed species incorporating existing theory which will greatly enhance the quality of information taken from the simple cyclic voltammogram.

3.2. Electron-Transfer Models

Two electron-transfer models were used for cyclic voltammetric simulation, namely, the models for non-adiabatic and adiabatic electron-transfer. The model for the specific case of non-adiabatic electron transfer (i.e., electron-transfer with weak electronic coupling between reactants) was described by Weber and Creager.[1] The electron-transfer theory known in this work as the adiabatic model was described previously by Finklea and Hanshew[2] and further developed by Forster and Faulkner.[3] These models are based on Marcus theory,[4,5,6,7] which underpins much of contemporary theory. In the adiabatic model, the cathodic rate constant is given by the integral over energy (ϵ) of three functions, namely;

1. The Fermi function for the metal, n(ϵ),
2. A Gaussian distribution of energy levels for acceptor states in the monolayer, $D_{Ox}(\epsilon)$,
3. A rate parameter for electron tunnelling at a given energy, p(ϵ).

$$k = A\int_{\infty}^{\infty} n(\varepsilon)D_{Ox}(\varepsilon)p(\varepsilon)d\varepsilon \tag{1}$$

The zero point of energy is taken as the Fermi level of the metal. The Fermi function gives the distribution of occupied states within the metal and is defined by

$$n(\varepsilon) = \left[1 + \exp(\varepsilon / k_B T)\right]^{-1} \tag{2}$$

where k_B is the Boltzmann constant.

The density of acceptor states for the adiabatic model is represented by

$$D_{Ox}(\varepsilon) = \exp\left[-(E + \eta - \lambda)^2 / (4\lambda k_B T)\right] \tag{3}$$

where λ is the reorganisation energy and η is the overpotential. The rate parameter for electron tunnelling for the adiabatic model is approximated by

$$P(\varepsilon) = (E_B - \varepsilon + e\eta/2)\exp(-\beta d) \tag{4}$$

where E_B is the average barrier height at zero overpotential and d is the electron transfer distance. β is the tunnelling constant and is given by

$$\beta = (2(2m)^{1/2}/\hbar)(E_B - \varepsilon + e\eta/2)^{1/2} \tag{5}$$

where m is the mass of the electron.

It is known[3] that the rate of electron tunnelling decreases exponentially with increasing distance and is controlled by the tunnelling parameter β. The standard rate

constant is related to the tunnelling parameter obtained at the formal potential β^o by the following equation;

$$k^o = k' \exp(-\beta^o d) \tag{6}$$

The anodic rate constant is obtained by replacing n(ϵ) with its compliment, 1-n(ϵ), and substituting D_{Ox} with D_{Red}, in which -λ is replaced with +λ.

Chidsey,[8] Creager,[1] and Murray,[9] have modelled non-adiabatic heterogeneous electron transfer for long-chain alkane-thiol monolayers using an expression similar to Equation 1 except that the energy dependent prefactor in the tunnelling probability expression is excluded. In this case the tunnelling probability is given by:

$$P(\varepsilon) = \exp(-\beta d) \tag{7}$$

In order to construct models using these expressions, the voltammetric scan is considered as a series of discrete small-amplitude potential steps over fixed time intervals whose duration depends on scan rate. The current at each interval is proportional to the amount of electroactive material that is oxidised or reduced in response to each potential step. Current is presented in dimensionless form as the fractional degree of oxidation per unit of dimensionless potential (i.e., potential normalised by the factor RT/F).

The expression for calculating dimensionless current is given in Equation 8.

$$i_{\text{dim}} = \frac{\Delta f}{\Delta E/(RT/F)} = \left(\frac{RT/F}{\Delta E}\right)\left(f_{t\,\text{arg}} - f_{init}\right)\left(1 - \exp\left[-\left(k_{red} + k_{ox}\right)\Delta t\right]\right) \tag{8}$$

where Δf is the change in the fractional degree of oxidation during a given interval, ΔE is the potential increment for each interval, f_{init} is the fractional degree of oxidation in a given interval before the potential step is applied, f_{targ} is a target fractional degree of oxidation calculated by using the Nernst equation at the step potential for a given interval, Δt is the time interval over which the potential is applied (Δt = ΔE / ν, where ν is the scan rate), and k_{red} and k_{ox} are the reductive and

oxidative electron-transfer rate constants at the step potential for a given interval. Voltammograms are calculated iteratively, starting with a value of f_{init} for the first interval calculated by application of the Nernst equation at the initial potential and then constantly updating f_{init} by the value of Δf calculated at each interval by using Equation 8.

3.2.1. Inputs to Both Models

To simulate a cyclic voltammogram with either the adiabatic model or the non-adiabatic model, the following inputs are used

- **Radius of microelectrode,**

- **Temperature;** measured in K.

- **Resolution**; the resolution is the interval of overpotential used in the calculation of the individual theoretical currents in the simulation.

- **Scan Rate,** the experimental scan rate in Vs^{-1}.

- **Limits of the integral** (e.g., -1 to +1.8 V); the computerised model allows checking of the sensitivity of the electron transfer model to the limits of the integral over energy. In theory, Equation 1 should be integrated from - ∞ to + ∞. However, states removed by more than approximately +/- 1 eV from the Fermi level do not contribute significantly to the observed current. Hence, limits of –1 to 1.8 V were used to minimise computation time and maximise accuracy.

- **Overpotential range** for the simulation. The overpotential range for the cyclic voltammetric simulation is chosen on the basis of experimental knowledge of the cyclic voltammetric response of the particular moieties under study, e.g., for fast scan rates the difference between the cathodic and anodic peak potentials will be large requiring a large overpotential range.

- **Formal Potential,** It is extremely important to have an accurate measurement for the formal potential as this directly influences the position of the anodic and cathodic branches on the potential axis and therefore directly affects the accuracy of the value for k^o which will be returned by the model.

- **An estimate of k^o**, the electron transfer rate constant and **an estimate of λ**, the reorganisation energy. Throughout this work, random values were the preferred choice for the starting values for k^o and λ giving a completely objective, non-biased starting point for the simplex algorithm.

- **Distance from Redox centre to electrode**; when dealing with a monolayer adsorbed on to a microelectrode, this distance can be controlled by the length of the bridging ligand. The rate of electron transfer is very dependent on this distance which is typically short for adiabatic (i.e., strongly coupled) reactions.

For the adiabatic model, one additional input is required, namely

- **Barrier height, E_B**; According to classical tunnelling theory,[2,10] the average barrier height at zero overpotential is given by the relation,

$$E_B = (9.48\beta^o)^2 \qquad (9)$$

where E_B is in kJ mol^{-1} and β^o is in $Å^{-1}$.

3.3. The Simplex Algorithm

The primary reason for simulating cyclic voltammograms is to obtain kinetic information for a system by comparing the simulated theoretical curve with an experimental response. That is to say, by varying the inputs to the model one can construct a similar cyclic voltammogram to the experimental CV and thus, gain information about the appropriate inputs. The variables in the simulation which are used to match the theoretical curve to the experimental are also known as the fitting parameters, k^o and λ.

This comparison of the theoretical simulated cyclic voltammogram to the experimental CV can be carried out in three ways, namely

1. *Visual Comparison.* This is the simplest way and can give a reasonable estimate for the rate constant, k^o. However, it is virtually impossible to determine λ, visually.
2. *Using a computer, one can "search the whole space"* by continuously running simulations at a particular k^o and a range of λs. Then run the simulations again at an increased k^o and a range of λs. Continue until the best fit, as determined by the minimum of the sum of the squares of the differences (or, indeed, the sum of the absolute differences) between the simulated curve and the experimental curve is found. The big disadvantage here, is the length of time taken to find the best fit which can take days rather than hours of computer time.
3. *Incorporate a "fitting" algorithm* into the model in order to efficiently "search the space" for the optimum k^o and λ.

Undoubtedly, method 3, is the best and most efficient way of carrying out this comparison and this is the primary comparison or fitting method used throughout this work.

The fitting algorithm incorporated into the electron transfer model is known as the simplex algorithm and this is, in so far as can be ascertained, the first time that this

algorithm has been used on the adiabatic model. The simplex algorithm is attributed to Nelder and Mead[11] and is coded into the electron transfer model by means of a Microsoft Excel macro. The simplex algorithm uses, mainly, two fitting parameters, k^o and λ, to minimise the sum of the squares of the differences between each point on the theoretical CV and the experimental CV. Other parameters are also used instead of, or in combination, with k^o and λ giving 3 and 4 parameter models.

3.4. Testing the Model/Simplex Combination

In order to test the new fitting model in a controlled way, theoretical cyclic voltammograms were generated using the adiabatic electron transfer theory with particular values of k^o and λ. The adiabatic model was chosen for the application of most of these detailed tests. A three-parameter model including barrier height as the third parameter was also created. The combined electron transfer / simplex model was then used on these theoretical CVs starting with random guesses for k^o, λ and E_B. In all cases the model found the correct values for k^o, λ and E_B. Of course, this theory does not take into account capacitive charging currents which can be present as "background" to the Faradaic currents. Therefore, to establish how the fitting model would deal with this more likely real-case scenario, various background currents were added to this theoretically "clean" data. These background currents were of three main types, namely,

1. Flat or horizontal background currents calculated as a percentage of the peak of the theoretical cyclic voltammetric current.
2. Sloped background currents increasing from left to right on the theoretical CV up to a maximum of a particular percentage of the peak current.
3. Sloped background currents increasing from right to left on the theoretical CV up to a maximum of a particular percentage of the peak current.

3.4.1. Effect of Adding "Capacitive" Current on Theoretical CVs

In this experiment, the adiabatic electron-transfer model was used to simulate the anodic branch of a cyclic voltammogram. In order to do this, a heterogeneous rate constant, k^o of 1100 s^{-1} and reorganisation energy, λ of 83.4 kJ mol^{-1} and barrier height of 192 kJ mol^{-1} were arbitrarily chosen as inputs to generate the curve. The peak current of the simulated curve was determined. A series of curves containing simulated background currents was then generated by adding percentages of the peak current varying from 0% (i.e., no background added) to 50% (i.e., one half of the

peak current added). The simplex starting from random values of k^o, λ, and barrier height, was then used on the series of curves to find values of three input parameters which correspond to the best fit. This experiment was repeated on further series of curves generated at different scan rates. Six different scan rates were used to generate different series of curves, namely, 1, 5, 10, 50, 500 and 1000 V s^{-1}.

Figure 3.1 illustrates the addition of horizontal background currents to the theoretical data.

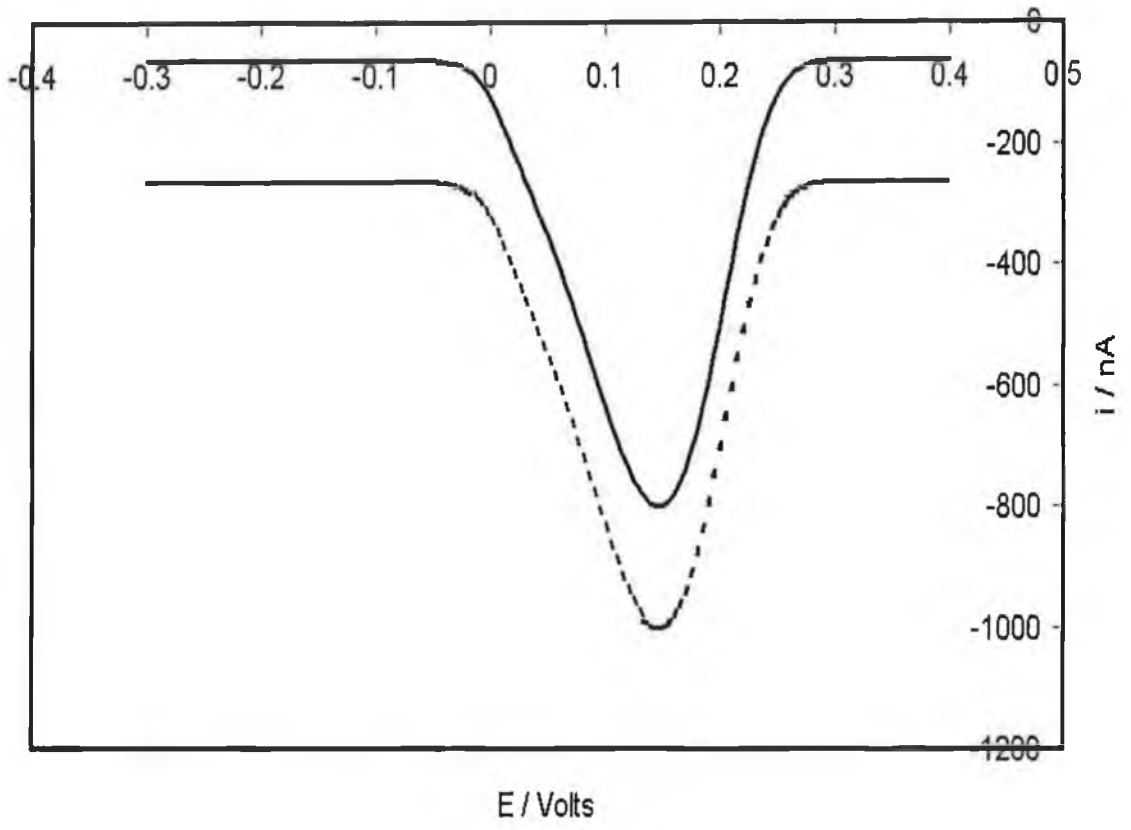

Figure 3.1. Simulated voltammetric response for 10 μm radius disk microelectrode modified with a monolayer with surface coverage of 9.5 x 10^{-11} moles $cm.^{-2}$ The electron transfer distance used in this simulation is 3 Å. The upper curve (———) is the best theoretical fit to the curve (-----) containing the theoretical background current. In this case, a background current equal to 25% of the peak current has been added. The scan rate is 1000 V s^{-1}. This graph illustrates the addition of horizontal background currents to the theoretical data in the absence of double layer charging. The theoretical values for λ, k^o, and barrier height are 83.4 kJ mol^{-1}, 1100 s^{-1}, and 192 kJ mol^{-1}, respectively. The simplex operating on the background distorted lower curve (-----) returns 107.2 kJ mol^{-1}, 1203 s^{-1}, 172.1 kJ mol^{-1}, respectively for λ, k^o, and barrier height.

Figure 3.2 illustrates the results and deviations obtained for just one of the simulation scan rates used, namely 1000 V s^{-1}.

In Figure 3.2, the following features of the adiabatic electron-transfer theory / simplex model are illustrated:

1. The model can cope with extremely high horizontal background currents and still produce meaningful results.
2. The percentage deviation of k^o is linear with added horizontal background current and much lower than that for λ, i.e., the model gives a better estimate for k^o than for λ when horizontal background currents are added.
3. The deviation of the barrier height rises quickly to a maximum of 10% and then remains constant.

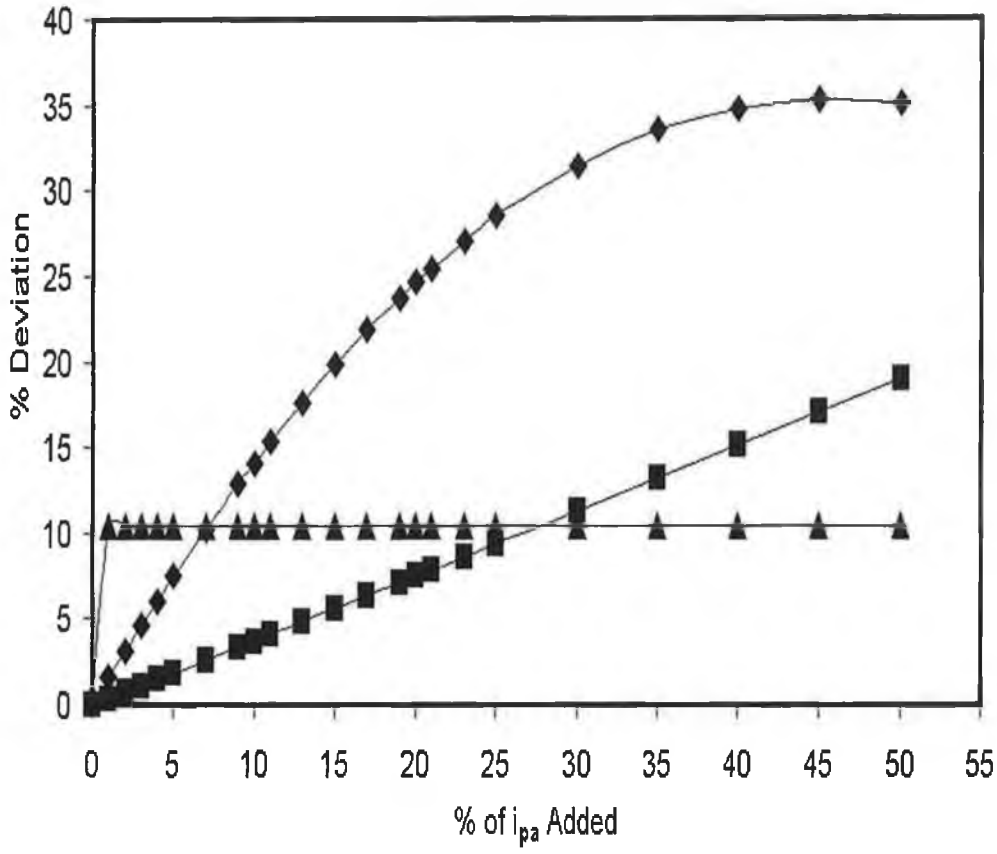

Figure 3.2. Deviation of the best fit values of λ (♦), k^o (■) and barrier height (▲) as horizontal background currents are added in systematically.

3.4.2. Sloped Background Current

In many cyclic voltammograms, capacitive background currents are present which vary in magnitude throughout the scan. This gives rise to sloped or skewed cyclic voltammograms. It is important to test how stable the model is when such background currents are present.

3.4.2.1. Sloped Background Current Type 1

In this experiment, the adiabatic electron-transfer model was used to simulate the anodic branch of a cyclic voltammogram. In order to do this, an heterogeneous rate constant, k^o of 1100 s^{-1}, reorganisation energy, λ of 83.4 kJ mol^{-1} and barrier height of 192 kJ mol^{-1} were arbitrarily chosen as inputs to generate the curve. The peak current of the simulated curve was determined. A series of curves containing simulated background currents were then generated containing sloped background currents. The slope of the background current was increased by using percentages of the peak current varying from 0% (i.e., no background added) to 42%. The simplex starting from random values of k^o, λ, and barrier height, was then used on the series of curves to find values of three input parameters which correspond to the best fit. This experiment was repeated on further series of curves generated at different scan rates. Three different scan rates were used to generate different series of curves, namely, 50, 500 and 1000 V s^{-1}. One example of these curves is given in Figure 3.3.

Result for Barrier Height

When as little as 1 % sloped background current of Type 1 is added, the 3 parameter fitting model (i.e., trying to find λ, k^o, and barrier height simultaneously) cannot find a realistic value for barrier height. This is an important limitation of the model and suggests that the theoretical treatment should concentrate on 2 parameters, namely, k^o and λ. It also suggests a lack of sensitivity of both the shape and position of the curve to changes in barrier height. With its inability to find barrier height when sloped background current is present, the fitting model is indicating that k^o and λ control the shape and position of the cyclic voltammogram.

In Figure 3.4, the results of the deviation of λ and k^o from the true values as Type 1 Sloped background current is added are displayed. From this figure, the following can be concluded:

1. The model is again very robust with respect to changes in the background current.
2. The percentage deviation of k^o from the theoretical value is again much less than that for λ showing that k^o can be accurately determined even in the presence of sloped backgrounds.

A similar method was used to generate simulated cyclic voltammograms containing background currents which had the opposite slope to those used in Type 1. As for Type 1, the background current is based on the equation Y=mX (i.e., goes through (0,0)).

Figure 3.5 is an example of this sloped background current. The results are displayed in Figure 3.6.

3.4.2.2. Sloped Background Current Type 2

Type 2 background current is based on the equation Y=mX + C (i.e., the theoretical background charging current is sloped and offset from the baseline).

Figure 3.7 is an example of Type 2 sloped background current. The results are displayed in Figure 3.8.

Another theoretical background current was constructed in exactly the same way as Type 2 except that it slopes in the opposite direction to Type 2.

Figure 3.9 is an example of this sloped background current. The results are displayed in Figure 3.10.

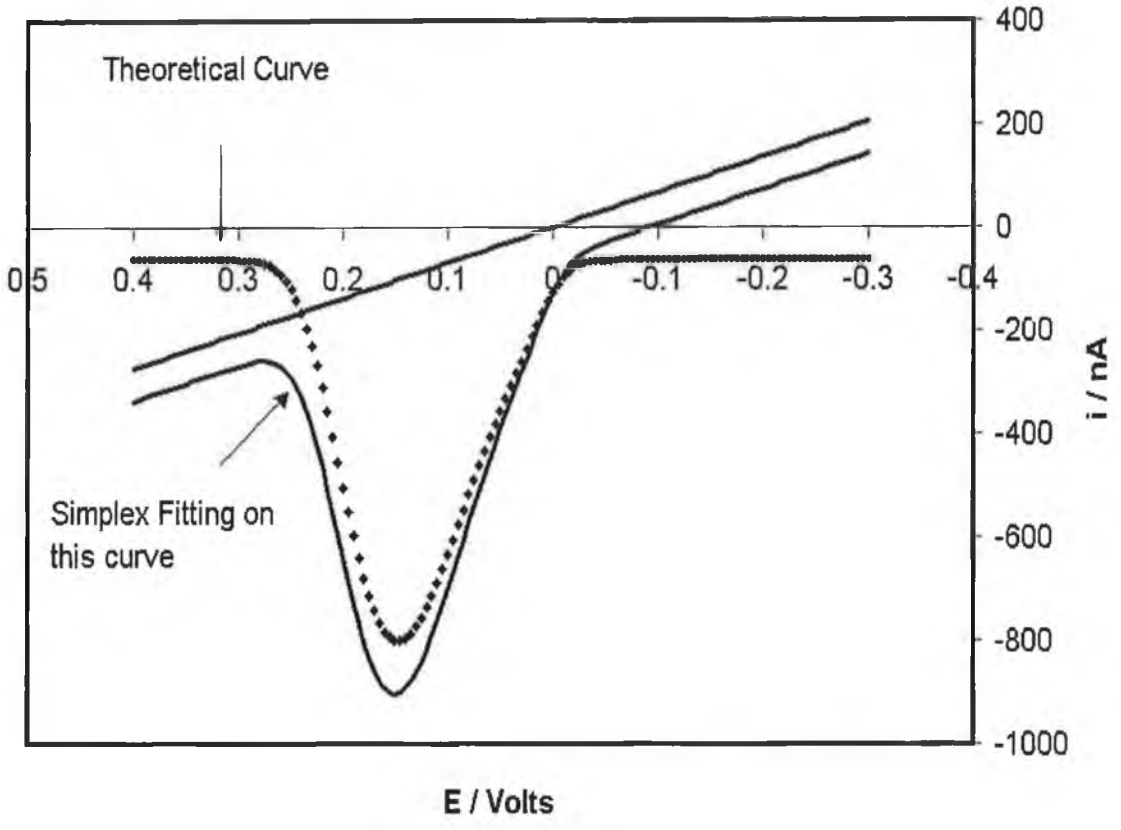

Figure 3.3. Simulated voltammetric response for 10 μm radius disk microelectrode modified with a monolayer. The upper curve (♦) is the best theoretical fit to the lower theoretical voltammogram (solid line). In this case, a background current equal to 27% of the peak current has been used to calculate the slope. The scan rate is 1000 V s^{-1}. The theoretical values for λ, k^o, and barrier height are 83.4 kJ mol^{-1}, 1100 s^{-1}, and 192 kJ mol^{-1}, respectively. The simplex operating on the background distorted lower curve (solid line) returns 65.1 kJ mol^{-1}, 1047 s^{-1}, respectively for λ, k^o.

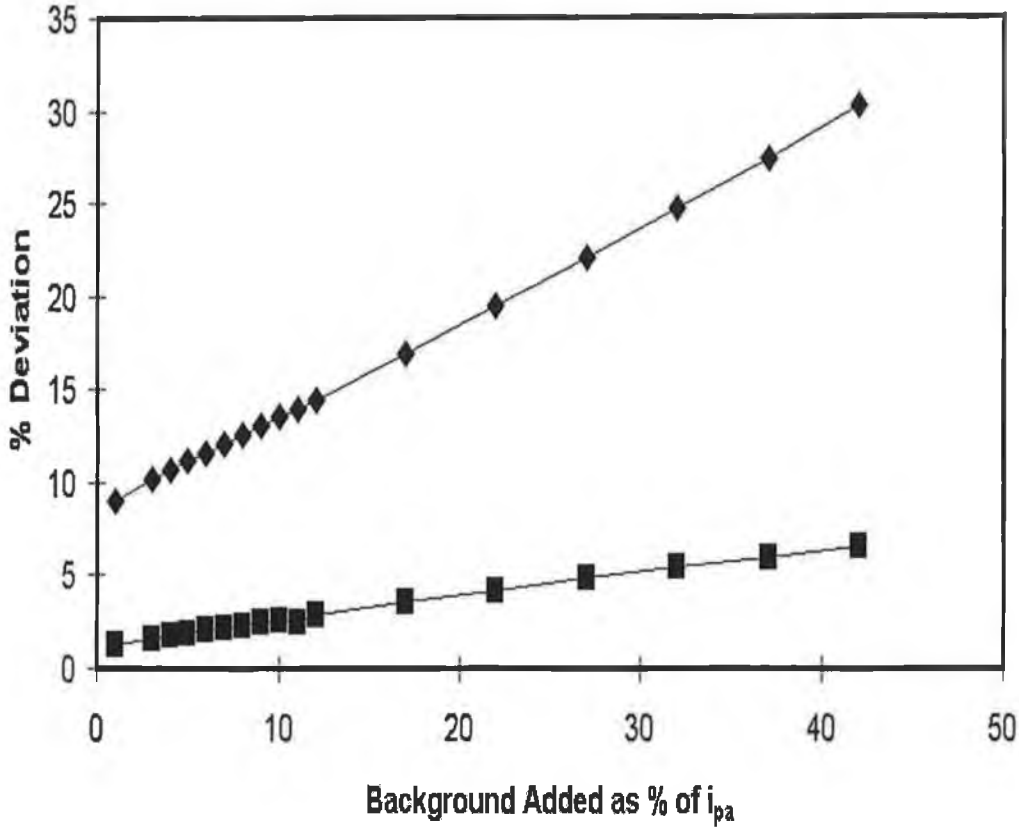

Figure 3.4. Deviation of the best fit values of λ (♦), k^o (■) as increasing sloped background currents (Type 1) are added to the anodic branch of the theoretical cyclic voltammogram.

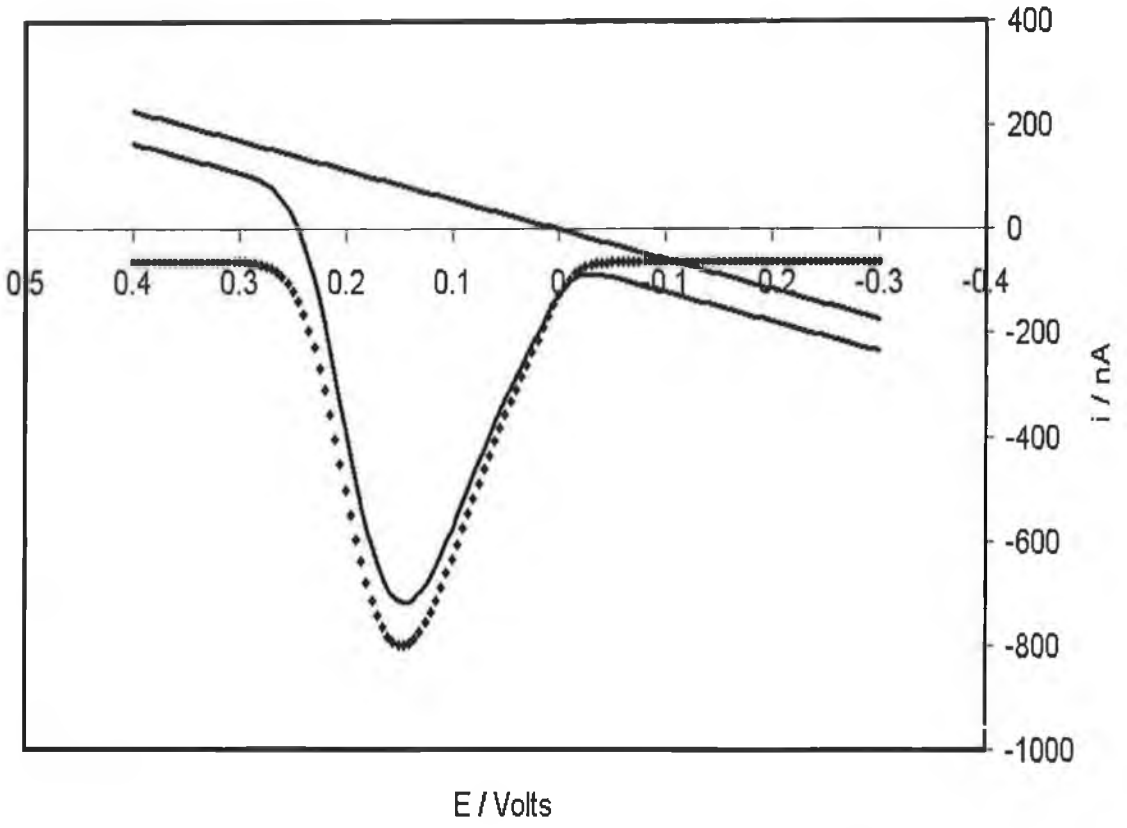

Figure 3.5. Simulated voltammetric response for 10 μm radius disk microelectrode modified with a monolayer with surface coverage of 9.5 x 10^{-11} moles $cm.^{-2}$ The electron transfer distance used in this simulation is 3 Å. The data points (♦) represent the best theoretical fit to the background distorted curve (solid line). In this case, a background current equal to 25% of the peak current has been used to calculate the slope. The scan rate is 1000 V s^{-1}. The theoretical values for λ, k^o, and barrier height are 83.4 kJ mol^{-1}, 1100 s^{-1}, and 192 kJ mol^{-1}, respectively. The simplex operating on the background distorted curve (solid line) returns 94.6 kJ mol^{-1}, 1144 $s^{-1}$and 172 kJ mol^{-1}, respectively for λ, k^o and the barrier height.

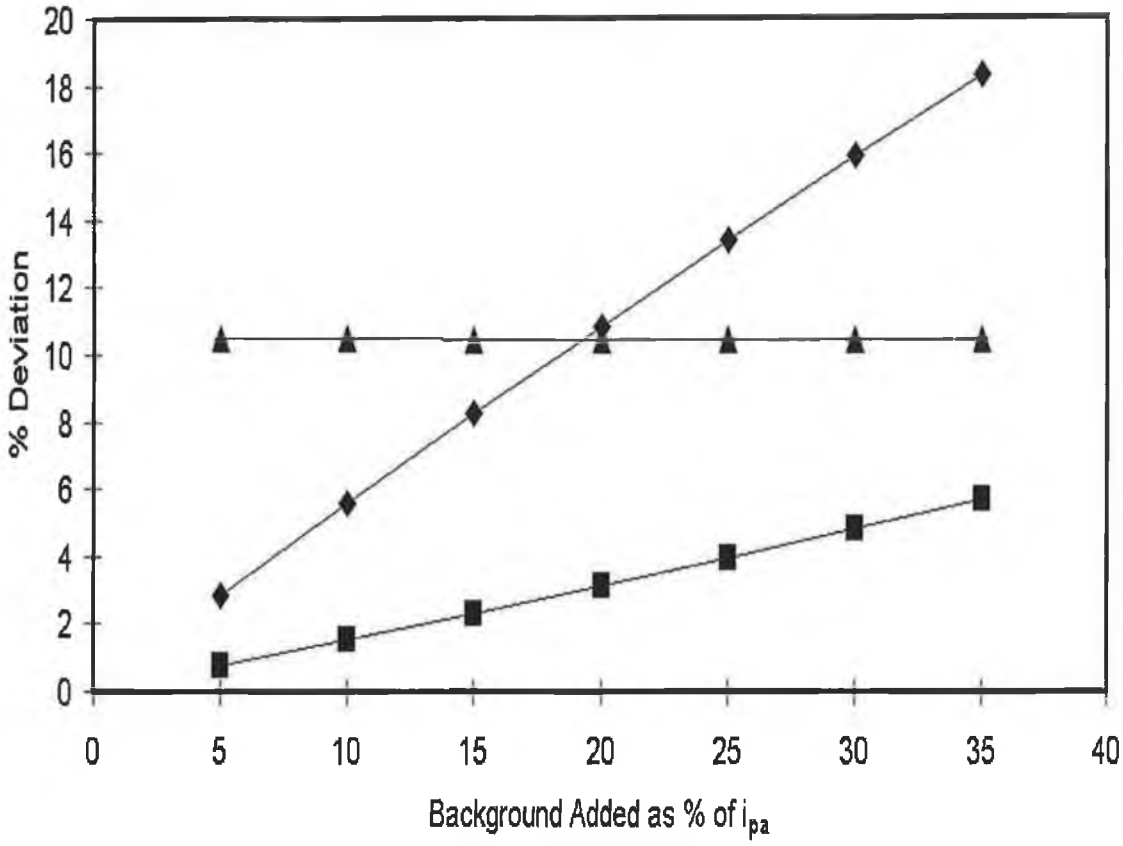

Figure 3.6. Deviation of the best fit values of λ (♦), k^o (■) and barrier height (▲) as increasing sloped background currents (Type 2) are added to the anodic branch of the simulated cyclic voltammogram.

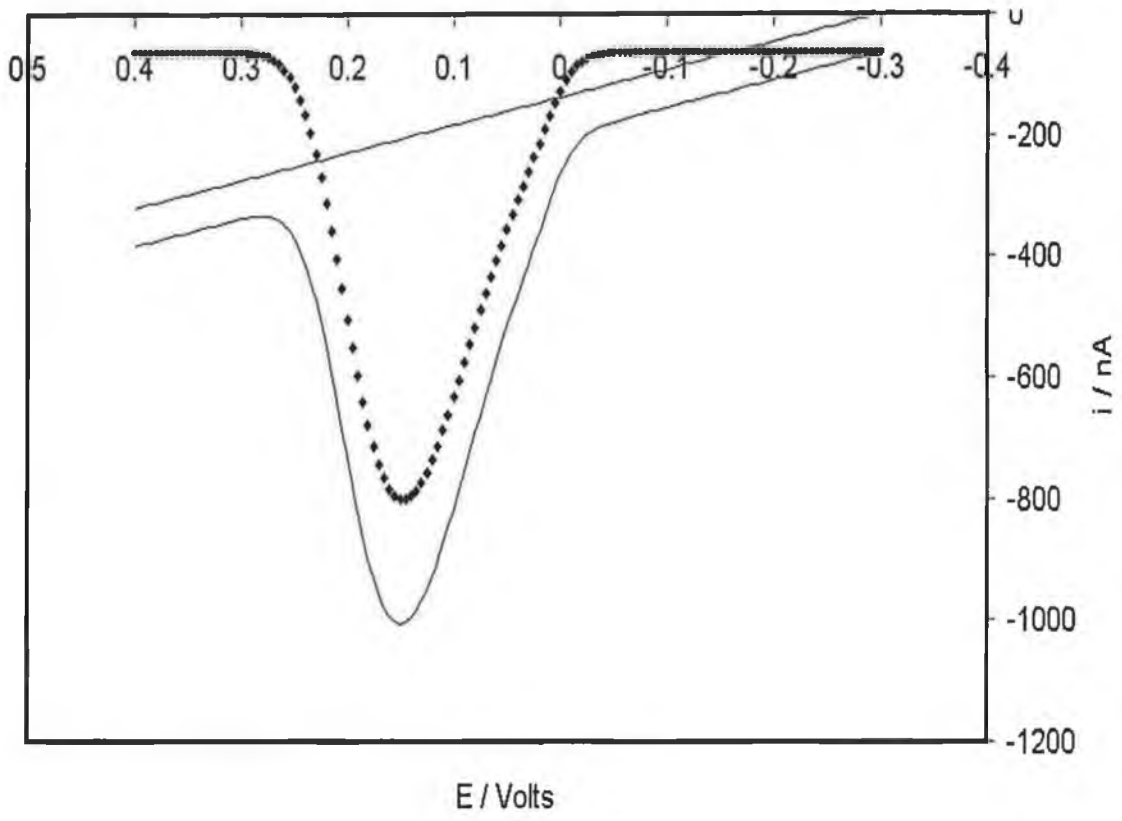

Figure 3.7. Simulated voltammetric response for 10 μm radius disk microelectrode modified with a monolayer with surface coverage of 9.5 x 10^{-11} moles cm.$^{-2}$ The electron transfer distance used in this simulation is 3 Å. The data points (♦) represent the best theoretical fit to the background distorted curve (solid line). In this case, a background current equal to 40% of the peak current has been used to calculate the slope. The scan rate is 1000 V s^{-1}. This graph illustrates the addition of sloped background currents to the ideal response. The theoretical values for λ, k^o, and barrier height are 83.4 kJ mol^{-1}, 1100 s^{-1}, and 192 kJ mol^{-1}, respectively. The simplex operating on the background distorted lower curve (solid line) returns 40.0 kJ mol^{-1}, 1100 s^{-1}, respectively for λ, k^o.

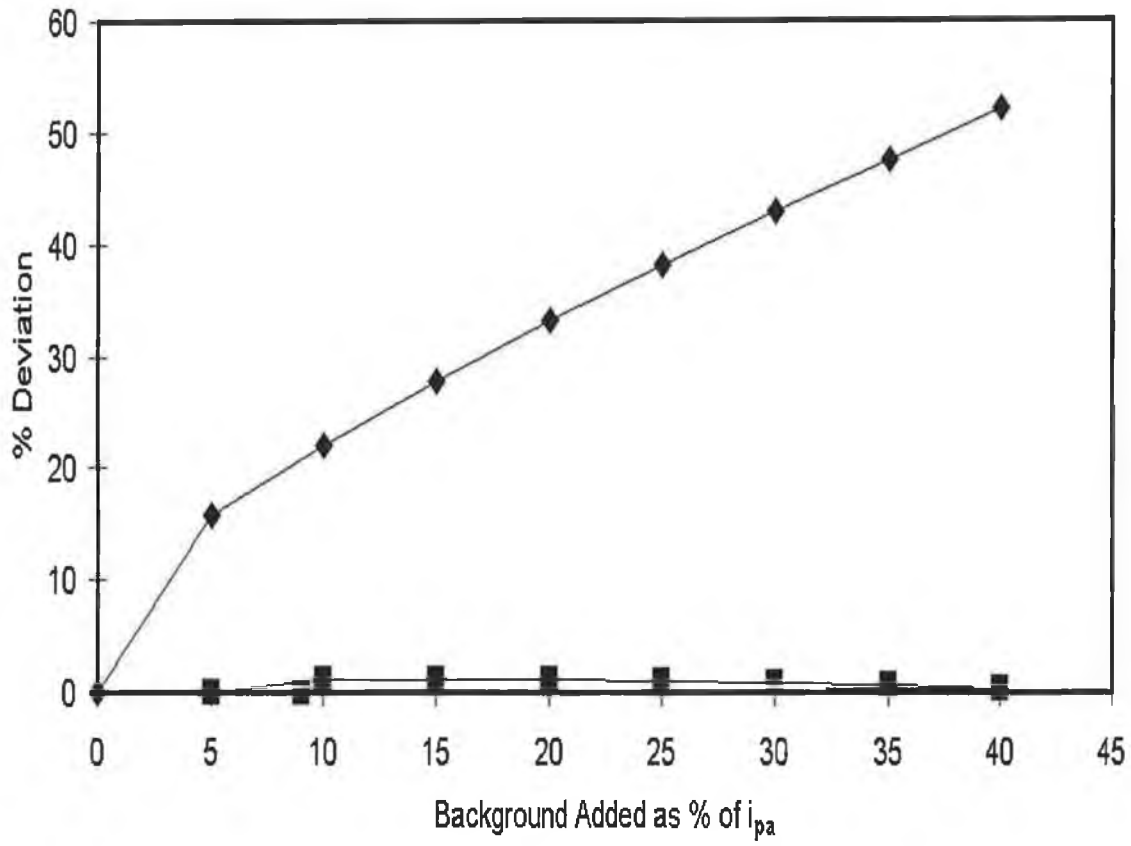

Figure 3.8. Deviation of the best fit values of λ (♦) and k^o (■) as increasing sloped background currents (Type 2) are added to the anodic branch of the simulated cyclic voltammogram. The striking feature illustrated in this figure is that with this type of background current, the model can find the correct value for k^o irrespective of the size of this background. Also, reasonable estimates for λ are obtained.

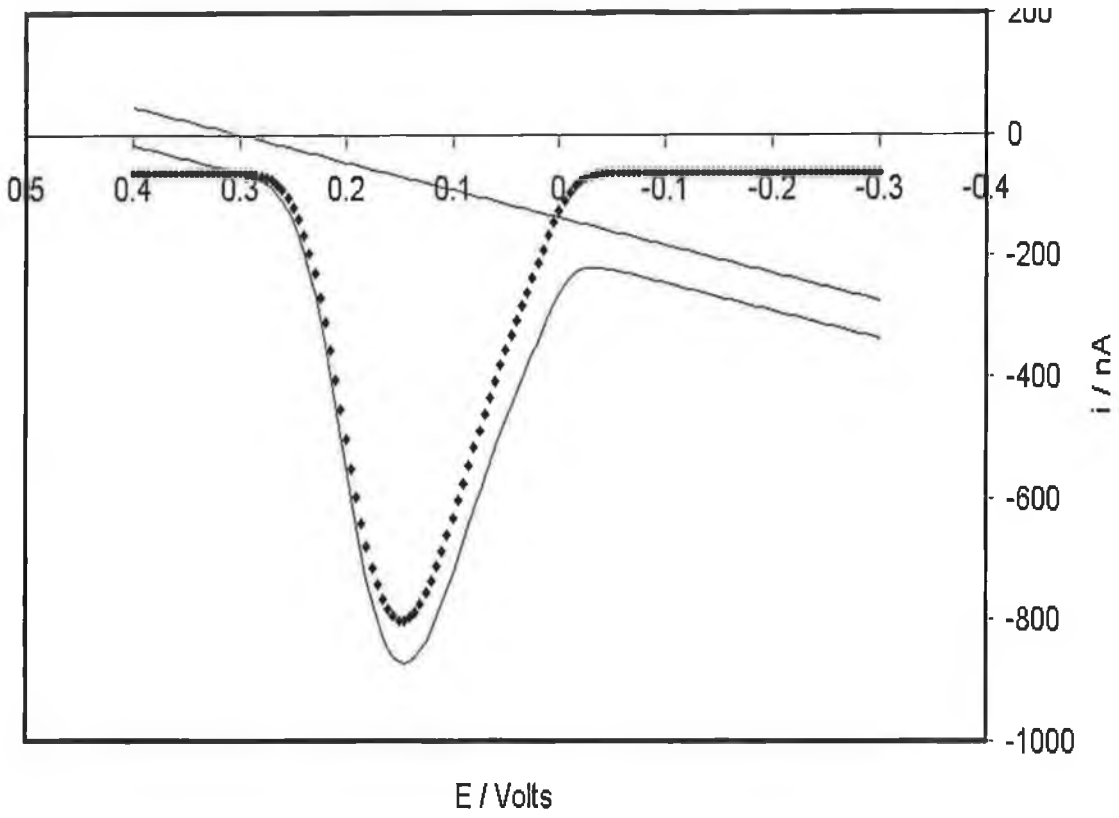

Figure 3.9. Simulated voltammetric response for 10 μm radius disk microelectrode modified with a monolayer with surface coverage of 9.5 x 10^{-11} moles $cm.^{-2}$ The electron transfer distance used in this simulation is 3 Å. The data points (♦) represent the best theoretical fit to the background distorted curve (solid line). In this case, a background current equal to 40% of the peak current has been used to calculate the slope. The scan rate is 1000 V s^{-1}. This graph illustrates the addition of sloped background currents to an ideal response. The theoretical values for λ, k^o, and barrier height are 83.4 kJ mol^{-1}, 1100 s^{-1}, and 192 kJ mol^{-1}, respectively. The simplex operating on the background distorted lower curve (solid line) returns 65.2 kJ mol^{-1}, 1237 s^{-1} and 171.9 kJ mol^{-1} respectively for λ, k^o and the barrier height.

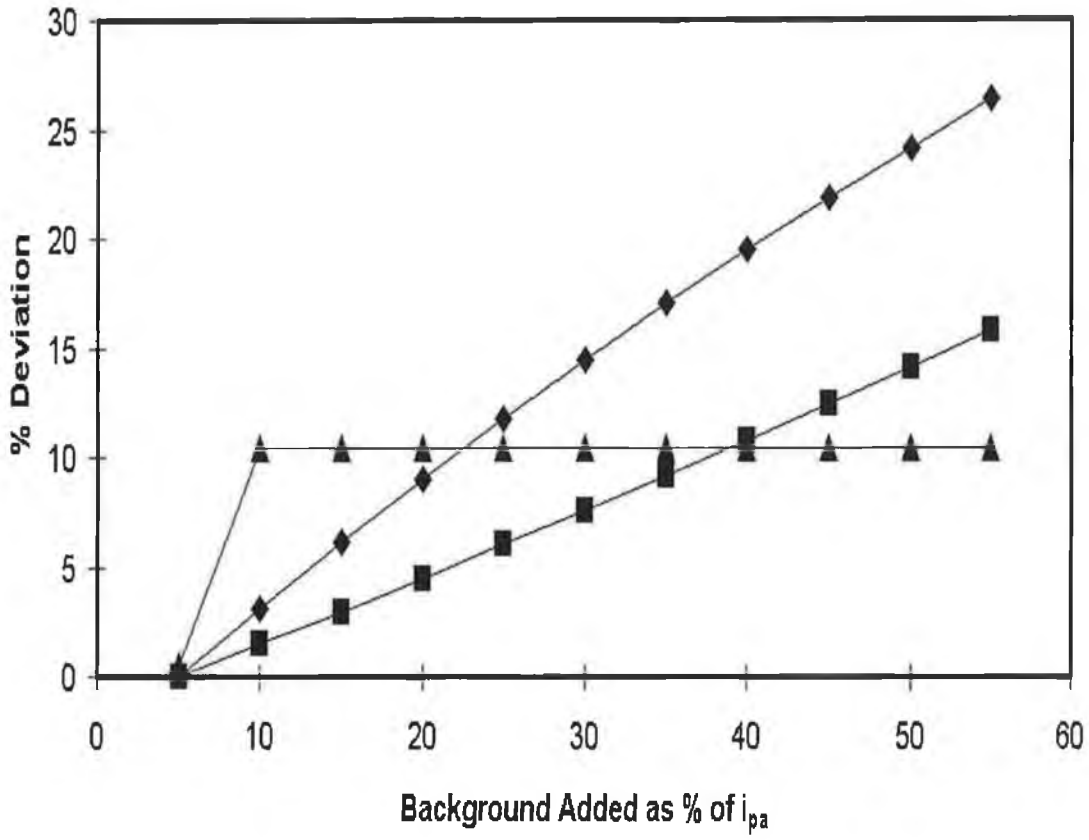

Figure 3.10. Deviation of the best fit values of λ (♦), k^o (■) and barrier height (▲) as increasing sloped background currents are added to the anodic branch of the simulated cyclic voltammogram.

3.4.2.3. Conclusions

1. Looking at the results produced by the adiabatic model for three parameters with capacitive backgrounds, it is concluded that, since all experimental data will have obvious backgrounds removed before fitting the model, the model designed in this work should be an extremely useful tool for extracting kinetic data, i.e., the standard heterogeneous rate constant k^o and the thermodynamic parameter, λ, the outer sphere reorganisation energy.

2. The results for barrier height show that the model can only determine this parameter when there is no background present or background which has zero or negative slope. This suggests that it may be more productive to find k^o and λ only, by fitting a two-parameter model to the experimental data.

3. While a good approximation is obtained for λ even in the presence of large background currents, k^o is significantly less sensitive to the presence of background currents.

4. Certain types of background current (e.g., Figure 3.7) do not affect the determination of k^o by the model.

3.5. Examples of Experimental Cyclic Voltammograms showing Actual Background Current

In the above experiments, the sensitivity of the model was tested using theoretically constructed cyclic voltammograms containing various types of background currents. These mathematically constructed background currents are typical of the type of background currents encountered experimentally.

For example, in Chapter 2, the synthesis of $[Ru(bpy)_2(4\text{-tetrazine})Cl]^+$ has been described. When this complex is adsorbed onto gold microelectrodes, it gives rise to cyclic voltammograms with the anodic branch showing distortion from background currents similar to Type 2, (See Figure 3.11). Figures 3.12 and 3.13 illustrate the type of backgrounds present in the oxidation branch of the voltammetric response for a 39 μm radius gold microelectrode modified with an $[Os(bpy)_2(4\text{-tetrazine})Cl]^+$ monolayer at 800 V s^{-1}. The supporting electrolyte is 1.0 M aqueous $LiClO_4$ with $HClO_4$ added. The pH is 0.87 and 6.01, respectively. This type of background is quite commonplace when using platinum or gold microelectrodes and is due to the onset of Pt or Au oxidation at higher overpotentials especially in acidic media.

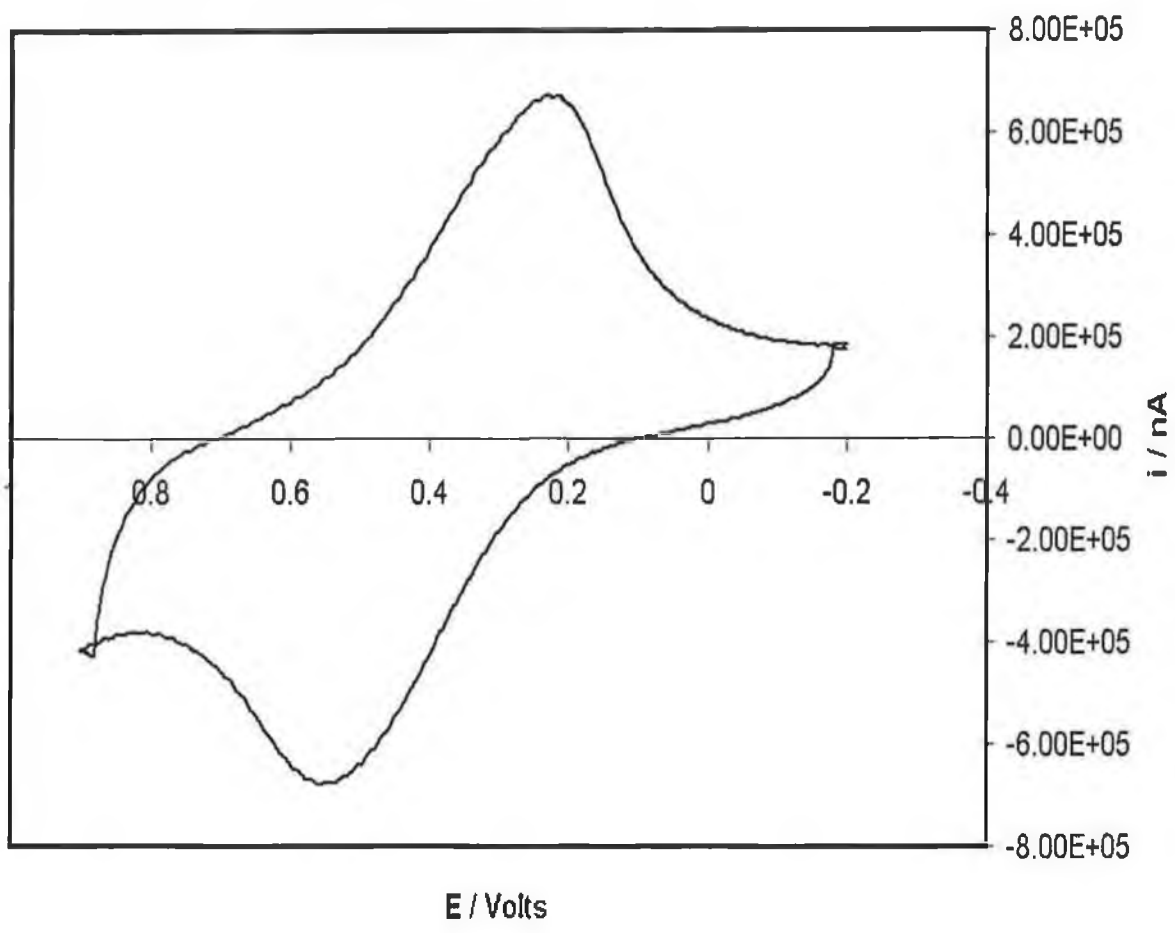

Figure 3.11. Voltammetric response for a 5 μm radius gold microelectrode modified with an $[Ru(bpy)_2(4\text{-tetrazine})Cl]^+$ monolayer at 1000 V s^{-1}, using a Ag/AgCl reference electrode. The supporting electrolyte is 1.0 M aqueous $NaClO_4$.

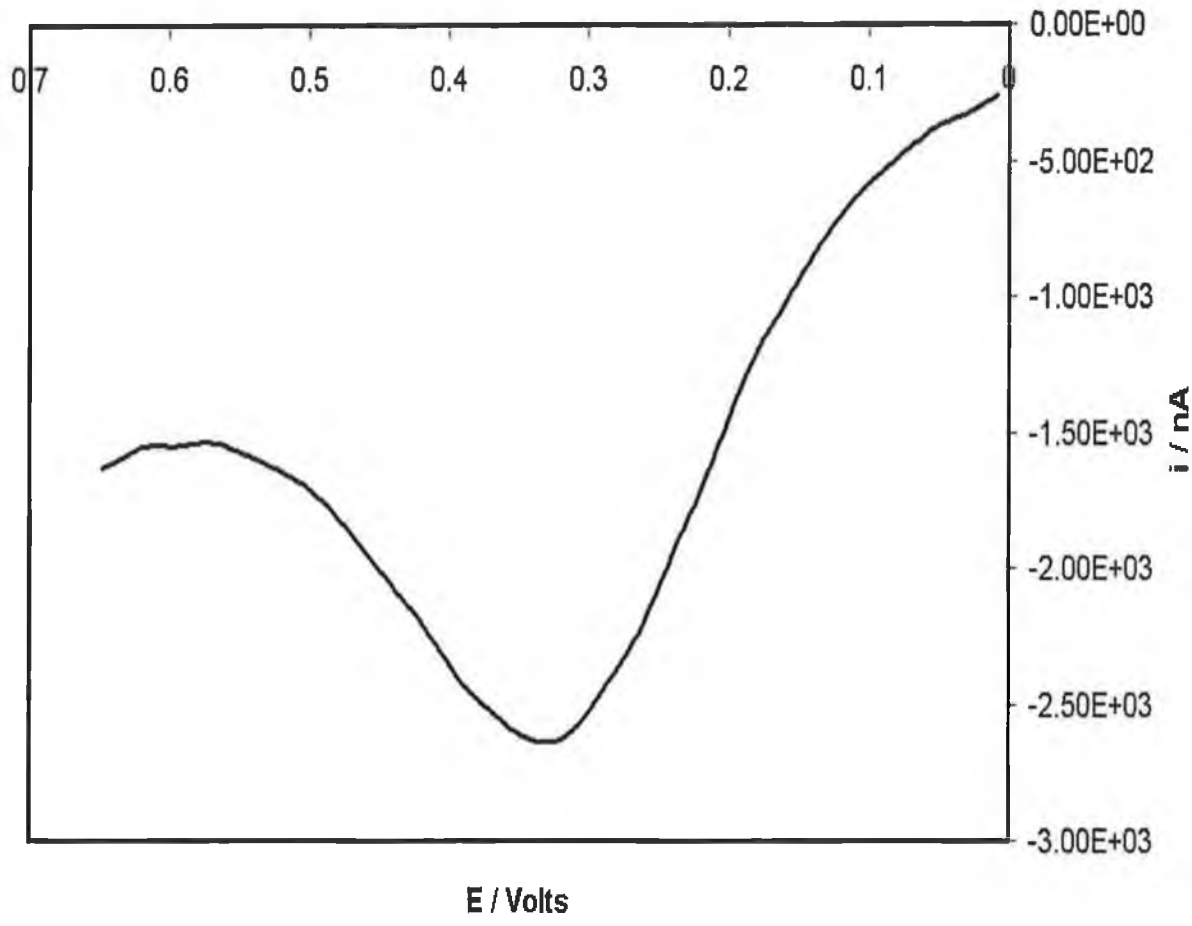

Figure 3.12. Anodic branch of the voltammetric response for 39 μm radius gold microelectrode modified with an $[Os(bpy)_2Cl(4\text{-tetrazine})]^+$ monolayer at 800 V s^{-1}, using a Ag/AgCl reference electrode. The supporting electrolyte is 1.0 M aqueous $LiClO_4$ with $HClO_4$ added giving a pH of 0.87.

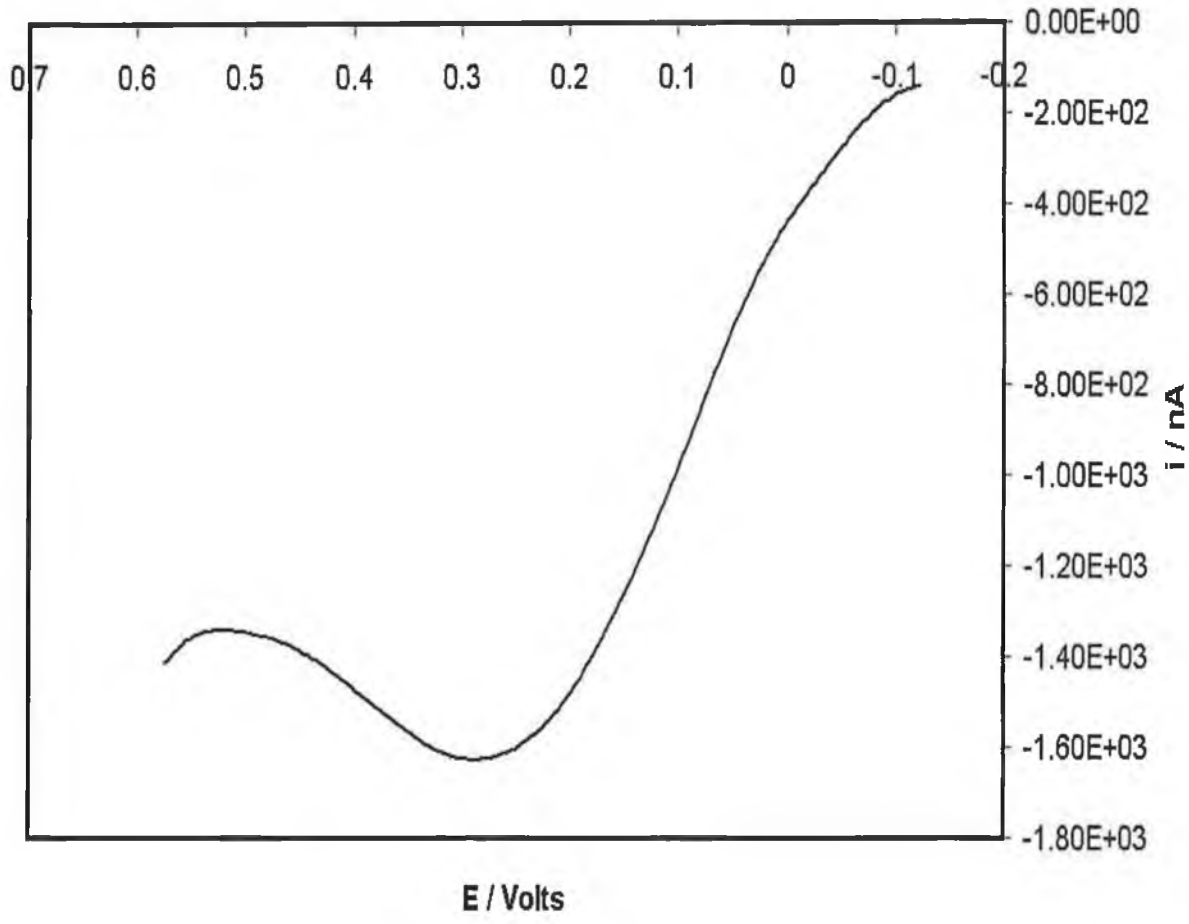

Figure 3.13. Voltammetric response for 39 μm radius gold microelectrodes modified with an $[Os(bpy)_2Cl(4\text{-tetrazine})]^+$ monolayer at 800 V s^{-1}, using a Ag/AgCl reference electrode. The supporting electrolyte is 1.0 M aqueous $LiClO_4$. The pH of the solution is 6.01.

3.6. Testing the Adiabatic Model on Theoretical Data at Different Scan Rates

Having completed the investigation of the performance of the adiabatic model in the presence of "capacitive" background currents, it is important to look at any other limitations that might exist. For example, how will the model determine k^o and λ if the scan rate is not fast enough to give significant peak to peak separation in the theoretical cyclic voltammogram?

In order to test the performance of the two parameter model (i.e., k^o and λ) on data generated by the model itself at different scan rates and known k^o and λ, the following procedure was carried out.

1. One oxidation curve was generated using the model with k^o and λ set at 1100 s^{-1} and 83.444 kJ mol^{-1} for each of the following scan rates, namely 1, 5, 10, 50, 500, and 1000 Vs^{-1}.
2. This theoretical data of known k^o and λ was then used as "experimental" input.
3. The simplex algorithm was then started with an opening guess for λ and k^o, of 10 kJ mol^{-1} and 1000 s^{-1}, respectively (other variants of the model were designed to prevent bias in the starting guess by using random numbers as the initial inputs for k^o and λ).
4. The simplex, having found the minimum, was restarted at the new k^o and λ, twice so as to be certain that the true minimum was found (i.e., finding the same k^o and λ found after re-invoking the simplex indicates that the true minimum has been found.
5. The exit condition for each simplex run was a difference of less than 0.0001% between consecutive steps on the simplex for both parameters.

The results are given in the following Table 3.1.

Table 3.1. Testing the model on data simulated using different scan rates. This table shows the output from the model. Theoretical data based on λ =83.4 kJ mol^{-1}, k^o=1100 s^{-1}. The simplex starts with λ = 10 kJ mol^{-1}, k^o=1000 s^{-1}. SSR is the sum of the squares of the residuals.

Scan rate V s^{-1}	1000	500	50	10	5	1
λ kJ mol^{-1}	83.4	83.4	83.4	84.6	65.8	15.5
k^o s^{-1}	1100.0	1100.0	1100.0	1100.1	1100.7	1138.8
SSR	1.09E-04	1.15E-04	1.19E-04	1.49E-04	1.33E-04	6.56E-06

3.6.1. Conclusions

1. For this data, the simplex fitting model has no difficulty finding the true values for k^o and λ for scan rates greater than 50 V s^{-1}. At this scan rate significant peak to peak separation occurs and the data contain significant kinetic information.
2. The results show an important limitation in the model in that the scan rates must be sufficiently fast so that the experimental response contains valid kinetic information.
3. The data shows that k^o is a more dominant factor than λ in that the simplex can find a reasonable estimate of k^o down to 1 V s^{-1}.

3.7. Effect of Restricting the Data to the Voltammetric Peak

When a two-parameter model is extended to include the barrier height, the computation time significantly increases and reduces the effectiveness of the model as a diagnostic cyclic voltammetric tool. The model described so far compares each experimental point to a theoretical point. Thus, the model operates on data points in the double layer charging region of the CV as well as the oxidation wave that contains kinetic information.

One might expect if the model focussed just on those points which define the voltammogram peak that successful fitting would be achieved. This would significantly reduce the computation time as, depending on the potential range and resolution, it is not unusual for more than 30% of all data points to lie in the double layer charging section of the voltammogram.

To test this approach, the program was modified so that the model only considered data around the peak potential. This was achieved by automatically examining the magnitude of the currents throughout the entire curve and determining the points at either side of the curve where a large percentage difference (typically 10%) existed between those points and their adjacent points.

The results are as given in the following tables:

Table 3.2. 3 Parameter model fitting complete voltammogram. The theoretical data is based on λ =83.4 kJ mol^{-1}, k^o=1100 s^{-1}, E_B = 192 kJ mol^{-1}. The simplex starts with λ = 1000 kJ mol^{-1}, k^o = 1000 s^{-1}, E_B = 1000 kJ mol^{-1}. These results illustrate that the model can find the true values for k^o and λ when the complete voltammogram is used in the simplex. The table shows the output from the model. SSR is the sum of the squares of the residuals.

Scan rate Vs^{-1}	1000	500	50
λ kJ mol^{-1}	83.4	83.4	83.5
k^o s^{-1}	1100.0	1100.0	1100.0
E_B kJ mol^{-1}	193.0	193.2	172.2
SSR	1.06E-04	1.14E-04	1.14E-04

Table 3.3. 3 Parameter model fitting data around the peak potential. The data around the peak potential is selected by finding the data where a large (10%) difference in current occurs between two adjacent points on either side of the cyclic voltammogram. No data in the double layer charging region were included. The simplex is only operating on those points around the peak potential. The theoretical data is based on λ =83.44 kJ mol^{-1}, k^{o}=1100 s^{-1} and E_B = 192 kJ mol^{-1}. The simplex starts with λ = 1000 kJ mol^{-1}, k^{o}=1000 s^{-1}, E_B =1000 kJ mol^{-1}. The table shows the output from the model. SSR is the sum of the squares of the residuals.

Scan rate Vs^{-1}	1000	500	50	10	5	1
λ kJ mol^{-1}	8207.7	6.4E+06	1.1E+04	230.5	195.9	202.3
k^{o} s^{-1}	175.9	816.9	970.7	701.0	734.5	17.0
E_B kJ mol^{-1}	8.6	2.0E+07	2529.7	541.9	1515.7	19.6
SSR	1.76E+03	2.45E+03	3.29E+01	1.05	3.00E-01	5.48E-02

Table 3.4. 3 Parameter model fitting data around the peak potential. The data around the peak potential is selected by finding the data where a (1%) difference in current occurs between two adjacent points on either side of the cyclic voltammogram. Some data in the double layer charging region were included. The theoretical data is based on λ = 83.4 kJ mol^{-1}, k^o=1100 s^{-1} and E_B = 192 kJ mol^{-1}. The simplex starts with λ = 1000 kJ mol^{-1}, k^o=1000 s^{-1}, E_B = 1000 kJ mol^{-1}. The table shows the output from the model. SSR is the sum of the squares of the residuals.

Scan rate Vs^{-1}	1000
λ kJ mol^{-1}	79.1
k^o s^{-1}	1094.9
E_B kJ mol^{-1}	1571.2
SSR	50.8

3.7.1. Conclusions

1. When peak points only are considered (i.e., points selected between two outer limits at which the first 10% current difference occurs along the curve), the model cannot find satisfactory solutions for k^o, λ or barrier height.
2. When peak points and some shoulder points are considered (i.e., points selected between the two outer limits at which the first 1 % current difference occurs along the curve), the estimate for λ and k^o are reasonably accurate but an incorrect solution for barrier height is found.
3. Considering these results, it is always best to use the model on complete cyclic voltammograms containing all regions, namely, horizontal, shoulder and peak in spite of the extended computation time.
4. The reason for the discrepancy between these results lies in the arbitrary nature of the selection of the outer limit points. By using the full data set all of the kinetic information across all potentials is used allowing accurate k^o and λ values to be determined. In particular, it appears that the curve shape, including those currents relatively far from E^0, contain valuable information about λ.

3.8. Using the Adiabatic Model to Understand Averaging Effects

The three parameter adiabatic model can be used as a tool to gain understanding of electron-transfer processes between redox moieties and microelectrodes. Many different theoretical and experimental electrochemical scenarios can be examined by the model with the only limitation being the electrochemist's imagination, e.g., what results would be obtained if a system was examined which had three independent sets of the three parameters, namely three different rate constants, three different reorganisation energies and three different barrier heights all present at the same time? Would the cyclic voltammogram obtained be simply the average current for the three sets of parameters?

In order to answer these questions, the following simple experiment was carried out:

1. Three different theoretical cyclic voltammograms were simulated with the model using different input parameters all at the same scan rate.
2. The current at each overpotential was averaged and one cyclic voltammogram produced.
3. This average cyclic voltammogram was then embedded into the model, which was invoked to search for the best fit for this CV by varying λ, k^o and E_B.
4. The starting guesses for the simplex in this case were λ =1000 $kJmol^{-1}$, k^o=1000 s^{-1} and E_B =1000 $kJmol^{-1}$.
5. This experiment was then repeated with only k^o changing, while λ and E_B were kept the same for each of the 3 cyclic voltammograms.

The results are given Tables 3.5 to 3.8.

Table 3.5. 3 Cyclic voltammograms were simulated using 3 different values for k^o, λ, and E_B. The currents at each overpotential were then averaged to construct an average cyclic voltammogram. This table gives the different values for k^o, λ and E_B used to construct the cyclic voltammograms.

Average data based on 3 CVs with different input parameters				Average
	CV1	CV2	CV3	CV4
λ kJ mol^{-1}	50	100	100.3	83.4
K^o s^{-1}	500	2000	800	1100
E_B kJ mol^{-1}	190	194	192	192

Table 3.6. 3 Cyclic voltammograms were simulated using 3 different values for k^o, λ, and E_B. The currents at each overpotential were then averaged to construct an average cyclic voltammogram. This table gives the best fit values of k^o, λ and E_B for the 3 individual cyclic voltammograms and the average cyclic voltammogram. SSR is the sum of the squares of the residuals. To verify that the first minimum SSR found is the true minimum, the simplex was re-invoked starting with the best fit values found for k^o, λ, and E_B at the first attempt.

Output from model :Convergence 1				Average Data
	CV1	CV2	CV3	Average CV4
Scan rate V s^{-1}	1000	1000	1000	1000
λ kJ mol^{-1}	49.1	100.0	96.4	23.9
k^o s^{-1}	496.6	2000.0	795.7	1172.2
E_B kJ mol^{-1}	1730.0	195.3	1154.8	2198.7
SSR	5.5	0.0	4.9	5058.7
Output from model :Convergence 2				
λ kJ mol^{-1}	50.0	100.0	100.3	23.9
k^o s^{-1}	500.0	2000.0	800.0	1172.2
E_B kJ mol^{-1}	190.4	195.3	193.0	2198.7
SSR	0.0	0.0	0.0	5058.7

Table 3.7. 3 Cyclic voltammograms were simulated using 3 different values for k^o, and 1 value for both λ, and E_B. The currents at each overpotential were then averaged to construct an average cyclic voltammogram. This table gives the values for k^o, λ and E_B used.

Average data based on	CV1	CV2	CV3	Average CV4
λ kJ mol^{-1}	83.4	83.4	83.4	83.4
k^o s^{-1}	500	800	2000	1100
E_B kJ mol^{-1}	192	192	192	192

Table 3.8. Three cyclic voltammograms were simulated using three different values for k^o and one value for both λ and E_B. The currents at each overpotential were then averaged to construct an average cyclic voltammogram. This table gives the best fit values of k^o, λ and E_B for the 3 individual cyclic voltammograms and the average cyclic voltammogram. SSR is the sum of the squares of the residuals. To verify that the first minimum SSR found is the true minimum, the simplex was re-invoked starting with the best fit values found for k^o, λ, and E_B at the first attempt.

Output from model :Convergence 1				
	CV1	CV2	CV3	Average CV4
Scan rate V s^{-1}	1000	1000	1000	1000
λ kJ mol^{-1}	83.4	83.4	83.4	28.3
k^o s^{-1}	500.0	800.0	2000.0	1124.2
E_B kJ mol^{-1}	192.0	192.0	192.0	2004.2
SSR	0.0	0.0	0.0	3975.0
Output from model :Convergence 2				
λ kJ mol^{-1}	83.4	83.4	83.4	28.3
k^o s^{-1}	500.0	800	2000.0	1124.4
E_B kJ mol^{-1}	192.0	192.0	192.0	2004.2
SSR	0.0	0.0	0.0	3975.0

3.8.1. Conclusions

1. The model indicates a system containing a range of the three parameters, λ, k^o, and E_B will not present cyclic voltammograms which are merely averaged over the ranges of λ, k^o, and E_B in the system.
2. This test highlights a significant limitation to the model. Intuitively, it would be expected that if distributions of values for λ, k^o, and E_B exist in a real system (this seems likely to be the case in practice), then the cyclic voltammogram obtained from the system would reflect the arithmetic mean of the currents present. Significantly, the electron-transfer model developed here does not support this assumption.
3. The combination of the simplex fitting algorithm with the adiabatic electron-transfer theory has allowed facile probing of the theory so that the limitations of the existing theory can be readily seen.
4. The model will require modification to allow for the likely presence of distributions of parameters in order to extract meaningful values from experimental data from systems containing those distributions.

3.9. Extending the Model to Search for Four Parameters

In order to test the limits of application of the adiabatic fitting model, a variant was designed which would search for four parameters simultaneously. The parameters chosen were k^o, λ, E_B and the electron transfer distance. The electron transfer distance not only controls the rate of electron transfer (i.e., k^o) but also can dictate whether the electron transfer process is adiabatic or not. Adiabatic electron transfer processes tend to occur when there is a short distances between the redox active centre and the surface of the microelectrode.

As before, a theoretical oxidation curve was constructed using the adiabatic theory based on certain values for the four parameters and then the fitting model was applied to search for these values.

The results are given in Table 3.9.

Table 3.9. Four parameter model searching for k^o, λ, E_B and electron transfer distance. The theoretical data based on λ =83.444 kJ mol^{-1}, k^o=1100 s^{-1}, E_B = 192 kJ mol^{-1} and electron transfer distance=3 Å. The simplex starts with λ = 1000 kJ mol^{-1}, k^o = 1000 s^{-1}, distance = 1 Å, E_B = 1 kJ mol^{-1}. The scan rate chosen is 1000 V s^{-1}. The table shows the output from the model. SSR is the sum of the squares of the residuals.

Scan rate V s^{-1}	1000
λ kJ mol^{-1}	83.4
k^o s^{-1}	1100.0
Distance Å	3.3
E_B kJ mol^{-1}	4.09E+02
SSR	1.07E-04

3.9.1. Conclusions

1. The adiabatic fitting model can find three out of the four parameters accurately, namely λ, k^o and distance. However, it cannot find the correct value for E_B.
2. The model as constructed is strongly dependent on k^o, λ, and the electron transfer distance with the sensitivity reducing in that order.
3. The curves constructed by the model are relatively weakly dependent on the value of E_B and therefore the correct value for the E_B is difficult to find.
4. Computation time becomes a limiting factor in the usefulness of the model when four parameters are being sought.
5. This investigation of the performance of the model has shown that for probing experimental cyclic voltammograms, only two parameters should be searched for, namely k^o and λ.

3.10. Scan Rate Dependence of the Non-Adiabatic Model

In order to test the performance of the two parameter non-adiabatic model (i.e., k^o and λ) on data generated by the model itself at different scan rates and known k^o and λ, the following procedure was carried out.

One oxidation curve was generated using the model with k^o and λ set at 1100 s^{-1} and 83.0 kJ mol^{-1}, respectively for each of the following scan rates, namely 1, 5, 10, 50, 500, and 1000 Vs^{-1}. This theoretical data of known k^o and λ was then embedded back into the model. The simplex algorithm was then started with an opening guess for λ and k^o, of 96.486 kJ mol^{-1} and 1000 s^{-1}, respectively (other variants of the model were designed to prevent bias in the starting guess by using random numbers as the initial inputs for k^o and λ.).

The simplex, having found the minimum, was restarted at the new k^o and λ estimates, two further times to ensure that the true minimum was found (i.e., same k^o and λ found after re-invoking the simplex is indicative of true minimum). The results are given in Table 3.10.

Table 3.10. Scan rate dependence of the 2 parameter non adiabatic model. Five theoretical cyclic voltammograms with five different scan rates were tested with the non adiabatic electron transfer model. SSR is the sum of the squares of the residuals. This table gives the best fit values for k^o and λ.

Scan rate $V\ s^{-1}$	1000	500	50	10	5	1
λ kJ mol^{-1}	83.0	83.0	83.0	83.9	83.9	51.1
$k^o\ s^{-1}$	1100.0	1100.0	1100.0	1100.0	1100.0	1105.9
SSR	9.96E-06	1.06E-05	1.09E-05	1.32E-05	1.39E-05	5.68E-06

3.10.1. Conclusions

1. For this data, the simplex fitting model has no difficulty finding the true values for k^o and λ for scan rates greater than 50 V s^{-1}. This situation corresponds to the scan rate at which significant peak to peak separation is observed.
2. The data shows that k^o is a more dominant factor than λ in that the simplex can find a reasonable estimate of k^o down to 1 Vs^{-1} where the peak to peak separation is greater than 100 mV.

The results show an important limitation to the model in that scan rates fast enough to display kinetic information must only be probed with the model. This is a lower limit on scan rate. The model can, of course, be modified to identify apriori inadequate data. As a first step, the model could determine the peak-to-peak separation of the oxidation and reduction curves for each scan rate. Then only data with a peak-to-peak separation greater than a critical minimum (e.g., 100 mV) would be considered for fitting by the model.

3.11. The Combined Adiabatic / Non Adiabatic Fitting Model

Having established that, prior to investigating experimental cyclic voltammetric data with the model and its variants, only two parameters, namely λ and k^o, should be simultaneously searched for, it was decided to construct a model which would contain both the adiabatic and non-adiabatic electron transfer theories. This was not intended to suggest that electron transfer for a given system can be simultaneously adiabatic and non-adiabatic or that a hybrid form of electron transfer can exist. The intention was to test whether a given system followed the adiabatic or non-adiabatic electron transfer theory.

This model was constructed using a weighting factor as a third parameter in the simplex fitting algorithm imbedded in the model. The construction of this combined electron-transfer model was carried out by the following steps:

1. The code for both the non-adiabatic model and the adiabatic model were placed in the same Microsoft Excel macro.
2. For each overpotential, a non-adiabatic and an adiabatic dimensionless current were calculated using the code.
3. The simplex fitting algorithm was modified to accept three parameters, namely, λ, k^o, and the adiabatic/non-adiabatic weighting factor (WF).
4. The relationship between the combined current, adiabatic current, non-adiabatic current and the weighting factor is given by the following equation:

$$i_{combined} = \frac{\left(i_{non-adiabatic} + (WF) i_{adiabatic}\right)}{WF + 1} \qquad (10)$$

The simplex is started with random guesses for λ and k^o while the starting point for the WF, weighting factor is usually 1, i.e., no bias for either theory. Obviously as the combined model proceeds to find the solution for the values, if it finds that the adiabatic electron-transfer theory fits the data more accurately than the non-adiabatic theory, then it will continually increase the weighting factor and vice versa. So the combined model can preferentially fit either theory to any system under investigation. As cyclic voltammograms produced separately from each theory look visually similar and in many cases are indistinguishable, the ability of the model to determine whether electron transfer is adiabatic or non-adiabatic in nature is felt to be a very important feature. Of course, in reality, the true value of the weighting factor, WF, can only be 0 or infinity, i.e., only one model or the other is appropriate for a given system.

Figure 3.14 shows the simplex as it progresses towards the solution (i.e., perfect match with "Experimental" data. The simplex starts with the values of λ = 10 kJ mol^{-1}, k^o = 120 s^{-1}, adiabatic factor = 1. An intermediate stage corresponding to λ = 30 kJ mol^{-1}, k^o = 360 s^{-1}, adiabatic factor = 0.1, is also shown. The simplex finds the perfect match (♦) with "experimental" data at the correct value of λ = 96 kJ mol^{-1}, k^o = 600 s^{-1}, adiabatic factor << 1.

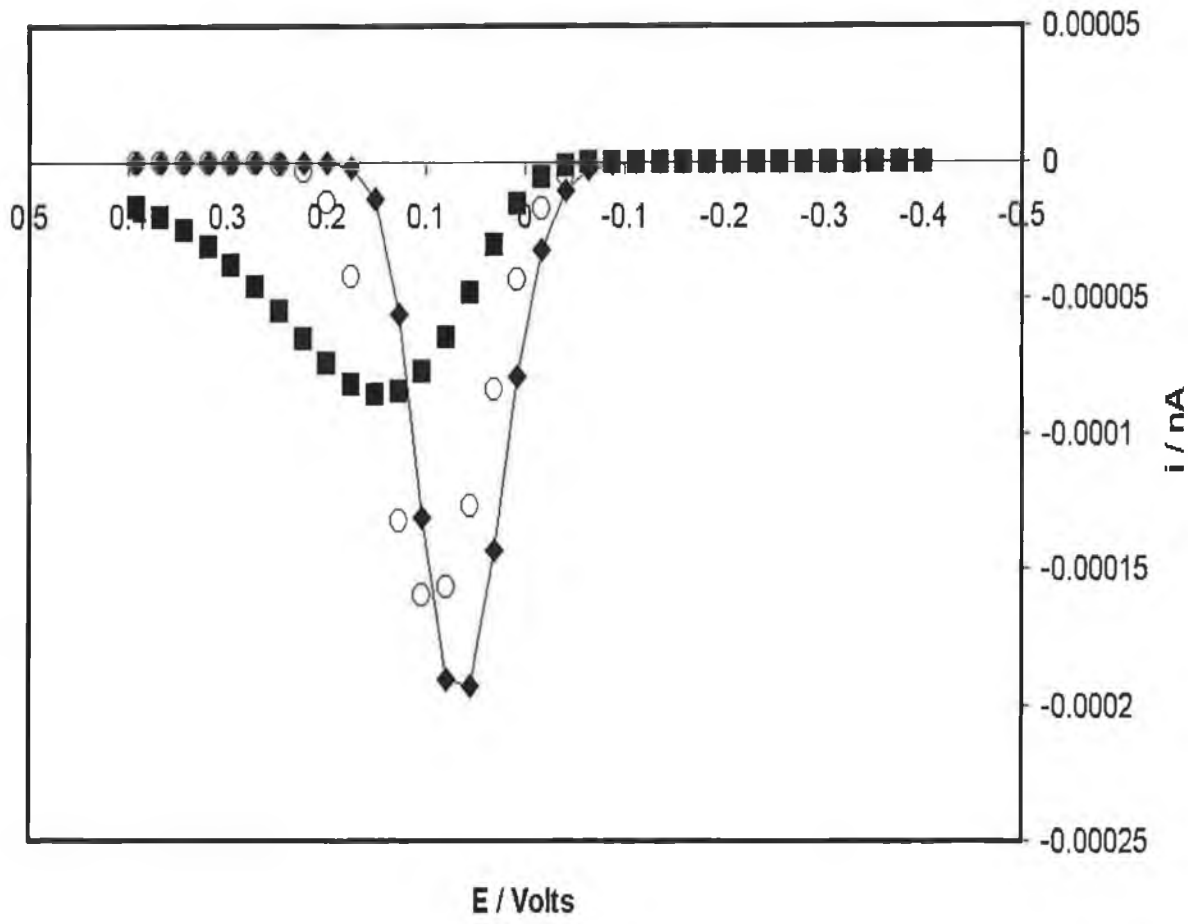

Figure 3.14. Shows the simplex as it progresses towards the solution (i.e., perfect match with "Experimental" data (–)). The simplex starts with the values of $\lambda = 10$ kJ mol^{-1}, $k^o = 120$ s^{-1}, adiabatic factor = 1, (■). An intermediate stage corresponding to $\lambda = 30$ kJ mol^{-1}, $k^o = 360$ s^{-1}, adiabatic factor = 0.1, (O) is also shown. The simplex finds the perfect match (♦) with "experimental" data at the correct value of $\lambda = 96$ kJ mol^{-1}, $k^o = 600$ s^{-1}, adiabatic factor $<< 1$.

3.11.1. Testing the Combined Electron-Transfer Model

This model variant is tested in a similar way to earlier ones by first generating theoretical data based on particular values of the reorganisation energy and the rate constant from either adiabatic or non-adiabatic electron-transfer theory. The model is then made to search for these values starting from guesses based on random numbers and a neutral value of 1 for the adiabatic/non-adiabatic weighting factor. The results are given in the following table.

Table 3.11. Simplex searching for solution for λ and k^o based on non-adiabatic electron-transfer theory using values of 96.48 kJ mol^{-1} and 600 s^{-1} for λ and k^o respectively. The starting values and the best fit values for λ and k^o are given in this table. The starting values for λ are random values from the range 1 to 100 kJ mol^{-1}. The starting values for k^o are random numbers from 1 to 1000 s^{-1}. The starting value for the adiabatic weighting factor is 1. The combined model was tested 11 times from different starting values and re-invoked twice after the initial convergence using the best fit values as starting estimates for λ, k^o and the adiabatic weighting factor. In this table, the results for 5 tests are shown. The results from the third simplex have been omitted.

Scan rate V s^{-1}	100	100	100	100	100
λ starting guess kJ mol^{-1}	35.89	24.31	53.37	36.76	29.71
k^o starting guess s^{-1}	768.40	825.55	574.64	176.69	634.93
λ result kJ mol^{-1}	96.48	96.48	96.48	125.65	35.66
k^o Result s^{-1}	600.00	600.00	600.00	603.61	634.93
Adiabatic Factor	0.000117	0.000117	0.000118	2.57E+07	0.000117
Sum of the square of the differences	1.35E-36	1.35E-36	1.35E-36	1.14E-30	3.56E-28

Second simplex starting from result of the first

λ result kJ mol^{-1}	96.48	96.48	96.48	96.48	96.48
k^o Result s^{-1}	600.00	600.00	600.00	600.00	600.00
Adiabatic Factor	0.000117	0.000117	0.000118	0.000117	0.000117
Sum of the square of the differences	2.93E-36	2.93E-36	2.94E-36	2.93E-36	1.35E-36

3.11.2. Conclusions

1. The fitting algorithm can find the true values for λ and k^o from the data.
2. The model correctly identifies the input data as data based on the non-adiabatic electron-transfer theory.
3. By continuously re-running the fitting model from different starting points, the presence of false local minima giving incorrect results is seen. Therefore, to have confidence in the result, the simplex should always be restarted from its result at least once.

Note: A similar test of the model was carried out using theoretical data based on adiabatic data.

3.12. Alternative Method for Determination of λ and k^o

An alternative method for determination of λ and k^o using the simplex algorithm is to use the dependence of peak potential on scan rate. This approach was described previously by Weber and Creager[1].

In earlier studies of redox kinetics in monolayers, the Laviron formalism[12] was used to predict how electron-transfer rate constants vary with applied potential. This formalism was based on the classic Butler-Volmer model of electrochemical kinetics.[13,14] The fundamental principle demonstrated by Laviron was that values for the heterogeneous self-exchange rate constant, k^o, and the electrochemical transfer coefficient, α, could be extracted for irreversibly adsorbed redox-active groups from the dependence of the voltammetric peak potentials on scan rate.

One aspect of Laviron's formalism that is particularly useful for analysing data is the prediction that, at scan rates for which the peak separation is greater than 200 mV, the anodic and cathodic peak potentials should both scale linearly with the log (scan rate). The slopes of the anodic and cathodic branches of a plot of peak potential vs. log (scan rate) can be used to estimate α. In fact, observation of such linear scaling of peak potential with log (scan rate) is diagnostic of the validity of the Butler-Volmer model.

However, application of Laviron's formalism has limited use as it is based on the simple, approximate Butler-Volmer model which, as has been discussed in Chapter 1, fails to predict the experimental observation that k^o becomes independent of overpotential for sufficiently large driving forces. The Butler-Volmer model considers the reaction surface to be linear rather than parabolic (i.e., potential energy varies linearly rather than parabolically along the reaction co-ordinate), and it ignores contributions to the rate from states in the electrode at any potential other than the applied potential (i.e., the Fermi level).

Marcus theory removes these inadequacies and is more appropriate when the reaction overpotential is not negligible in comparison to its reorganisation energy, λ.

In the work carried out by Weber and Creager[1], the code for calculating rate constants, voltammograms, and peak potential vs. log (scan rate) curves was incorporated into the simplex algorithm. The simplex used the two fitting parameters, λ and k^o, to minimise the sum of the squares of the differences between the calculated peak potential and the measured peak potential at each scan rate for which a point was measured.

This method has the advantage of significantly reducing the distortion caused by the presence of background currents in that a horizontal shift down of the anodic branch of the voltammogram does not change the peak potential. Indeed, the presence of a sloping background current will only cause a marginal change in the observed peak potential. Using this system, one can imagine that adjustment for background is almost unnecessary.

The major disadvantage, however, is that a lot of kinetic and thermodynamic information contained in the cyclic voltammogram is not used in the analysis in that only the peak potential (i.e., one datum from the CV) is used for each scan rate. So for twenty different scan rates, say, the simplex will be changing the estimates for λ and k^o in order to minimise the differences between the twenty experimental peak potentials and the twenty theoretical peak potentials. Given that the results for the technique used in this work (i.e., comparison of all points on the cyclic

voltammogram) are good even when large distortions from background currents are present, it is clear that minimising the sum of squares of the differences between each experimental and theoretical current on the cyclic voltammogram (i.e., hundreds of data for each scan rate depending on the resolution) will statistically and electrochemically produce more reliable estimates of λ and k^o.

In order to make an objective comparison between the two methods, namely, the full cyclic voltammogram method (i.e., present model) and the peak potential vs. scan rate method (i.e., Weber and Creager's[1]), a model was constructed based on peak potential vs. scan rate. Theoretical data generated from the adiabatic electron-transfer theory was generated using k^o 1100 s^{-1} and λ 83.44 kJ mol^{-1} as inputs. Data was generated at 6 different scan rates, namely 1000, 500, 50, 10, 5, and 1 Vs^{-1}. Next, 12 arbitrary points were chosen at which to examine the sum of the squares of the differences. These points are given in Table 3.12.

Taking the sum of the differences squared (i.e., SSR or SS) at these 12 points, for each method and setting the sum of the differences squared for Point 1 (the furthest away from the exact fit) at 100%, it can be illustrated how the SS changes as the simplex moves towards the correct values. Figure 3.15 shows this analysis.

In testing the peak potential vs. scan rate method, the simplex was started from many different starting points and re-invoked several times and it quickly became apparent that it was far more difficult for the algorithm to find its way to the correct values. In many cases the algorithm found its way into local minima and even by re-invoking the simplex, the algorithm could not proceed to the solution. Figure 3.15 illustrates the reason for this. As this figure shows, the full cyclic voltammogram method operating on just one set of scan rate data (i.e., 1000 V s^{-1}) has a much steeper slope to follow than the peak potential vs. scan rate method (operating on 6 different sets of data). The peak potential vs. scan rate method has a major drop from Point 1 to Point 2 and then a small gradual slope from Point 2 to Point 12. The simplex algorithm is much more likely to "get stuck" in local minima when the slope of the SSR line is gradual and also when this slope, itself, changes markedly (e.g., Slope from Point 1 to Point 2 differs greatly from slope from Point 2 to Point 12).

Table 3.12. Data points used in the analysis of the sum of the differences squared for the full cyclic voltammogram method and the peak potential vs. scan rate method.

Data Point	k^o s^{-1}	λ kJ mol^{-1}
1, Starting	10	1
2	100	10
3	200	20
4	300	30
5	400	40
6	500	50
7	600	60
8	700	70
9	800	80
10	900	83.44
11	1000	83.44
12, Ending	1100	83.44

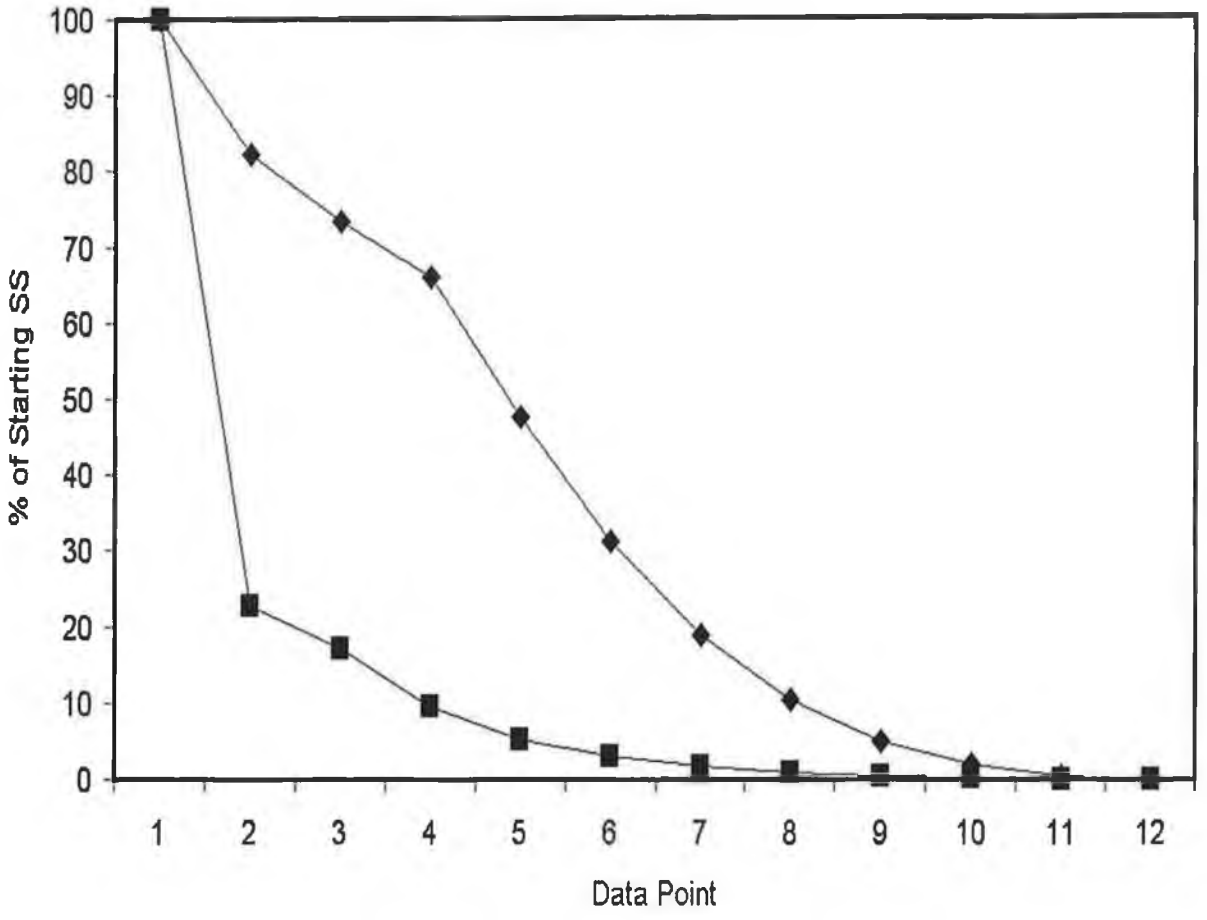

Figure 3.15. Shows how the sum of the differences squared (SS) changes as the full cyclic voltammogram method (♦) and the peak potential vs. scan rate method (■) move from an arbitrary starting point (k^o 10 s^{-1}, λ 1 kJ mol^{-1}) to the correct fit (k^o 1100 s^{-1}, λ 83.44 kJ mol^{-1}).

Figure 3.16 shows what happens when the starting estimates for k^o and λ are improved, and it is seen that there is little difference between the two methods. However, these starting values are now 45% and 60% of the correct values for k^o and λ, respectively. So, one needs to have a good estimate of the correct values for the peak potential vs. scan rate method to work. This somewhat defeats the purpose which is to provide the electrochemist with a tool which can be applied to cyclic voltammetric data and produce realistic values for k^o and λ without any prior knowledge from another technique. On the other hand, the full cyclic voltammetric method can find the correct values from any random starting points (no prior knowledge necessary).

Is it possible, however to improve the performance of the peak potential vs. scan rate method? Well, if the number of sets of data with different scan rates are increased and also the potential resolution is improved, then the performance of this model should be enhanced. This was done by creating 19 sets of data with scan rates ranging from 10,000 V s^{-1} to 100 V s^{-1} (compared to six sets, previously) and by increasing the resolution from 5 mV to 1 mV. The analysis of the sum of the differences squared was then repeated and compared to the full cyclic voltammogram method and this is given in Figure 3.17. As Figure 3.17 shows there is only a marginal improvement in the slope of the line and there is still much greater likelihood of the simplex getting caught in local, false, minima. This is in spite of the fact that with this optimised peak potential vs. scan rate method, the computation time has been lengthened by a factor of 95 over the full cyclic voltammogram method.

Thus, the results of this objective analysis of the two possible methods, namely the full cyclic voltammogram method and the peak potential vs. scan rate method clearly justify the selection of the full cyclic voltammogram method as the preferred method for use on the experimental data in later chapters.

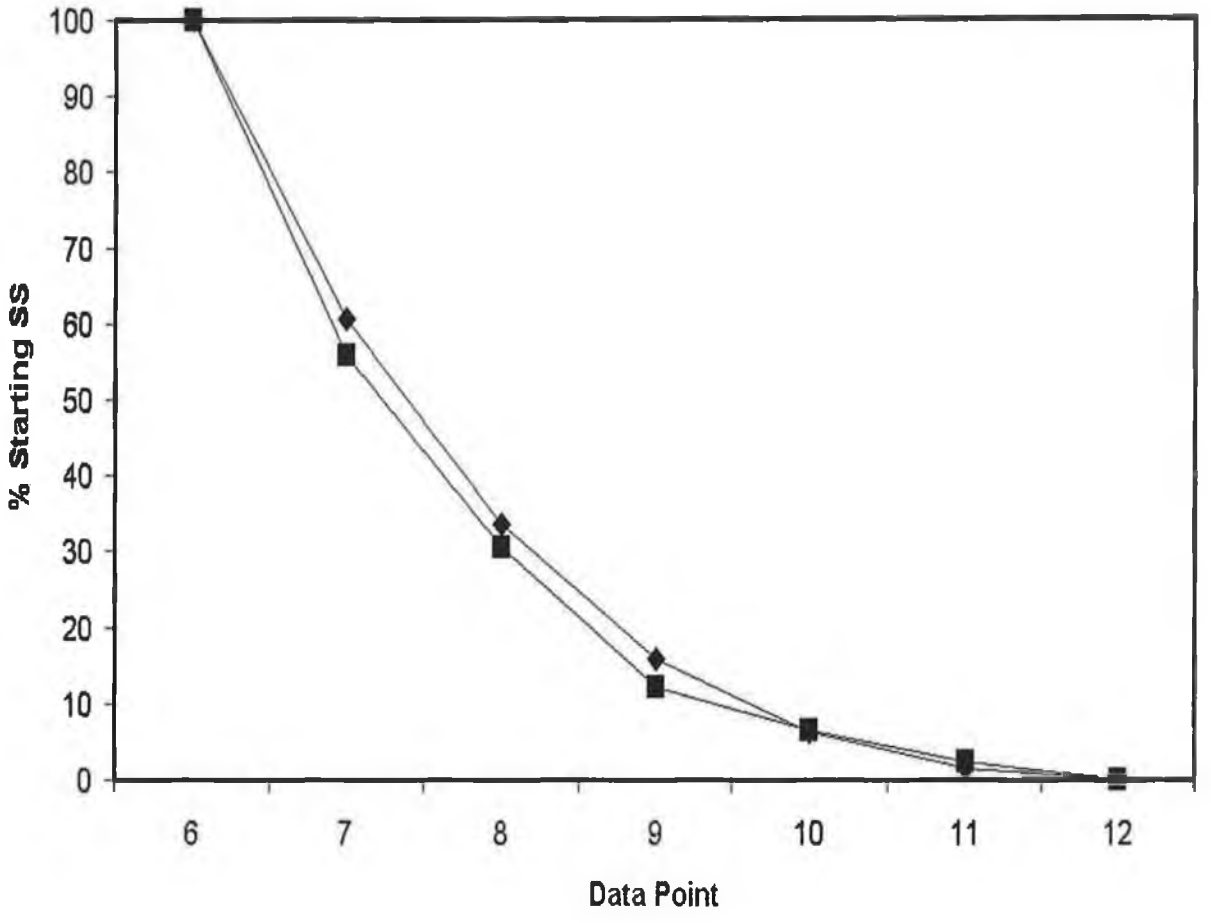

Figure 3.16. Shows how the sum of the differences squared (SS) changes as the full cyclic voltammogram method (♦) and the peak potential vs. scan rate method (■) move from an arbitrary starting point (k^o 500 s^{-1}, λ 50 kJ mol^{-1}) to the correct fit (k^o 1100 s^{-1}, λ 83.44 kJ mol^{-1}).

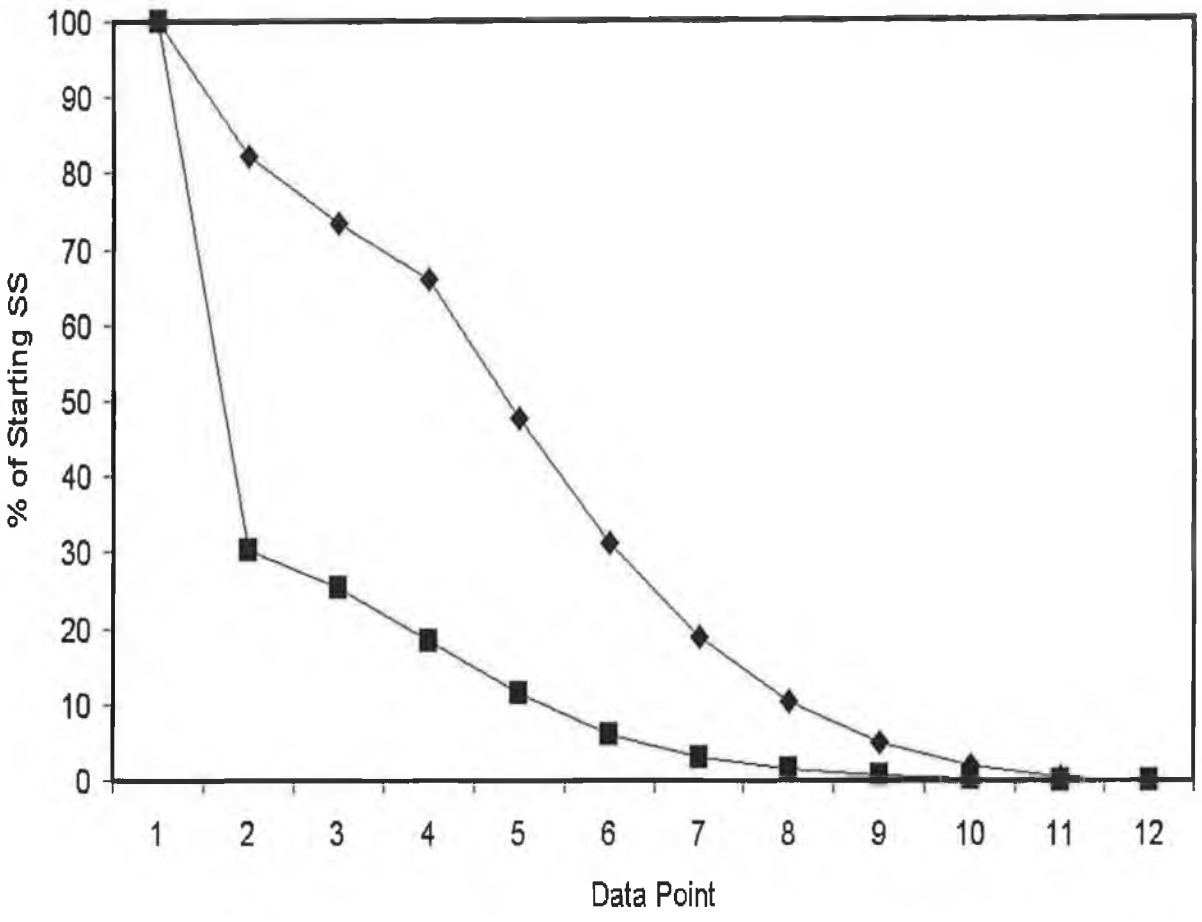

Figure 3.17. Shows how the sum of the differences squared (SS) changes as the full cyclic voltammogram method (♦) and the peak potential vs. scan rate method (■) move from an arbitrary starting point (k^o 500 s^{-1}, λ 50 kJ mol^{-1}) to the correct fit (k^o 1100 s^{-1}, λ 83.44 kJ mol^{-1}). In this case, the peak potential vs. scan rate method has been optimised by a 5-fold increase in potential resolution and the use 19 sets of data at different scan rates (compared to six, previously).

3.13. Overall Conclusions

Adiabatic and non-adiabatic electron transfer theory has been embedded using visual basic into a Microsoft Excel macro containing a simplex algorithm. Various versions of this model have been created including a combined adiabatic and non adiabatic electron transfer model. Detailed testing of this model has shown it to be a very robust, informative tool for the analysis of cyclic voltammograms. Searching for just two parameters, k^o and λ, (as opposed to more) is the most productive method. Using the simplex algorithm to find k^o and λ by minimising the sum of the squares of the differences between each current on the experimental and theoretical cyclic voltammogram has been shown to be far superior than the alternative method based on peak potentials at different scan rates.

This chapter has been mainly a theoretical evaluation of the newly constructed electron transfer model. In subsequent chapters, this model will be used on actual experimental data.

3.14. References

1 Weber, K.; Creager, S. E. *Anal. Chem.* **1994**, *66*, 3164.

2 Finklea, O.H.; Hanshew, D. D. *J. Am. Chem. Soc.* **1992**, *9*, 3173.

3 Forster, R. J.; Faulkner, L. R. *J. Am. Chem. Soc.* **1994**, *116*, 5444.

4 Marcus, R. A. *J. Chem. Phys.* **1956**, *24*, 4966.

5 Marcus, R. A. *J. Chem. Phys.* **1965**, *43*, 679.

6 Marcus, R. A. *Ann. Rev. Phys. Chem.* **1964**, *15*, 155.

7 Marcus, R. A. *Electrochim. Acta.* **1968**, *13*, 955.

8 Chidsey, C. E. D. *Science* **1991**, *251*, 919.

9 Tender, L.; Carter, M. T.; Murray, R. W. *Anal. Chem.* **1994**, *66*, 3173.

10 Bockris, J.O'M.; Khan, S. U. M. *Quantum Electrochemistry*; Plenum Press: New York, **1979**; Chapter 8.

11 Nelder, Mead, *Computer. J.*, **1965**, *79*, 308.

12 Laviron, E. *J. Electroanal. Chem.* **1979**, *101*, 19.

13 Butler, J. A. V. *Trans. Faraday Soc.*, **1924**, *19*, 729.

14 Erdey-Gruz, T.; Volmer, M. *Z. Physik. Chem.* **1930** *150A*, 203.

CHAPTER 4

Conjugated vs. Non-Conjugated Bridges : Heterogeneous Electron Transfer Dynamics of Osmium Polypyridyl Monolayers

4.1. Introduction

The production of "molecular wires" that promote fast heterogeneous electron transfer between a remote redox centre and a metal surface is important for high speed molecular electronics applications, e.g., molecule-based computing. One notable strategy in this area is to use conjugated rather than aliphatic bridges to achieve faster electron transfer rates. For example, conjugated molecules of [1,1':4',1"-terphenyl]-4-methanethiol (TP) have been embedded in self-assembled monolayers of insulating n-alkanethiols, and the conductivity of single molecules measured.[1] Also, Creager and co-workers[2] recently probed the electron transfer rates for ferrocene groups attached to gold electrodes via conjugated oligo(phenylethynyl) bridges of variable length. Significantly, they found that the extrapolated rate constants at short distances were nearly the same for conjugated and aliphatic bridges. Moreover, for short electron transfer distances, the observed rates were consistent with those expected for an adiabatic electron transfer suggesting strong electronic coupling between the redox centres and the electrode. In this context, experiments with self-assembled monolayers consisting of osmium 2,2′6′,2″terpyridine complexes attached to an electrode surface by 4′-(3-pyridyl)-2,2′:6′,2″-terpyridine, were performed recently. The heterogeneous electron transfer rate constants for this system do not show a substantial increase compared to those found for comparable aliphatic bridges.[3] However, directly comparing heterogeneous electron transfer rate constants will provide an insight into the strength of electronic coupling only if the free energy of activation is identical for conjugated and non-conjugated bridges. For example, switching from a non-conjugated to a conjugated bridging ligand may alter the structure of the monolayer making the local dielectric content and hence outer sphere reorganisation energies different in the two cases.

In this chapter, the effect of using a conjugated, *trans*-1,2-bis(4-pyridyl)ethylene, bpe, vs. a non-conjugated bridge, 1,2-bis(pyridyl)ethane, p2p, on the heterogeneous electron transfer rate constants for $[Os(bpy)_2Cl]^+$ moieties attached to the surface of platinum microelectrodes (Figure 4.1) is probed. Cyclic voltammetry has been used to measure the rate of heterogeneous electron transfer for monolayers of $[Os(bpy)_2Cl(bpe)]^+$ using scan rates up to 10000 V s^{-1}. These data have been compared with previous reports[4,5,6] on the non-conjugated bridge, 1,2-

bis(pyridyl)ethane. To determine whether differences in electronic coupling or the free energy of activation are responsible for the observed differences in k°, the complete voltammograms have been fitted using the overlap integral approach based on the Marcus relation described in detail in Chapters 1 and 3.

In a comparative study on these osmium complexes in solution phase, the solution phase heterogeneous rate constants are measured and the results are compared to the rate constants measured for the adsorbed monolayers.

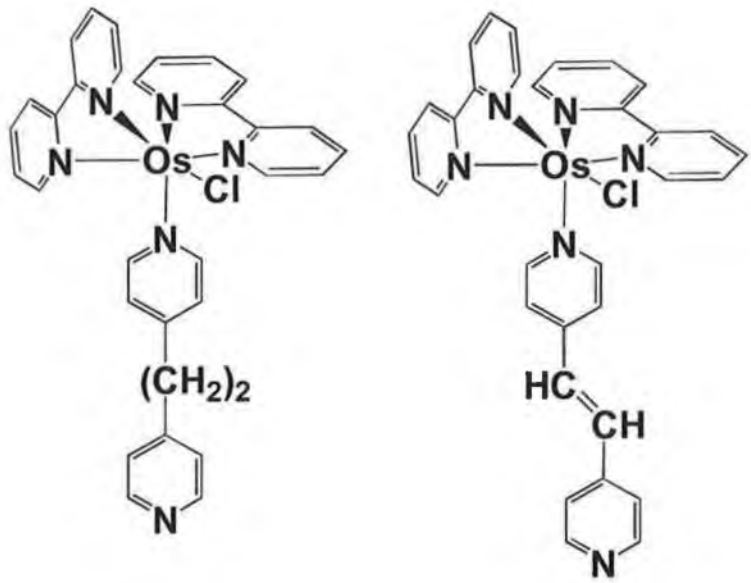

Figure 4.1. Structure of $[Os(bpy)_2Cl(p2p)]^+$, (I) $[Os(bpy)_2Cl(bpe)]^+$, (II) where bpy is 2,2′-bipyridyl, p2p is 1,2-bis(4-pyridyl)ethane and bpe is *trans*-1,2-bis(4-pyridyl)ethylene.

4.2. General Electrochemical Properties

The syntheses of the complexes, the instrumentation used and the technique for preparation of the monolayers have been described in Chapter 2.

Figure 4.2 shows a typical background corrected cyclic voltammogram for a spontaneously adsorbed monolayer of $[Os(bpy)_2Cl(bpe)]^+$ on a 25 μm radius platinum microdisk as the scan rate, υ, is systematically varied from 0.1 to 2 V s^{-1}. The formal potential for the osmium monolayer is 0.28 V which agrees closely with that found for this complex by Abruña[7,8] and with values reported for monolayers assembled from the complex $[Os(bpy)_2Cl(p2p)]^+$ where p2p is the corresponding non-conjugated bridge 1,2-bis(4-pyridyl)ethane)[5,7] ($E^{\circ\prime}$ = 0.31 V).

The limiting surface coverage of the complex at equilibrium is 7.0±0.5 x 10^{-11} mol cm^{-2} and does not increase further by increasing the concentration of the complex in solution or the deposition time. This saturation coverage is smaller than found by Acevedo and Abruña[4,7] for monolayers of the same complex, but lies within the range measured previously for related systems.[8,10,12] The full width at half-maximum, FWHM, is between 100 and 120 mV at slow scan rates (< 5 Vs^{-1}) which is slightly higher than the ideal case of 90.6 mV for a one-electron transfer. This broadening is consistent with weak repulsive interactions between the adsorbates most likely arising from their cationic character.[9,10]

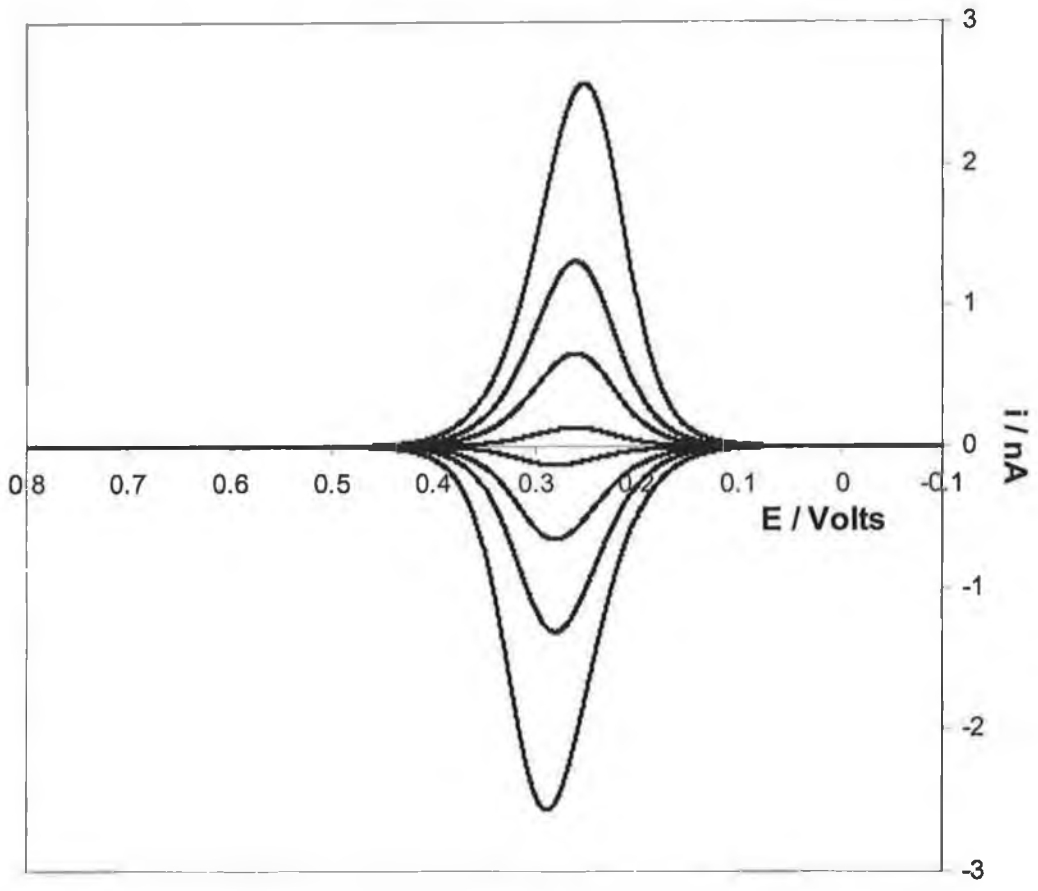

Figure 4.2. Background corrected cyclic voltammograms for a spontaneously adsorbed $[Os(bpy)_2Cl(bpe)]^+$ monolayer on a 25 μm radius platinum microdisk electrode, using a Ag/AgCl reference electrode. The supporting electrolyte is aqueous 0.1 M $LiClO_4$. The scan rate from top to bottom is 2, 1, 0.5 and 0.1 V s^{-1}. Cathodic currents are up anodic currents are down.

4.3. Electron Transfer Dynamics

As discussed in Chapter 1, Section 1.5.4, the standard heterogeneous electron transfer rate constant, k°, depends on both a frequency factor and a Franck-Condon barrier:[11,12,13]

$$k^{\circ} = A_{et} \exp(-\Delta G^{\neq} / RT) \qquad (1)$$

where A_{et} is the pre-exponential factor (κ_{el} the electronic transmission coefficient and υ_n the nuclear frequency factor) and $\Delta G^{\neq}$ is the electrochemical free energy of activation.[14]

One approach to decoupling these two contributions is to use classical temperature-resolved measurements of k° to measure the free energy of activation, $\Delta G^{\neq}$, allowing A_{et} to be determined. In this way, information about the strength of electronic coupling can be obtained.[6,15,16] A second method involves measuring electron-transfer rate constants at a single temperature over a broad range of reaction driving forces. For example, Finklea and Hanshew,[17] have assembled a model describing through-space electron tunnelling which provides a good description of electron tunnelling in monolayers of this kind.[5] This model has been described in detail in Chapter 3. In this model, the cathodic rate constant is given by integral over energy (E) of three functions: (a) the Fermi function for the metal n(E), (b) a Gaussian distribution of energy levels for acceptor states in the monolayer $D_{Ox}(E)$, and (c) a probability factor describing electron tunnelling at a given energy, P(E).

$$k_{Ox}(\eta) = A \int_{-\infty}^{\infty} D_{Ox}(\varepsilon)\ n(\varepsilon)\ P(\varepsilon)\ d\varepsilon \qquad (2)$$

The zero point of energy is defined as the Fermi level of the metal at the particular overpotential of interest. The Fermi function describes the distribution of occupied states within the metal and is defined by:

$$n(\varepsilon) = \left(\frac{1}{1 + \exp[(\varepsilon - \varepsilon_F)/kT]} \right) \tag{3}$$

where k_B is the Boltzmann constant. The density of acceptor states is derived from the Marcus theory,[18,19] and can be represented by Equation 4.

$$D_{Ox}(\varepsilon) = \exp\left[-\frac{(\varepsilon + \eta - \lambda)^2}{4k\lambda T} \right] \tag{4}$$

where λ is the reorganisation energy. The probability of direct elastic tunnelling[20,21] through a trapezoidal energy barrier of height E_B can be approximated by Equation 5:

$$P(e) = (E_B - \varepsilon + e\eta/2)\exp(-\beta d) \tag{5}$$

where E_B is the average barrier height at zero overpotential (taken here as 2.0 eV), and d is the electron transfer distance.

Chidsey,[22] Creager,[23] and Murray,[24] have modelled non-adiabatic heterogeneous electron transfer for long-chain alkane-thiol monolayers using an expression similar to Equation 2 except that the energy dependent prefactor in the tunnelling probability expression is excluded.

The current for the reaction of an immobilised redox centre following first order kinetics is:[24]

$$i_F = nFA(k_{Ox}(\eta)\,\Gamma_{Red,\eta} - k_{Red}(\eta)\,\Gamma_{Ox,\eta}) \tag{6}$$

where $\Gamma_{Red,\eta}$ and $\Gamma_{Ox,\eta}$ are the instantaneous surface coverages of the oxidised and reduced species and $k_{Ox}(\eta)$ and $k_{Red}(\eta)$ are the reaction rate constants and are given by Equation 2 with or without a tunnelling probability function. In using Equation 6 to model the voltammetric response, the electron transfer distance, d, is taken as 10 Å leaving only two freely adjustable parameters, k° and $\Delta G^{\neq}$ (=λ / 4). Both of these models have been used in a finite difference simulation to determine k° and $\Delta G^{\neq}$. To

achieve this objective, the model developed in Chapter 3 was used. This model incorporates the Nelder and Mead simplex[25] algorithm to find the values of k° and $\Delta G^{\neq}$ that minimise the sum of the square of the residuals between the theoretical and experimental currents observed in anodic branches of the linear sweep voltammograms.

Figure 4.3 shows the experimental background corrected cyclic voltammogram for a dense $[Os(bpy)_2Cl(bpe)]^+$ monolayer deposited on a 5 μm radius platinum microelectrode where the scan rate is 6000 V s^{-1}. Cell resistances and calculations of ohmic loss are given in Chapter 2. Figure 4.3 illustrates the best fits obtained from Equations 2 – 6 for models that include and exclude through-space tunnelling through a trapezoidal barrier. In both cases the residual sum of squares between theory and experiment was minimised *only* for the oxidative branch and then the best fit estimates of k° and $\Delta G^{\neq}$ obtained were used to predict the cathodic branch of the voltammogram. For both models, the optimum k° was (9.4±0.9) x 10^3 s^{-1} and $\Delta G^{\neq}$ was 11.4 ±0.8 kJ mol^{-1}.

Figure 4.3 shows that excellent agreement is observed between the experimental and theoretical anodic peak potentials and both peak currents. Moreover, there is general agreement between the theoretical and experimental currents along the full anodic branch. However, poorer agreement is observed for the cathodic branch which may arise from oxidation state dependent electronic coupling or more likely, differences in the reorganisation energy caused by changes in the monolayer's solvation as it is oxidised.[26] Figure 4.3 reveals that while the quality of the fit obtained using the two models are broadly comparable, the peak currents predicted by Finklea's through-space tunnelling model more closely match the experimental values. That these voltammograms are best-described by a through-space tunnelling model agrees with previous investigations[5] where a value of 1.6±0.2 $Å^{-1}$ was obtained for the distance dependent tunnelling parameter, β. A through-space rather than through-bond mechanism is somewhat surprising given the aromatic character of the *trans*-1,2-bis(4-pyridyl)ethylene bridge. However, it is important to note that the electron transfer distance examined here, 10 Å, is considerably shorter than that traditionally explored using alkane-thiol self-assembled monolayers, 20 - 30 Å. Quantum

mechanical spillover of the metal electron density beyond the electrode/monolayer interface, and the delocalised character of the electron density on the electrode, may be relatively more important for these short bridging ligands. Furthermore, electric field effects may influence the electron transfer dynamics because the length of the bridge and the double layer thickness are comparable.[16]

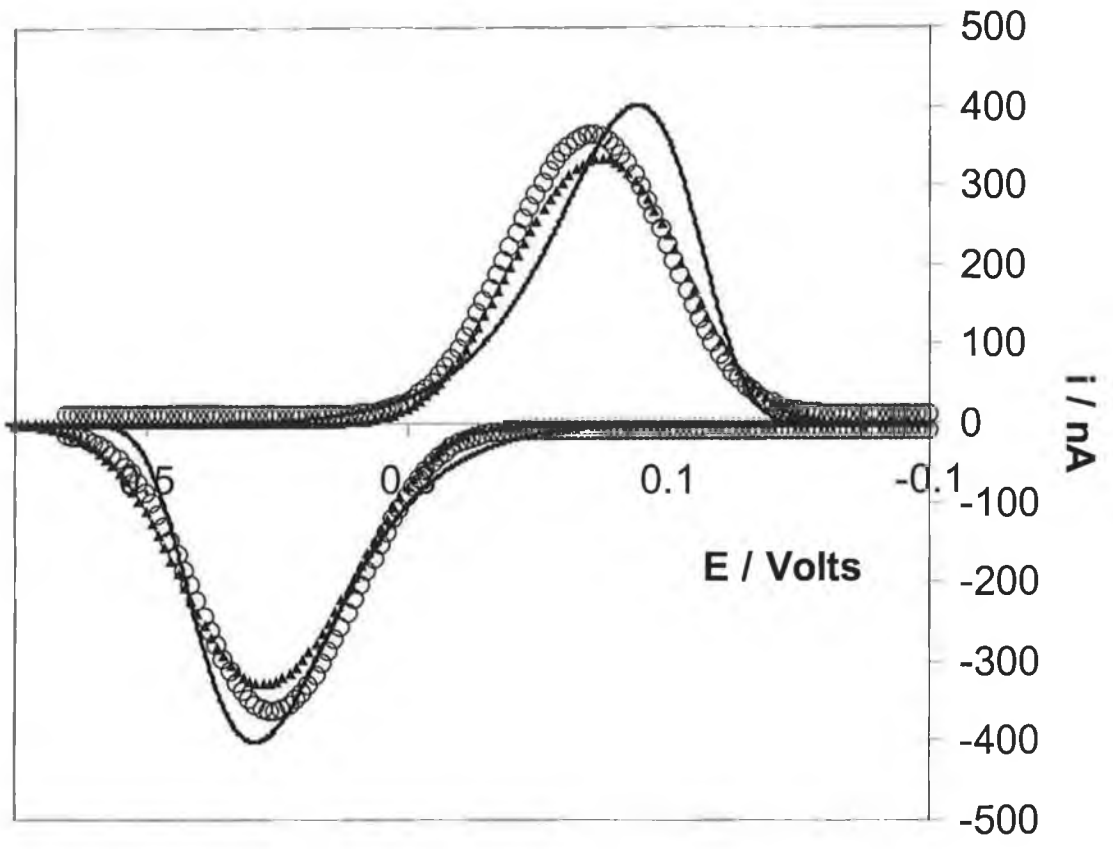

Figure 4.3. Cyclic voltammograms for a spontaneously adsorbed $[Os(bpy)_2Cl(bpe)]^+$ monolayer on a 25 μm radius platinum microdisk electrode at a scan rate of 6000 V s^{-1}. The solid line denotes experimental data, while ○ and ▲ denote the best-fit theoretical responses generated using the Finklea and Chidsey models, respectively. Both theoretical responses correspond to a k° of $9.4x10^3$ s^{-1} and a $\Delta G^{\neq}$ of 11.4 kJ mol^{-1}. The supporting electrolyte is aqueous 0.1 M $LiClO_4$.

An important test of the reliability of the standard heterogeneous electron transfer rate constants obtained by fitting the cyclic voltammograms is to investigate the scan rate dependence. In this way, an insight into the dispersion in the kinetics can be obtained. Figure 4.4 shows the fits obtained at scan rates of 1000, 3000 and 6000 V s^{-1}. In each case the same fitting parameters for the Finklea model, i.e., a k° of $9.4x10^{3}$ s^{-1} and a $\Delta G^{\neq}$ of 11.4 kJ mol^{-1}, were used. For each scan rate, there is satisfactory agreement between the theoretical model and the experimental currents of the anodic branch of the voltammogram. That the experimental responses at different timescales are accurately modelled using the same two parameters indicates that the heterogeneous electron transfer rate constants are all similar for individual adsorbates corresponding to indistinguishable microenvironments and electron transfer distances. This nearly ideal behaviour contrasts with that observed for ferrocene alkane thiol monolayers[22,23] where it is difficult to achieve satisfactory agreement between theory and experiment over the entire voltammogram due to oxidation state dependent lateral interactions.

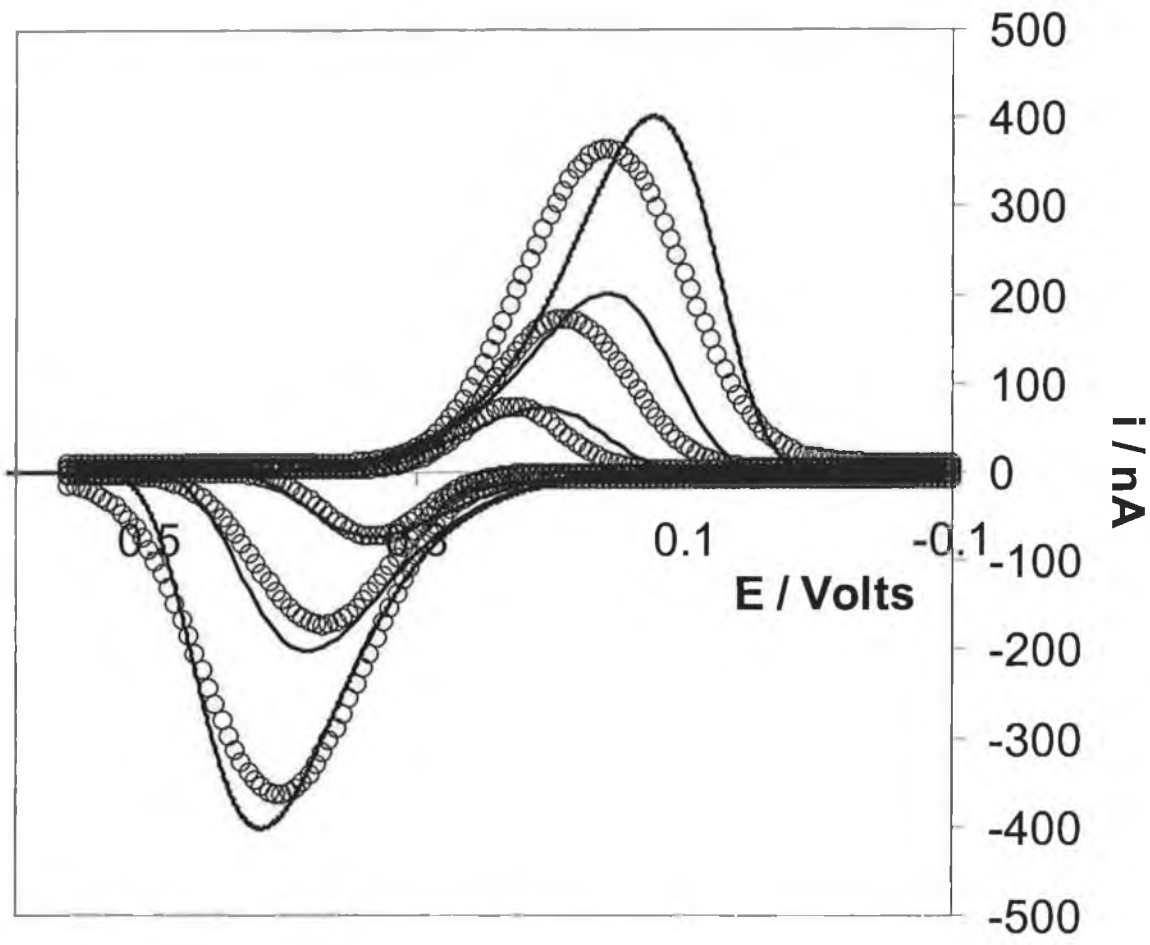

Figure 4.4. Experimental ——— and theoretical voltammograms O generated using the through-space tunnelling model due to Finklea, for a spontaneously adsorbed $[Os(bpy)_2Cl(bpe)]^+$ monolayer on a 25 μm radius platinum microdisk electrode. From top to bottom, the scan rates are 6000, 3000 and 1000 V s^{-1}. In all cases, the theoretical responses were generated using a k° of $9.4x10^3$ s^{-1} and a $\Delta G^{\neq}$ of 11.4 kJ mol^{-1}.

Given the difficulties of accurately removing background charging currents from experimental voltammograms, an alternative procedure is to probe the dependence of the anodic and cathodic peaks potentials, $E_{p,a}$ and $E_{p,c}$, on the voltammetric scan rate. Figure 4.5 illustrates the dependence of the peak-to-peak separation, ΔE_P, on the voltammetric scan rate for $8000 \geq \upsilon \geq 5$ Vs^{-1}. For scan rates up to approximately 100 Vs^{-1}, ΔE_P is insensitive to the scan rate before increasing significantly. There are two important processes that could contribute to the observed response. First, ohmic loss due to the higher current density at higher scan rate.[27] Second, slow heterogeneous electron transfer across the electrode/monolayer interface. As discussed previously, in experiments of this kind, the iR drop is kept below 8 mV by carefully selecting the radius of the microelectrode. Thus, while high quality data can be obtained from a monolayer coated 25 μm radius microdisk for $\upsilon < 100$ Vs^{-1}, for higher scan rates 1 μm radius electrodes are used.[28] Moreover, the same slope is observed in Figure 4.5 if the experiments are repeated in more conducting solutions that contain a higher concentration of supporting electrolyte. This observation also indicates that secondary processes, e.g., ohmic loss, or the dynamics of ion pairing, do not contribute significantly to the observed response. The behaviour illustrated in Figure 4.5 is consistent with the dynamics of heterogeneous electron transfer influencing the voltammetric response at high scan rates.

Figure 4.5 shows the peak potentials predicted by the models assembled by Chidsey[22] and Finklea[17] using values of k° and $\Delta G^{\neq}$ of 9.4×10^3 s^{-1} and 11.4 kJ mol^{-1}, respectively. In common with the analysis of the complete voltammograms, there is good agreement between theory and experiment for the anodic branch but somewhat poorer agreement for the cathodic data. As discussed by Creager,[23] the peak potentials are rather insensitive to the reorganisation energy allowing accurate values of k° to be obtained essentially independently of λ. Figure 4.5 also shows the predictions of the classical Butler-Volmer theory[27] which tends to overestimate the apparent heterogeneous electron transfer rate constant. While, the Butler-Volmer theory is reasonably accurate under these conditions, it is shown in Figure 4.5 that the models based on the Marcus theory fit more closely to the experimental data at higher scan rates.

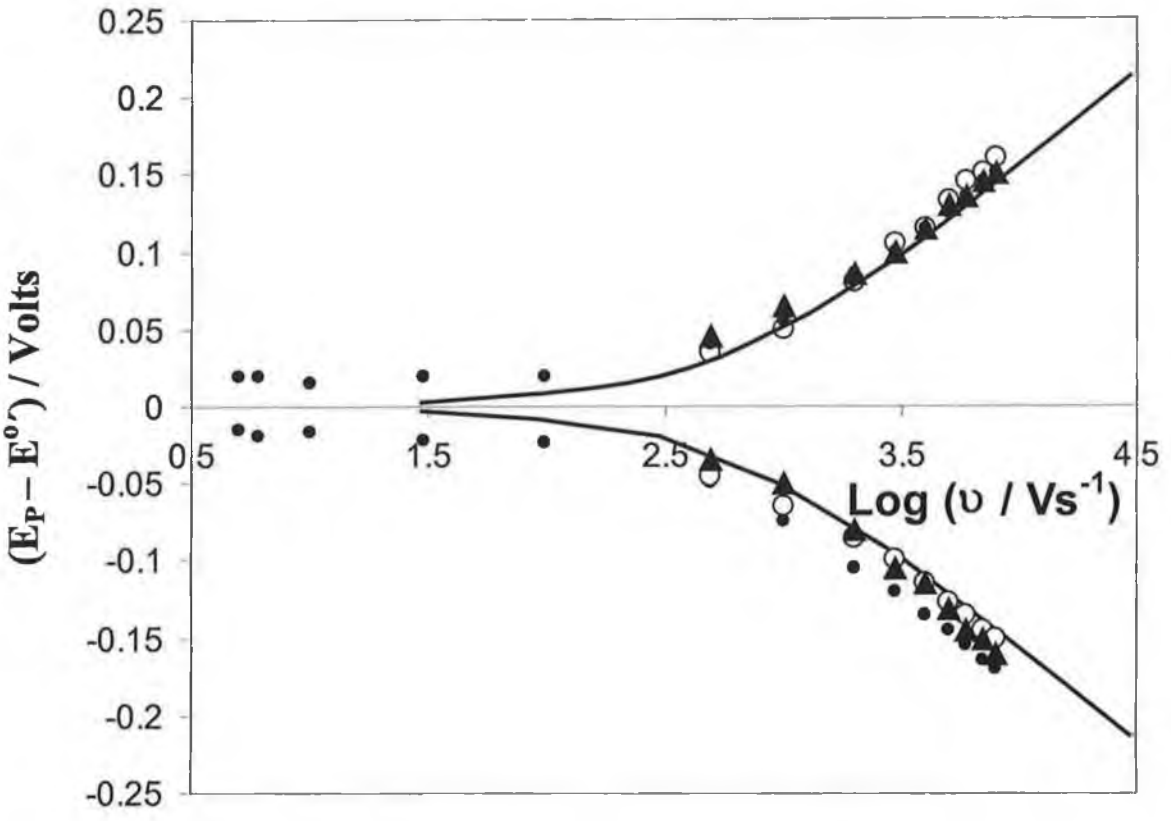

Figure 4.5. Plot of (E_p - E°′) vs. log (scan rate) for a spontaneously adsorbed monolayer of $[Os(bpy)_2Cl(bpe)]^+$. The experimental data are denoted by ● while ○ and ▲ denote best-fit theoretical responses generated using the models assembled by Finklea and Chidsey, respectively. Both theoretical responses correspond to a k° of $9.4x10^3$ s^{-1} and a $\Delta G^{\neq}$ of 11.4 kJ mol^{-1}. The solid line denotes the prediction of the Butler-Volmer theory ($\alpha = 0.5$, $k^\circ = 9.4x10^3$ s^{-1}). The supporting electrolyte is 0.1 M $NaClO_4$.

As described previously,[5,7,29] the voltammetric response of $[Os(bpy)_2Cl(p2p)]^+$ monolayers is generally similar to that presented above for the bpe bridged systems. The voltammetric response for the p2p bridged system has been modelled and values of (3.05±0.26) x 10^5 s^{-1} and 8.7±1.2 kJ mol^{-1} for k° and $\Delta G^{\neq}$, respectively, have been obtained.

The reliability of the standard heterogeneous electron transfer rate constants obtained by fitting the cyclic voltammograms is verified by investigating the scan rate dependence. Figure 4.6 shows the fits obtained at scan rates of 1000, 3000 and 6000 and 20000 V s^{-1}. In each case the same fitting parameters for the Finklea model, i.e., a k° of 3.05x10^5 s^{-1} and a $\Delta G^{\neq}$ of 8.7 kJ mol^{-1}, were used. For each scan rate, there is satisfactory agreement between the theoretical model and the experimental currents of the anodic branch of the voltammogram. The fact that Finklea's through-space tunnelling model closely match the experimental values is indicative of a through-space rather than through-bond electron transfer pathway.

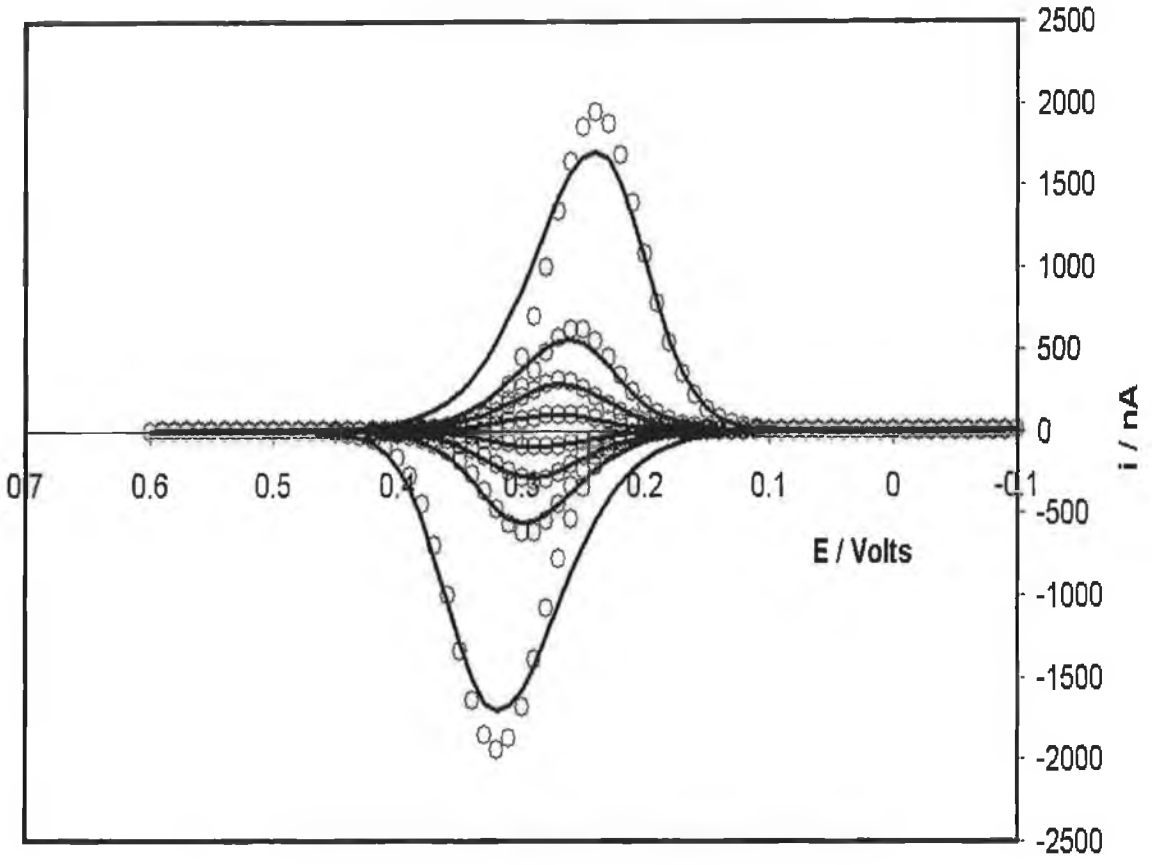

Figure 4.6. Experimental ——— and theoretical voltammograms O generated using the through-space tunnelling model due to Finklea, for a spontaneously adsorbed $[Os(bpy)_2Cl(p2p)]^+$ monolayer on a 10 μm radius platinum microdisk electrode. From top to bottom, the scan rates are 20000, 6000, 3000 and 1000 V s^{-1}. In all cases, the theoretical responses were generated using a k° of 3.05×10^5 s^{-1} and a $\Delta G^{\neq}$ of 8.7 kJ mol^{-1}.

4.4. Accuracy of the Electron Transfer Model

It is of paramount importance to compare the values obtained for k^o and $\Delta G^{\neq}$ from the CV fitting model with those obtained by an independent technique. Table 4.1 gives the values obtained from CV fitting and those independently determined using high speed chronoamperometry.[30]

As is clear from Table 4.1, the values for k^o and $\Delta G^{\neq}$ extracted from the experimental cyclic voltammograms by the electron transfer model are identical to those measured by chronoamperometry to within experimental error. This result is of fundamental importance to the usefulness of the electron transfer model. It suggests that the model can extract accurate values for both k^o and $\Delta G^{\neq}$ from experimental cyclic voltammograms. This issue of the accuracy of the model will be revisited in Chapter 5 where a different but related system will be experimentally examined.

Table 4.1. Rate constants, free energies of activation and pre-exponential factors for the $Os^{2+/3+}$ redox reaction occurring within $[Os(bpy)_2Cl(L)]^+$ monolayers where L is trans-1,2-bis(4-pyridyl)ethylene (bpe) or 1,2-bis(4-pyridyl) ethane (p2p)[a] determined using cyclic voltammetry (i.e., CV) and chronoamperometry (i.e., CA).

	CV		**CA**		
Bridging Ligand	**10^{-3} k° / s-1**	**$\Delta G^{\neq}$ / kJ mol^{-1}**	**10^{-3} k° / s-1**	**$\Delta G^{\neq}$ / kJ mol^{-1}**	**10^{-6} A_{et} / s^{-1}**
Bpe	9.4±0.9	11.4±0.8	8.6±0.3	12.6±1.1	0.9(0.3)
p2p	305±26	8.7±1.2	287±22	9.8±0.8	11.1(0.5)

[a] Supporting electrolyte is 0.1 M aqueous $LiClO_4$.

Table 4.1 indicates that despite the bpe bridge being conjugated, the heterogeneous electron transfer rate constant is approximately a factor of thirty smaller than that found for the aliphatic bridge, 1,2-bis(4-pyridyl)ethane. However, as discussed above, in trying to elucidate the effect of changes in bridge structure, e.g., conjugation, it is important to determine the pre-exponential factors since these are sensitive to the degree of electronic coupling across the bridge. While both the $\Delta G^{\neq}$ values agree with that predicted by the Marcus relation for outer sphere reorganisation[31] to within 20%, $\Delta G^{\neq}$ is smaller for the p2p system. This difference in the free energy of activation most likely corresponds to a different monolayer structure in the two circumstances and would correspond to more nonpolar environment within the p2p bridged monolayer. This could be explained by a reduction in the static dielectric constant at the electrode / monolayer interface. This issue will be discussed in more detail in Chapter 6.

The values of k° and $\Delta G^{\neq}$ in conjunction with Equation 1 have been used to estimate pre-exponential factors for both the bpe and p2p bridged monolayers. The data are given in Table 4.1. These data reveal that the prefactors are approximately 6 orders of magnitude smaller than the value of unity, expected for an adiabatic electron transfer, i.e., one involving strong coupling between the localised redox states of the monolayer and delocalised metallic states of the electrode. As has already been stated in Section 4.3, the pre-exponential factor is equal to the product of κ_{el} the electronic transmission coefficient and υ_n the nuclear frequency factor. κ_{el} the electronic transmission coefficient, is a measure of the electronic coupling, and ranges in values from much less than 1 (i.e., non-adiabatic or weakly coupled) to values close to or equal to 1 (i.e., adiabatic or strongly coupled). Therefore, when two systems have similar values for υ_n the nuclear frequency factor, the difference in the pre-exponential factors indicates a difference in κ_{el} and therefore determines the relative levels of electronic coupling. So, the most significant result contained in Table 4.1 is that the pre-exponential factor is approximately an order of magnitude higher for the p2p than the bpe bridge indicating that the redox centre and electrode are more strongly coupled for the aliphatic system.

This result is consistent with the through-space tunnelling mechanism already proposed for both the bpe and p2p bridged systems in that the less rigid p2p bridge probably has sufficient flexibility to reduce the electron transfer distance below the value of 10 Å expected on the basis of a rigid-rod model. It is important to note that unlike a through-space pathway, the electron transfer distance for through-bond tunnelling mechanisms is independent of the monolayer's conformation. Therefore, the decrease in heterogeneous electron transfer rate constant observed here on going from a non-conjugated to a conjugated bridge, is not expected for a through-bond tunnelling mechanism.

4.5. Measurement of Standard Rate Constants of Complexes in Solution

Having measured the diffusion coefficients for the $[Os(bpy)_2Cl(p2p)]^+$, $[Os(bpy)_2Cl(bpe)]^+$ and $[Ru(bpy)_2Cl(4\text{-}tet)]^+$ and reported them to be (1.62±0.02) x 10^{-7} cm^2 s^{-1}, (1.38±0.01) x 10^{-6} cm^2 s^{-1} and (3.9±0.2) x 10^{-5} cm^2 s^{-1}, respectively, in Chapter 2, it is now possible to proceed to measure their standard rate constants in solution. These results will be useful for comparison with measurements of the heterogeneous rate constants of adsorbed monolayers of the osmium complexes that have just been discussed.

To estimate k_{Soln}^{o} for these species in solution, cyclic voltammograms where the redox process is under kinetic rather than diffusion control are used. The criteria for a process exclusively under diffusion control have been described in detail in Chapter 2. For the kinetic study, the cyclic voltammograms at lower scan rates that correspond to diffusion control are ignored and those at the highest scan rates for which ohmic drop is still negligible are selected. These cyclic voltammograms at higher scan rates correspond to the process under kinetic control and the peak to peak separation, i.e., the difference between the anodic peak potential and the cathodic peak potential, ΔE_p, can be used to determine the rate constant. For a totally reversible compound, the difference in the potentials between the anodic peak current and the cathodic peak current (ΔE_p) is 59 mV for an electron transfer involving one electron. When the electron transfer reaction is quasi-reversible, the rate of electron

transfer is too slow to keep the redox couple in equilibrium as the potential is changed. Thus, ΔE_p increases with the scan rate.

This increase in the peak to peak separation, ΔE_p with increasing scan rate may be used to determine the standard electron transfer rate constant following the method described by Nicholson.[32] Working curves which relate ΔE_p to a kinetic parameter (ψ) have been published[33] and are illustrated in Figures 4.7 and 4.8. Figure 4.7 gives the complete set of data for the kinetic parameter (ψ). Figure 4.8 represents a section of the data selected on the basis of the experimental range of ΔE_p found in this solution phase study. In order to select accurate values for the kinetic parameter (ψ), a sixth order polynomial has been fitted to the section of the curve shown in Figure 4.8.

The rate constant for a reduction is given by the following equation:

$$k^o = \psi\left[D_0 \pi \nu \left(\frac{nF}{RT}\right)\right]^{1/2}\left(\frac{D_R}{D_o}\right)^{\alpha/2} \qquad (7)$$

where ψ is the kinetic parameter, D_0 is the diffusion coefficient, ν is the scan rate, n is the number of electrons, F is the Faraday constant, R is the gas constant, T is the temperature, D_R is the diffusion coefficient for the reduced species, D_o is the diffusion coefficient for the oxidised species and α is the transfer coefficient. For these experimental systems the ratio of the diffusion coefficients is equal to 1.

Using Equation 7 and Figure 4.8, the rate constants for $[Os(bpy)_2Cl(p2p)]^+$, $[Os(bpy)_2Cl(bpe)]^+$, and $[Ru(bpy)_2Cl(4\text{-}tet)]^+$ can be calculated using the diffusion coefficients measured as described in Chapter 2. By taking the ΔE_p for a number of different scan rates where the process is under kinetic rather than diffusional control and averaging the results, the k_{Soln}^o for the complexes have been estimated.

For comparison with the rate constants measured for the adsorbed monolayers, the standard rate constant (i.e., k_{Soln}^o cm s^{-1}) has been converted to a first order heterogeneous electron transfer rate constant (k_{Soln}^o s^{-1}). This is achieved, by

assuming a fixed distance of closest approach of the complex to the electrode. In this case, the assumption is made that most of the molecules concerned in this study would have a distance of closest approach to the electrode of 10 Å. Of course, the molecules are in solution and therefore can approach the electrode in any orientation. Therefore, the distance of 10 Å is just an estimate used to facilitate the comparison to the rate constants measured for the adsorbed species.

So to convert from cm s^{-1} to s^{-1}, a factor of 10 Å or 1 x 10^{-7} cm is used to divide by.

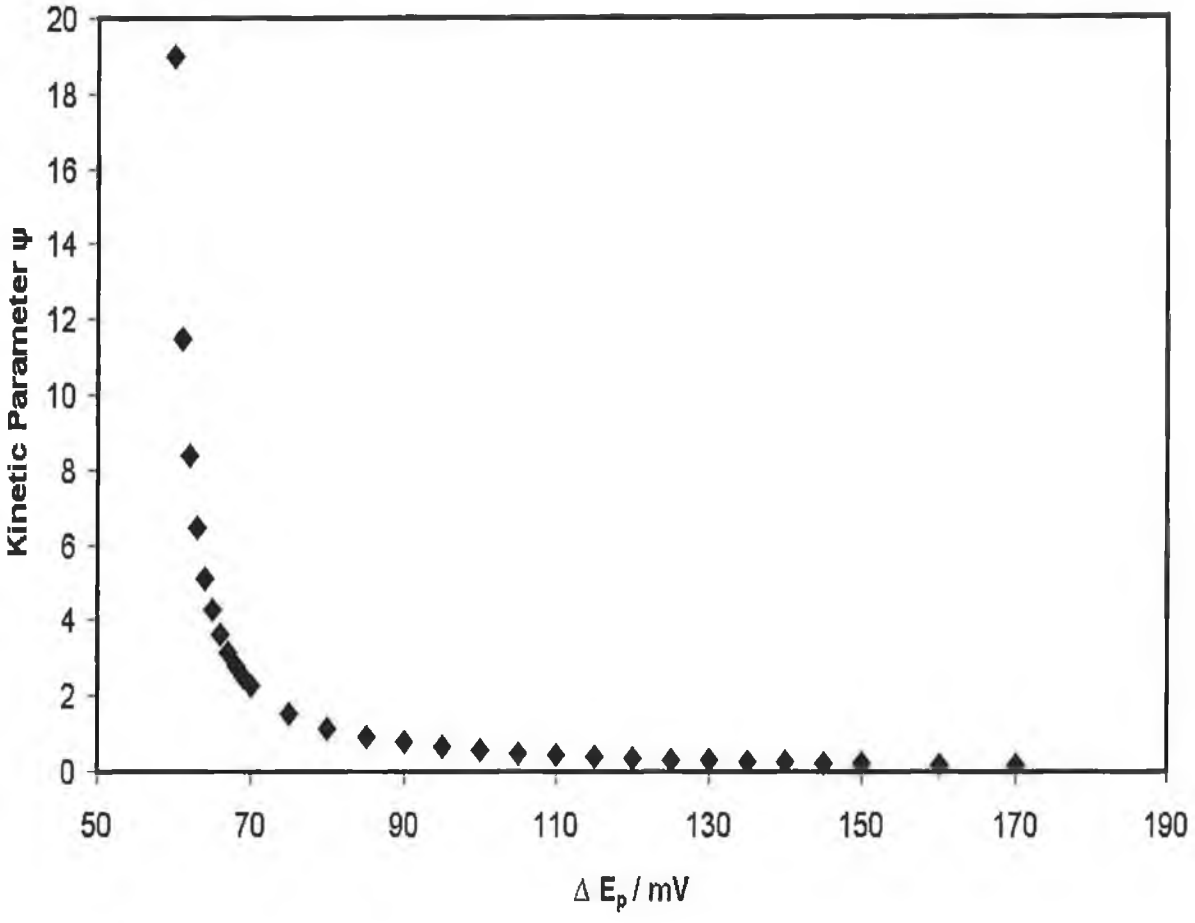

Figure 4.7. Plot of the kinetic parameter, ψ (♦), against the difference in the potentials between the anodic peak current and the cathodic peak current (ΔE_p). over the full range.[32]

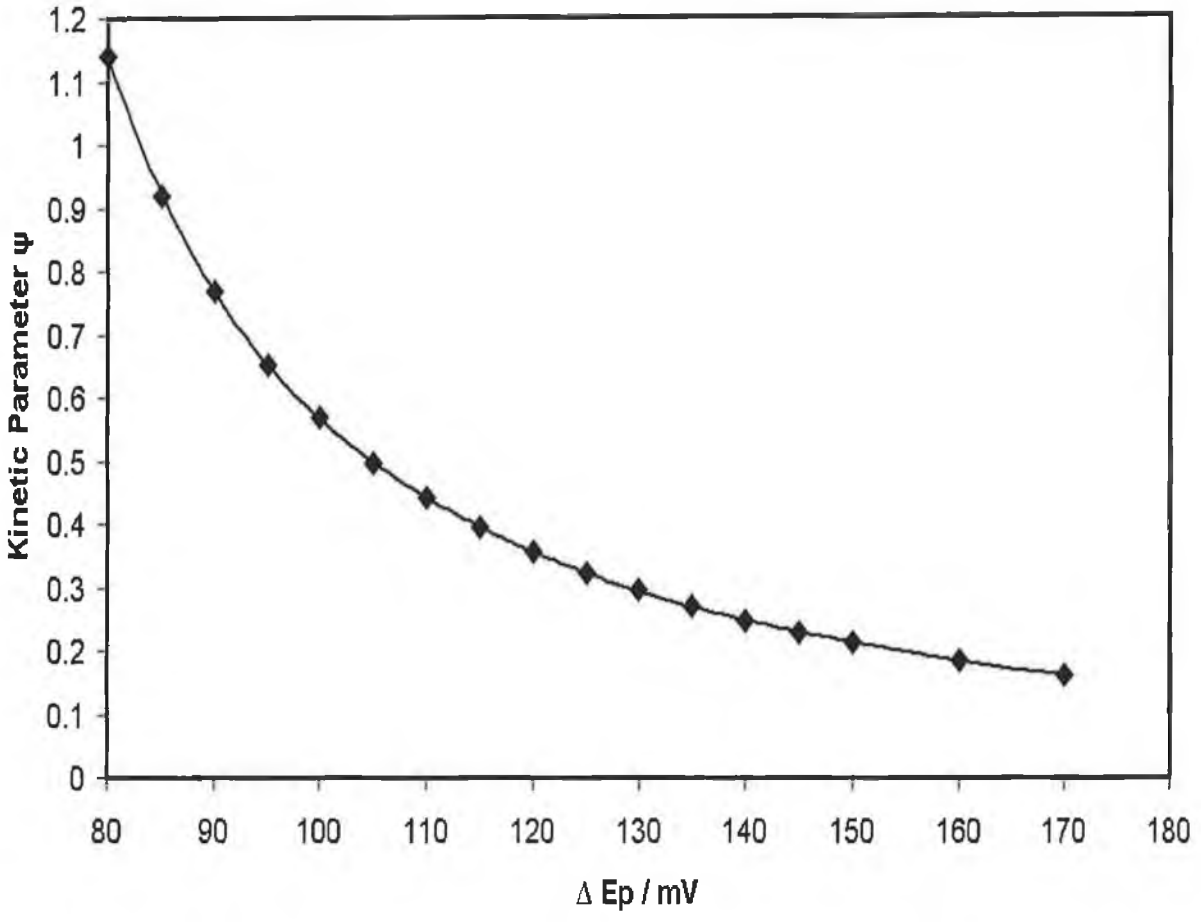

Figure 4.8. Plot of the kinetic parameter, ψ, (♦), against the difference in the potentials between the anodic peak current and the cathodic peak current (ΔE_p) over a reduced range. This reduced range is selected to correspond to the range of ΔE_p found in the experimental systems under study here. The solid line is the best fit based on a sixth order polynomial.[32]

Table 4.2. The standard rate constants and first order heterogeneous rate constants for $[Os(bpy)_2Cl(p2p)]^+$, $[Os(bpy)_2Cl(bpe)]^+$, $[Ru(bpy)_2Cl(4\text{-}tet)]^+$, bpy is 2,2′-bipyridyl, p2p is 1,2-bis(4-pyridyl)ethane, bpe is *trans*-1,2-bis(4-pyridyl)ethylene, 4-tet is 3,6-bis(4-pyridyl)-1,2,4,5-tetrazine. These measurements were carried out with the complexes in solution.

Complex	**$10^3\ k_{Soln}^{o}$ cm s^{-1}**	**$10^{-4}\ k_{Soln}^{o}$ s^{-1}**
$[Os(bpy)_2Cl(p2p)]^+$	2.4(0.2)	2.4(0.2)[a]
$[Os(bpy)_2Cl(bpe)]^+$	10.2(2.0)	10.2(2.0)[b]
$[Ru(bpy)_2Cl(4\text{-}tet)]^+$	43.7(1.2)	43.7(1.2)

[a] The corresponding rate constant for the adsorbed monolayer is (30.5±2.6) x 10^4 s^{-1}.

[b] The corresponding rate constant for the adsorbed monolayer is (0.94±0.09) x 10^4 s^{-1}.

4.5.1. Comparison of Standard Rate Constants

Table 4.2, above gives the results for the standard rate constants and first order heterogeneous rate constants for $[Os(bpy)_2Cl(p2p)]^+$, $[Os(bpy)_2Cl(bpe)]^+$, and $[Ru(bpy)_2Cl(4\text{-}tet)]^+$.

The rate constants have the same order as that of the measured diffusion coefficients in Table 2.3, with the complex with the aliphatic bridge having the lowest while the complex with the six membered aromatic ring in the bridge has the highest. As for the diffusion coefficients, this data does not allow complete elucidation of the factors determining the rate constants. The fact that the propensity for ion-pairing may be significantly different for these complexes must not be ignored and this may explain the observed differences in rate constants.

Comparing the rate constants of the osmium complexes measured in solution phase to those of the same complexes when adsorbed gives us the following. The complex with the p2p bridging ligand has a significantly larger rate constant when adsorbed to the surface of a microelectrode. This may be explained by the flexibility of the p2p bridge allowing the redox centre to get closer to the electrode and therefore reducing the electron transfer distance and increasing the rate of electron transfer. The "solvent drag " described earlier will not be a factor in the case of adsorption. The fact that the osmium complex containing the bridging ligand with the double bond has a smaller rate constant when adsorbed supports this view as the double bond will not allow the same type of flexibility. Therefore, when adsorbed, the complex with the bpe ligand will most likely have the length of the bridging ligand (i.e., 10 Å) as the distance of closest approach, whereas in solution, the average distance of closest approach is likely to be smaller than 10 Å.

4.6. Conclusions

Monolayers of $[Os(bpy)_2Cl(bpe)]^+$ have been formed and their electrochemical properties investigated. Using the new model, the voltammetric response observed at high scan rates has been studied where heterogeneous electron transfer across the metal/monolayer interface influences the experimental response. Somewhat surprisingly, despite the conjugated bridge and short electron transfer distance, for the $[Os(bpy)_2$ bpe $Cl]^+$ the voltammetric response is best modelled as a through-space tunnelling process.

The determination of the heterogeneous rate constant, k^o and $\Delta G^{\neq}$ from cyclic voltammograms has been easily achieved by the use of the electron transfer model described in Chapter 3. The values extracted by the have been shown to be identical to those determined by chronoamperometry. This model has been shown to be an important diagnostic tool for use in adsorption studies.

The standard heterogeneous electron transfer rate constant, $k°$, for the conjugated bridge is $9.4x10^3$ s^{-1} which is approximately a factor of 30 *smaller* than that observed for a longer, aliphatic bridge, 1,2-bis(4-pyridinyl)ethane. Modelling the complete voltammogram allows the contributions from electronic coupling and free energy of activation to be decoupled. This analysis reveals free energies of activation of 8.7 ± 1.2 and 11.4 ± 0.8 kJ mol^{-1} for the bpe and p2p bridges, respectively. That the voltammetric response is best described using a through-space tunnelling model, and both the standard heterogeneous electron transfer rate constants and pre-exponential factors are larger for the non-conjugated ligand, suggest that heterogeneous electron transfer proceeds via a through-space tunnelling mechanism.

Rate constants for osmium and ruthenium complexes in solution have been measured. The ruthenium complex has the highest rate constant. In the case of the osmium complexes, comparisons have been drawn between the rates of electron transfer in adsorbed monolayers and those of the same complexes in solution. It has been found that while the complex containing the longer aliphatic bridge, 1,2-bis(4-pyridinyl)ethane has a higher rate constant than the complex with the conjugated

bridge in the adsorbed monolayers, the opposite is true in studies of the complexes in solution. Possible explanations for these findings have been given.

The electrochemical properties of the $[Os(bpy)_2Cl(bpe)]^+$ and $[Os(bpy)_2Cl(p2p)]^+$ complexes in solution will be returned to again in Chapter 5 when the effect of the electrode material on their voltammetric response will be explored.

4.6. References

1 Ishida, T.; Mizutani, W.; Akiba, U.; Umemura, K.; Inoue, A.; Choi, N.; Fujihira, M.; Tokumoto, H.; *J. Phys. Chem. B* **1999**, *103*, 1686.

2 Weber, K. S; Creager, S. E. *J. Electroanal. Chem.* **1998**, *458*, 17.

3 Figgemeier, E; Zimmermann Y.; Houscroft, C. E.; Constable, E. C. *to be published*

4 Acevedo, D.; Abruña H. D. *J. Phys. Chem.* **1991**, *95*, 9590.

5 Forster, R. J.; Faulkner, L. R. *J. Am. Chem. Soc.* **1994**, *116*, 5444.

6 Forster, R. J.; Faulkner, L. R. *J. Am. Chem. Soc.* **1994**, *116*, 5453.

7 Acevedo, D.; Bretz, R.L.; Tirado, J. D.; Abruña H. D. *Langmuir* **1994**, *10*, 1300.

8 Acevedo, D.; Bretz, R.L.; Tirado, J. D.; Abruña H. D. *Langmuir* **1994**, *10*, 1971.

9 Brown, A. P.; Anson, F. C. *Anal. Chem.* **1977**, *49*, 1589.

10 Laviron, E. *J. Electroanal. Chem.* **1974**, *52*, 395.

11 Bagchi, G. *Ann. Rev. Chem.* **1989**, *40*, 115.

12 Sutin, N. *Acc. Chem. Res.* **1982**, *15*, 275.

13 Barr, S. W.; Guyer, K. L.; Li, T. T.-T.; Liu, H. Y.; Weaver, M. J. *J. Electrochem. Soc.* **1984**, *131*, 1626.

14 Sutin, N. Brunschwig, B. S. *ACS Symp. Ser.* **1982**, *198*, 105.

15 Forster, R. J.; Vos, J. G. and Keyes, T. E. *The Analyst.*, **1998**, *123*, 1905.

16 Forster, R. J.; O'Kelly, J. P. *J. Phys. Chem.* **1996**, *100*, 3695.

17 Finklea, H. O.; Hanshew, D. D. *J. Am. Chem. Soc.* **1992**, *114*, 3173.

18 Marcus, R. A. *J. Chem. Phys.* **1956**, 24, 966.

19 Marcus, R. A. *J. Phys. Chem.* **1963**, *67*, 853.

20 Schmickler, W. *J. Electroanal. Chem.* **1977**, *82*, 65.

21 Bockris, J. O'M.; Khan, S. U. M. *Quantum Electrochemistry,* Plenum Press, New York, 1979, Chap. 8

22 Chidsey, C. E. D. *Science* **1991**, *251*, 919.

23 Weber, K.; Creager, S. E. *Anal. Chem.* **1994**, *66*, 3164.

24 Tender, L.; Carter, M. T.; Murray, R. W. *Anal. Chem.* **1994**, *66*, 3173.

25 Ebert, K.; Ederer, H.; Isenhour, T. L *Computer Applications in Chemistry: An Introduction for PC Users;* VCH Publishers: New York, 1989.

26 Hupp, J. T.; Weaver, M. J. *J. Phys. Chem.* **1984**, *88*, 6128.

27 Bard, A. J.; Faulkner, L. R. *Electrochemical Methods, Fundamentals and Applications*, John Wiley & Sons; New York, 1980.

28 Forster, R. J. *Phys. Chem. Chem. Phys.* **1999**, *1*, 1543.

29 Forster, R. J.; Faulkner, L. R. *Anal. Chem.* **1995**, *67*, 1232

30 Forster, R. J. *Private communication*, **July 2001**

31 Weaver, M. J. *Chem. Rev.* **1992**, *92*, 463.

32 Nicholson, R. S., *Anal. Chem.*, **1965**, *37*, 1351.

33 Heinze, J, *Ber. Bunsenges. Phys. Chem.*, **1981**, *85*, 1096

CHAPTER 5

Effect of Electrode Density of States on the Heterogeneous Electron Transfer Dynamics of Osmium Containing Monolayers

5.1. Introduction

As has been stated already, redox active monolayers promise to provide the detailed understanding of electron transfer across interfaces and across molecular species necessary for the rational design of ultra small scale electronic devices using molecular and solid-state components. While attention has been focused on the role that distance, structure and the redox composition of the monolayer play in dictating the rate and mechanism of electron transfer,[1] the effect of changing the nature of the electrode material has not been probed with the same intensity. This is, in part, due to a major deficiency in the cyclic voltammetric area. This deficiency is that while cyclic voltammetric experiments are relatively easy to carry out on redox active monolayers, the extraction of accurate kinetic and thermodynamic parameters can be quite difficult. However, this thesis directly addresses this problem through the newly constructed electron transfer model described in detail in Chapter 3.

That the nature of the electrode material has not attracted great attention is surprising given that long-held theory predicts that for non-adiabatic electron transfer involving weakly coupled reactants that the heterogeneous electron transfer rates should be directly proportional to the density of states, ρ_F, in the electrode.[2] However, a recent theoretical model developed by Marcus and Gosavi[3] predicts that the coupling strength between the redox centre and states within the electrode will make the electron transfer rate less sensitive to ρ_F. Some attempts have been made to test the effect of the changing the electrode material on the electron transfer dynamics. For example, Parsons and co-workers[4] probed the effect of using platinum, palladium, iridium, rhodium, gold and mercury electrodes on the heterogeneous electron transfer dynamics of benzoquinone. They found that the standard rate constants obtained on the six metals varied by a factor less than two leading to the conclusion that the rate is independent of the nature of the electrode. Moreover, Iwasita and co-workers[5] investigated the $[Ru(NH_3)_6]^{2+/3+}$ couple at several electrodes where the density of states differs by approximately an order of magnitude, but they found that the exchange current density was independent of the electrode material. These investigations involving solution phase reactants are likely to be compromised by double layer effects, adsorption and reaction adiabaticity.

Adsorbed monolayers represent an alternative approach to investigating this issue and are attractive in that diffusive mass transport is eliminated, double layer effects may be less pronounced and the reaction can be rendered non-adiabatic simply by controlling the electron transfer distance and the composition of the bridging ligand. Li, Liu, and Weaver[6] probed the reduction kinetics of adsorbed [$Co^{III}(NH_3)_5$ thiophenecarboxylate] complexes on mercury, gold and copper electrodes. The heterogeneous electron transfer rate constants, k°, were found to be in the order Hg $\gtrsim$ Au > Cu. However, the rate constants for gold and copper depended on the surface coverage and the effect of bridge conjugation on the adiabaticity of the reaction complicate a detailed interpretation of their results. Moreover, these studies have not considered the possibility that the free energy of activation may depend on the electrode material.

In this chapter, spontaneously adsorbed monolayers of $[Os(OMe\text{-}bpy)_2Cl(p3p)]^{1+}$ (Figure 5.1) formed on carbon-fibre, mercury, platinum gold, copper and silver microelectrodes are discussed. OMe is 4,4′-dimethoxy-2,2′-bipyridyl and p3p is 1,4-trimethylene dipyridine. This complex has a low redox potential making it possible to probe the electrochemical properties even on rather electropositive metals. The voltammetric response is unusually ideal across a wide range of experimental timescales, temperatures and electrolyte solutions making it an attractive model system for probing density of states issues. Of particular interest is probing how the different orbitals of these metals that contribute to the overall density of states influence the electron transfer dynamics. For example, the *s* electrons dominate ρ_F for metals such as gold and silver while the higher density of states for platinum arises predominantly because its *d* orbitals lie near the Fermi level. The Marcus-Gosavi[3] model predicts that the efficiency with which these different orbitals couple with the localised molecular states of the adsorbate may vary significantly. To address these issues, detailed measurements of the potential dependence of k^o have been performed. These results confirm that the electron transfer is non-adiabatic and that the free energy of activation is dictated by outer sphere reorganisation of solvent dipoles. These results will impact areas as diverse as corrosion, sensor development and heterogeneous catalysis.

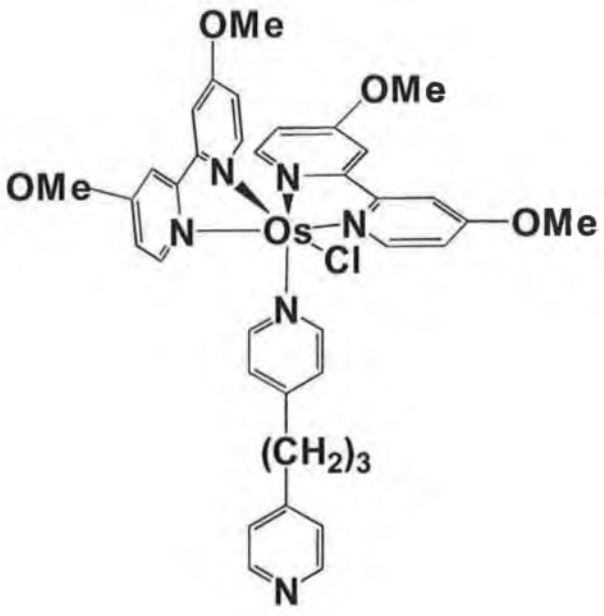

Figure 5.1. Structure of $[Os(OMe\text{-}bpy)_2Cl(p3p)]^+$, where bpy is 2,2′-bipyridyl, OMe is 4,4′-dimethoxy-2,2′-bipyridyl and p3p is 1,4-trimethylene dipyridine.

5.2. General Electrochemical Properties

Figure 5.2 shows representative cyclic voltammograms obtained at 5 V s^{-1} for $[Os(OMe\text{-}bpy)_2Cl(p3p)]^+$ monolayers spontaneously adsorbed on carbon, gold, mercury and platinum microelectrodes, where the supporting electrolyte is aqueous 1.0 M $NaClO_4$. The instrumentation used is described in Chapter 2. The formal potentials, E°′, are 0.048, 0.030, 0.120 and 0.060 V for gold, platinum, mercury and carbon electrodes, respectively. In contrast, the E°′ observed for the complex dissolved in acetonitrile is 0.010±0.008 V irrespective of the electrode material used. That E°′ shifts in a positive potential direction indicates that it is more difficult to oxidise the Os^{2+} redox centre when it is adsorbed. Moreover, the differences observed in E°′ suggest that the electron density on the metal centre depends on the identity of the electrode material. These differences reflect changes in the free energy of adsorption on the different materials which increase by up to 8.6 kJ mol^{-1} on going from gold to mercury.

Under these slow scan rate conditions, the voltammetric response is consistent in all respects with that expected for an electrochemically reversible reaction involving a surface-confined species.[7] For example, the peak shapes are independent of scan rate, υ, at least over the range 1 to 5 V s^{-1}, and the peak height scales linearly with the scan rate unlike the $\upsilon^{1/2}$ dependence observed for the complex dissolved in DMF and which have been demonstrated for the series of osmium and ruthenium complexes in solution in Chapter 2. As the potential is scanned, the reduced (R) and oxidised (O) forms of the redox couple coexist near E°′. Where there are no lateral interactions between surface confined redox centres, or where the interactions between O and O, R and R, and O and R are large but similar to one another, a FWHM of 90.6 mV is expected for a reaction involving the transfer of a single electron.[8] Therefore, while the overall electrochemical response of these monolayers is close to ideal, voltammetric data of this type do not provide a meaningful insight into the extent of lateral interactions in these monolayers.

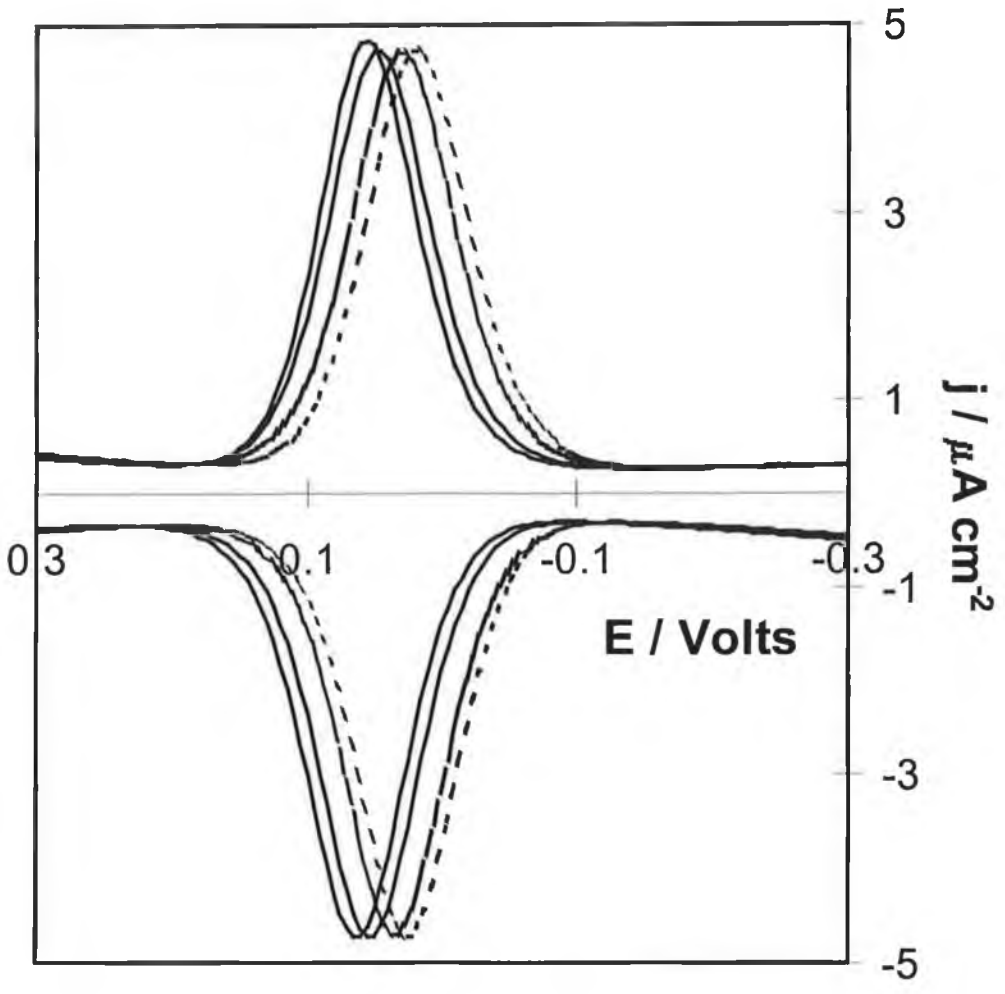

Figure 5.2. Cyclic voltammograms for the $Os^{2+/3+}$ redox reaction within spontaneously adsorbed $[Os(OMe\text{-}bpy)_2\ p3p\ Cl]^+$ monolayers, using a Ag/AgCl reference electrode. From left to right the electrode material is carbon, gold, platinum and mercury. The scan rate is 50 V s^{-1} and the surface coverage is (1.0±0.1) x 10^{-10} mol cm^{-2}. The supporting electrolyte is aqueous 1.0 M $NaClO_4$.

Irrespective of the identity of the electrode material, the surface coverage, Γ, of the redox centres as determined by integrating the Faradaic charge under the $Os^{2+/3+}$ wave is $(1.0\pm0.1) \times 10^{-10}$ mol cm^{-2}, corresponding to an area occupied per molecule of (168 ± 17) $Å^2$. The surface coverage does not increase further if the concentration of the surface active complex in solution or the deposition time are increased. This limiting surface is typical of that observed by Forster and co-workers[9,10] and others for related systems.[11,12] That Γ is independent of the electrode material indicates that the packing density is controlled by the size of the adsorbate and perhaps lateral interactions rather than by the inter-atomic spacing of the metal or carbon lattice.

5.3. Electron Transfer Dynamics.

Figure 5.3 illustrates the high speed voltammetric behaviour observed for monolayers immobilised on carbon and platinum microelectrodes. The peak-to-peak separations, ΔE_P, are significantly larger than those observed at long experimental timescales. Uncompensated cell resistance and slow heterogeneous electron transfer could contribute to the observed behaviour. Where the working electrode is a 5 μm radius microelectrode, the uncompensated resistance as measured using potential step chronoamperometry is 8125 ± 275 Ω irrespective of whether the electrode is carbon or platinum. Taken in conjunction with the peak maximum peak current observed for the platinum microelectrode, 885 nA, this cell resistance leads to an iR drop of approximately 5 mV. This ohmic loss is negligible compared to the peak-to-peak separations of 275 and 60 mV observed for $[Os(OMe\text{-}bpy)_2Cl(p3p)]^+$ monolayers adsorbed on a carbon fibre and platinum microelectrodes, respectively. Therefore, it appears that heterogeneous electron transfer influences the voltammetric response at these high scan rates. Moreover, that ΔE_P is very much larger for monolayers on carbon than on platinum, indicates that the standard heterogeneous electron transfer rate constant, k°, depends on the identity of electrode material.

As discussed elsewhere, k° depends on both a frequency factor and a Franck-Condon barrier.[13,14,15] The electron transfer theory has been described in Chapter 1 and the model developed on this theory has been discussed in Chapter 3. As has been stated in Chapter 3, to fit the experimental voltammograms, the Nelder and Mead simplex[16] algorithm has been used to find the values of k° and $\Delta G^{\neq}$ that minimise the sum

square residuals between the theoretical and experimental currents observed in anodic branches of the linear sweep voltammograms. Figure 5.3 shows the fits obtained for $[Os(OMe\text{-}bpy)_2Cl(p3p)]^+$ monolayers immobilised on both platinum and carbon fibre microelectrodes. In both cases satisfactory agreement is observed between theory and experiment for the platinum and carbon electrodes indicating that the electron transfer can be satisfactorily described as a non-adiabatic process. The optimised values for k° are $6x10^4$ and $4x10^3$ s^{-1} for platinum and carbon electrodes, respectively. The fit shown in Figure 5.3 is for a common $\Delta G^{\neq}$ of 6.8 kJ mol^{-1}. This analysis suggests that the free energy of activation is independent of the identity of the electrode material and that k° is larger for the platinum electrode because of a larger pre-exponential factor. However, the quality of the fit shown in Figure 5.3 is not particularly sensitive to $\Delta G^{\neq}$, e.g., increasing $\Delta G^{\neq}_{Pt}$ by 25 % increases the residual sum of squares between the predicted and experimental peak currents by less than 10%. Therefore, while fitting of the cyclic voltammograms can provide a convenient approach for the determination of k°, for this system it appears to provide only an approximate value for $\Delta G^{\neq}$. In contrast, temperature resolved chronoamperometry can be used to accurately probe both the potential dependence of the heterogeneous electron transfer rate and the free energy of activation.[17,18]

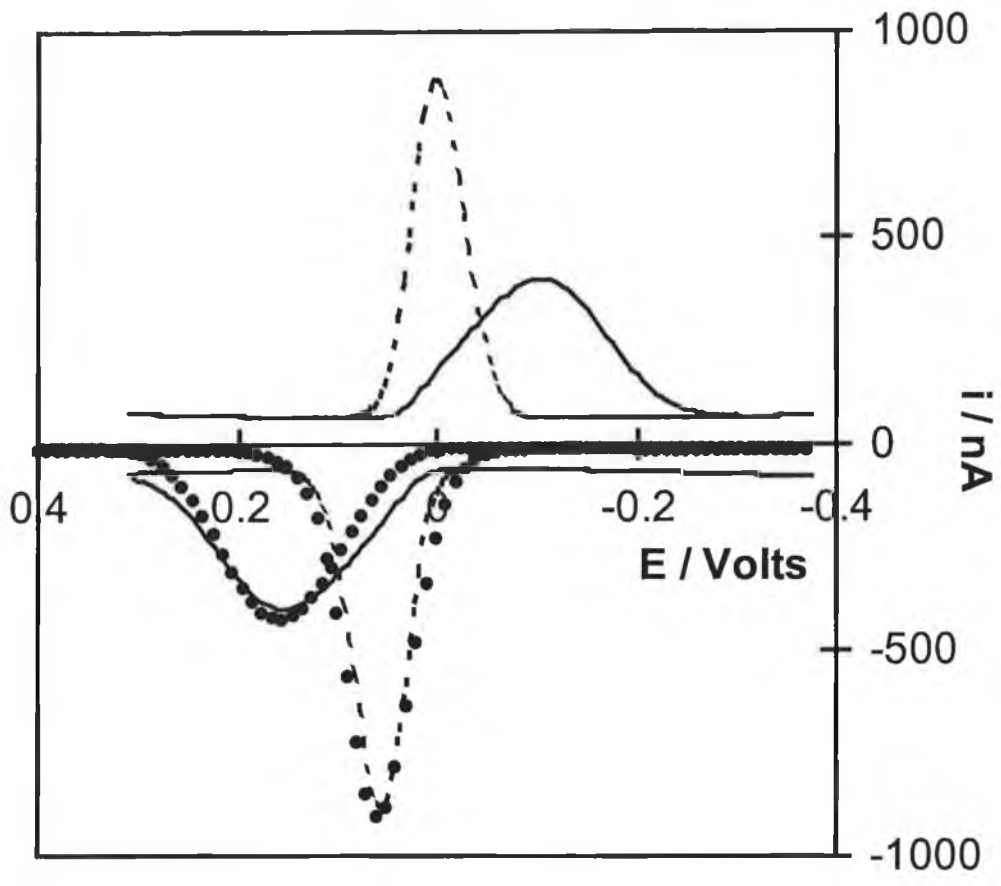

Figure 5.3. Voltammetric response for 10μm radius ——— carbon and ----- platinum microelectrodes modified with an $[Os(OMe\text{-}bpy)_2\ p3p\ Cl]^{1+}$ monolayer, using a Ag/AgCl reference electrode. The scan rate is 2000 V s^{-1} and the supporting electrolyte is 1.0 M aqueous $NaClO_4$. The data points represent theoretical fits to a non-adiabatic electron transfer model in which k° is $4x10^3$ and $6x10^4$ s^{-1} for carbon and platinum, respectively. The free energy of activation, $\Delta G^{\neq}$, is 6.8 kJ mol^{-1} for both electrodes.

5.4. Voltammetric Response For 2 μm Radius Microelectrodes

Cyclic voltammograms were obtained at different scan rates for $[Os(OMe\text{-}bpy)_2Cl(p3p)]^+$ monolayers spontaneously adsorbed on carbon, silver, gold, mercury and platinum microelectrodes, 2 μm radius, where the supporting electrolyte is aqueous 1.0 M $NaClO_4$. In the case of carbon, the scan rates used were 1000, 5000, and 10000 V s^{-1}. The voltammetric response for the other modified microelectrodes was determined at primarily two scan rates, namely 10000 and 15000 V s^{-1}.

The simplex allows detailed examination of the voltammetric response in many different ways. It is interesting to look at the quality of the fit under various starting conditions and to compare the value derived for k° from the experimental voltammetric response with that given by an independent method (e.g., chronoamperometry). In this study, k° has been determined with the non-adiabatic model in three different ways, namely

a) using the $\Delta G^{\neq}$ determined from chronoamperometry,
b) allowing the simplex to find the best fit by varying both $\Delta G^{\neq}$, and k°,
c) as for b) but with a third variable in the simplex, namely the surface coverage.

Now, a description is given of each of these methods for determining k^o in the following sections.

5.4.1. Using the Model with Only One Variable, k^o

If the $\Delta G^{\neq}$ value, that has been independently determined from chronoamperometry is used, as an input, i.e., not a variable, in the model, the simplex has only one variable to change in order to find the best fit. The major advantage in doing this is that computation time is minimised. The deficiency is, of course, that the value for $\Delta G^{\neq}$ must have already been measured. But what about the accuracy of the value of k^o extracted from the model in this way? What can be observed about the quality of the fit, visually and mathematically, with this method?

In order to answer these questions, the voltammetric response for these 2 μm radius carbon, silver, gold, mercury, and platinum microelectrodes modified with an $[Os(OMe\text{-}bpy)_2Cl(p3p)]^{1+}$ monolayer, was tested in the model using the value for $\Delta G^{\neq}$ measured by chronoamperometry. In all cases in this section, the non-adiabatic model was used.

Figure 5.4 shows the response for the 2 μm radius carbon microelectrode modified with the $[Os(OMe\text{-}bpy)_2Cl(p3p)]^{1+}$ monolayer along with the quality of the theoretical fit. The values extracted from the cyclic voltammograms for k° are 4023 s^{-1} and 4075 s^{-1} for the 5000 and 10000 V s^{-1} scan rates, respectively. The residual sum of squares between the predicted and experimental currents is 1.9×10^{-15} and 1.3×10^{-14}, respectively. The free energy of activation used in the model is that determined by chronoamperometry, $\Delta G^{\neq}$, 6.8 kJ mol^{-1}. The only variable used in determining these theoretical fits is k^0. The quality of the fit for all the microelectrodes under these conditions had some common features. In the first case, the fit was visually the worst when compared to the other methods used. Not unexpectedly therefore, the minimum of the sum of the squares of the differences (i.e., when the optimum k^o is found) was the highest. This is because the simplex has only one parameter (i.e., k^o) which it is allowed to vary.

But what about the accuracy of the values found for k^o? Apart from observing that a similar value for k^o is extracted from both cyclic voltammograms at scan rates of 5000 and 10000 V s^{-1}, which is certainly encouraging, it cannot be claimed at this stage that the true value for k^o has been found. To determine the accuracy of k^o, the value determined for k^o must be compared to a value determined by an independent technique, namely chronoamperometry. This issue will be returned to later in this chapter.

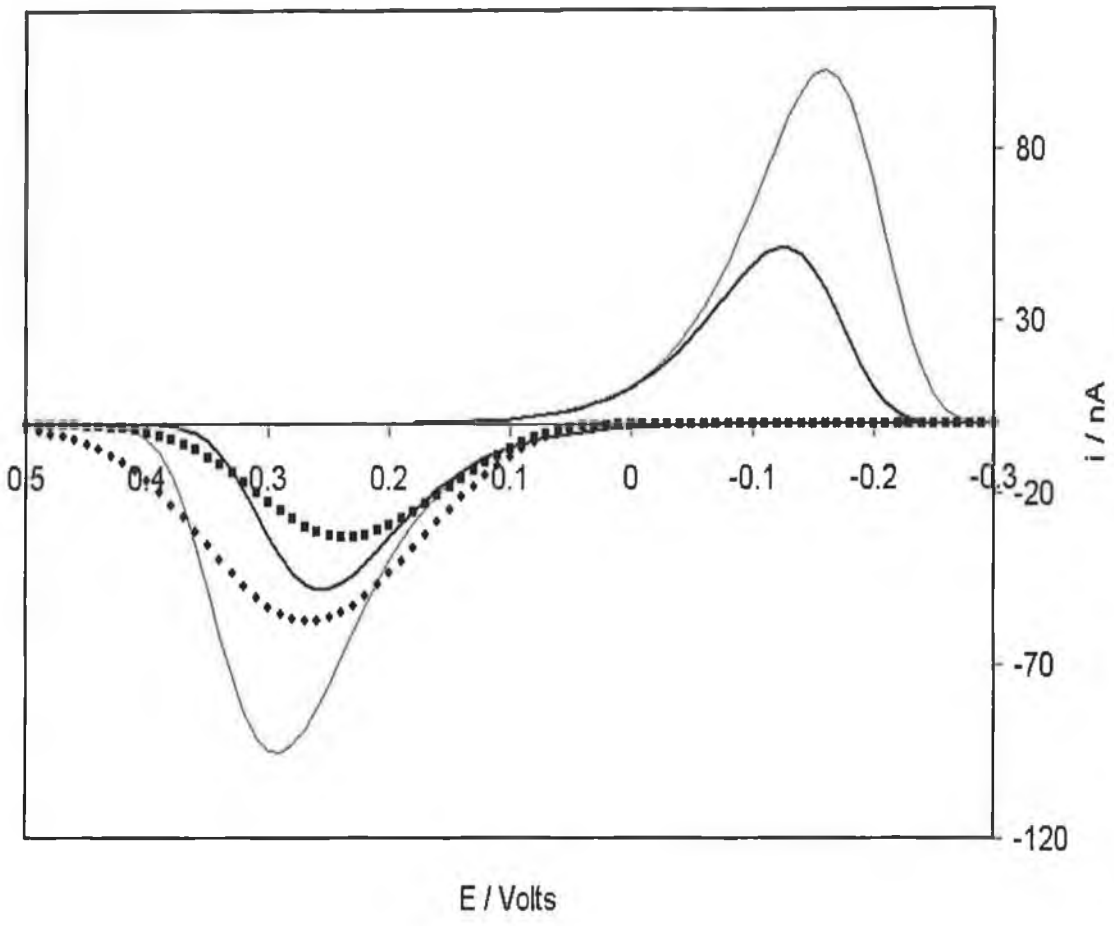

Figure 5.4. Voltammetric response for 2μm radius carbon microelectrodes modified with an $[Os(OMe\text{-}bpy)_2Cl(p3p)]^{1+}$ monolayer, using a Ag/AgCl reference electrode. The scan rates are (top to bottom) 10,000 and 5000 V s^{-1} (solid lines). The supporting electrolyte is 1.0 M aqueous $NaClO_4$. The data points (■,●) represent the theoretical fits of a non-adiabatic electron transfer model in which k° is 4023 s^{-1} and 4075 s^{-1} for the 5000 and 10000 V s^{-1} scan rates, respectively. The residual sum of squares between the predicted and experimental currents is 1.9 x 10^{-15} and 1.3 x 10^{-14}, respectively. The free energy of activation used in the model is that determined by chronoamperometry, $\Delta G^{\neq}$, 6.8 kJ mol^{-1}. The only variable used in determining these theoretical fits is k^0.

5.4.2. Using the Model with Two Variables, $\Delta G^{\neq}$ and k^{o}

In this case, the model is used to find k^{o} without having a predetermined value for $\Delta G^{\neq}$. Allowing the simplex algorithm to vary two parameters instead of one improves greatly the visual and mathematical fit of the theoretical best fit cyclic voltammograms to the experimental CVs. The reason that the fit looks visibly better and has a lower minimum of the sum of the differences squared is due to the fact the simplex can vary both the value for k^{o} and $\Delta G^{\neq}$.

In Figure 5.5, the response is shown for the 2 μm radius carbon microelectrode modified with the $[Os(OMe\text{-}bpy)_2Cl(p3p)]^{1+}$ monolayer along with the quality of the theoretical fit. This improved fit and lower sum of the differences squared, when two parameters instead of one are used, is obtained, not just for the carbon microelectrode, but for all of the microelectrodes.

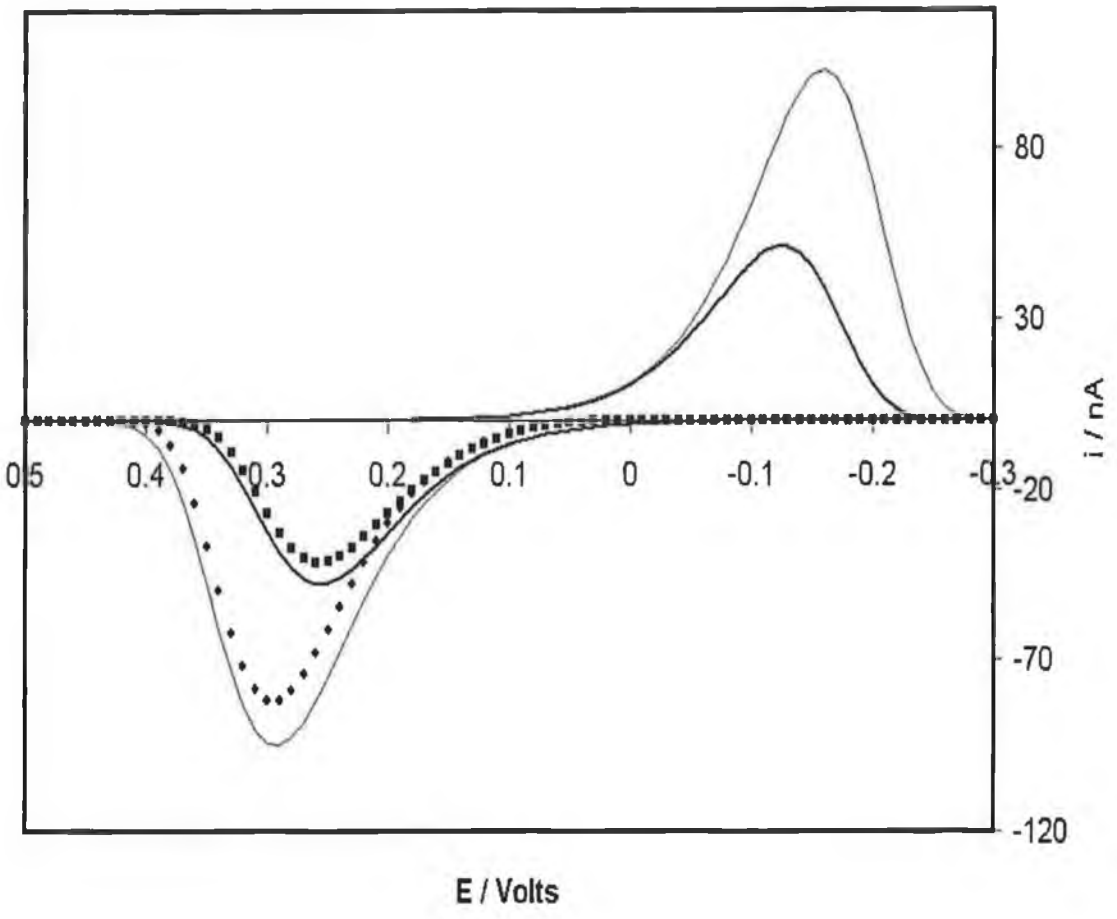

Figure 5.5. Voltammetric response for 2μm radius carbon microelectrodes modified with an $[Os(OMe\text{-}bpy)_2Cl(p3p)]^{1+}$ monolayer, using a Ag/AgCl reference electrode. The scan rates are (top to bottom) 10,000 and 5000 V s^{-1} (solid lines). The supporting electrolyte is 1.0 M aqueous $NaClO_4$. The data points (■,●) represent the theoretical fits of a non-adiabatic electron transfer model in which k° is 2225 s^{-1} and 1866 s^{-1} for the 5000 and 10000 V s^{-1} scan rates, respectively. The sum of the differences squared between the predicted and experimental currents is 6.8 x 10^{-16} and 3 x 10^{-15}, respectively. The free energies of activation giving the minimum SS are 105 kJ mol^{-1} and 464 kJ mol^{-1}. There are two variables used in determining these theoretical fits, namely k^{o}, and $\Delta G^{\neq}$.

5.4.3. Using the Model with Three Variables, $\Delta G^{\neq}$, k^{o} and Surface Coverage

Because it was observed that the theoretically determined peak current was invariably less in absolute terms than the experimental peak current, irrespective of which electrode material was used, it was decided to allow the simplex algorithm to vary the surface coverage, Γ, as a third parameter along with k^{o} and $\Delta G^{\neq}$. This would allow the simplex to calculate currents that would match exactly the current in and around the experimental peak. Would this method improve the estimates for k^{o} and $\Delta G^{\neq}$? Would the final estimate of the surface coverage, Γ, as determined by the simplex be a realistic value?

Once again, the power of the combination of the electron transfer theory with the simplex algorithm to determine k^{o} is shown. It is known from experiment that the surface coverage expected for this bulk concentration is $(1.0\pm0.1) \times 10^{-10}$ mol cm^{-2}. However, by allowing the simplex to optimise this value, the visual and mathematical fits (lowest sum of the squares of the differences) are dramatically improved. The simplex increases the surface coverage in all cases to values between $1.2\text{-}1.4 \times 10^{-10}$ mol cm^{-2} which gives us a convergence between the theoretical and experimental peak currents which, in turn, reduces the sum of the squares of the differences. As before, the values obtained for k^{o} need to be verified by an independent method. However, very significantly, the ability to determine $\Delta G^{\neq}$ has not been improved.

Figure 5.6 shows the response for the 2 μm radius carbon microelectrode modified with the $[Os(OMe\text{-}bpy)_2Cl(p3p)]^{1+}$ monolayer along with the quality of the theoretical fit using the three parameters as described.

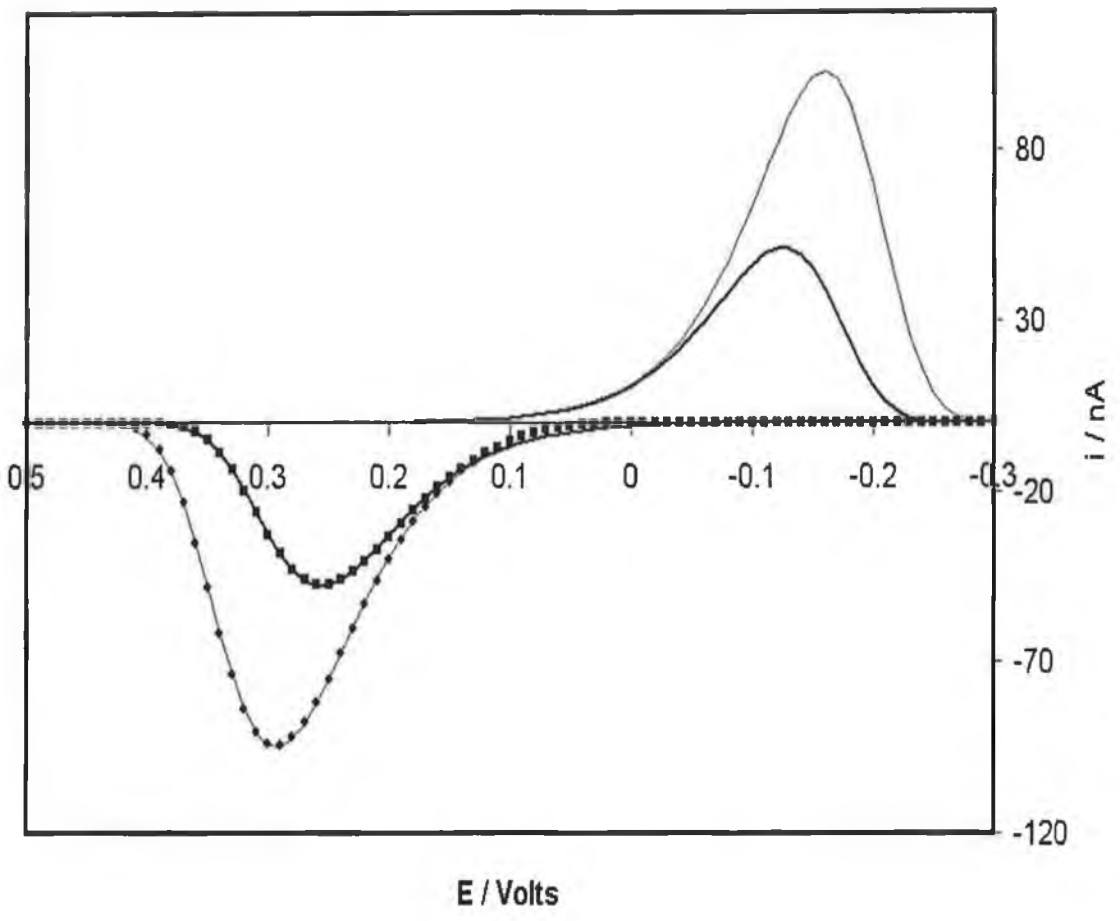

Figure 5.6. Voltammetric response for 2μm radius carbon microelectrodes modified with an $[Os(OMe\text{-}bpy)_2Cl(p3p)]^{1+}$ monolayer, using a Ag/AgCl reference electrode. The scan rates are (top to bottom) 10,000 and 5000 V s^{-1} (solid lines). The supporting electrolyte is 1.0 M aqueous $NaClO_4$. The data points (■,●) represent the theoretical fits of a non-adiabatic electron transfer model in which k° is 2488 s^{-1} and 2214 s^{-1} for the 5000 and 10000 Vs^{-1} scan rates, respectively. The residual sum of squares (i.e., SS) between the predicted and experimental currents is 3.6 x 10^{-17} and 3.7 x 10^{-17}, respectively. The free energies of activation giving the minimum SS are 31 kJ mol^{-1} and 45 kJ mol^{-1}. The surface coverage, Γ is allowed to change to improve the quality of the fit. The best fit is given with surface coverages of 1.3 x 10^{-10} mol cm^{-2} and 1.4 x 10^{-10} mol cm^{-2}, respectively. There are three variables used in determining these theoretical fits, namely k^0, $\Delta G^{\neq}$ and the surface coverage, Γ.

5.4.4. The Silver, Gold, Mercury, and Platinum Microelectrodes

Because similar features were found with the silver, gold, mercury, and platinum microelectrodes to those already described and discussed for the carbon microelectrode, it was decided in the interest of clarity to only show the responses and theoretical fits for the third case, i.e., allowing the simplex to find the optimum values for k^o, $\Delta G^{\neq}$ and the surface coverage, Γ.

Figures 5.7, 5.8, 5.9, and 5.10 display the responses and theoretical fits for the $[Os(OMe\text{-}bpy)_2Cl(p3p)]^{1+}$ monolayer adsorbed to the 2 μm radius silver, gold, mercury and platinum microelectrodes using the simplex with the variables, k^o, $\Delta G^{\neq}$ and the surface coverage, Γ.

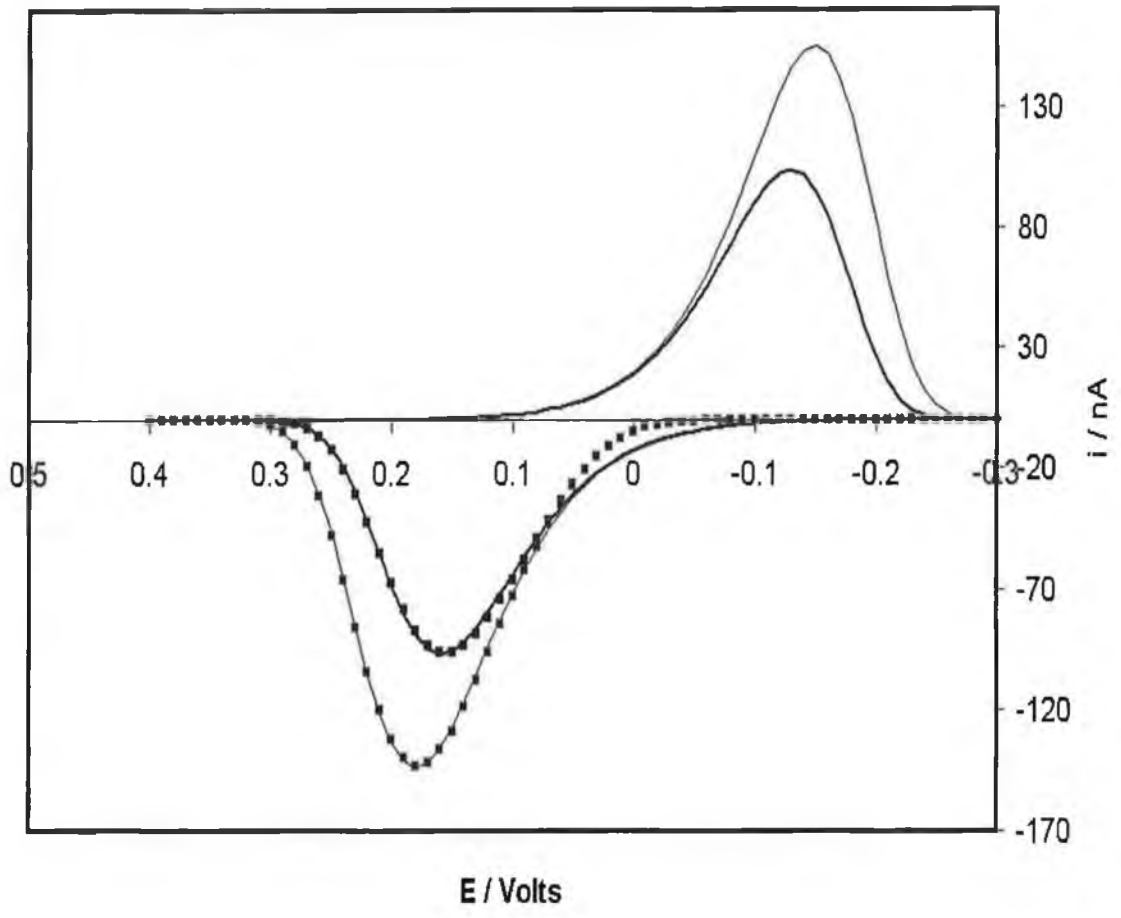

Figure 5.7. Voltammetric response for 2 μm radius silver microelectrodes modified with an $[Os(OMe\text{-}bpy)_2Cl(p3p)]^{1+}$ monolayer, using a Ag/AgCl reference electrode. The scan rates are (top to bottom) 10,000 and 5000 V s^{-1} (solid lines). The supporting electrolyte is 1.0 M aqueous $NaClO_4$. The data points (■,●) represent the theoretical fits of a non-adiabatic electron transfer model in which k° is 11677 s^{-1} and 11336 s^{-1} for the 10000 V s^{-1} and 15000 V s^{-1} scan rates, respectively. The residual sum of squares (i.e., SS) between the predicted and experimental currents is 5.1 x 10^{-17} and 6.1 x 10^{-16}, respectively. The free energies of activation giving the minimum SS are 31 kJ mol^{-1} and 45 kJ mol^{-1}. The surface coverage, Γ is allowed to change to improve the quality of the fit. The best fit is given with surface coverage of 1.3 x 10^{-10} mol cm^{-2} for both scan rates. There are three variables used in determining these theoretical fits, namely k^0, $\Delta G^{\neq}$ and the surface coverage, Γ.

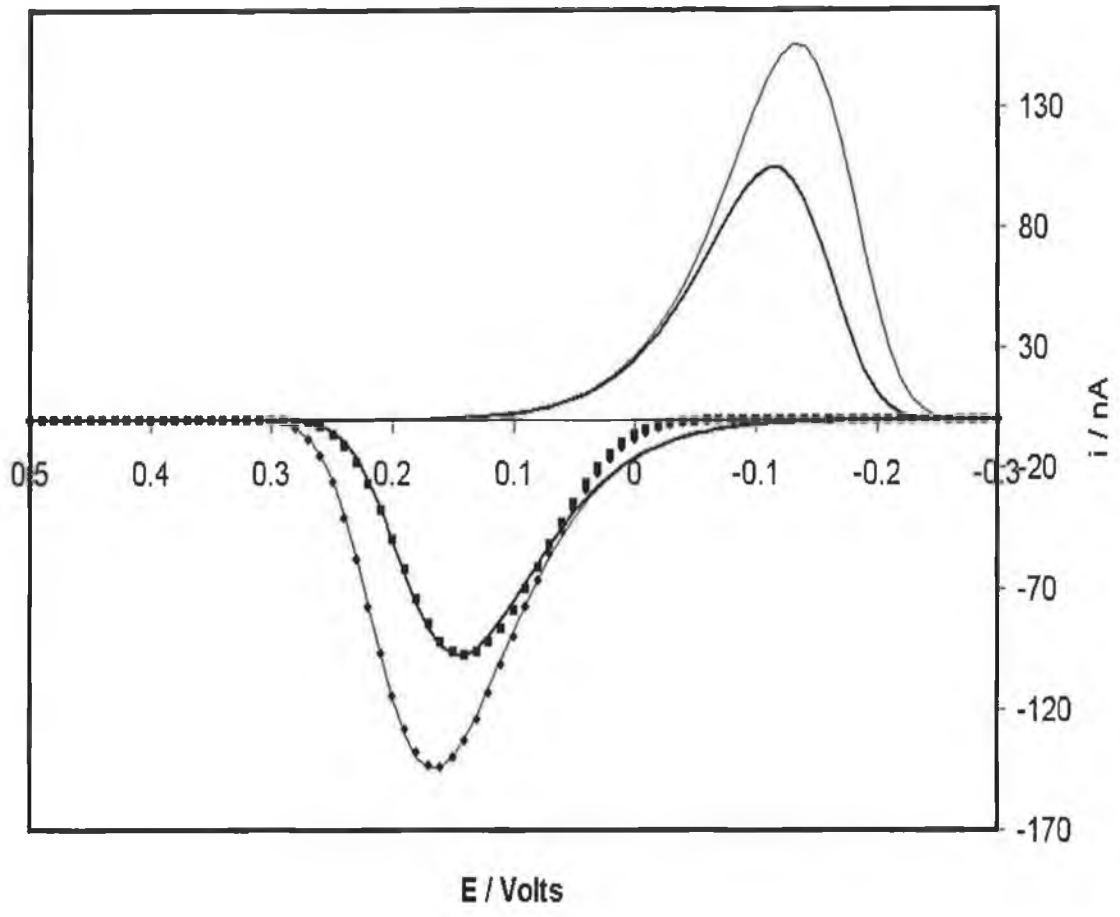

Figure 5.8. Voltammetric response for 2 μm radius gold microelectrodes modified with an $[Os(OMe\text{-}bpy)_2Cl(p3p)]^{1+}$ monolayer, using a Ag/AgCl reference electrode. The scan rates are (top to bottom) 10,000 and 5000 V s^{-1} (solid lines). The supporting electrolyte is 1.0 M aqueous $NaClO_4$. The data points (■,●) represent the theoretical fits of a non-adiabatic electron transfer model in which k° is 15654 s^{-1} and 12294 s^{-1} for the 10000 V s^{-1} and 15000 V s^{-1} scan rates, respectively. The residual sum of squares (i.e., SS) between the predicted and experimental currents is 7.5 x 10^{-16} and 6.4 x 10^{-16}, respectively. The free energies of activation giving the minimum SS are 14 kJ mol^{-1} and 23 kJ mol^{-1}. The surface coverage, Γ is allowed to change to improve the quality of the fit. The best fit is given with surface coverage of 1.3 x 10^{-10} mol cm^{-2} for both scan rates. There are three variables used in determining these theoretical fits, namely k^0, $\Delta G^{\neq}$ and the surface coverage, Γ.

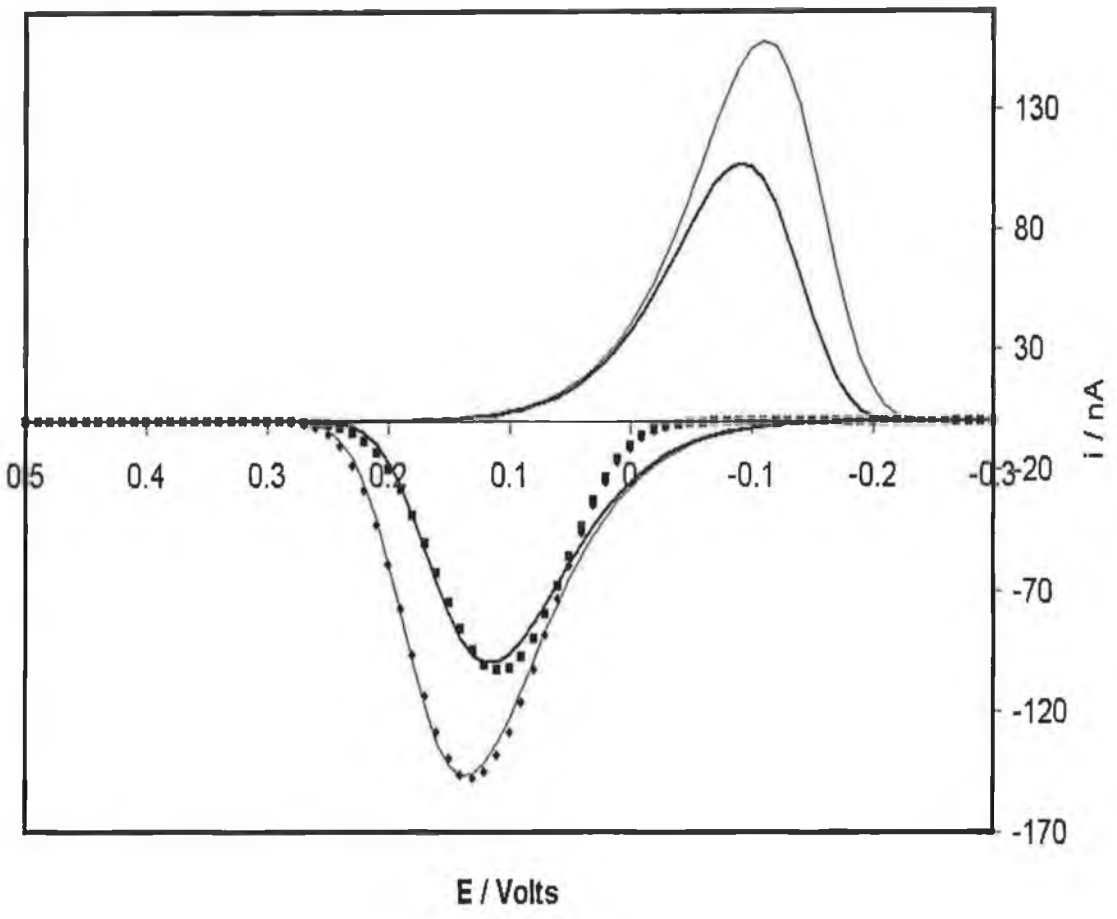

Figure 5.9. Voltammetric response for 2 μm radius mercury microelectrodes modified with an $[Os(OMe\text{-}bpy)_2Cl(p3p)]^{1+}$ monolayer, using a Ag/AgCl reference electrode. The scan rates are (top to bottom) 10,000 and 5000 V s^{-1} (solid lines). The supporting electrolyte is 1.0 M aqueous $NaClO_4$. The data points (■,●) represent the theoretical fits of a non-adiabatic electron transfer model in which k° is 33351 s^{-1} and 27964 s^{-1} for the 10000 V s^{-1} and 15000 V s^{-1} scan rates, respectively. The residual sum of squares (i.e., SS) between the predicted and experimental currents is 1.9×10^{-15} and 2.1×10^{-15}, respectively. The free energies of activation giving the minimum SS are 6 kJ mol^{-1} and 11 kJ mol^{-1}. The surface coverage, Γ is allowed to change to improve the quality of the fit. The best fit is given with surface coverages of 1.2×10^{-10} mol cm^{-2} and 1.3×10^{-10} mol cm^{-2}, respectively. There are three variables used in determining these theoretical fits, namely k^0, $\Delta G^{\neq}$ and the surface coverage, Γ.

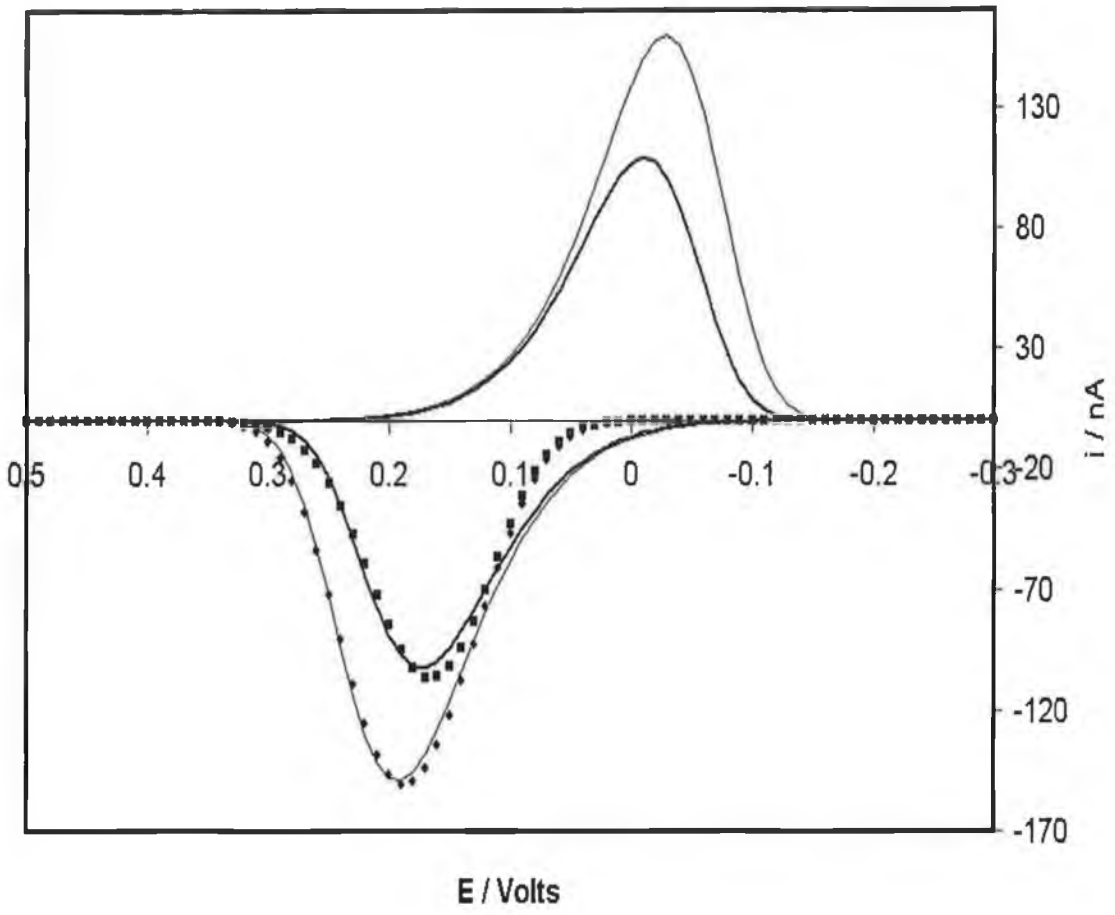

Figure 5.10. Voltammetric response for 2 μm radius platinum microelectrodes modified with an $[Os(OMe\text{-}bpy)_2Cl(p3p)]^{1+}$ monolayer, using a Ag/AgCl reference electrode. The scan rates are (top to bottom) 10,000 and 5000 V s^{-1} (solid lines). The supporting electrolyte is 1.0 M aqueous $NaClO_4$. The data points (■,●) represent the theoretical fits of a non-adiabatic electron transfer model in which k° is 42517 s^{-1} and 33351 s^{-1} for the 10000 and 15000 V s^{-1} scan rates, respectively. The residual sum of squares (i.e., SS) between the predicted and experimental currents is 2.2 x 10^{-15} and 2.5 x 10^{-15}, respectively. The free energies of activation giving the minimum SS are 5 kJ mol^{-1} and 10 kJ mol^{-1}. The surface coverage, Γ is allowed to change to improve the quality of the fit. The best fit is given with surface coverages of 1.2 x 10^{-10} mol cm^{-2} and 1.3x10^{-10} mol cm^{-2}, respectively. There are three variables used in determining these theoretical fits, namely k^0, $\Delta G^{\neq}$ and the surface coverage, Γ.

5.4.5. Sensitivity to k^o

The Figures 5.4 to 5.10 show the relative insensitivity of the non-adiabatic model to $\Delta G^{\neq}$ for this system referred to earlier. However, the model is highly sensitive to changes in k^o. This feature of the model was noted earlier in Chapter 3 when the model was tested with various theoretical background currents added to the simulated cyclic voltammograms.

But sensitivity to a parameter, while essential for fitting purposes, does not tell us about the accuracy of the model's optimum value for that parameter. To assess the accuracy of the optimum values for k^o, an independent technique, namely chronoamperometry must be used to measure k^o and then compare.

At this point, a discussion on chronoamperometry is given and this fundamentally important question of the accuracy of the values given by the newly constructed model for k^o will be returned to later in the chapter.

5.5. Chronoamperometry

For an ideal electrochemical reaction involving a surface bound species, the Faradaic current following a potential step that changes the redox composition of the monolayer exhibits a single exponential decay in time according to:[19,20]

$$i_F(t) = kQ \exp(-kt) \quad (1)$$

where k is the apparent rate constant for the overall reaction, and Q is the total charge passed in the redox transformation.

Figure 5.11 illustrates typical examples of the current-time transients observed for the $Os^{3+} + e^- \rightarrow Os^{2+}$ redox reaction of $[Os(OMe\text{-}bpy)_2\ p3p\ Cl]^+$ monolayers on different electrode materials. In these experiments the overpotential η ($\equiv E - E^{o\prime}$) was 0.05 V. In order to use these data to accurately measure k, the response time of the electrode must be shorter than the time constant for heterogeneous electron transfer. The RC time constants for the different electrodes, where R is the total cell resistance and C is the interfacial capacitance, have been obtained by stepping the potential from –0.100 to –0.050 V. The monolayer is not redox active at these potentials and the current decays follow single exponential kinetics due to double layer charging. In the experimental chapter, Table 2.2, p. 84, contains the resistance, capacitance and RC time constants for each of the electrodes. Table 2.2 shows that irrespective of the electrode material, the 5 μm radius electrodes all have response times that are less than 750 ns. This result means that double layer charging will only contribute to the currents observed in Figure 5.11 only at timescales shorter than approximately 2 μs. Therefore, the heterogeneous electron transfer rate constant can be measured by analysing the current-time transients at relatively longer timescales. Beyond the issue of convolution between double-layer charging currents and the Faradaic response, Table 2.2 also confirms that current-time transients of Figure 5.11 are not compromised by ohmic effects. For example, the total cell resistance for the 10 μm radius silver electrode is approximately 8 kΩ. Therefore, the iR drop will be less than 10 mV for times longer than approximately 8 μs. The inset of Figure 5.11 supports this analysis since, in accordance with Equation 1, semi-log current vs. time plots are

linear over at least 1.5 lifetimes. Deviations from linearity would be expected if substantial ohmic drop effects were present. Uncompensated resistance causes the applied potential, and hence the apparent rate, to evolve with time. Therefore, iR drop would produce negative deviations in the observed current at short times.[21]

That heterogeneous electron transfer is characterised by a single rate constant indicates that for each electrode material electron transfer is characterised by a single electron transfer distance, reorganisation energy and microenvironment. Further evidence supporting the predominance of a single rate constant at high concentrations of supporting electrolyte is obtained by examining the intercept of the semi-log plot at zero time. As indicated by Equation 1, the intercept for a single exponential decay is ln (kQ). It is found that the charges passed in chronoamperometry agree with those found in slow scan cyclic voltammetry to within 10 %. This agreement indicates that all of the surface confined molecules are redox active on a microsecond timescale.

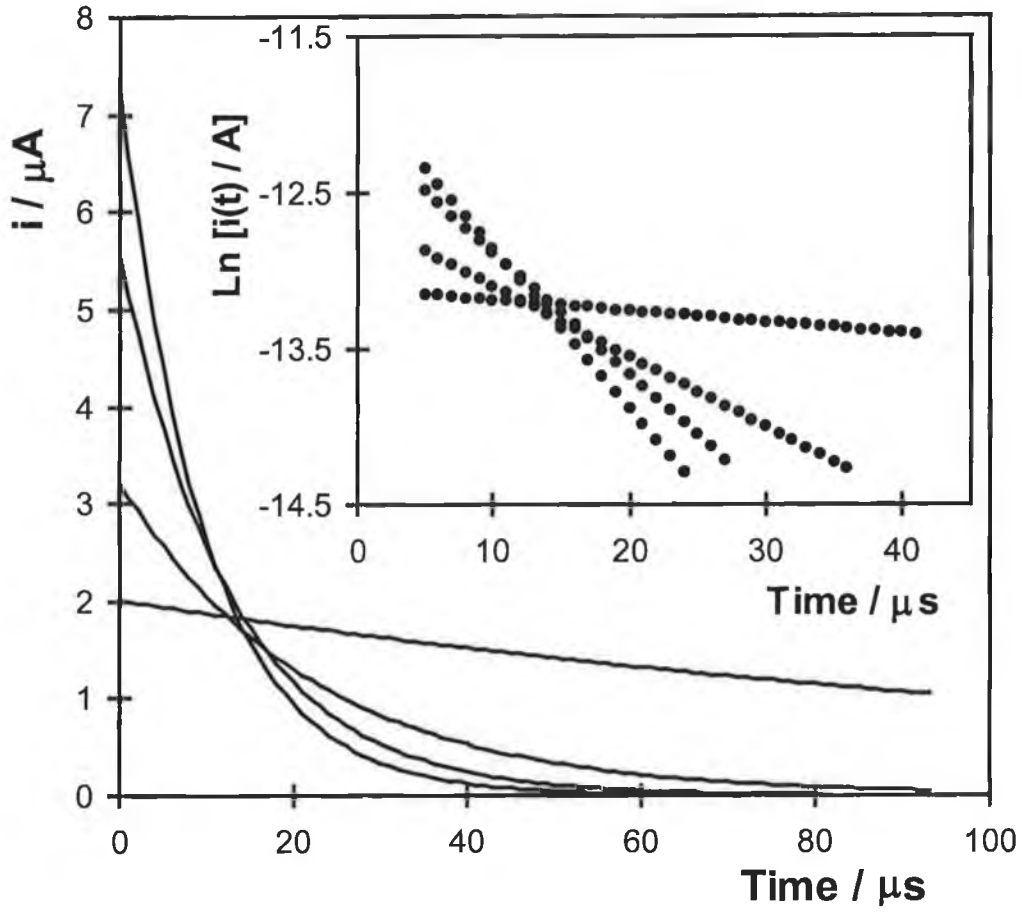

Figure 5.11. Current response for $[Os(OMe\text{-}bpy)_2Cl(p3p)]^{1+}$ monolayers following a potential step where the overpotential η was 50 mV. From top to bottom on the left hand side the decays are for platinum, mercury, gold (5 μm) and carbon (12.5 μm). The supporting electrolyte is aqueous 1.0 M $NaClO_4$. The inset shows ln $i_F(t)$ vs. t plots for the Faradaic reaction.

Table 5.1 contains the standard heterogeneous electron transfer rate constants, k°, obtained by extrapolating the potential dependent rate constants to zero overpotential. The observation that k° depends on the nature of the electrode material is striking. In experiments of this kind, it is important to consider the influence of double layer effects on k° which occur when the potential at the plane of electron transfer, ϕ_{PET}, is not equal to the potential in solution. However, for the monolayers considered here, double layer effects do not appear to be important for the following reasons. First, k° increases by less than 5% on going from 0.1 to 1.0 M supporting electrolyte. If double layer effects were significant, then the compression of the double layer brought about by increasing the electrolyte concentration would be expected to alter ϕ_{PET} thus changing the apparent heterogeneous electron transfer rate constant.

Second, the monolayers appear to be solvated and the double layer most likely sets up *within* the monolayer rather than at the monolayer/solution interface. For example, the interfacial capacitance is independent of the bulk electrolyte concentration C_B, for C_B>0.2 M and a limiting value of 25±5 μF cm^{-2} is observed at –0.1 V. This value is independent of the electrode material used. This limiting value of the interfacial capacitance is considerably larger than that associated with a solvent free monolayer[22] suggesting that the films are solvated.

Third, the potentials of zero charge (PZC) becomes more positive in the order Hg<Au<Pt. In the presence of double layer effects, one would anticipate that these PZCs would lead to k°s in the sequence Hg>Au>Pt. Table 5.1 clearly demonstrates that this is not the case for these monolayers.

As discussed above, an important feature of heterogeneous electron transfer is that the rate constant will depend on the density of states within the electrode only if there is weak electronic coupling between the remote redox centre and the electrode surface. Therefore, it is important to probe the adiabaticity of the reaction. Moreover, caution must be exercised to ensure that apparent differences in k° are not caused by variations in the free energy of activation, rather than by density of states or coupling effects.

Table 5.1. Standard heterogeneous electron transfer rate constants, k°, Activation Enthalpies, $\Delta H^{\neq}$, Reaction Entropies, $\Delta S_{RC}°$, Free Energies of Activation, $\Delta G^{\neq}$ and Pre-exponential Factors for the metal based redox reaction within $[Os(OMe\text{-}bpy)_2Cl(p3p)]^{1+/2+}$ monolayers on different electrode materials.[a] All parameters measured by Dr. R. J. Forster.

	10^{-4} k° / s^{-1}	$\Delta H^{\neq}$ / kJ mol^{-1}	$\Delta S^{\neq}$/ J mol^{-1} K^{-1}	$\Delta G^{\neq}$ / kJ mol^{-1}	$\kappa_{el}\nu_n$ / s^{-1}, [b]
Platinum	4.0(0.2)	11.3(0.7)	28(4.5)	7.3(0.5)	7.6(1.1)
Mercury	3.1(0.3)	10.6(1.1)	26(5)	6.9(1.2)	5.0(0.8)
Gold	1.8(0.2)	11.2(0.5)	32(3)	6.6(0.3)	2.6(0.2)
Silver	1.3(0.2)	11.2(0.6)	30(4)	6.9(0.3)	2.1(0.1)
Carbon	0.3(0.03)	11.1(0.5)	30(4)	6.8(0.4)	0.5(0.04)

[a] Standard deviations are for at least three individual monolayers. Supporting electrolyte is aqueous 1.0 M $NaClO_4$.

[b] Pre-exponential factor extracted from the standard heterogeneous electron transfer rate constant using $\Delta G^{\neq}$.

5.6. Pre-exponential Factor.

Table 5.1 contains values of A_{et} ($\equiv \kappa_{el}\ \upsilon_n$) that have been determined using the experimental values of $\Delta G_c^{\neq}$ and k°. Significantly, irrespective of the identity of the electrode material, these prefactors are approximately six orders of magnitude smaller than those expected for an adiabatic electron transfer reaction.[23] Moreover, given that the free energies of activation are similar to that expected for a simple outer sphere reaction, these low rate constants are caused by the reaction being non-adiabatic, i.e., $\kappa_{el} << 1$. Table 5.1 also reveals that the pre-exponential factor is sensitive to the identity of the electrode material with the lowest value being observed for carbon while $\kappa_{el}\upsilon_n$ is largest for platinum. This large difference might be expected given the known sensitivity of heterogeneous electron transfer to the density of edge-planes in carbon electrodes.[24,25] More significant perhaps, are the differences observed between Pt and Au. The density of states, ρ_F, of platinum is approximately 7.5 times[26] that of gold which would be expected to cause a proportional increase in A_{et}. However, an increase of less than 3 is observed. Marcus and Gosavi[3] have considered this issue for a highly non-adiabatic electron transfer involving an $[Ru(NH_3)_5$ pyridine$]^{2+}$ redox centre tethered to an alkanethiol monolayer containing 15 methylene spacer groups. This model predicts that the ratio k_{Pt} / k_{Au} will depend only weakly on the electron transfer distance or the overpotential. More significantly, it highlights the importance of considering the identity of the orbitals that are responsible for increasing ρ_F and how efficiently these orbitals couple with those of the redox centre/bridge. Rather than a simple proportionality between k° and ρ_F, k° depends on ρ_F modulated by the square of the coupling strength. The Marcus and Gosavi model predicts a ratio of $A_{ET,Pt}$ / $A_{ET,\ Au}$ of 1.8 compared to the ratio of 2.9(0.6) observed here. Therefore, the experimental results reported here indicate that while the increased density of states found in Pt arising from *d*-orbitals are not entirely ineffective for coupling, their coupling efficiency is well below that found for the dominant *sp*-states of gold.

5.7. The Accuracy of the Model

In this section, the accuracy of the values for k^o given by the model is discussed. As has already been stated, it is necessary to compare these values for k^o to those measured by chronoamperometry.

Table 5.2 gives the standard heterogeneous electron transfer rate constants, k^o, determined by chronoamperometry and cyclic voltammetry for the metal based redox reaction within $[Os(OMe\text{-}bpy)_2Cl(p3p)]^{1+/2+}$ monolayers on different electrode materials. There are three cyclic voltammetric results, namely CV1, CV2, and CV3. CV1 gives the value determined for k^o using the non-adiabatic model calculated using the value for $\Delta G^{\neq}$, the free energy of activation, as determined by chronoamperometry. CV2 gives the value determined for k^o using the non-adiabatic model calculated with $\Delta G^{\neq}$, the free energy of activation, as a variable in the simplex algorithm. CV3 gives the value determined for k^o using the non-adiabatic model calculated with $\Delta G^{\neq}$, the free energy of activation, and the surface coverage, Γ, as variables in the simplex algorithm.

Figures 5.12, 5.13, and 5.14 illustrate the comparison of the 3 values for k^o from the cyclic voltammetric model to the value measured by chronoamperometry. The most striking feature of these figures is how well the rate constants measured by the two separate techniques match each other. The slope and R^2 of the best fit lines are essentially equal to 1. This demonstrates the excellent agreement between the values for k^o measured by chronoamperometry and those extracted by the model from the cyclic voltammograms. The excellent agreement with the chronoamperometric method is powerful evidence of both the veracity of the non-adiabatic electron transfer theory and the usefulness of the fitting model. This is unequivocal proof that the model is fulfilling its main objective, i.e., to extract accurate values for k^o from cyclic voltammetry.

Table 5.2. Standard heterogeneous electron transfer rate constants, k°, determined by chronoamperometry and cyclic voltammetry for the metal based redox reaction within $[Os(OMe\text{-}bpy)_2Cl(p3p)]^{1+/2+}$ monolayers on different electrode materials. CV1 gives the value determined for k^o using the non-adiabatic model calculated using the value for $\Delta G^{\neq}$, the free energy of activation, as determined by chronoamperometry. CV2 gives the value determined for k^o using the non-adiabatic model calculated with $\Delta G^{\neq}$, the free energy of activation, as a variable in the simplex algorithm. CV3 gives the value determined for k^o using the non-adiabatic model calculated with $\Delta G^{\neq}$, the free energy of activation, and the surface coverage, Γ, as variables in the simplex algorithm.

	Chrono	**CV1**	**CV2**	**CV3**
	10^{-4} k^o / s^{-1}	**10^{-4} k^o / s^{-1} [a]**	**10^{-4} k^o / s^{-1} [a]**	**10^{-4} k^o / s^{-1} [a]**
Platinum	4.0(0.2)	3.9(0.2)	3.7(0.5)	3.8(0.5)
Mercury	3.1(0.3)	3.3(0.1)	3.0(0.3)	3.1(0.3)
Gold	1.8(0.2)	1.8(0.1)	1.3(0.8)	1.4(0.2)
Silver	1.3(0.2)	1.5(0.1)	1.0(0.3)	1.2(0.02)
Carbon	0.3(0.03)	0.4(0.1)	0.2(0.03)	0.2(0.4)

[a] The reported value for k^o is the average of the values determined from experiments at two scan rates, namely 10000 V s^{-1} and 15000 V s^{-1} for all the materials except carbon. For carbon, the reported k^o is the average of the values determined from three scan rates, namely, 1000 V s^{-1}, 5000 V s^{-1} and 10000 V s^{-1}. Supporting electrolyte is aqueous 1.0 M $NaClO_4$.

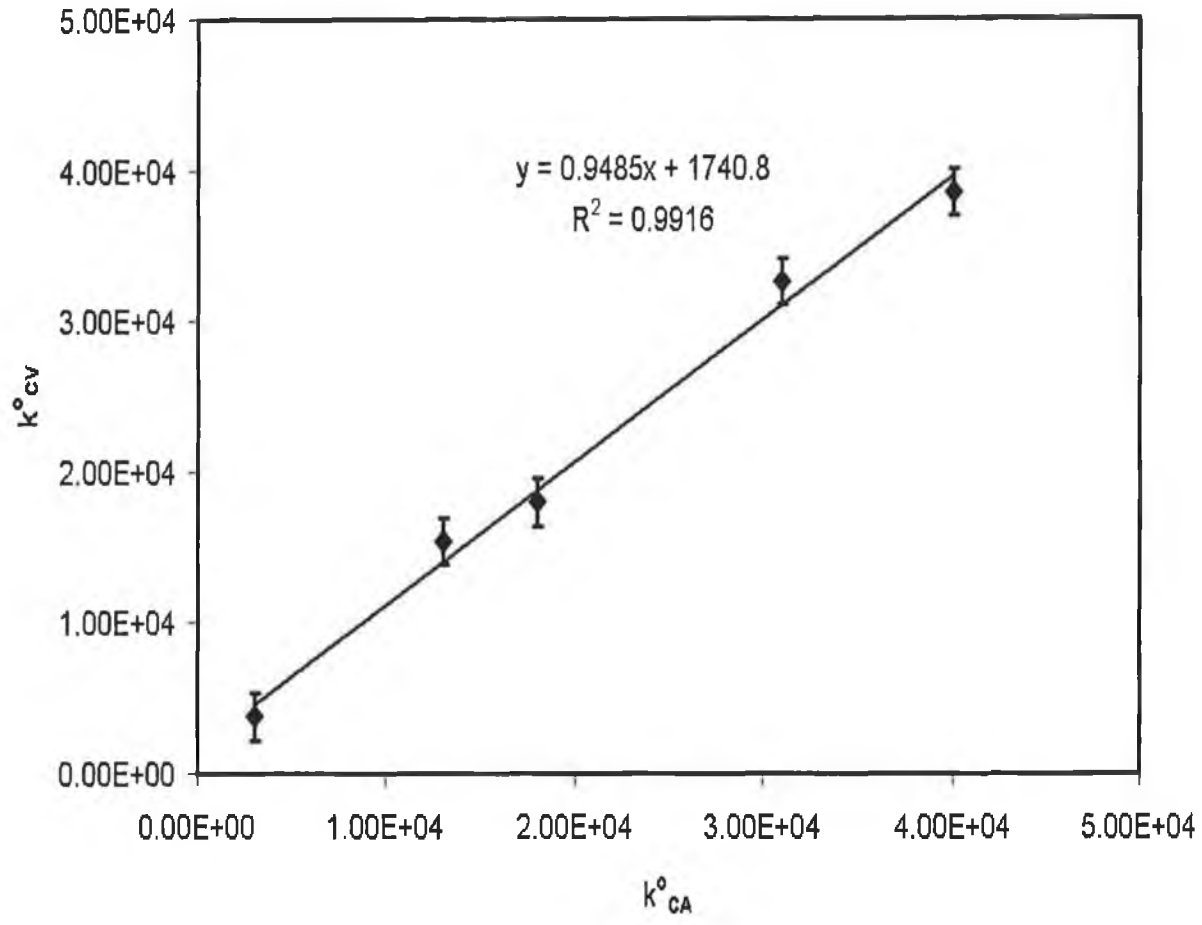

Figure 5.12. Standard heterogeneous electron transfer rate constants, k°, determined by chronoamperometry and cyclic voltammetry for the metal based redox reaction within $[Os(OMe\text{-}bpy)_2Cl(p3p)]^{1+/2+}$ monolayers on different electrode materials. The data points represent the average value for k° for carbon (lowest), silver, gold, mercury and platinum (highest) microelectrodes. This figure displays the CV1 data from Table 5.2. The cyclic voltammetric k° values were generated using the non-adiabatic model calculated using the value for $\Delta G^{\neq}$, the free energy of activation, as determined by chronoamperometry.

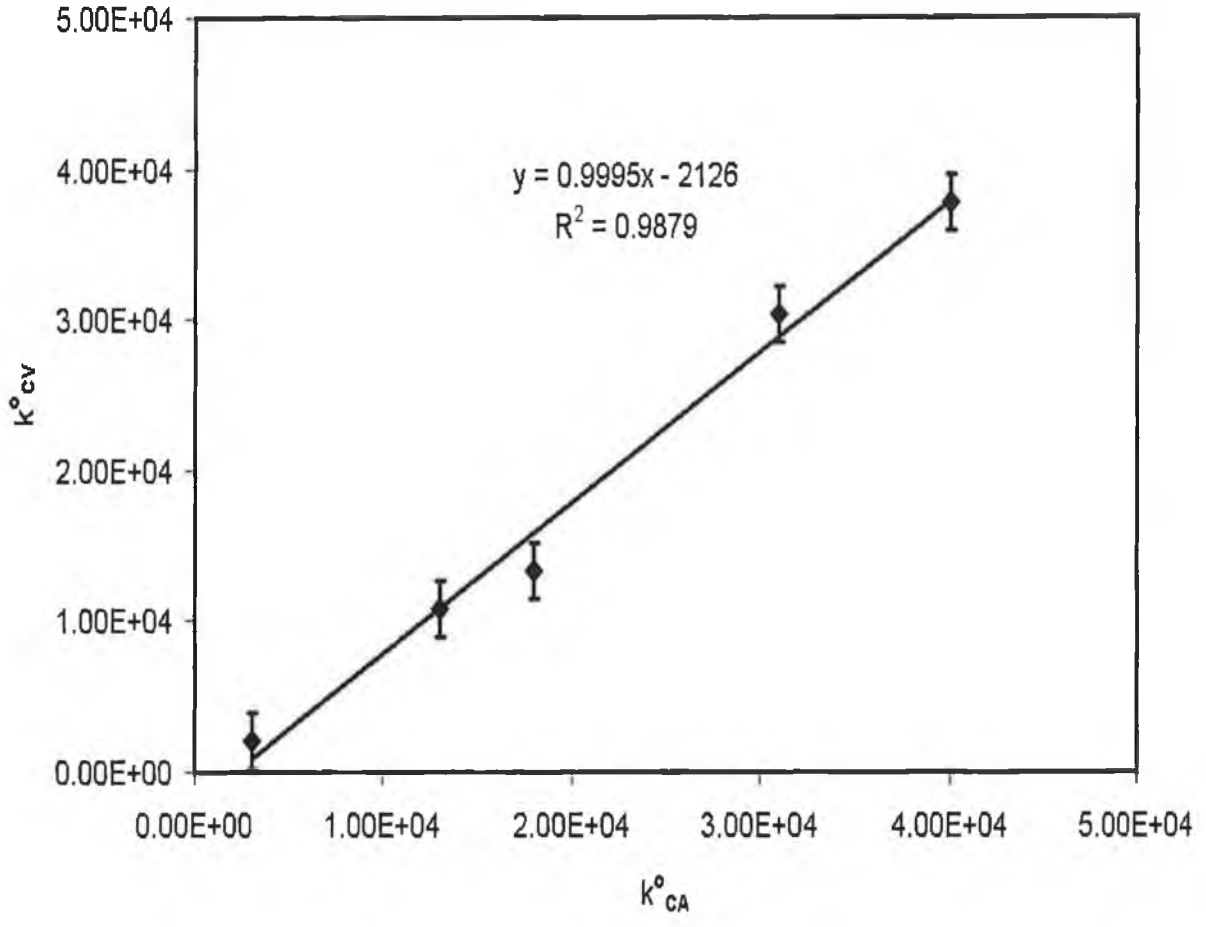

Figure 5.13. Standard heterogeneous electron transfer rate constants, k°, determined by chronoamperometry and cyclic voltammetry for the metal based redox reaction within $[Os(OMe\text{-}bpy)_2Cl(p3p)]^{1+/2+}$ monolayers on different electrode materials. The data points represent the average value for k^o for carbon (lowest), silver, gold, mercury and platinum (highest) microelectrodes. This figure displays the CV2 data from Table 5.2. The cyclic voltammetric k^o values were generated using the non-adiabatic model calculated using both k^o and the $\Delta G^{\neq}$, the free energy of activation, as variables in the simplex algorithm.

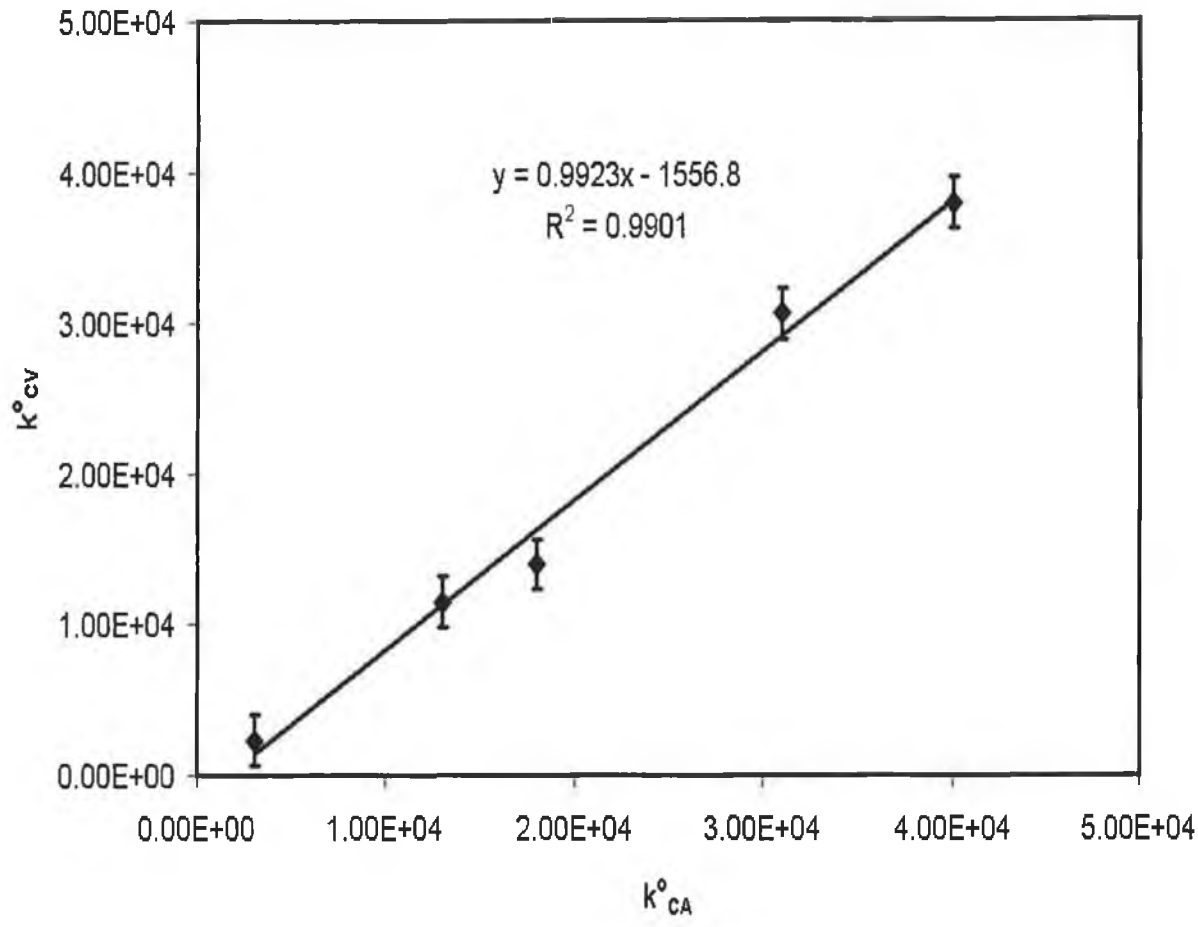

Figure 5.14. Standard heterogeneous electron transfer rate constants, k°, determined by chronoamperometry and cyclic voltammetry for the metal based redox reaction within $[Os(OMe\text{-}bpy)_2Cl(p3p)]^{1+/2+}$ monolayers on different electrode materials. The data points represent the average value for k^o for carbon (lowest), silver, gold, mercury and platinum (highest) microelectrodes. This figure displays the CV3 data from Table 5.2. The cyclic voltammetric k^o values were generated using the non-adiabatic model calculated using both k^o and the $\Delta G^{\neq}$, the free energy of activation, and the surface coverage, Γ, as variables in the simplex algorithm.

5.8. Standard Rate Constants Measured for Osmium Complexes in Solution using Different Electrodes.

Our results demonstrate the profound effect that the electrode material has on the electrochemical properties of an adsorbed monolayer. However, what effect does the electrode material have on the electrochemical properties of solution phase species?

In order to answer this question, a parallel study was carried out on solution phase species. The rate constants for the solutions of $[Os(bpy)_2Cl(p2p)]^+$ and $[Os(bpy)_2Cl(bpe)]^+$ were measured using the solutions prepared as described in Chapter 2. The method used is described in detail in Chapter 4. Three different macroelectrodes were used, namely, platinum, gold, and carbon with radii of 1, 1, and 1.5 mm, respectively.

Table 5.3, gives the results of these experiments. Significantly, as in the case of the adsorbed monolayers, the rate constants for the solution phase species appear to be determined by the electrode material, the rates measured for platinum being the highest. These solution phase results emphasise the known difficulties with consistent electrode preparation. In the study on the adsorbed species, it has been shown that the gold microelectrodes give rate constants that are slower than platinum but faster than carbon. In this study on solution phase species, with one complex, the rate constant measured on the gold macroelectrode is higher than the rate constant measured on carbon. The opposite is found with the second complex in that the rate constant is higher on carbon. These results are more likely to relate to the method of preparation of these electrodes rather than to the nature of the electrode material.

Table 5.3. The standard rate constants and first order heterogeneous rate constants for $[Os(bpy)_2Cl(p2p)]^+$ and $[Os(bpy)_2Cl(bpe)]^+$, bpy is 2,2′-bipyridyl, p2p is 1,2-bis(4-pyridyl)ethane, bpe is *trans*-1,2-bis(4-pyridyl)ethylene, when measured on the platinum macroelectrode.

Electrode	**$[Os(bpy)_2Cl(p2p)]^+$**		**$[Os(bpy)_2Cl(bpe)]^+$**	
	10^4 k cm s^{-1}	10^{-3} k^o s^{-1}	10^4 k cm s^{-1}	10^{-3} k^o s^{-1}
Platinum	24.0(2)	24.0(2)	100(16)	100(16)
Gold	6.2(1)	6.2(1)	24(2)	24(2)
Carbon	1.2(0.1)	1.2(0.1)	40(10)	40(10)

5.9. Conclusions

Adsorbed monolayers of $[Os(OMe\text{-}bpy)_2Cl(p3p)]^{1+}$ have been formed on platinum, mercury, gold, silver and carbon microelectrodes, OMe-bpy is 4,4′-dimethoxy-2,2′-bipyridyl and p3p is 1,4-trimethylene dipyridine. They exhibit nearly ideal electrochemical responses as the potential and experimental timescale are varied over a wide range. These monolayers have been used to probe the effect of changing the density of electronic states within the electrode on the heterogeneous electron transfer rate. High scan rate cyclic voltammetry reveals that the free energy of activation is consistent with that expected for a simple outer sphere reaction. The experimental pre-exponential factors are consistent with those expected for a non-adiabatic reaction in which there is weak electronic coupling between the delocalised metallic states on the electrode and the localised redox states of the osmium complex. The ratio of the pre-factors for platinum and gold is 2.9±0.7 compared with a ratio of 7.5 for the density of states. Therefore, these experimental data indicate that the non-adiabatic rate of heterogeneous electron transfer does not depend simply on the density of states within the electrode. In contrast, consistent with the theoretical considerations of Marcus and Gosavi, it is found that it depends on the density of states modulated by the square of the coupling.

A parallel study on redox active species dissolved in acetonitrile has shown that the rate constant is, as for adsorbed species, highest on the platinum macroelectrode.

The electron transfer model described in Chapter 3 has successfully identified the electron transfer process, in the study of the adsorbed monolayers, as non-adiabatic. This model has extracted values for k^o for these monolayers which are in excellent agreement with those measured by chronoamperometry. Different treatments of cyclic voltammetric data have been investigated with the model and the usefulness of the model as an electrochemical diagnostic tool has, once again, been demonstrated.

5.10. References

1 Finklea, H. O. "*Encyclopedia of Analytical Chemistry*", Wiley, New York, **2000**.

2 Parsons, R. *Surface Sci.* **1964,** *2*, 418.

3 Gosavi, S.; Marcus, R. A. *J. Phys. Chem. B*; **2000,** *104*, 2067.

4 Capon, A.; Parsons, R. *J. Electroanal. Chem.* **1973**, *46*, 215.

5 Iwasita, T.; Schmickler, W.; Schultze, J. *J. Am. Chem. Soc.*, **1984**, *106*, 1233.

6 Barr, S. W.; Guyer, K. L.; Li, T. T-T.; Liu, H. Y.; Weaver, M. J. *J. Electrochem. Soc.* **1984,** *131*, 1626.

7 Laviron, E. *J. Electroanal. Chem.* **1974**, *52*, 395.

8 Brown, A. P.; Anson, F. C. *Anal. Chem.* **1977**, *49*, 1589.

9 Forster, R. J.; Faulkner, L. R. *J. Am. Chem. Soc.* **1994**, *116*, 5453.

10 Forster, R. J.; O'Kelly, J. P. *J. Phys. Chem.* **1996**, *100*, 3695.

11 Acevedo, D.; Abrûna, H. D. *J. Phys. Chem.* **1991**, *95*, 9590.

12 Acevedo, D.; Bretz, R. L.; Tirado, J. D.; Abrûna, H. D. *Langmuir*, **1994**, *10*, 1300.

13 Bagchi, G. *Ann. Rev. Chem.* **1989**, *40*, 115.

14 Sutin, N. *Acc. Chem. Res.* **1982**, *15*, 275.

15 Barr, S. W.; Guyer, K. L.; Li, T. T.-T.; Liu, H. Y.; Weaver, M. J. *J. Electrochem. Soc.* **1984**, *131*, 1626.

16 Ebert, K.; Ederer, H.; Isenhour, T. L *Computer Applications in Chemistry: An Introduction for PC Users;* VCH Publishers: New York, **1989**.

17 Forster, R. J. *Inorg. Chem.* **1996**, *35*, 3394.

18 Forster, R. J. *Anal. Chem.* **1996**, *68*, 3143.

19 Finklea, H. O.; Hanshew, D. D. *J. Am. Chem. Soc.* **1992**, *114*, 3173.

20 Chidsey, C. E. D. *Science*, **1991**, *251*, 919.

21 Bard, A. J.; Faulkner, L. R. *Electrochemical Methods : Fundamentals and Applications,* Wiley, New York, **1980**.

22 Porter, M. D.; Bright, T. B.; Allara, D. L.; Chidsey, C. E. D. *J. Am. Chem. Soc.* **1987**, *109*, 3559.

23 Weaver, M. J. *Chem. Rev.* **1992**, *92*, 463.

24 Ray, K. G.; McCreery, R. L. *J. Electroanal. Chem.*, **1999**, *469*, 150.

25 McCreery, R. L.; Cline, K. K.; McDermott, C. A.; McDermott, M. T., *Colloids and Surfaces A*: **1994**, *93*, 211.

26 Papaconstantopoulous, D. A., *Handbook of Band Structure of Elemental Solids*, **1986**, Plenum Press, New York.

CHAPTER 6

Conclusions

6.1. Introduction

In this chapter, the major findings, observations and conclusions of this work are summarised, major conclusions drawn and interconnections between the different results discussed. From the outset, one of the primary objectives was to build an electron transfer model which would allow accurate kinetic and thermodynamic information to be rapidly extracted from the cyclic voltammetric response of an adsorbed monolayer. This model needed to combine modern electron transfer theory with a searching algorithm that could accurately fit the voltammetric response. Having constructed and tested the electron transfer model, it was then possible to investigate the voltammetric response of adsorbed complexes which were similar to each other but, nonetheless had significant structural differences. In this way, new studies such as the investigation of the effect of the nature of the bridging ligand on the heterogeneous electron transfer process were carried out. Moreover, by using one complex adsorbed to electrodes fabricated from different materials, the influence of the nature of the electrode material on the heterogeneous electron transfer process was also assessed. The effect of the nature of the electrode material had not previously been examined to any great extent. In parallel to the adsorption phase experimental work, solution phase studies was carried out in order to characterise certain complexes and to complement the adsorption studies allowing contrasts to be drawn between the results from the different phases. The work should, in its entirety, contribute significantly to a greater understanding of the heterogeneous electron transfer process.

Having chosen the electron transfer theory, it was then necessary to select a suitable algorithm for fitting the theoretically predicted cyclic voltammogram to the experimental voltammetric response and, thereby, extracting the heterogeneous rate constant and the Marcus reorganisation energy. The chosen algorithm was the downhill simplex method attributed to Nelder and Mead.[1] This algorithm was chosen because it requires only function evaluations, is applicable to the complicated integrals that define modern electron transfer theory, it does not require derivatives to be calculated and because it had been used successfully, for interpreting voltammetric, data by Weber and Creager.[2]

6.2. Synthesis and Characterisation of Surface Active Osmium and Ruthenium Complexes

In Chapter 2, the synthesis and characterisation of a number of osmium and ruthenium complexes was described. The complexes chosen had a number of attractive electrochemical properties and structural features, e.g., all of the complexes exhibit nearly ideal reversible voltammetric responses and contain a free pyridine group that is capable of adsorbing onto a variety of electrode materials. Specifically, the $[Os(bpy)_2Cl(p2p)]^+$ complex where bpy is 2,2′-bipyridyl and p2p is 1,2-bis(4-pyridyl)ethane has two methylene groups at the centre of the bridging ligand. In contrast, the $[Os(bpy)_2Cl(bpe)]^+$complex, where bpe is *trans*-1,2-bis(4-pyridyl)ethylene, has a double bond in the bridging ligand giving a conjugated bridge. In this way, the effect of bond conjugation in the bridging ligand on the rate of electron transfer could be probed. The surface active complex, $[Os(OMe\text{-}bpy)_2Cl(p3p)]^+$, where OMe is 4,4′-dimethoxy-2,2′-bipyridyl and p3p is 1,4-trimethylene dipyridine was selected for the study on the influence of the nature of the electrode material on voltammetric response. The methoxy groups are electron donating and this complex has a low redox potential making it possible to probe the electrochemical properties even on rather electropositive metals.

The $[Os(bpy)_2Cl(4\text{-bpt})]^+$complex, where 4-bpt is 3,5-bis(2-pyridyl)1,2,4- triazole, has a five membered ring at the centre of the bridging ligand giving greater electronic delocalisation than the p2p and bpe ligands. The $[Ru(bpy)_2Cl(4\text{-tet})]^+$ complex, where 4-tet is 3,6-bis(4-pyridyl)-1,2,4,5-tetrazine, has a six membered ring at the centre of the bridging ligand. These complexes allowed the effect of a high degree of aromaticity in the bridging ligand to be assessed electrochemically.

As well as electrochemical techniques, spectroscopy was used as a corroborative technique to probe certain effects. The effect of conjugation of the bridging ligand was explored in terms of its influence on the UV-vis absorption spectra of osmium complexes in solution in acid media. By demonstrating the decrease in the absorption at 400 nm due to the protonation of the conjugated bridging ligand, the reduction in electron density at the metal and head groups allowed by the conjugation in the bridge has been demonstrated qualitatively. This spectroscopic evidence suggests that the

extent of electronic coupling between the metal and the bridging ligand is stronger when the bridge contains a double bond.

6.3. Construction and Testing of the Electron Transfer Computer Model

For the voltammetric studies on the adsorbed complexes, an electron transfer computer model was constructed. Finklea and Hanshew[3] had assembled a model describing through-space electron tunnelling which provides a good description of electron tunnelling in monolayers of thiols with pendant redox centres ($HS(CH_2)_nCONHCH_2pyRu(NH_3)_5^{2+}$, n = 10, 11, 15). Chidsey,[4] Creager[2], and Murray,[5] had modelled nonadiabatic heterogeneous electron transfer for long chain alkanethiol monolayers using similar expressions to those of Finklea and Hanshew except that the energy-dependent prefactor in the tunnelling probability expression was excluded.

In the model developed in this work, both the adiabatic and nonadiabatic electron transfer models were combined in a unique way so that the simplex algorithm could select which model most closely matched the experimental data. Moreover, the heterogeneous rate constants and the Marcus reorganisation energies for the adsorbed species were found by fitting the complete voltammograms rather than the peak potentials as had been reported previously.[2] The model was tested with theoretical data containing various capacitive background currents and found to be, in spite of these distortions, very sensitive for k^o, the heterogeneous electron transfer rate constant. As the distortions were increased, the model became less sensitive for λ, the Marcus reorganisation energy. For example, in the case of a theoretical voltammetric response distorted with a horizontal background current having a current value equal to 25% of the anodic peak current response, the value determined for k^o was distorted by approximately 10%. The error in the value determined for λ, however, was much higher at 30%.

Novel tests were carried out on the model. The sensitivity for k^o, and λ at different scan rates was investigated and a lower limit on scan rate was determined. Currents in the double layer charging region were excluded and only the data in the oxidation

peak were used. Surprisingly, in this case, the model had difficulty finding the true values for k^o and λ. The model was extended to search for E_B, the barrier height, and the electron transfer distance, respectively. Because the model became insensitive to these parameters as soon as any capacitive background currents were present and because computation times were too long, searches were subsequently restricted to looking for two parameters, namely k^o and λ.

The present model which is based on comparing the full cyclic voltammogram was compared theoretically to Creager's[2] method which uses the dependence of peak potential on scan rate. It was found to be superior in that only one cyclic voltammogram was necessary and the simplex did not get rapped in local minima to the same extent as with the peak potential vs. scan rate method.

These theoretical tests had shown the model to be an extremely powerful diagnostic tool for extracting k^o and λ from a single cyclic voltammogram. The next objective was to use the model on actual experimental systems and the first task was to probe the influence, on k^o and λ, of a double bond rather than a single bond in the bridging ligand.

6.4. Conjugated vs. Non-Conjugated Bridges

The production of "molecular wires" that promote fast heterogeneous electron transfer between a remote redox centre and a metal surface is important for high speed molecular electronics applications, e.g., molecule-based computing. One notable strategy in this area is to use conjugated rather than aliphatic bridges to achieve faster electron transfer rates.

The effect of using a conjugated, *trans*-1,2-bis(4-pyridyl)ethylene, bpe, vs. a non-conjugated bridge, 1,2-bis(pyridyl)ethane, p2p, on the heterogeneous electron transfer rate constants for $[Os(bpy)_2Cl]^+$ moieties attached to the surface of platinum microelectrodes was probed. It might be expected that the presence of the conjugated bond in the bridging ligand would give rise to a higher rate constant and a through-bond tunnelling mechanism due to the greater electronic delocalisation associated with the double bond.

Using the new model, the voltammetric response observed at high scan rates was studied where heterogeneous electron transfer across the metal/monolayer interface influences the experimental response. Somewhat surprisingly, despite the conjugated bridge and short electron transfer distance, for the $[Os(bpy)_2Cl\ (bpe)]^+$ the voltammetric response is best modelled as a through-space tunnelling process.

With this through-space tunnelling model, excellent agreement was observed between the experimental and theoretical anodic peak potentials and both peak currents. Moreover, there was general agreement between the theoretical and experimental currents along the full anodic branch. However, poorer agreement was observed for the cathodic branch which may arise from oxidation state dependent electronic coupling or more likely, differences in the reorganisation energy caused by changes in the monolayer's solvation as it is oxidised.[6] The modelling revealed that while the quality of the fit obtained using the two models were broadly comparable, the peak currents predicted by Finklea's through-space tunnelling model more closely matched the experimental values. That these voltammograms were best-described by a through-space tunnelling model agrees with previous investigations[7] where a value of $1.6\pm0.2\ Å^{-1}$ was obtained for the distance dependent tunnelling parameter, β. A through-space rather than through-bond mechanism was unexpected given the aromatic character of the *trans*-1,2-bis(4-pyridyl)ethylene bridge. However, it is important to note that the electron transfer distance examined here, 10 Å, is considerably shorter than that traditionally explored using alkane-thiol self-assembled monolayers, 20 - 30 Å. Quantum mechanical spillover of the metal electron density beyond the electrode/monolayer interface, and the delocalised character of the electron density on the electrode, may be relatively more important for these short bridging ligands.

The standard heterogeneous electron transfer rate constant, k°, for the conjugated bridge was determined to be $9.4x10^3\ s^{-1}$ which is approximately a factor of 30 *smaller* than that observed for a longer, aliphatic bridge, 1,2-bis(4-pyridinyl)ethane. This result is consistent with the through-space tunnelling mechanism already proposed in that the less rigid p2p bridge probably has sufficient flexibility to reduce the electron

transfer distance below the value of 10 Å expected on the basis of a rigid-rod model. It is important to note that unlike a through-space pathway, the electron transfer distance for through-bond tunnelling mechanisms is independent of the monolayer's conformation. Therefore, the decrease in heterogeneous electron transfer rate constant observed here on going from a non-conjugated to a conjugated bridge, is not expected for a through-bond tunnelling mechanism.

Modelling the complete voltammogram allows the contributions from electronic coupling and free energy of activation to be decoupled. This analysis reveals free energies of activation of 8.7±1.2 and 11.4±0.8 kJ mol^{-1} for the bpe and p2p bridges, respectively. This difference in the free energy of activation most likely corresponds to a different monolayer structure in the two circumstances and would correspond to more nonpolar environment within the p2p bridged monolayer. This issue is considered further in Section 6.6.

The accuracy of the values for k^0 and $\Delta G^{\neq}$ obtained from the model was determined by comparing to those values determined by an independent technique. The rate constants and the $\Delta G^{\neq}$ values given by the model from the voltammetric responses of both complexes with the conjugated and non-conjugated bridges were, to within experimental error, identical to those values obtained using chronoamperometry. This independent verification proves the accuracy and utility of the cyclic voltammetry model.

For this study on the influence of conjugation in the bridging ligand, platinum and gold microelectrodes were used. It has been shown by the determination of pre-exponential factors that the level of coupling between the localised redox states of the monolayer and the delocalised metallic states of the electrode is much smaller than that expected for an adiabatic electron transfer. Also, it has been determined that the pre-exponential factor is approximately an order of magnitude higher for the p2p than for the bpe bridge indicating that the redox centre and electrode are more strongly coupled for the aliphatic system. However, these investigations focused on the effect of changing the structure of the bridging ligand. A relevant question at this point would be to ask about the role of the material on the other side of the electrode /

monolayer interface, namely the electrode material, itself. The role of the electrode material in electron transfer processes was investigated next, in Chapter 5 and the main conclusions are summarised in the next section.

6.5. Effect of the Electrode Density of States

While attention has been focused on the role that distance, structure and the redox composition of the monolayer play in dictating the rate and mechanism of electron transfer,[8] the effect of changing the nature of the electrode material has not been probed with the same intensity. The newly constructed electron transfer model described in detail in Chapter 3 allowed the influence of the nature of the electrode material on the voltammetric response of adsorbed monolayers to be investigated.

Adsorbed monolayers of $[Os(OMe\text{-}bpy)_2Cl(p3p)]^{1+}$ were formed on platinum, mercury, gold, silver and carbon microelectrodes, OMe-bpy is 4,4′-dimethoxy-2,2′-bipyridyl and p3p is 1,4-trimethylene dipyridine. They exhibited nearly ideal electrochemical responses as the potential and experimental timescale were varied over a wide range. These monolayers were used to probe the effect of changing the density of electronic states within the electrode on the heterogeneous electron transfer rate. High scan rate cyclic voltammetry revealed that the free energy of activation was consistent with that expected for a simple outer sphere reaction.

The rate constant is given by the following equation:

$$k^{\circ} = A_{et} \exp(-\Delta G^{\neq} / RT) \qquad (1)$$

where A_{et} is the pre-exponential factor (the product of κ_{el} the electronic transmission coefficient and υ_n the nuclear frequency factor) and $\Delta G^{\neq}$ is the electrochemical free energy of activation. The values of A_{et} were determined using the experimental values of $\Delta G^{\neq}$ and k°. Significantly, irrespective of the identity of the electrode material. these prefactors were approximately six orders of magnitude smaller than those expected for an adiabatic electron transfer reaction.[9] Moreover, given that the free energies of activation were similar to that expected for a simple outer sphere reaction, these low rate constants are caused by the reaction being non-adiabatic, i.e.,

$\kappa_{el} << 1$. The pre-exponential factor was also shown to be sensitive to the identity of the electrode material with the lowest value being observed for carbon while $\kappa_{el}\upsilon_n$ is largest for platinum. This large difference might be expected given the known sensitivity of heterogeneous electron transfer to the density of edge-planes in carbon electrodes.[10,11] More significant perhaps, were the differences observed between Pt and Au. The density of states, ρ_F, of platinum is approximately 7.5 times[12] that of gold which would be expected to cause a proportional increase in A_{et}. However, an increase of less than 3 was observed. Marcus and Gosavi[13] have considered this issue for a highly non-adiabatic electron transfer involving an $[Ru(NH_3)_5$ pyridine$]^{2+}$ redox centre tethered to an alkanethiol monolayer containing 15 methylene spacer groups. This model predicts that the ratio k_{Pt} / k_{Au} will depend only weakly on the electron transfer distance or the overpotential. More significantly, it highlights the importance of considering the identity of the orbitals that are responsible for increasing ρ_F and how efficiently these orbitals couple with those of the redox centre/bridge. Rather than a simple proportionality between k° and ρ_F, k° depends on ρ_F modulated by the square of the coupling strength. The Marcus and Gosavi model predicts a ratio of $A_{et,Pt}$ / $A_{et,\ Au}$ of 1.8 compared to the ratio of 2.9(0.6) observed here. Therefore, the experimental results reported here indicate that while the increased density of states found in Pt arising from *d*-orbitals are not entirely ineffective for coupling, their coupling efficiency is well below that found for the dominant *sp*-states of gold.

The electron transfer model described in Chapter 3 successfully identified the electron transfer process, in the study of the adsorbed monolayers, as non-adiabatic. For the second time, the model extracted values for k° for adsorbed monolayers which were in excellent agreement with those measured by chronoamperometry. This independent verification of the results from the model was of paramount importance as it demonstrates the accuracy of the model. Different treatments of cyclic voltammetric data were investigated with the model and the usefulness of the model as an electrochemical diagnostic tool was, once again, demonstrated.

6.6. Discussion of the Electron Transfer Rate Constants and Reorganisation Energies.

In this work, the heterogeneous electron transfer rate constant, k^o and the free energy of activation, $\Delta G^{\neq}$, were determined from the voltammetric responses of three redox active adsorbed species on platinum microelectrodes.

The reasons for the higher rate constant for the p2p bridged system relative to the bpe bridged system have already been discussed in Section 6.4 of this chapter. In Table 6.1, these values are given again along with the value for the p3p bridged system. From Table 6.1, it can be seen that the p3p bridged system, as well, has a higher rate constant (by a factor of four) than the bpe bridged system. The reasons for this are precisely the same as those for the p2p, bpe bridged systems comparison. This result is consistent with the through-space tunnelling mechanism already proposed for both the bpe and p2p bridged systems in that the less rigid p3p bridge probably has sufficient flexibility to reduce the electron transfer distance below that for the bpe bridged system. However, the effective electron transfer distance is likely to be larger for the p3p bridge than for the p2p bridge explaining the slower rate constant of p3p relative to p2p bridged system. This comparison between the rate constants determined for the p2p and p3p bridged systems illustrates the fundamental experimental fact that the rate of electron transfer (as Marcus theory predicts) depends on electron transfer distance.

Table 6.1 also gives the free energies of activation, $\Delta G^{\neq}$ for the three redox active species under investigation in this work. Significantly, the p3p bridged system has the lowest value for $\Delta G^{\neq}$ and, again, the explanation is the same as for the comparison between the bpe and p2p bridged systems. This difference in the free energy of activation most likely corresponds to a different monolayer structure and would correspond to more nonpolar environment within the p3p bridged monolayer.

To look at this in more detail, it is possible to calculate the Marcus predicted static dielectric constants from this equation from Chapter 1,

$$\Delta G_{os} = \frac{n^2 e^2}{32\pi\varepsilon_o r}\left(\frac{1}{\varepsilon_{op}} - \frac{1}{\varepsilon_s}\right) \qquad (2)$$

where n is the number of electrons transferred, e is the electronic charge, ε_o is the permittivity of free space, r is the molecular radius, ε_{op} and ε_s are the optical and static dielectric constants, respectively. Using a molecular radius of 7.5 Å for these complexes,[14] and the optical and static dielectric constants of bulk water, 1.77 and 78.54, respectively, a value of 12.8 kJ mol^{-1} is predicted by Marcus for ΔG_{OS}. This value is greater than the values determined for $\Delta G^{\neq}$ (See Table 6.1).

Both Finklea[3] and Chidsey[4] have reported a similar discrepancy. One explanation for the substantial disagreement between the Marcus predicted ΔG_{OS} and the measured $\Delta G^{\neq}$s is that the local static dielectric constant at the electrode / electrolyte interface may be substantially smaller than that of bulk water. This explanation may be tested by using the values already determined for $\Delta G^{\neq}$ in Equation 2 for ΔG_{OS}. The calculated values for the static dielectric constants at the electrode/electrolyte interface, using the measured $\Delta G^{\neq}$s, are given in Table 6.1 and are substantially less than the value for bulk water. A higher value for the static dielectric constant implies a more polar environment at the electrode/electrolyte interface. Therefore, according to this explanation, it is clear that the bpe bridged system is more polar than both the p2p and p3p bridged system, with the p3p bridged system having the lowest polarity.

Table 6.1. Rate constants, free energies of activation for the $Os^{2+/3+}$ redox reaction occurring within $[Os(bpy)_2Cl(bpe)]^+$, $[Os(bpy)_2Cl(p2p)]^+$ and $[Os(OMe\text{-}bpy)_2Cl(p3p)]^{1+}$ monolayers where bpe is *trans*-1,2-bis(4-pyridyl)ethylene, p2p 1,2-bis(4-pyridyl) ethane, OMe-bpy is 4,4′-dimethoxy-2,2′-bipyridyl and p3p is 1,4-trimethylene dipyridine.[a] ϵ_s is the Marcus predicted static dielectric constant.

Complex	**10^{-3} k° / s-1**	**$\Delta G^{\neq}$ / kJ mol^{-1}**	**ϵ_s**
$[Os(bpy)_2Cl(bpe)]^+$	9.4(0.9)	11.4(0.8)	13.8
$[Os(bpy)_2Cl(p2p)]^+$	305(26)	8.7(1.2)	5.3
$[Os(Ome\text{-}bpy)_2Cl(p3p)]^{1+}$	40(2)	7.3(0.5)	4.0

[a] Supporting electrolyte is 0.1 M aqueous $LiClO_4$.

6.7. Final Conclusions

The usefulness of the combined simplex / Marcus electron transfer model has been demonstrated, and in the future it will allow high quality kinetic data to be obtained under different experimental conditions, e.g., solvent, temperature, ionic strength.

The simplex algorithm, itself, has been substantially modified in order to operate successfully with these systems. Limits to prevent overflow errors, specific exit conditions to sense local minima, automatic re-starts on detection of local minima and the ability to sequentially process any number of experimental cyclic voltammograms have all been incorporated into the simplex algorithm. Random numbers (within a realistic range) were used as the preferred starting points for the algorithm in order to establish that the simplex would find the solution from any starting point. These modifications allowed the model to successfully complete the examination of the experimental data and, in all cases, to report the correct results.

In the next and final chapter, the technological context of the electron transfer model is outlined as the future applications for the model are discussed.

6.8. References

1 Nelder; Mead, *Computer. J.* **1965**, *79*, 308.

2 Weber, K.; Creager, S. E. *Anal. Chem.* **1994**, *66*, 3164.

3 Finklea, H. O.; Hanshew, D. D. *J. Am. Chem. Soc.* **1992**, *114*, 3173.

4 Chidsey, C. E. D. *Science* **1991**, *251*, 919.

5 Tender, L.; Carter, M. T.; Murray, R. W. *Anal. Chem.* **1994**, *66*, 3173.

6 Hupp, J. T.; Weaver, M. J. *J. Phys. Chem.* **1984**, *88*, 6128.

7 Forster, R. J.; Faulkner, L. R. *J. Am. Chem. Soc.* **1994**, *116*, 5444.

8 Finklea, H. O. "*Encyclopedia of Analytical Chemistry*", Wiley, New York, **2000**.

9 Weaver, M. J. *Chem. Rev.* **1992**, *92*, 463.

10 Ray, K. G.; McCreery, R. L. *J. Electroanal. Chem.*, **1999**, *469*, 150.

11 McCreery, R. L.; Cline, K. K.; McDermott, C. A.; McDermott, M. T., *Colloids and Surfaces A*: **1994**, *93*, 211.

12 Papaconstantopoulous, D. A., *Handbook of Band Structure of Elemental Solids*, **1986**, Plenum Press, New York.

13 Gosavi, S.; Marcus, R. A. *J. Phys. Chem. B*; **2000**, *104*, 2067.

14 (a) Goodwin, H. A.; Kepert, D. L.; Patrck, J. M.; Skelton, B. W.; White, A. H. *Aust. J. Chem.* **1984**, *37*,1817. (b) Ferguson, J. E.; Love, J. L.; Robinson, W. T. *Inorg. Chem.* **1972**, *11*, 1662. (c) Rillema, D. P.; Jones, D. S.; Levy, H. A. J. *Chem. Soc., Chem. Commun.* **1979**, 849.

CHAPTER 7

Future Applications for the Electron Transfer Model

7.1. Introduction

In this final chapter, the intention is to discuss new areas of application for the developments in this thesis. Over the time span of this work, the computation time for the heterogeneous electron transfer model has decreased dramatically from days to tens of minutes due primarily to the increase in microprocessor speed in personal computers. So the complexity of the function at the centre of the model no longer prevents the finding of the solution in "real time". Therefore, as computer microprocessor speeds increase, this model could be combined with even more complex functions and still produce results as experiments are being carried out. By replacing the function in the model with other mathematical functions based on the relevant theory, the model could be used in many different fields. In this chapter, some areas in which the model or more accurately, variants of the model can be applied with useful effect will be explored.

7.2. Distributions in Electrochemical Parameters

It has been demonstrated how the model based on heterogeneous electron transfer theory can find the true values for k^o, the heterogeneous rate constant, and the thermodynamic parameter, λ, from simple cyclic voltammograms of adsorbed monolayers. Of course, in searching for the true value for k^o, there is an implicit assumption. This assumption is that there is, in fact, only one true value for k^o.

Researchers conducting experiments into adsorbed monolayers are attempting to control the microenvironment within which the electron transfer process takes place. By controlling vital parameters such as the electron transfer distance or the type of bonds through which the electron transfer might proceed, they can gain an understanding of how these processes occur. This understanding may then be brought forward and perhaps, applied into other technological areas, i.e., solid state electronics, catalysis, or corrosion studies. However, the attempt to control all variables in the microenvironment can sometimes be only partially successful. This can cause unexplained differences between the experimental results and those expected from theory, e.g., experimental cyclic voltammetric peaks are often broader than theory would predict. One explanation for this could be that the electron transfer

process is occurring at more than one rate. Instead of only one true value for the heterogeneous rate constant k^o, there is in fact a distribution of k^o values in the cyclic voltammetric response.

This is not a rare occurrence, e.g., in biological systems, particularly, there are often multiple electron transfer pathways each with a different rate constant. In fact, one of the suggested causes for apparent nonideal voltammograms has been kinetic dispersion.[1] This phenomenon is closely linked to the distribution of formal potentials.[2] Any spread of formal potentials will lead to an apparent dispersion in electron transfer rates. Distribution of formal potentials is indicated by peak broadening of reversible voltammograms provided that other causes of peak broadening can be ruled out. Kinetic dispersion is probably caused by double layer effects.[3] Moreover, researchers can design experiments intended to produce a response based on a number of different rates of electron transfer, e.g., adsorbing mixed species with different bridging ligands with varying electron transfer distances. Existing electron transfer theory does not consider the experimental possibility of a distribution of electron transfer rates at a microelectrode. So how can the new model be used to investigate this?

Presently, the sequence of events within the model is the following. Random starting guesses (within realistic values) for k^o and λ are made by the program. At each overpotential, a theoretical current is calculated using these values for k^o and λ in the integral function based on the Marcus electron transfer theory. The difference between each theoretical current and the corresponding (i.e., at the same overpotential) experimental current is squared. The total sum of the differences squared is calculated and logged into the simplex algorithm.

The simplex algorithm then changes the values for k^o and λ and recalculates new theoretical currents based on these values. In fact, the first three theoretical cyclic voltammograms simulated are based on (k^o, λ), (1.2 x k^o, λ) and (k^o, 1.2 x λ). The pair of input values which results in the lowest value for the sum of squares of the differences becomes the starting pair of values for the next cycle of the simplex. This

cycle is repeated until the best fit values for k^o and λ are found having the minimum sum of the squares of the differences.

There are a number of methods that could be used to build the ability to simulate a distribution of k^o values into model. Bearing in mind, that one cannot know in advance whether such a distribution of k^o values exists in the experimental system, the simplex could be allowed "to decide" whether a distribution of k^o values is present and how wide that distribution is. How would this issue be approached?

For a start, three parameters, k^o, λ, and a new "distribution factor" would be searched for. This distribution factor would be present as a divisor of whatever the simplex estimate of k^o is. By using a For....Next loop around the calculation of each theoretical current, several theoretical currents based on different estimates for k^o would be calculated at each overpotential and then averaged. The distribution factor would control both the width of the k^o distribution and the number of k^o values present in the distribution. The average theoretical current would be compared to the experimental and thus, the simplex could narrow the distribution or widen it depending on the affect on the sum of the differences squared.

For example, the loop might have the following sequence:

FOR (k^o estimate) = (k^o estimate)- (k^o estimate)/distribution factor
TO (k^o estimate) = (k^o estimate)+ (k^o estimate)/distribution factor
STEP (k^o estimate)/distribution factor
CALCULATE THEORETICAL CURRENT
NEXT (k^o estimate)
CALCULATE THE AVERAGE THEORETICAL CURRENT
RETURN

If the distribution factor starting value = 1 and the k^o estimate = 4×10^4 s^{-1} then just one theoretical current would be calculated for k^o estimate = 4×10^4 s^{-1} at each overpotential, i.e., no distribution present. The simplex could change this distribution factor to 0.5, say. Then three theoretical currents would be calculated based on three values for k^o, namely 2×10^4, 4×10^4 and 6×10^4 s^{-1}.

So the simplex, could return a value of 1 for the distribution factor along with its estimates for k^o and λ, indicating that the theoretical best fit is found when there is no distribution of k^o present. On the other hand it could return a value other than 1 indicating the presence of a distribution of k^o values and an estimate of the width of that distribution.

There would be at least two practical consequences of this approach. The theoretical cyclic voltammetric peak would broaden depending on the width of the k^o distribution. Therefore, a theoretical peak broadening effect would have been successfully built into the model. The second consequence of this would be that the computation time would increase in direct proportion to the number of different k^o values estimated to be in the distribution by the simplex. However, with the inevitable increase in microprocessor speed referred to in the introduction, the computation time would not be a problem in the future.

The logic outlined above for a model incorporating a distribution of k^o values could equally be applied to a model checking for the presence of a distribution of formal potentials in the experimental system. Again, theoretical peak broadening would occur with the model controlling the width using variations in the formal potential. When it is considered that any of the relevant parameters or combinations of these parameters could be treated in this way, it becomes obvious just how powerful the model is as a diagnostic tool.

7.3. Application to Solution Phase Studies

The electron transfer model as constructed is designed to be a tool for the electrochemist conducting studies of adsorbed monolayers. However, there is no reason why the model cannot be constructed with the theoretical equations suitable for simulation of the cyclic voltammetric response of solution phase species.

In Chapter 2, diffusion coefficients were measured for several osmium and ruthenium complexes. The solution phase properties of these complexes were investigated. This was carried out by extracting a small number of data from individual cyclic

voltammograms in a series. The peak current and the peak to peak separation are particularly important and are determined for each CV and then the diffusion coefficient and the first order standard rate constant can be estimated.

However, in the case of adsorption of a monolayer, it has been seen that by comparing the complete theoretical cyclic voltammogram to an experimental cyclic voltammogram as opposed to extracting one datum, i.e., the peak potential, more accurate kinetic and thermodynamic information can be obtained. It is possible and, indeed, likely that there is a similar parallel in the cyclic voltammetry of solution phase species. The mass transport and kinetic equations used to predict the current flowing as a function of time or potential due to a particular electrochemical mechanism at a given electrode geometry would be used in the simulation. The simplex would vary rate constants, transfer coefficients and / or diffusion coefficients in order reduce the sum of the squares of the differences between the simulated theoretical cyclic voltammogram and the experimental voltammogram. This method could then be compared to the standard procedure which was described in Chapter 2. From what has been shown here with respect to the extraction of kinetic and thermodynamic parameters from cyclic voltammetric studies of adsorbed species, it seems likely that this approach would be far superior to the standard approach for studies of solution phase species.

7.4. Correcting for Capacitive Current

In Chapter 3, it was shown how "robust" the model is with respect to extracting accurate values for k^o and λ from cyclic voltammetric data containing large capacitive background currents. Nevertheless, it was shown how these capacitive background currents could distort the cyclic voltammogram so that the values returned by the model for k^o and λ deviate from the true values. Therefore, it would be always initially attempted to correct for capacitive current before running the model. This is a time consuming first step.

There are three approaches to correcting for capacitive current: experimental background subtraction, background subtraction and theoretical modelling. In experimental background subtraction, the current obtained from a CV collected in the absence of electroactive species is subtracted from current collected in the presence of electroactive species. This procedure assumes that the double layer remains the same in the two experiments, which is generally true because the double layer properties are most strongly related to the excess electrolyte. A background subtraction also eliminates the distortion due to residual Faradaic current from electrolyte and solvent impurities.

Theoretical modelling of capacitive background currents is more difficult, since capacitance is an undetermined (usually) function of potential. The best method would be to incorporate an automated data "cleanup" step at the start of the model. This would be, in fact, a sort of theoretical background subtraction performed on the experimental data prior to the launch of the electron transfer model. The steps involved in background subtraction are fairly straightforward but are carried out manually at the present time. These steps involve calculating the slope of the background current-overpotential line. Then the background current is calculated at each overpotential using the equation of the line. This theoretical background current is finally subtracted from the experimental current. The model is applied to this background subtracted experimental data. It would be relatively easy to automate these steps using a Microsoft Excel macro that would greatly speed up the analysis of experimental cyclic voltammograms.

7.5. Application in Biological Systems

An important consequence of the small size of microelectrodes is that they can be placed inside biological tissues and used to monitor chemical concentrations in this environment. In fact, microelectrodes presently serve as important tools in biomedical research.[4,5]

Carbon fibre is the preferred electrode material for in vivo use because it is less prone to fouling by adsorption of proteins than gold or platinum. These microelectrodes when implanted in the brain can be used to examine the dynamic concentration changes of the neurotransmitter dopamine.[6] In humans, it has been shown that a depletion of dopamine in the brain leads to Parkinson's disease. In thin slices, of brain tissue, the electrodes can be used to simultaneously detect neurotransmitter secretion and oxygen use. Neurotransmitters are secreted by neurons and act on specific receptors located on adjacent neurons. In this way, chemical communication between these cells is known to occur. Thus, many measurements using carbon fibre electrodes in vivo have focussed on measurements in the central nervous system.

The measurement of oxygen by electrochemical methods gives insight into blood flow into the tissue as well as metabolism. The electrochemical measurement of ascorbic acid in brain tissue in response to various stimuli has provoked considerable interest in the role which this molecule plays in the brain. But this role, has yet to be fully defined. All of these studies were carried out without the aid of a model which would correctly determine the electrochemical parameters at the centre of these processes in the brain. A model such as that described here would find numerous applications in biomedical research, e.g., in many cases in this area, precise mechanisms for processes in the brain are not fully understood. A simulator could be constructed using various mechanistic possibilities and then could try to match these theories to the experimental response. It would then select the best fit from the various theoretical possibilities. In this way, the simulator could contribute to the elucidation of the correct pathways in these processes.

7.6. Integrated Electrochemical Diagnostic System

At the outset in Chapter 1, it was stated that one of the objectives of this work was to construct a model for the study of electron transfer across the electrode / monolayer interface. As this objective has now been achieved, it is appropriate to consider how to expand this objective into electrochemistry generally. It has already been pointed out in this chapter how the model could be applied into studies of monolayers with unusual properties (distributions of k^o or formal potentials), solution phase studies and for capacitive background current correction.

It is now possible, using the model as a "template", to develop a fully integrated electrochemical diagnostic system. This system would incorporate all existing electrochemical theory and would bring this theory to the electrochemical workstation. At present, the ubiquitous computer is used to make the relevant calculations from the electrochemical data, e.g., in cyclic voltammetry, the peak potentials, peak currents and the peak areas are reported with the cyclic voltammogram. However, there is no interpretation by the computer program of the electrochemical significance of the CV.

It should now be possible to bring sophisticated electrochemical interpretation to the instrument workstation. Does the CV or series of CVs correspond to the response for solution phase species exclusively? Is there any adsorption electron transfer process taking place simultaneously? What is the diffusion ccefficient and first order heterogeneous rate constant? What is the number of electrons involved? If it is a response from an adsorbed species, does the adiabatic or non-adiabatic Marcus electron transfer theory apply to the system? Answers to all these questions and others would be available immediately following the experiment. So the electrochemical interpretation would become instantly part of the experimental work and would immediately influence the choice of following experiments and experimental conditions.

The development of an integrated electrochemical diagnostic system would be of immense value to the electrochemical researcher.

7.7. References

1 Honeychurch, M. J., Rechnitz, G. A., *Electroanalysis*, **1998**, *10*, 7

2 Honeychurch, M. J., Rechnitz, G. A., *Electroanalysis*, **1998**, *10*, 285

3 Creager, S. E., Weber, K, *Langmuir,* **1993,** *9*, 844.

4 Pereira, A. C.; Fertonani, F. L.; Neto, G. D., *Talanta,* **2001,** *53,* 801.

5 Smith, P. J. S.; Trimarchi, J., *AM J Physiol-Cell PH,* **2001,** *280,* C1.

6 Bath, B. D.; Michael, B. J.; Trafton, B. J., *Anal. Chem.,* **2000,** *72*, 5994.

Appendix A

Code for the Combined Adiabatic / Non-Adiabatic Electron Transfer Model

Comments on the Code

In this appendix, the code for the Microsoft Excel 97 macro used for the combined adiabatic / non-adiabatic electron transfer model is given. The computer language is Visual Basic. This code represents just one of the many different versions of the model used throughout this work.

In this version, the search for 3 parameters, namely λ (i.e., LOS or C(1)), k^o (i.e., k or C(2)), and the Adiabatic factor (i.e., C(3)) is started with random guesses for the first 2 and the Adiabatic factor =1. After the best fit has been found, the model will restart the search using the first best fit values as starting values. Finding the same values for the best fit a second time indicates a true minimum has been found. A result for the Adiabatic value which is greater than 1 indicates that the electron transfer is adiabatic. If a value less than 1 is preferred, the electron transfer is non-adiabatic according to the model. The anodic branch of cyclic voltammograms for the same system but at different scan rates can be processed consecutively by this code as it will move to the next data set after the best fit has been found.

As the simplex changes the input values for λ, k^o and the Adiabatic factor, very small and very large numbers can be generated. If the numbers calculated are greater or smaller than certain limits, an overflow error will occur causing execution to stop. In order to prevent this and to allow the model to work through the data without interruptions, the calculated values are kept between certain limits which are called overflow limits. In the model, the overflow limit is set to 200 which will limit the maximum value calculated to exp(200) and the minimum value calculated to exp(-200). Keeping all calculated values within these limits prevents the generation of overflow errors which halt execution.

This exit condition, i.e., when the best fit is found, used in this version occurs when the difference between consecutive estimates for λ and k^o is less than exp(-20). The model displays the progress of the simplex on a chart and outputs the results for each scan rate on a spreadsheet. The code is given next:

```
Sub CombinedET()
Sheets("data").Select
Range("a20:f1000").Clear
Sheets("chart2").Select

pos = Worksheets("ox").Cells(9, 2).Value
tt = 4

ActiveWorkbook.Save
RLOS = Worksheets("ox").Cells(6, 5).Value
RK = Worksheets("ox").Cells(7, 5).Value
1: Dim XX(1000), YY(1000), zzz(1000), adiab(1000), nad(1000), HE(20)
   Dim SIMP(21, 20), LSQ(21), OP(20)
   Dim MEAN(20), REFL(20), DREFL(20), CONTR(20)
   Dim c(5)
If l = 1 Then l = 0: RLOS = Worksheets("ox").Cells(6, 5).Value: RK =
Worksheets("ox").Cells(7, 5).Value
np = Worksheets("ox").Cells(1, pos).Value
sp = 1
ep = np
tt = 4
If pos > (Worksheets("ox").Cells(3, 6).Value + 2) Then GoTo e:
Worksheets("ox").Cells(12, 2).Value = Worksheets("ox").Cells(18, pos).Value
'RANDOM GUESS FOR LOS AND K
Worksheets("ox").Cells(9, 5).Value = RLOS
Worksheets("ox").Cells(10, 5).Value = RK
Worksheets("ox").Cells(11, 5).Value = 1
Worksheets("ox").Range("E9: H10").NumberFormat = "general"
2: Worksheets("out").Cells(1, pos).Value = Worksheets("ox").Cells(18, pos).Value:
ActiveWorkbook.Save
Index = 20
Sum = 0
sum1 = 0
Sum2 = 0
sum3 = 0
R = 8.31: f = 96485
t = Worksheets("ox").Cells(8, 2).Value
res = Worksheets("ox").Cells(11, 2).Value
scanrate = Worksheets("ox").Cells(12, 2).Value
dt = Worksheets("ox").Cells(14, 2).Value
nernst = Worksheets("ox").Cells(15, 2).Value
norm = Worksheets("ox").Cells(2, 4).Value
radius = Worksheets("ox").Cells(4, 2).Value
area = 1 * 3.142 * (radius * 0.0001) ^ 2
barrierheight = Worksheets("ox").Cells(3, 2).Value
dist = Worksheets("ox").Cells(1, 2).Value


'Limits To prevent overflow
limit = 200
```

```
dredmax = Exp(limit)
dred1max = Exp(limit)
dredmin = Exp(-limit)
dred1min = Exp(-limit)
summax = Exp(limit)
tunnelmax = Exp(limit)
tunnel1max = Exp(limit)
sum2min = Exp(-limit)
summin = Exp(-limit)
tunnelmin = Exp(-limit)
tunnel1min = Exp(-limit)
sum2max = Exp(limit)
ssmax = Exp(limit)
ssmin = Exp(-limit)
betamax = limit
beta1max = limit
oxmax = Exp(limit)
oxmin = Exp(-limit)
ox1max = Exp(limit)
ox1min = Exp(-limit)
smax = limit
smin = -limit
Idimmax = Exp(limit)
E0 = Worksheets("ox").Cells(16, pos).Value

400   GoTo 20000: Rem  start the MAIN program
15000 Rem ******************************************
15010 Rem *** Subroutine: FUNCTION OF REGRESSION   ***
15100 Rem ******************************************
15200
brak1max = (limit)
brak1min = (-limit)
brak2max = (limit)
brak2min = (-limit)
summax = Exp(limit)
tunnel1max = Exp(limit)
apass = apass + 1

x = x - E0

'ADIABATIC ELECTRON TRANSFER

        'INTEGRATION

        For e = -1 To 1.8 Step 0.02
      afermi = 1 - ((1 + Exp(f * (e) / (R * t)))) ^ -1
      abeta = (Abs(((barrierheight * 1000) - f * e + (f * x / 2)) / f)) ^ 0.5
 If abeta > betamax Then abeta = betamax
      abeta1 = (Abs(((barrierheight * 1000) - f * e) / f)) ^ 0.5
```

```
 If abeta1 > beta1max Then abeta1 = beta1max
      atunnel = ((((barrierheight * 1000) - f * e + (f * x / 2))) * Exp(-abeta * dist))
      atunnel1 = ((((barrierheight * 1000) - f * e) * Exp(-abeta1 * dist)))
      If atunnel > tunnelmax Then atunnel = tunnelmax
      If atunnel1 > tunnel1max Then atunnel1 = tunnel1max

      If c(1) = 0 Then c(1) = 1
      adredc = ((-(((f * e) + (c(1) * 1000) - (f * x))) ^ 2 / (4 * (c(1) * 1000) * R * t)))

      If adredc > limit Then adredc = (limit)
      If adredc < -limit Then adredc = -limit

            adred = Exp(adredc)
      adred1c = ((-(((f * e) + (c(1) * 1000))) ^ 2 / (4 * (c(1) * 1000) * R * t)))
      If adred1c > limit Then adred1c = (limit)
      If adred1c < -limit Then adred1c = -limit

           adred1 = Exp(adred1c)
      aOx = afermi * adred * atunnel
 If aOx > oxmax Then aOx = oxmax
 If aOx < oxmin Then aOx = oxmin

      aOx1 = afermi * adred1 * atunnel1
If aOx1 > ox1max Then aOx1 = ox1max
If aOx1 < ox1min Then aOx1 = ox1min

      aSum = aOx
      aSum = aSum + asum1
      asum1 = aSum
      aSum2 = aOx1
      aSum2 = aSum2 + asum3
      asum3 = aSum2
If aSum > summax Then aSum = summax
If aSum < summin Then aSum = summin
If aSum2 > sum2max Then aSum = sum2max
If aSum2 < sum2min Then aSum = sum2min
 Next e
 If aSum > summax Then aSum = summax
   aaS = aSum

 If aSum2 = 0 Then aSum2 = 1
 If c(2) = 0 Then c(2) = 1
        If apass = 1 Then
              anormal = c(2) / aSum2
              aaS = aaS * anormal
              apass = 2
              afinit = 0:
              affinal = (Exp((x) * nernst)) / (1 + (Exp((x) * nernst)))
              aidim = (-(scanrate * 0.00001 * area) - ((nernst * res) ^ -1 * ((affinal -
afinit) * (1 - Exp(-aaS * dt))) / norm))
```

```
                ay = aidim
                If i = sp Then aOffset = aidim
                ay = aidim - aOffset

              adiab(i) = ay
              GoTo jump:
            End If
            anormal = c(2) / aSum2
            aaS = aaS * anormal
 If aaS < smin Then aaS = smin
            affinal = (Exp((x) * nernst)) / (1 + (Exp((x) * nernst)))
            i = i - 1
            x = XX(i) - E0
            affinalp = (Exp((x) * nernst)) / (1 + (Exp((x) * nernst)))
            i = i + 1
            x = XX(i) - E0
            afinit = affinalp - ((affinalp - afinit) * Exp(-aaS * dt))
    If aidim > Idimmax Then aidim = Idimmax
            aidim = (-(scanrate * 0.00001 * area) - ((nernst * res) ^ -1 * ((affinal -
afinit) * (1 - Exp(-aaS * dt))) / norm))
      If aidim > Idimmax Then aidim = Idimmax
          If i = sp Then aOffset = aidim
            ay = aidim - aOffset

adiab(i) = ay
aSum = 0
asum1 = 0
aSum2 = 0
asum3 = 0
jump:
brak1max = (limit)
brak1min = (-limit)
brak2max = (limit)
brak2min = (-limit)
summax = Exp(limit)
tunnel1max = Exp(limit)

pass = pass + 1:

'NON ADIABATIC ELECTRON TRANSFER

For e = -1 To 1.96 Step 0.02
      fermi = 1 + Exp(f * (e - x) / (R * t))
      fermi1 = 1 + Exp(f * (e) / (R * t))
      If c(1) = 0 Then c(1) = 1
      brak1 = ((f * (x - e + x - (c(1) / (f / 1000)))) ^ 2) / (4 * f * (c(1) / (f / 1000)) * R *
t)
      If brak1 > brak1max Then brak1 = brak1max
      If brak1 < brak1min Then brak1 = brak1min
      brak2 = ((f * (-e - (c(1) / (f / 1000)))) ^ 2) / (4 * f * (c(1) / (f / 1000)) * R * t)
```

```
        If brak2 > brak2max Then brak2 = brak2max
        If brak2 < brak2min Then brak2 = brak2min

        tunnel1 = Exp(-brak1)
        If tunnel1 > tunnel1max Then tunnel1 = tunnel1max
        tunnel2 = Exp(-brak2)
        dox = (fermi - 1) / fermi
        dox1 = (fermi1 - 1) / fermi1
        DRED = 1 / fermi
        Ox = tunnel1 * dox
        Ox1 = tunnel2 * dox1
        Sum2 = Ox1
        Sum2 = Sum2 + sum3
        sum3 = Sum2
        Sum = Ox
        Sum = Sum + sum1
        sum1 = Sum
If Ox > oxmax Then Ox = oxmax
 If Ox < oxmin Then Ox = oxmin


If Ox1 > ox1max Then Ox1 = ox1max
If Ox1 < ox1min Then Ox1 = ox1min

If Sum > summax Then Sum = summax
If Sum < summin Then Sum = summin
If Sum2 > sum2max Then Sum = sum2max
If Sum2 < sum2min Then Sum = sum2min
Next e
If Sum > summax Then Sum = summax
s = Sum
        If pass = 1 Then
                normal = c(2) / Sum2
                s = s * normai
                pass = 2
                finit = 0:
                ffinal = (Exp((x) * nernst)) / (1 + (Exp((x) * nernst)))
                idim = -((nernst * res) ^ -1 * ((ffinal - finit) * (1 - Exp(-s * dt))) /
norm)

If i = sp Then Offset = idim
            y = idim - Offset
 nad(i) = y
 y = (y + Abs(c(3)) * ay) / (Abs(c(3)) + 1)
  zzz(i) = y
                Return
            End If
            normal = c(2) / Sum2
            s = s * normal
            If s < smin Then s = smin
```

```
            ffinal = (Exp((x) * nernst)) / (1 + (Exp((x) * nernst)))
            i = i - 1
            x = XX(i) - E0
            ffmalp = (Exp((x) * nernst)) / (1 + (Exp((x) * nernst)))
            i = i + 1
            x = XX(i) - E0
            finit = ffmalp - ((ffinalp - finit) * Exp(-s * dt))
            idim = -((nernst * res) ^ -1 * ((ffinal - finit) * (1 - Exp(-s * dt))) / norm)
            y = idim
          If i = sp Then Offset = idim
            y = idim - Offset

nad(i) = y
y = (y + Abs(c(3)) * ay) / (Abs(c(3)) + 1)

zzz(i) = y
Sum = 0
sum1 = 0
Sum2 = 0
sum3 = 0
Worksheets("ox").Cells(12, 5) = counter
counter = counter + 1
15999 Return

20000 Rem ******************************************
20010 Rem *** MAIN program                    ***
20020 Rem ******************************************
20100 n = 3: Rem number of parameters
20110 n1 = n + 1
20150 GoSub 25000
20200
20210
20220
20300
20321 For i = 1 To n
If Worksheets("ox").Cells(i + 8, 5).Value < 0 Then Worksheets("ox").Cells(i + 8,
5).Value = Worksheets("ox").Cells(i + 8, 5).Value * -1
c(i) = Worksheets("ox").Cells(i + 8, 5).Value
If c(i) < 0 Then c(i) = c(i) * -1
c(i) = Worksheets("ox").Cells(i + 8, 5).Value
If c(i) = 0 Then c(i) = 1
c(i) = Worksheets("ox").Cells(i + 8, 5).Value


OP(i) = c(i)
Next i
20350 GoSub 22000: Rem initial simplex is generated
20380 GoSub 23000: Rem sorting of the simplex
21100  'GoSub 26000: Rem output of the whole simplex
21110 GoSub 24000: Rem output of the best point
```

```
21120 GoSub 27000: Rem mean vector without high point
21200 GoSub 32000: GoSub 33000: GoSub 34000
21210 LSQH = LSQ(n1)
21220 If (LREFL > LSQ(n1)) Then GoTo 21280
21230   For i = 1 To n: SIMP(n1, i) = REFL(i): Next i
21240   LSQ(n1) = LREFL
21280 If (LDREFL > LSQ(n1)) Then GoTo 21340
21290   For i = 1 To n: SIMP(n1, i) = DREFL(i): Next i
21300   LSQ(n1) = LDREFL
21340 If (LCONTR > LSQ(n1)) Then GoTo 21400
21350   For i = 1 To n: SIMP(n1, i) = CONTR(i): Next i
21360   LSQ(n1) = LCONTR
21400 If (LSQ(n1) < LSQH) Then GoTo 21500
21420 GoSub 35000: Rem Contraction towards best point
21500 Rem
21600 GoTo 20380
21890 Stop
21900 Rem ##############################################
21910 Rem ### MAIN program ends here            ###
21920 Rem ##############################################

      22000 Rem ******************************************
22010 Rem *** Subroutine: Initial Simplex        ***
22020 Rem ******************************************
22040 For i = 1 To n
If c(i) < 0 Then c(i) = c(i) * -1
If c(i) = 0 Then c(i) = 1

22050   SIMP(1, i) = c(i)

      22060 Next i
22070 GoSub 30000
22080 LSQ(1) = ss
22100 For j = 1 To n
22120   c(j) = 1.2 * c(j)
22140   GoSub 30000
22160   LSQ(j + 1) = ss
22200   For i = 1 To n
22220     SIMP(j + 1, i) = c(i)
22240   Next i
22260   c(j) = OP(j)
22300 Next j
22900 Return
23000 Rem ******************************************
23010 Rem *** Subroutine: Sorting the Simplex     ***
23020 Rem ******************************************
23100 For j = 1 To n
23120   LSQMIN = LSQ(j): IMIN = j
23140   For i = j To n1
23160     If LSQMIN < LSQ(i) Then GoTo 23240
```

```
23180    LSQMIN = LSQ(i): IMIN = i
23240   Next i
23300   For i = 1 To n
23320    HE(i) = SIMP(j, i)
23340    SIMP(j, i) = SIMP(IMIN, i)
23360    SIMP(IMIN, i) = HE(i)
23380   Next i
23400   LSQH = LSQ(j): LSQ(j) = LSQ(IMIN): LSQ(IMIN) = LSQH
23500 Next j
23700 Return

      24000 Rem ******************************************
24010 Rem *** Subroutine: OUTPUT              ***
24020 Rem ******************************************
24100
24120 For i = 1 To n
24181 Worksheets("ox").Cells(i + 8, 5) = SIMP(1, i)
24182 Worksheets("ox").Cells(i + 8, 6) = SIMP(n1, i)
 If Worksheets("ox").Cells(i + 8, 5).Value < 0 Then Worksheets("ox").Cells(i + 8,
5).Value = Worksheets("ox").Cells(i + 8, 5).Value * -1
 If Worksheets("ox").Cells(i + 8, 6).Value < 0 Then Worksheets("ox").Cells(i + 8,
6).Value = Worksheets("ox").Cells(i + 8, 6).Value * -1
 If Worksheets("ox").Cells(i + 8, 5).Value = 0 Then Worksheets("ox").Cells(i + 8,
5).Value = 1
 If Worksheets("ox").Cells(i + 8, 6).Value = 0 Then Worksheets("ox").Cells(i + 8,
6).Value = 1
 If SIMP(1, i) = 0 Then SIMP(1, i) = 1
  Worksheets("ox").Cells(i + 8, 8).Value = Abs(((SIMP(1, i) - SIMP(n1, i)) / SIMP(1,
i)) * 100)
  Next i
GoSub 24183

      'EXIT CONDITION
Worksheets("ox").Cells(10, 9) = Worksheets("ox").Cells(10, 7)
lso = Worksheets("ox").Cells(10, 9)
Worksheets("ox").Cells(10, 7) = LSQ(1)
cond = Abs((LSQ(1) - lso) / LSQ(1))
If cond < 10 ^ -20 Or end1 = 1 Then out = out + 1: end1 = 1 Else end1 = 0

If zz = 1 And out = 50 Then GoSub 24183: out = 0: zz = 0: tt = tt + 10:
Worksheets("out").Cells(tt, pos).Value = Worksheets("ox").Cells(9, 5).Value: tt = tt +
1: Worksheets("out").Cells(tt, pos).Value = Worksheets("ox").Cells(10, 5).Value: tt =
tt + 1: Worksheets("out").Cells(tt, pos).Value = Worksheets("ox").Cells(11, 5).Value:
tt = tt + 1: Worksheets("out").Cells(tt, pos).Value = Worksheets("ox").Cells(10,
7).Value: counter = 0: z = 0: l = l + 1: pos = pos + 1: GoTo 1:
If out = 50 Then GoSub 24183: out = 0: Worksheets("out").Cells(tt - 2, pos).Value =
RLOS: Worksheets("out").Cells(tt - 1, pos).Value = RK: Worksheets("out").Cells(tt,
pos).Value = Worksheets("ox").Cells(9, 5).Value: tt = tt + 1:
Worksheets("out").Cells(tt, pos).Value = Worksheets("ox").Cells(10, 5).Value: tt = tt
```

```
+ 1: Worksheets("out").Cells(tt, pos).Value = Worksheets("ox").Cells(11, 5).Value: tt
= tt + 1: Worksheets("out").Cells(tt, pos).Value = Worksheets("ox").Cells(12,
5).Value: counter = 0: z = 0: zz = zz + 1: GoTo 2:
If counter > 5 * 10 ^ 5 Then GoSub 24183: out = 0: zz = 0: tt = tt + 15:
Worksheets("out").Cells(tt, pos).Value = Worksheets("ox").Cells(9, 5).Value: tt = tt +
1: Worksheets("out").Cells(tt, pos).Value = Worksheets("ox").Cells(10, 5).Value: tt =
tt + 1: Worksheets("out").Cells(tt, pos).Value = Worksheets("ox").Cells(11, 5).Value:
tt = tt + 1: Worksheets("out").Cells(tt, pos).Value = Worksheets("ox").Cells(10,
7).Value: counter = 0: z = 0: l = l + 1: pos = pos + 1: GoTo 1:
If counter > 5 * 10 ^ 5 Then GoSub 24183: out = 0: Worksheets("out").Cells(tt - 2,
pos).Value = RLOS: Worksheets("out").Cells(tt - 1, pos).Value = RK:
Worksheets("out").Cells(tt, pos).Value = Worksheets("ox").Cells(9, 5).Value: tt = tt +
1: Worksheets("out").Cells(tt, pos).Value = Worksheets("ox").Cells(10, 5).Value: tt =
tt + 1: Worksheets("out").Cells(tt, pos).Value = Worksheets("ox").Cells(11, 5).Value:
tt = tt + 1: Worksheets("out").Cells(tt, pos).Value = Worksheets("ox").Cells(12,
5).Value: counter = 0: z = 0: zz = zz + 1: GoTo 2:
z = 0
Worksheets("ox").Cells(10, 7).NumberFormat = "general"

24200 Return

        25000 Rem **********************************************
25010 Rem *** Subroutine: READ DATA            ***
25080 Rem **********************************************
25100
25200
25201 For i = sp To ep 'Step 2
25400 XX(i) = Worksheets("ox").Cells(19 + i, 2).Value
        YY(i) = Worksheets("ox").Cells(19 + i, pos).Value
        Next i
Return


        26000 Rem **********************************************
26010 Rem *** Subroutine: Printing all Simplex    ***
26020 Rem **********************************************
26100 For i = 1 To n1
26120   For j = 1 To n
26140     Worksheets("ox").Cells(i, 8).Value = SIMP(i, j)
26160   Next j
26180   Worksheets("ox").Cells(i, 8).Value = LSQ(i)
26200 Next i
26500 Return
27000 Rem **********************************************
27010 Rem *** Subroutine: Mean without high point  ***
27020 Rem **********************************************
27100 For i = 1 To n: MEAN(i) = 0: Next i
27120 For j = 1 To n
27130   For i = 1 To n
27140     MEAN(j) = MEAN(j) + SIMP(i, j)
```

```
27160   Next i
27180   MEAN(j) = MEAN(j) / n
27200 Next j
27290 Return
```

30000 Rem **********

```
30010 Rem *** Subroutine: SQUARED SUM          ***
30020 Rem *** The sum of the squared deviations   ***
30030 Rem *** is evaluated in this section.      ***
30100 Rem **********
```

'RESET VALUES

```
30200 ss = 0
Sum = 0
sum1 = 0
Sum2 = 0
sum3 = 0
ffinal = 0
finit = 0
ffinalp = 0
aSum = 0
asum1 = 0
aSum2 = 0
asum3 = 0
affinal = 0
afinit = 0
affinalp = 0

30300 For i = sp To ep 'Step 2
30350   x = XX(i): GoSub 15000: y = y - YY(i)
If ss > ssmax Then ss = ssmax
If ss < ssmin Then ss = ssmin
If Abs(y) > (ssmax) ^ 0.5 Then y = (ssmax) ^ 0.5
30400   ss = ss + y * y:
If ss > ssmax Then ss = ssmax
If ss < ssmin Then ss = ssmin
Next i
30500 Return
```

32000 Rem **********

```
32010 Rem *** Subroutine: Reflection point       ***
32020 Rem **********
32100 For i = 1 To n
32120   REFL(i) = 2 * MEAN(i) - SIMP(n1, i)
32140   c(i) = REFL(i)
32160 Next i
32180 GoSub 30000
32200 LREFL = ss
```

```
32500 Return

      33000 Rem ******************************************
33010 Rem *** Subroutine: Double Reflection Point  ***
33020 Rem ******************************************
33100 For i = 1 To n
33120   DREFL(i) = 3 * MEAN(i) - 2 * SIMP(n1, i)
33140   c(i) = DREFL(i)
33160 Next i
33180 GoSub 30000
33200 LDREFL = ss
33500 Return

      34000 Rem ******************************************
34010 Rem *** Subroutine: Contraction Point       ***
34020 Rem ******************************************
34100 For i = 1 To n
34120   CONTR(i) = (MEAN(i) + SIMP(n1, i)) * 0.5
34140   c(i) = CONTR(i)
34160 Next i
34180 GoSub 30000
34200 LCONTR = ss
34500 Return
35000 Rem ******************************************
35010 Rem *** Subroutine: Contraction towards the  ***
35020 Rem ***          best point            ***
35030 Rem ******************************************
35100 For IC = 2 To n1
35120   For j = 1 To n
35140     SIMP(IC, j) = 0.5 * (SIMP(1, j) + SIMP(IC, j))
35160     c(j) = SIMP(IC, j)
35180   Next j
35200   GoSub 30000: LSQ(IC) = ss
35220 Next IC
35900 Return


      'DISPLAY PROGRESS OF SIMPLEX ON CHART
24183 For i = sp To ep
Worksheets("data").Cells(i + 19, 1).Value = XX(i)
Worksheets("data").Cells(i + 19, 2).Value = YY(i)
Worksheets("data").Cells(i + 19, 3).Value = zzz(i)
Worksheets("data").Cells(i + 19, 4).Value = adiab(i)
Worksheets("data").Cells(i + 19, 5).Value = nad(i)
Next i
Worksheets("ox").Cells(12, 10).NumberFormat = "general"
Sheets("chart2").Select
pn = Worksheets("ox").Cells(4, 6).Text
pn = CStr(pn)
```

```
Sheets("chart2").Select
ActiveChart.TextBoxes.Delete
ActiveChart.TextBoxes.Add(5, 17.5, 500, 25.5).Select
Selection.Interior.ColorIndex = xlNone
Selection.Characters.Text = pn
With Selection.Font
.Name = "arial"
.FontStyle = "regular"
.Size = 10
.Strikethrough = False
.OutlineFont = False
.Shadow = False
.Underline = True
.ColorIndex = xlAutomatic
End With

        Return
e:

60050 End Sub
```

Appendix B

Published Paper 1

Conjugated vs Nonconjugated Bridges: Heterogeneous Electron Transfer Dynamics of Osmium Polypyridyl Monolayers

Langmuir, 2000, *16,* 7671-7875.

Conjugated vs Nonconjugated Bridges: Heterogeneous Electron Transfer Dynamics of Osmium Polypyridyl Monolayers

Robert J. Forster,*,† Egbert Figgemeier,†,‡ Paul Loughman,† Anthea Lees,† Johan Hjelm,§ and Johannes G. Vos†

National Centre for Sensor Research, School of Chemical Sciences, Dublin City University, Dublin 9, Ireland, and Department of Physical Chemistry, Uppsala University, Box 532, S-75121 Uppsala, Sweden

Received May 6, 2000

Introduction

The production of "molecular wires" that promote fast heterogeneous electron transfer between a remote redox center and a metal surface is important for high-speed molecular electronics applications, e.g., molecule-based computing. One notable strategy in this area is to use conjugated rather than aliphatic bridges to achieve faster electron-transfer rates. For example, conjugated molecules of [1,1′:4′,1″-terphenyl]-4-methanethiol (TP) have been embedded in self-assembled monolayers of insulating *n*-alkanethiols and the conductivity of single molecules measured.[1] Also, Creager and co-workers[2] recently probed the electron transfer rates for ferrocene groups attached to gold electrodes via conjugated oligo(phenylethynyl) bridges of variable length. Significantly, they found that the extrapolated rate constants at short distances were nearly the same for conjugated and aliphatic bridges. Moreover, for short electron-transfer distances, the observed rates were consistent with those expected for an adiabatic electron transfer suggesting strong electronic coupling between the redox centers and the electrode. In this context, experiments with self-assembled monolayers consisting of osmium 2,2′6′,2″-terpyridine complexes attached to an electrode surface by 4′-(3-pyridyl)-2,2′:6′,2″-terpyridine were performed recently. The heterogeneous electron-transfer rate constants for this system do not show a substantial increase compared to those found for comparable aliphatic bridges.[3] However, directly comparing heterogeneous electron transfer rate constants will provide an insight into the strength of electronic coupling only if the free energy of activation is identical for conjugated and nonconjugated bridges. For example, switching from a nonconjugated to a conjugated bridging ligand may alter the structure of the monolayer making the local dielectric content and hence outer sphere reorganization energies different in the two cases.

We report here on the effect of using a conjugated, *trans*-1,2-bis(4-pyridyl)ethylene, bpe, vs a nonconjugated bridge, 1,2-bis(pyridyl)ethane, p2p, on the heterogeneous electron-transfer rate constants for $[Os(bpy)_2Cl]^+$ moieties attached to the surface of platinum microelectrodes (Chart 1). Cyclic voltammetry has been used to measure the rate of heterogeneous electron transfer for monolayers of $[Os(bpy)_2(bpe)Cl]^+$ using scan rates up to 10 000 V s^{-1}. These data have been compared with previous reports[4-6] on the nonconjugated bridge, 1,2-bis(pyridyl)ethane. To determine whether differences in electronic coupling or the free energy of activation are responsible for the observed differences in k^o, the complete voltammograms have been fitted using an overlap integral approach based on the Marcus relation.

Chart 1

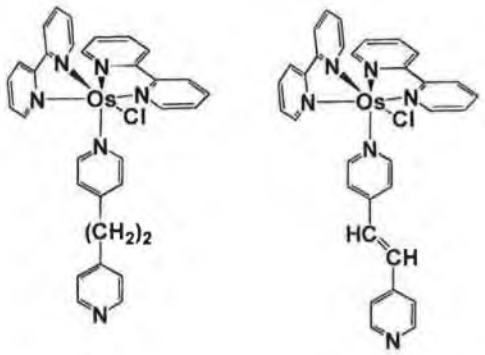

p2p: 1,2-bis(4-pyridyl)ethane bpe : *trans*-1,2-bis(4-pyridyl)ethylene

Experimental Section

Reagents and Synthesis. The complex was synthesized using methods similar to those published previously.[7] $[Os(bpy)_2(bpe)Cl](PF_6)_2$ was synthesized by first refluxing $[Os(bpy)_2Cl_2]$ (0.22 g, 3.5×10^{-4} mol) in dry methanol (10 cm^3) until completely dissolved. *trans*-1,2Bis(4-pyridyl)ethylene) (0.07 g, 3.8×10^{-4} mol) was added over 1 h, and the resulting solution was refluxed for a further 12 h. After this period the reaction mixture was cooled and added dropwise to a concentrated aqueous solution of NH_4PF_6. Elemental analysis, NMR, HPLC, and UV−vis spectroscopy all indicate that the compound is obtained in the form $[Os(bpy)_2(bpeH)Cl](PF_6)_3$, where the free pyridine group is protonated. That the unbound pyridine moiety of the 1,2-bis-(4-pyridyl)ethylene ligand is protonated is not unexpected since the synthesis was carried out in dry methanol. This protonation does not persist in aqueous media, and the complex is capable of forming spontaneously adsorbed monolayers.

Electrochemistry. Cyclic voltammetry was performed using a CH Instruments model 660 electrochemical workstation and a conventional three-electrode cell with a BAS Ag/AgCl electrode as reference. Microelectrodes were fabricated from platinum and gold microwires (Goodfellow Metals Ltd.) of radii between 1 and 25 μm by sealing them into soft glass using a procedure described previously.[5] The microdisk electrodes were prepared by mechanical polishing and voltammetric cycling in dilute acid in order to create a clean polycrystalline surface of known microscopic area. Typically the surface roughness was between 1.3 and 1.6. RC cell time constants were between 0.03 and 3 μs, depending on the electrode radius and the supporting electrolyte concentration.

Preparation of Monolayers. Spontaneously adsorbed monolayers were typically formed by placing a freshly prepared electrode in a 2 mM solution of the complex dissolved in aqueous acetone (50:50 v/v) containing 0.1 M $LiClO_4$ as supporting electrolyte. The electrode was poised at 0.1 V vs Ag/AgCl during the 30 min deposition cycle. Prior to deposition, all solutions

† Dublin City University.

‡ Current address: Institute for Inorganic Chemistry, University of Basel, Spitalstrasse 51, 4056 Basel, Switzerland.

§ Uppsala University.

(1) Ishida, T.; Mizutani, W.; Akiba, U.; Umemura, K.; Inoue, A.; Choi, N.; Fujihira, M.; Tokumoto, H. *J. Phys. Chem. B* **1999**, *103*, 1686.
(2) Weber, K. S.; Creager, S. E. *J. Electroanal. Chem.* **1998**, *458*, 17.
(3) Figgemeier, E.; Zimmermann Y.; Houscroft, C. E.; Constable, E. C. To be submitted for publication.
(4) Acevedo, D.; Abruña, H. D. *J. Phys. Chem.* **1991**, *95*, 9590.
(5) Forster, R. J.; Faulkner, L. R. *J. Am. Chem. Soc.* **1994**, *116*, 5444.
(6) Forster, R. J.; Faulkner, L. R. *J. Am. Chem. Soc.* **1994**, *116*, 5453.
(7) Forster, R. J. *Inorg. Chem.* **1996**, *35*, 3394.

10.1021/la000718s CCC: $19.00
Published on Web 08/31/2000

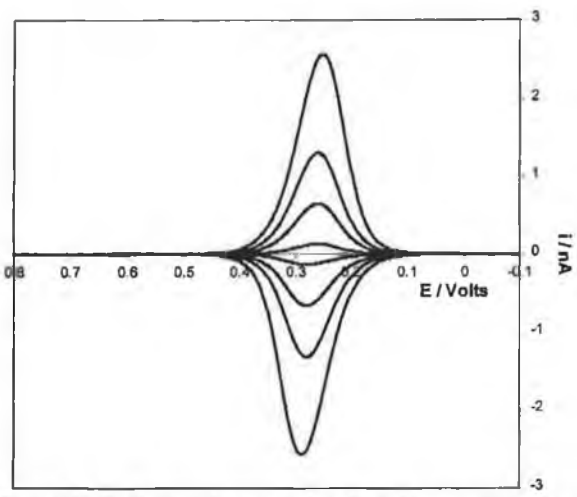

Figure 1. Background-corrected cyclic voltammograms for a spontaneously adsorbed $[Os(bpy)_2(bpe)Cl]^+$ monolayer on a 25 μm radius platinum microdisk electrode. The supporting electrolyte is aqueous 0.1 M $LiClO_4$. The scan rate from top to bottom is 2, 1, 0.5, and 0.1 V s^{-1}. Cathodic currents are up, and anodic currents are down.

were degassed for at least 15 min using nitrogen, and a blanket of nitrogen was maintained over the solution during all experiments.

Results and Discussion

General Electrochemical Properties. Figure 1 shows a typical background corrected cyclic voltammogram for a spontaneously adsorbed monolayer of $[Os(bpy)_2(bpe)Cl]^+$ on a 25 μm radius platinum microdisk as the scan rate, v, is systematically varied from 0.1 to 2 V s^{-1}. The formal potential for the osmium monolayer is 0.28 V, which agrees closely with that found for this complex by Abruña[8,9] and with values reported for monolayers assembled from the complex $[Os(bpy)_2(p2p)Cl]^+$, where p2p is the corresponding nonconjugated bridge 1,2-bis(4-pyridyl)ethane)[5,8] ($E^{\circ\prime}$ = 0.31 V).

The limiting surface coverage of the complex at equilibrium is $(7.0 \pm 0.5) \times 10^{-11}$ mol cm^{-2} and does not increase further by increasing the concentration of the complex in solution or the deposition time. This saturation coverage is smaller than that found by Acevedo and Abruña[4,8] for monolayers of the same complex but lies within the range measured previously for related systems.[8,11,13] The full width at half-maximum, fwhm, is between 100 and 120 mV at slow scan rates (<5 V s^{-1}), which is slightly higher than the ideal case of 90.6 mV for a one-electron transfer. This broadening is consistent with weak repulsive interactions between the adsorbates most likely arising from their cationic character.[10,11]

Electron-Transfer Dynamics. The standard heterogeneous electron-transfer rate constant, k°, depends on both a frequency factor and a Franck–Condon barrier[12–14]

$$k^\circ = A_{et} \exp(-\Delta G^{\ddagger}/RT) \quad (1)$$

where A_{et} is the pre-exponential factor (equal to the product of Γ_n the nuclear tunneling factor, κ_{el} the electronic transmission coefficient, and v_n the nuclear frequency factor) and $\Delta G^{\ddagger}$ is the electrochemical free energy of activation.[15]

One approach to decoupling these two contributions is to use classical temperature-resolved measurements of k° to measure the free energy of activation, $\Delta G^{\ddagger}$, allowing A_{et} to be determined. In this way, information about the strength of electronic coupling can be obtained.[6,16,17] A second method involves measuring electron-transfer rate constants at a single temperature over a broad range of reaction driving forces. For example, Finklea and Hanshew,[18] have assembled a model describing through-space electron tunneling which provides a good description of electron tunneling in monolayers of this kind.[5] In this model, the cathodic rate constant is given by integral over energy (E) of three functions: (a) the Fermi function for the metal $n(E)$, (b) a Gaussian distribution of energy levels for acceptor states in the monolayer $D_{Ox}(E)$, and (c) a probability factor describing electron tunneling at a given energy, $P(E)$.

$$k_{Ox}(\eta) = A\int_{-\infty}^{\infty} D_{Ox}(E)\, n(E)\, P(E)\, d\epsilon \quad (2)$$

The zero point of energy is defined as the Fermi level of the metal at the particular overpotential of interest. The Fermi function describes the distribution of occupied states within the metal and is defined by

$$n(E) = \left(\frac{1}{1 + \exp[(\epsilon - \epsilon_{f,})/kT]}\right) \quad (3)$$

where k_B is the Boltzmann constant. The density of acceptor states is derived from the Marcus theory[19,20] and is represented by eq 4

$$D_{Ox}(E) = \exp\left[-\frac{(E + \eta - \lambda)^2}{4k\lambda T}\right] \quad (4)$$

where λ is the reorganization energy. The probability of direct elastic tunneling[21,22] through a trapezoidal energy barrier of height E_B can be approximated by eq 5

$$P(E) = (E_B - E + e\eta/2) \exp(-\beta d) \quad (5)$$

where E_B is the average barrier height at zero overpotential (taken here as 2.0 eV) and d is the electron-transfer distance.

Chidsey,[23] Creager,[24] and Murray[25] have modeled nonadiabatic heterogeneous electron transfer for long-chain alkanethiol monolayers using an expression similar

(8) Acevedo, D.; Bretz, R. L.; Tirado, J. D.; Abruña, H. D. *Langmuir* **1994**, *10*, 1300.
(9) Acevedo, D.; Bretz, R. L.; Tirado, J. D.; Abruña, H. D. *Langmuir* **1994**, *10*, 1971.
(10) Brown, A. P.; Anson, F. C. *Anal. Chem.* **1977**, *49*, 1589.
(11) Laviron, E. *J. Electroanal. Chem.* **1974**, *52*, 395.
(12) Bagchi, G. *Annu. Rev. Chem.* **1989**, *40*, 115.
(13) Sutin, N. *Acc. Chem. Res.* **1982**, *15*, 275.
(14) Barr, S. W.; Guyer, K. L.; Li, T. T.-T.; Liu, H. Y.; Weaver, M. J. *J. Electrochem. Soc.* **1984**, *131*, 1626.
(15) Sutin, N. Brunschwig, B. S. *ACS Symp. Ser.* **1982**, *No. 198*, 105.
(16) Forster, R. J.; Vos, J. G.; Keyes, T. E. *Analyst (Cambridge, U.K.)* **1998**, *123* 1905.
(17) Forster, R. J.; O'Kelly, J. P. *J. Phys. Chem.* **1996**, *100*, 3695.
(18) Finklea, H. O.; Hanshew, D. D. *J. Am. Chem. Soc.* **1992**, *114*, 3173.
(19) Marcus, R. A. *J. Chem. Phys.* **1956**, 24, 966.
(20) Marcus, R. A. *J. Phys. Chem.* **1963**, *67*, 853.
(21) Schmickler, W. *J. Electroanal. Chem.* **1977**, *82*, 65.
(22) Bockris, J. O'M.; Khan, S. U. M. *Quantum Electrochemistry*; Plenum Press: New York, 1979; Chapter 8
(23) Chidsey, C. E. D. *Science* **1991**, *251*, 919.
(24) Weber, K.; Creager, S. E. *Anal. Chem.* **1994**, *66*, 3164.
(25) Tender, L.; Carter, M. T.; Murray, R. W. *Anal. Chem.* **1994**, *66*, 3173.

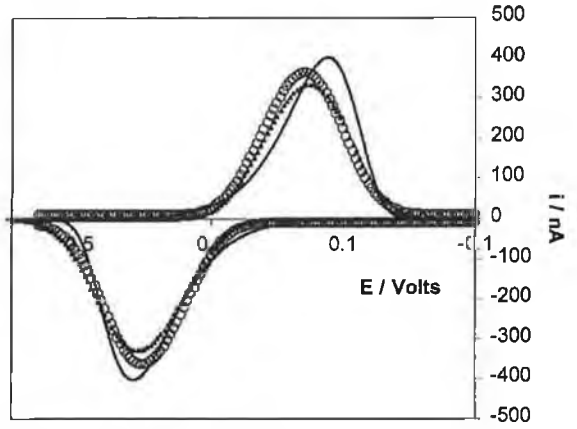

Figure 2. Cyclic voltammograms for a spontaneously adsorbed $[Os(bpy)_2(bpe)Cl]^+$ monolayer on a 25 μm radius platinum microdisk electrode at a scan rate of 6000 V s^{-1}. The solid line denotes experimental data, while ○ and ▲ denote the best-fit theoretical responses generated using the Finklea and Chidsey models, respectively. Both theoretical responses correspond to a k° of 9.4×10^3 s^{-1} and a $\Delta G^\ddagger$ of 11.4 kJ mol^{-1}. The supporting electrolyte is aqueous 0.1 M $LiClO_4$.

to eq 2 except that the energy-dependent prefactor in the tunneling probability expression is excluded.

The current for the reaction of an immobilized redox center following first-order kinetics is[25]

$$i_F = nFA(k_{Ox}(\eta)\,\Gamma_{Red,\eta} - k_{Red}(\eta)\Gamma_{Ox,\eta}) \qquad (6)$$

where $\Gamma_{Red,\eta}$ and $\Gamma_{Ox,\eta}$ are the instantaneous surface coverages of the oxidized and reduced species and $k_{Ox}(\eta)$ and $k_{Red}(\eta)$ are the reaction rate constants and are given by eq 2 with or without a tunneling probability function. In using eq 6 to model the voltammetric response, the electron-transfer distance, d, is taken as 10 Å leaving only two freely adjustable parameters, k° and $\Delta G^\ddagger$ ($=\lambda/4$). We have used both of these models in a finite difference simulation to determine k° and $\Delta G^\ddagger$. To achieve this objective, we have used the Nelder and Mead Simplex[26] algorithm to find the values of k° and $\Delta G^\ddagger$ that minimize the sum square residuals between the theoretical and experimental currents observed in anodic branches of the linear sweep voltammograms.

Figure 2 shows the experimental background corrected cyclic voltammogram for a dense $[Os(bpy)_2(bpe)Cl]^+$ monolayer deposited on a 5 μm radius platinum microelectrode where the scan rate is 6000 V s^{-1}. The overall cell resistance in this experiment is approximately 18 kΩ. Given that the peak current in Figure 2 is approximately 400 nA, the ohmic loss will be less than 8 mV, which is negligible compared with the observed ΔE_p of approximately 310 mV. Figure 2 illustrates the best fits obtained from eqs 2–6 for models that include and exclude through-space tunneling through a trapezoidal barrier. In both cases the residual sum of squares between theory and experiment was minimized *only* for the oxidative branch and then the best fit estimates of k° and $\Delta G^\ddagger$ obtained were used to predict the cathodic branch of the voltammogram. For both models, the optimum k° was $(9.4 \pm 0.9) \times 10^3$ s^{-1} and $\Delta G^\ddagger$ was 11.4 ± 0.8 kJ mol^{-1}.

Figure 2 shows that excellent agreement is observed between the experimental and theoretical anodic peak potentials and both peak currents. Moreover, there is general agreement between the theoretical and experimental currents along the full anodic branch. However, poorer agreement is observed for the cathodic branch, which may arise from oxidation state dependent electronic coupling or, more likely, differences in the reorganization energy caused by changes in the monolayer's solvation as it is oxidized.[27] Figure 2 reveals that while the quality of the fit obtained using the two models is broadly comparable, the peak currents predicted by Finklea's through-space tunneling model more closely match the experimental values. That these voltammograms are bet described by a through-space tunneling model agrees with previous investigations[5] where a value of 1.6 ± 0.2 $Å^{-1}$ was obtained[5] for the distant dependent tunneling parameter, β. A through-space rather than through-bond mechanism is somewhat surprising given the aromatic character of the *trans*-1,2-bis(4-pyridyl)ethylene bridge. However, it is important to note that the electron-transfer distance examined here, 10 Å, is considerably shorter than that traditionally explored using alkanethiol self-assembled monolayers, 20–30 Å. Quantum mechanical spillover of the metal electron density beyond the electrode/monolayer interface, and the delocalized character of the electron density on the electrode, may be relatively more important for these short bridging ligands. Furthermore, electric field effects may influence the electron-transfer dynamics because the length of the bridge and the double layer thickness are comparable.[17]

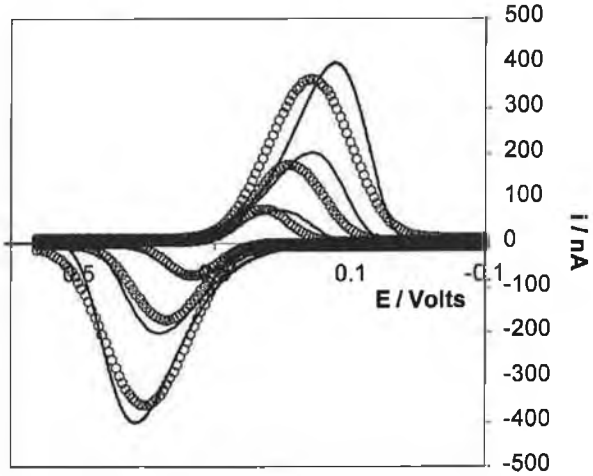

Figure 3. Experimental (—) and theoretical (○) voltammograms generated using the through-space tunneling model due to Finklea, for a spontaneously adsorbed $[Os(bpy)_2(bpe)Cl]^+$ monolayer on a 25 μm radius platinum microdisk electrode. From top to bottom, the scan rates are 6000, 3000, and 1000 V s^{-1}. In all cases, the theoretical responses were generated using a k° of 9.4×10^3 s^{-1} and a $\Delta G^\ddagger$ of 11.4 kJ mol^{-1}.

An important test of the reliability of the standard heterogeneous electron-transfer rate constants obtained by fitting the cyclic voltammograms is to investigate the scan rate dependence. In this way, an insight into the dispersion in the kinetics can be obtained. Figure 3 shows the fits obtained at scan rates of 1000, 3000, and 6000 V s^{-1}. In each case the same fitting parameters for the Finklea model, i.e., a k° of 9.4×10^3 s^{-1} and a $\Delta G^\ddagger$ of 11.4 kJ mol^{-1}, were used. For each scan rate, there is satisfactory agreement between the theoretical model and the experimental currents of the anodic branch of the voltammogram. That the experimental responses at different

(26) Ebert, K.; Ederer, H.; Isenhour, T. L. *Computer Applications in Chemistry: An Introduction for PC Users*; VCH Publishers: New York, 1989.

(27) Hupp, J. T.; Weaver, M. J. *J. Phys. Chem.* **1984**, *88*, 6128.

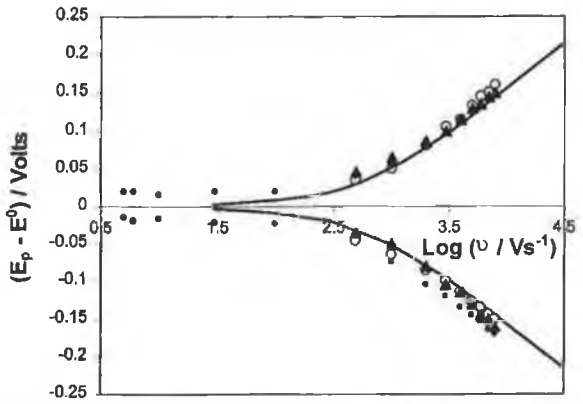

Figure 4. Plot of $(E_p - E^\circ)$ vs log(sweep rate) for a spontaneously adsorbed monolayer of $[Os(bpy)_2(bpe)Cl]^+$. The experimental data are denoted by ● while ○ and ▲ denote best-fit theoretical responses generated using the models assembled by Finklea and Chidsey, respectively. Both theoretical responses correspond to a k° of 9.4×10^3 s^{-1} and a $\Delta G^\ddagger$ of 11.4 kJ mol^{-1}. The solid line denotes the prediction of the Butler–Volmer theory ($\alpha = 0.5$, $k^\circ = 9.4 \times 10^3$ s^{-1}). The supporting electrolyte is 0.1 M $NaClO_4$.

time scales are accurately modeled using the same two parameters indicates that the heterogeneous electron transfer rate constants are all similar for individual adsorbates corresponding to indistinguishable microenvironments and electron transfer distances. This nearly ideal behavior contrasts with that observed for ferrocene alkanethiol monolayers[23,24] where it is difficult to achieve satisfactory agreement between theory and experiment over the entire voltammogram due to oxidation state dependent lateral interactions.

Given the difficulties of accurately removing background charging currents from experimental voltammograms, an alternative procedure is to probe the dependence of the anodic and cathodic peaks potentials, $E_{p,a}$ and $E_{p,c}$, on the voltammetric scan rate. Figure 4 illustrates the dependence of the peak-to-peak separation, ΔE_P, on the voltammetric scan rate for $8000 \geq \upsilon \geq 5$ V s^{-1}. For scan rates up to approximately 100 V s^{-1} ΔE_P is insensitive to the scan rate before increasing significantly. There are two important processes that could contribute to the observed response: first, ohmic loss due to the higher current density at higher scan rate;[28] second, slow heterogeneous electron transfer across the electrode/monolayer interface. As discussed previously, in experiments of this kind, the iR drop is kept below 5 mV by carefully selecting the radius of the microelectrode. Thus, while high-quality data can be obtained from a monolayer coated 25 μm radius microdisk for $\upsilon < 100$ V s^{-1}, for higher scan rates 1 μm radius electrodes are used.[29] Moreover, the same slope is observed in Figure 4 if the experiments are repeated in more conducting solutions that contain a higher concentration of supporting electrolyte. This observation also indicates that secondary processes, e.g., ohmic loss, or the dynamics of ion pairing, do not contribute significantly to the observed response. The behavior illustrated in Figure 4 is consistent with the dynamics of heterogeneous electron-transfer influencing the voltammetric response at high scan rates.

Figure 4 shows the peak potentials predicted by the models assembled by Chidsey[23] and Finklea[18] using values of k° and $\Delta G^\ddagger$ of 9.4×10^3 s^{-1} and 11.4 kJ mol^{-1}, respectively. In common with the analysis of the complete voltammograms, there is good agreement between theory and experiment for the anodic branch but somewhat poorer agreement for the cathodic data. As discussed by Creager,[24] the peak potentials are rather insensitive to the reorganization energy allowing accurate values of k° to be obtained essentially independently of λ. Figure 4 also shows the predictions of the classical Butler–Volmer theory[28] which tends to overestimate the apparent heterogeneous electron-transfer rate constant.

Table 1. Rate Constants, Free Energies of Activation, and Pre-exponential Factors for the $Os^{2+/3+}$ Redox Reaction Occurring within $[Os(bpy)_2(L)Cl]^+$ Monolayers Where L Is *trans*-1,2-Bis(4-pyridyl)ethylene (bpe) or 1,2-Bis(4-pyridyl)ethane (p2p)[a]

bridging ligand	$10^{-3}k^\circ$/s^{-1}	$\Delta G^\ddagger$/kJ mol^{-1}	$10^{-6}A_{et}$/s^{-1}
bpe	9.4 ± 0.9	11.4 ± 0.8	0.9 ± 0.3
p2p	305 ± 26	8.7 ± 1.2	11.1 ± 0.5

[a] Supporting electrolyte is 0.1 M aqueous $LiClO_4$.

As described previously,[5,8,30] the voltammetric response of $[Os(bpy)_2(p2p)Cl]^+$ monolayers is generally similar to that presented above for the bpe-bridged systems. We have modeled the voltammetric response for the p2p-bridged system and found values $(3.00 \pm 0.26) \times 10^5$ s^{-1} and 8.7 ± 1.2 kJ mol^{-1} for k° and $\Delta G^\ddagger$, respectively. This k° is indistinguishable from that determined previously using potential step chronoamperometry conducted on a microsecond time scale.[30] Therefore, it appears that despite the bpe bridge being conjugated the heterogeneous electron transfer rate constant is approximately a factor of 30 smaller than that found for the aliphatic bridge, 1,2-bis-(4-pyridyl)ethane. However, as discussed above, in trying to elucidate the effect of changes in bridge structure, e.g., conjugation, it is important to determine the pre-exponential factors since these are sensitive to the degree of electronic coupling across the bridge.[7] Table 1 contains the free energies of activation for both the bpe and p2p systems. While both the $\Delta G^\ddagger$ values agree with that predicted by the Marcus relation for outer sphere reorganization[31] to within 20%, $\Delta G^\ddagger$ is smaller for the p2p system. This difference in the free energy of activation most likely corresponds to a different monolayer structure in the two circumstances and would correspond to more nonpolar environment within the p2p-bridged monolayer.

We have used the values of k° and $\Delta G^\ddagger$ in conjunction with eq 1 to estimate pre-exponential factors for both the bpe- and p2p-bridged monolayers. The data are summarized in Table 1. These data reveal that the prefactors are approximately 6 orders of magnitude smaller than those expected for an adiabatic electron transfer, i.e., one involving strong coupling between the localized redox states of the monolayer and delocalized metallic states of the electrode. However, the most significant result contained in Table 1 is that the pre-exponential factor is approximately an order of magnitude higher for the p2p than for the bpe bridge indicating that the redox center and electrode are more strongly coupled for the aliphatic system.

This result is consistent with the through-space tunneling mechanism in that the less rigid p2p bridge probably has sufficient flexibility to reduce the electron-transfer distance below the value of 10 Å expected on the basis of a rigid-rod model. It is important to note that unlike a

(28) Bard, A. J.; Faulkner, L. R. *Electrochemical Methods, Fundamentals and Applications*; John Wiley & Sons: New York, 1980.
(29) Forster, R. J. *Phys. Chem. Chem. Phys.* **1999**, *1*, 1543.
(30) Forster, R. J.; Faulkner, L. R. *Anal. Chem.* **1995**, *67*, 1232.
(31) Weaver, M. J. *Chem. Rev.* **1992**, *92*, 463.

through-space pathway, the electron-transfer distance for through-bond tunneling mechanisms is independent of the monolayer's conformation. Therefore, the *decrease* in heterogeneous electron-transfer rate constant observed here on going from a nonconjugated to a conjugated bridge is not expected for a through-bond tunneling mechanism.

Conclusions

Monolayers of $[Os(bpy)_2(bpe)Cl]^+$ have been formed and their electrochemical properties investigated. We have modeled the voltammetric response observed at high scan rates where heterogeneous electron transfer across the metal/monolayer interface influences the experimental response. Somewhat surprisingly, despite the conjugated bridge and short electron-transfer distance, the voltammetric response is best modeled as a through-space tunneling process. The standard heterogeneous electron-transfer rate constant, k^o, for the conjugated bridge is 9.4 $\times 10^4$ s^{-1} which is approximately a factor of 30 *smaller* than that observed for a longer, aliphatic bridge, 1,2-bis-(4-pyridinyl)ethane. Modeling the complete voltammogram allows the contributions from electronic coupling and free energy of activation to be decoupled. This analysis reveals free energies of activation of 8.7 ± 1.2 and 11.4 ± 0.8 kJ mol^{-1} for the bpe and p2p bridges, respectively. That the voltammetric response is best described using a through-space tunneling model and both the standard heterogeneous electron-transfer rate constants and preexponential factors are larger for the nonconjugated ligand suggest that heterogeneous electron-transfer proceeds via a through-space tunneling mechanism.

Acknowledgment. The authors thank the EC TMR Programme (Contract Number CT96-0076) for financial assistance.

LA000718S

Appendix C

Published Paper 2

Effect of Electrode Density of States on the heterogeneous Electron-Transfer Dynamics of Osmium-Containing Monolayers

J. Am. Chem. Soc., **2000**, *122*, 11948.

Effect of Electrode Density of States on the Heterogeneous Electron-Transfer Dynamics of Osmium-Containing Monolayers

Robert J. Forster,*,† Paul Loughman,† and Tia E. Keyes‡

Contribution from the National Centre for Sensor Research, School of Chemical Sciences, Dublin City University, Dublin 9, Ireland, and School of Chemistry, Dublin Institute of Technology, Dublin 4, Ireland

Received July 17, 2000. Revised Manuscript Received September 6, 2000

Abstract: Dense monolayers of $[Os(OMe\text{-}bpy)_2(p3p)Cl]^{1+}$, where OMe-bpy is 4,4′-dimethoxy-2,2′-bipyridyl and p3p is 4,4′-trimethylenedipyridine, have been formed by spontaneous adsorption onto clean platinum, mercury, gold, silver, carbon, and copper microelectrodes. These systems have been used to probe the influence of the electrode density of states on the rate of electron transfer across the electrode/monolayer interface. Monolayers on each material exhibit well-defined voltammetry for the $Os^{2+/3+}$ redox reaction where the supporting electrolyte is aqueous 1.0 M $NaClO_4$. The high scan rate (>2000 V s^{-1}) voltammetric response has been modeled using a nonadiabatic electron-transfer model. The standard heterogeneous electron-transfer rate constant, k^o, depends on the identity of the electrode material, e.g., k^o is 6×10^4 and 4×10^3 s^{-1} for platinum and carbon electrodes, respectively. Chronoamperometry, conducted on a microsecond time scale, has been used to probe the potential dependence of the heterogeneous electron-transfer rate constant. These values range from $(4.0 \pm 0.2) \times 10^4$ to $(3.0 \pm 0.3) \times 10^3$ s^{-1} on going from platinum to carbon electrodes. Temperature-resolved chronoamperometry and cyclic voltammetry reveal that the electrochemical activation enthalpy, $\Delta H^{\ddagger}$, and the reaction entropy, $\Delta S_{RC}{}^{\ddagger}$, are both independent of the electrode material having values of 11.1 ± 0.5 kJ mol^{-1} and 29.6 ± 2.4 J mol^{-1} K^{-1}, respectively. The effect of electrode material on the preexponential factors is discussed in terms of the electrode density of states. These experimental data indicate that the heterogeneous electron-transfer rate for a nonadiabatic process is not simply proportional to the density of states but is modulated by the electronic coupling efficiency. Moreover, the matrix coupling elements, H_{AB}, are between 0.1 and 0.5 J mol^{-1}, which is approximately 4 orders of magnitude smaller than those found from studies of intervalence charge-transfer intensities within comparable dimeric complexes.

Introduction

Processes as diverse as corrosion inhibition, charging and discharging of batteries, electroanalysis, and medical device operation involve electron transfer across an interface consisting of metallic and molecular species.[1] Failure to develop comprehensive theoretical models that describe how the properties of *both* components dictate the overall rates of electron transfer will impede the development of molecule-based electronics.[2] A two-pronged approach to addressing this issue is most likely to lead to success. A powerful mechanistic insight into the factors that influence electron transfer across molecular species has been obtained using ordered monolayers of redox active materials on electrodes. In recent years they have helped revolutionize our understanding of the role that distance, structure, and the redox composition of the monolayer play in dictating the rate and mechanism of electron transfer.[3] However, the effect of changing the nature of the electrode material has not been probed with the same intensity. This situation is surprising given that traditional theory predicts that for electron transfer involving weakly coupled reactants the heterogeneous electron transfer rates should be directly proportional to the density of states, ρ_F, in the electrode.[4] However, a recent theoretical model developed by Marcus and Gosavi[5] predicts that the coupling strength between the redox center and the electrode will make the electron-transfer rate less sensitive to ρ_F. This observation offers an important new approach to controlling the rate of nonadiabatic heterogeneous electron transfer.

Some attempts have been made to test the effect of changing the electrode material on the electron-transfer dynamics.[6,7,8] Although some discrepancies exist, the general conclusion of these investigations was that the rate of heterogeneous electron transfer is independent of the nature of the electrode. However, measurements involving solution phase reactants are highly sensitive to the purity and history of the electrode, to the pretreatment regime, to double layer effects, and to adsorption of the analyte. Moreover, one cannot easily control the strength of electronic coupling between the electrode and the reactant.

* To whom correspondence should be addressed.
† School of Chemical Sciences.
‡ Dublin Institute of Technology.

(1) Bard, A. J.; Abruña, H. D.; Chidsey C. E. D.; Faulkner, L. R.; Feldberg, S. W.; Itaya, K.; Majda, M.; Melroy, O. S.; Murray, R. W.; Porter, M, D.; Soriaga, M. P.; White, H. S. *J. Phys. Chem.* **1993**, *97*, 7147.
(2) Stoddart, J. F. In *Frontiers in Supramolecular Organic Chemistry and Photochemistry*; Schneider, H. J., Dürr, H., Eds.; VCH: Weinheim, Germany, 1990.
(3) Finklea, H. O. In *Encyclopedia of Analytical Chemistry*; Meyers, R. A., Ed.; Wiley: New York, 2000.
(4) Parsons, R. *Surf. Sci.* **1964**, *2*, 418.
(5) Gosavi, S.; Marcus, R. A. *J. Phys. Chem. B* **2000**, *104*, 2067.
(6) Capon, A.; Parsons, R. *J. Electroanal. Chem.* **1973**, *46*, 215.
(7) Iwasita, T.; Schmickler, W.; Schultze, J. *J. Am. Chem. Soc.* **1984**, *106*, 1233.
(8) Van Venrooij, T. G. J.; Sluyters-Rehbach, M.; Sluyters, J. H. *J. Electroanal. Chem.* **1996**, *419*, 61.

10.1021/ja002616u CCC: $19.00
Published on Web 00/00/0000 PAGE EST: 7.6

Chart 1

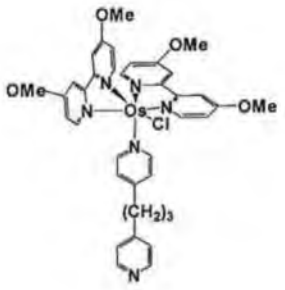

Adsorbed monolayers represent an alternative approach to investigating this issue. They are attractive in that diffusive mass transport is eliminated, double layer effects may be less pronounced, and the reaction can be rendered nonadiabatic simply by controlling the electron-transfer distance or the structure of the bridging ligand. Weaver and co-workers[9] probed the reduction kinetics of adsorbed [$Co^{III}(NH_3)_5$ thiophenecarboxylate] complexes on mercury, gold, and copper electrodes. The heterogeneous electron-transfer rate constants, $k°$, were found to be in the order Hg $\gtrsim$ Au > Cu. However, the rate constants for gold and copper depended on the surface coverage and the effect of bridge conjugation on the adiabaticity of the reaction makes it difficult to extract quantitative information from these experiments. Moreover, these studies did not consider the possibility that the electrode material might influence the free energy of activation.

Here, we have formed spontaneously adsorbed monolayers of $[Os(OMe\text{-}bpy)_2(p3p)Cl]^+$ (Chart 1) on carbon-fiber, mercury, platinum, gold, copper, and silver microelectrodes, where OMe is 4,4′-dimethoxy-2,2′-bipyridyl and p3p is 4,4′-trimethylenedipyridine. This complex has a low redox potential (≈0.05 V) making it possible to probe the electrochemical properties even on rather electropositive metals. The voltammetric response is unusually ideal across a wide range of experimental time scales, temperatures, and electrolyte solutions making it an attractive model system for probing density of states issues. In particular, we are interested in probing how the different orbitals of these metals that contribute to the overall density of states influence the electron-transfer dynamics. For example, the s electrons dominate ρ_F for metals such as gold and silver while the higher density of states for platinum arises predominantly because its d orbitals lie near the Fermi level. The Marcus−Gosavi[5] model predicts that the efficiency with which these different orbitals couple with the localized molecular states of the adsorbate may vary significantly. To address these issues, we have performed detailed measurements of both the potential and temperature dependence of k. These results confirm that the electron transfer is nonadiabatic and that the free energy of activation is dictated by outer-sphere reorganization of solvent dipoles.

Experimental Section

Materials. The surface-active complex $[Os(OMe\text{-}bpy)_2(p3p)Cl]PF_6$ was prepared from $[Os(OMe\text{-}bpy)_2Cl_2]$, which was synthesized as described by Heller and co-workers.[10] A 138 mg (0.2 mmol) amount of $[Os(OMe\text{-}bpy)_2\ Cl_2]$ was placed in 40 cm^3 of methanol and refluxed for 10 min to ensure complete dissolution. A solution of 40 mg (0.2 mmol) of 1,4-trimethylenedipyridine dissolved in 10 cm^3 of methanol was added, and the solution was refluxed for 15 h. The progress of the reaction was monitored using HPLC and cyclic voltammetry. After the reaction was complete, the volume was reduced to 5 cm^3 by rotary evaporation. Ammonium hexafluorophosphate (95+%, Aldrich) was then added, and the dark purple product was collected by filtration and washed with diethyl ether. The product was recrystallized from aqueous methanol to give dark purple-black crystals, yield 160 mg, 82%. Anal. Calcd for $C_{37}H_{38}O_4N_6OsClPF_6$: C, 44.37; H, 3.79; N, 8.39. Found: C, 44.8; H, 3.3; N, 8.2. The complex was further characterized using IR, UV−vis, NMR, and cyclic voltammetry.

Apparatus. Electrochemical cells were of conventional design and were thermostated to within ±0.2 °C using a Julabo F10-HC refrigerated circulating bath. All potentials are quoted with respect to a Ag/AgCl reference electrode. Cyclic voltammetry was performed using a CH Instruments model 660 Electrochemical Workstation and a conventional three-electrode cell. All solutions were degassed using nitrogen, and a blanket of nitrogen was maintained over the solution during all experiments.

In high-speed chronoamperometry,[11] a custom built function generator−potentiostat, with a rise time of less than 10 ns, was used to apply potential steps of variable pulse width and amplitude directly to a two-electrode cell. A Pt foil and an Ag/AgCl reference electrode were combined to form a counter electrode. The foil lowered the resistance and provided a high-frequency path.

Microelectrodes were fabricated from platinum, gold, copper, and silver microwires (Goodfellow Metals Ltd.) as well as carbon fibers of radii between 1 and 25 μm by sealing them under vacuum in soft glass.[12] Where appropriate, the real or microscopic surface area of the electrodes was found by calculating the charge under the oxide or hydrogen adsorption−desorption peaks.[13] Typically, the surface roughness factor was between 1.3 and 1.6. The surface roughness of the carbon microelectrode was estimated as 2.2 on the basis of scanning electron microscopy images.

RC cell time constants, measured in blank electrolyte solution, were between 0.01 and 0.5 μs depending on the electrode material and radius as well as the supporting electrolyte concentration. The interfacial kinetics were measured only at times greater than about 5−10 *RC*. This condition was satisfied by selecting a microelectrode of appropriate radius.

Spontaneously adsorbed monolayers were formed in-situ using a 10 μM solution of the metal complex in the electrolyte solution of interest. Unless otherwise stated, all electrochemical measurements were performed with this concentration of $[Os(OMe\text{-}bpy)_2(p3p)Cl]^+$ in solution. A low concentration of the surface active complex in solution improved the stability of the monolayers yet minimized the diffusional contribution to the overall current in chronoamperometry or cyclic voltammetry. For example, at a 5 μm radius microelectrode the solution phase component contributes less than 5% to the overall Faradaic current for scan rates greater than 5 V s^{-1}.

A nonisothermal cell, where the reference electrode was isolated from the main compartment by a salt bridge and held at room temperature, was used for the temperature-resolved experiments. The nonisothermal salt bridge contained saturated KCl since it has a low resistance, and the salt remains soluble at the lowest temperature employed (−5 °C). The high electrolyte concentration and the design of the bridge minimize any systematic error in the reported temperature effects on $E°'$ due to changes in the liquid junction potential with temperature.[14]

Results and Discussion

General Electrochemical Properties. Figure 1 shows representative cyclic voltammograms obtained at 50 V s^{-1} for $[Os(OMe\text{-}bpy)_2(p3p)Cl]^+$ monolayers spontaneously adsorbed on carbon, gold, mercury, and platinum microelectrodes, where the

(9) Barr, S. W.; Guyer, K. L.; Li, T. T-T.; Liu, H. Y.; Weaver, M. J. *J. Electrochem. Soc.* **1984**, *131*, 1626.
(10) Taylor, C.; Kenaussis, G.; Katakis, I.; Heller, A. *J. Electroanal. Chem.* **1995**, *396*, 511.
(11) Xu, C. Ph.D. Thesis, University of Illinois at Urbana-Champaign, 1992.
(12) Faulkner, L. R.; Walsh, M. R.; Xu, C. *Contemporary Electroanalytical Chemistry*; Plenum Press: New York, 1990.
(13) Trasatti, S.; Petrii, O. A. *J. Electroanal. Chem.* **1992**, *327*, 354.
(14) Yee, E. L.; Cave, R. J.; Guyer, K. L.; Tyma, P. D.; Weaver, M. J. *J. Am. Chem. Soc.* **1979**, *101*, 1131.

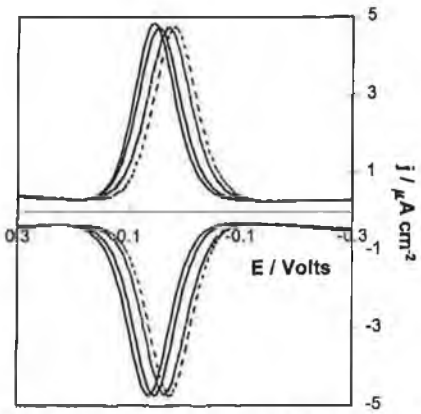

Figure 1. Cyclic voltammograms for the $Os^{2+/3+}$ redox reaction within spontaneously adsorbed $[Os(OMe\text{-}bpy)_2(p3p)Cl]^+$ monolayers. From right to left the electrode material is platinum gold, carbon, and mercury. The scan rate is 50 V s^{-1}, and the surface coverage is $1.0 \pm 0.1 \times 10^{-10}$ mol cm^{-2}. The supporting electrolyte is aqueous 1.0 M $NaClO_4$.

supporting electrolyte is aqueous 1.0 M $NaClO_4$. The formal potentials, $E^{\circ\prime}$, are 0.030, 0.048, 0.060, and 0.120 V for platinum, gold, carbon, and mercury electrodes, respectively. In contrast, the $E^{\circ\prime}$ observed for the complex dissolved in acetonitrile is 0.010 ± 0.008 V irrespective of the electrode material used. The shift in $E^{\circ\prime}$ toward more positive potentials indicates that it is more difficult to oxidize the Os^{2+} redox center when it is adsorbed. Moreover, the differences observed in $E^{\circ\prime}$ suggest that the electron density on the metal center depends on the identity of the electrode material. These differences reflect changes in the free energy of adsorption on the different materials which increase by up to 8.6 kJ mol^{-1} on going from gold to mercury.

Under these slow scan rate conditions, the voltammetric response is consistent in all respects with that expected for an electrochemically reversible reaction involving a surface-confined species.[15] For example, the peak shapes are independent of scan rate, υ, at least over the range 1 to 5 V s^{-1}, and the peak height scales linearly with the scan rate unlike the $\upsilon^{1/2}$ dependence observed for the complex dissolved in acetonitrile. Consistent with the transfer of a single electron per redox center, the full width at half-maximum is between 100 and 110 mV.[16]

Irrespective of the identity of the electrode material, the surface coverage, Γ, of the redox centers, as determined by integrating the Faradaic charge under the $Os^{2+/3+}$ wave, is $(1.0 \pm 0.1) \times 10^{-10}$ mol cm^{-2}, corresponding to an area occupied per molecule of 168 ± 17 Å^2. The surface coverage does not increase further if the concentration of the surface active complex in solution or the deposition time are increased. This limiting surface is typical of that reported previously by us[17,18] and others for related systems.[19,20] The insensitivity of the saturation coverage to the electrode material indicates that the packing density is controlled by the size of the adsorbate and perhaps lateral interactions rather than by the interatomic spacing of the metal or carbon lattice.

Electron-Transfer Dynamics. Figure 2 illustrates the high-speed voltammetric behavior observed for monolayers immobilized on carbon and platinum microelectrodes. The peak-to-peak separations, ΔE_P, are significantly larger than those observed at long experimental time scales. Uncompensated cell resistance and slow heterogeneous electron transfer could contribute to the observed behavior. Where the working electrode is a 5 μm radius microelectrode, the uncompensated resistance as measured using potential step chronoamperometry is 8125 ± 275 Ω irrespective of whether the electrode is carbon or platinum. Taken in conjunction with the peak maximum peak current observed for the platinum microelectrode, 885 nA, this cell resistance leads to an iR drop of approximately 5 mV. This ohmic loss is negligible compared to the peak-to-peak separations of 275 and 60 mV observed for $[Os(OMe\text{-}bpy)_2(p3p)Cl]^+$ monolayers adsorbed on a carbon fiber and platinum microelectrodes, respectively. Therefore, it appears that heterogeneous electron transfer influences the voltammetric response at these high scan rates. Moreover, that ΔE_P is very much larger for monolayers on carbon than on platinum indicates that the standard heterogeneous electron-transfer rate constant, k°, depends on the identity of electrode material.

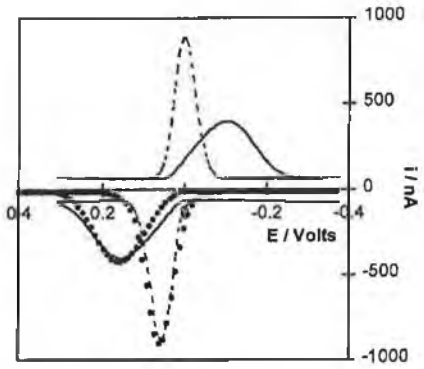

Figure 2. Experimental voltammetric responses for 5 μm radius carbon (—) and platinum (---) microelectrodes modified with $[Os(OMe\text{-}bpy)_2(p3p)Cl]^+$ monolayers. The scan rate is 2000 V s^{-1}, and the supporting electrolyte is 1.0 M aqueous $NaClO_4$. The data points represent optimized fits to a nonadiabatic electron-transfer model in which k° is 4×10^3 and 6×10^4 s^{-1} for carbon and platinum, respectively. The free energy of activation, $\Delta G^\ddagger$, is 6.8 kJ mol^{-1} for both electrode materials.

As discussed elsewhere, k° depends on both a frequency factor and a Franck–Condon barrier and is described by[21–23]

$$k^\circ = A_{et} \exp(-\Delta G^\ddagger/RT) \qquad (1)$$

where A_{et} is the preexponential factor and $\Delta G^\ddagger$ is the electrochemical free energy of activation.[24] For an adiabatic reaction, the prefactor is given by the product of k_{el} the electronic transmission coefficient and υ_n a frequency factor dictated either by nuclear or solvent motion. In contrast, for a nonadiabatic reaction $k_{el} \ll 1$ and the prefactor is dictated by the electron hopping frequency in the activated complex, υ_{el}.

To understand how differences in the density of states influence electron-transfer dynamics, it is essential to decouple the contributions from electronic coupling effects (A_{et}) and free energies of activation ($\Delta G^\ddagger$).[18,25] This separation may be important for measurements of this kind since distinct film

(15) Laviron, E. *J. Electroanal. Chem.* **1974**, *52*, 395.
(16) Brown, A. P.; Anson, F. C. *Anal. Chem.* **1977**, *49*, 1589.
(17) Forster, R. J.; Faulkner, L. R. *J. Am. Chem. Soc.* **1994**, *116*, 5453.
(18) Forster, R. J.; O'Kelly, J. P. *J. Phys. Chem.* **1996**, *100*, 3695.
(19) Acevedo, D.; Abrûna, H. D. *J. Phys. Chem.* **1991**, *95*, 9590.
(20) Acevedo, D.; Bretz, R. L.; Tirado, J. D.; Abrûna, H. D. *Langmuir* **1994**, *10*, 1300.
(21) Bagchi, G. *Annu. Rev. Chem.* **1989**, *40*, 115.
(22) Sutin, N. *Acc. Chem. Res.* **1982**, *15*, 275.
(23) Li, T. T.-T.; Guyer, K. L.; Barr, S. W.; Weaver, M. J. *J. Electroanal. Chem.* **1984**, *164*, 27.
(24) Sutin, N.; Brunschwig, B. S. *ACS Symp. Ser.* **1982**, *No. 198*, 105.
(25) Forster, R. J.; Vos, J. G. and Keyes, T. E. *Analyst* **1998**, *123*, 1905.

structures may cause the local microenvironment and hence $\Delta G^{\ddagger}$ to depend on the identity of the electrode material.

One approach to decoupling these two contributions is to measure electron-transfer rate constants at a single temperature over a wide range of driving forces. For example, Chidsey,[26] Creager,[27] and Murray[28] have modeled the cyclic voltammograms obtained for long-chain ferrocene alkanethiol according to a nonadiabatic electron-transfer model.

In this model, the anodic rate constant is given by the integral over energy (ϵ) of three functions: (a) the Fermi function for the metal $n(\epsilon)$; (b) a Gaussian distribution of energy levels for acceptor states in the monolayer $D_{Ox}(\epsilon)$; (c) a probability factor describing electron tunneling at a given energy, $P(\epsilon)$.

$$k_{Ox}(\eta) = A\int_{-\infty}^{\infty} D_{Ox}(\epsilon)\, n(\epsilon)\, P(\epsilon)\, d\epsilon \qquad (2)$$

The zero point of energy is defined as the Fermi level of the metal at the particular overpotential of interest. The Fermi function describes the distribution of occupied states within the metal and is defined by

$$n(E) = \left(\frac{1}{1 + \exp[(\epsilon - \epsilon_F)/k_B T]}\right) \qquad (3)$$

where ϵ is the energy of a given state in the electrode, ϵ_F is the Fermi level of the electrode, i.e., the applied overpotential, and k_B is the Boltzmann constant. The density of acceptor states is derived from the Marcus theory[29,30] and is represented by eq 4,

$$D_{Ox}(\epsilon) = \exp\left[-\frac{(\epsilon + \eta - \lambda)^2}{4k\lambda T}\right] \qquad (4)$$

where λ is the reorganization energy ($\equiv 4\Delta G^{\ddagger}$). The distance dependence of electron tunneling[31,32] is given by eq 5, where d

$$P(\epsilon) = \exp(-\beta d) \qquad (5)$$

is the electron-transfer distance. Previous investigations[17] suggest that β is close to 1.6 $Å^{-1}$ for this bridging ligand.

The voltammetric current for the reaction of an immobilized redox center following first-order kinetics is given by[28]

$$i_F = nFA(k_{Ox}(\eta)\Gamma_{Red,\eta} - k_{Red}(\eta)\Gamma_{Ox,\eta}) \qquad (6)$$

where $\Gamma_{Red,\eta}$ and $\Gamma_{Ox,\eta}$ are the instantaneous surface coverages of the oxidized and reduced species and $k_{Ox}(\eta)$ and $k_{Red}(\eta)$ are the reaction rate constants given by eq 2 or its complement in which $n(\epsilon)$ is replaced with $(1 - n(\epsilon))$ and $-\lambda$ is replaced by $+\lambda$ in eq 4. Energy minimized molecular modeling indicates that the electron transfer distance, d, is approximately 13.6 Å. Therefore, in using eq 6 to model the voltammetric response, there are only two freely adjustable parameters, k° and $\Delta G^{\ddagger}$ ($=\lambda/4$). To fit the experimental voltammograms, we have used the Nelder and Mead Simplex[33] algorithm to find the values of k° and $\Delta G^{\ddagger}$ that minimize the sum square residuals between the theoretical and experimental currents observed in anodic branches of the linear sweep voltammograms. Figure 2 shows the fits obtained for $[Os(OMe\text{-}bpy)_2(p3p)Cl]^+$ monolayers immobilized on both platinum and carbon fiber microelectrodes. In both cases satisfactory agreement is observed indicating that the electron transfer can be satisfactorily described as a nonadiabatic process. Under these circumstances, one would expect the rate of heterogeneous electron transfer to depend directly on the density of states in the electrode.

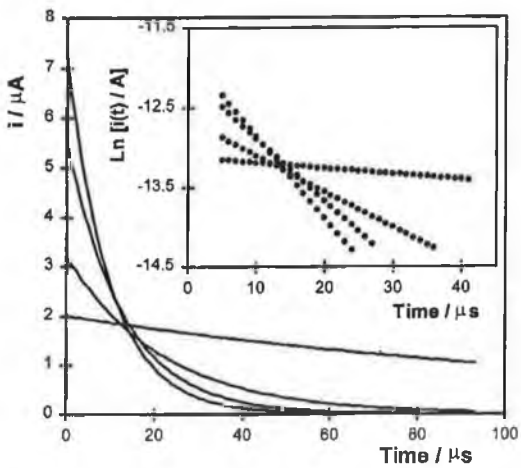

Figure 3. Current response for $[Os(OMe\text{-}bpy)_2(p3p)Cl]^+$ monolayers following a potential step where the overpotential η was 50 mV. From top to bottom on the left-hand side the decays are for platinum, mercury, gold (5 μm), and carbon (12.5 μm). The supporting electrolyte is aqueous 1.0 M $NaClO_4$. The inset shows ln $i_F(t)$ vs t plots for the Faradaic reaction.

The optimized values for k° are 6×10^4 and 4×10^3 s^{-1} for platinum and carbon electrodes, respectively. These values are independent of the scan rate to within 15% for $1000 \leq \upsilon \leq 10\,000$ V s^{-1}. The fit shown in Figure 2 is for a common $\Delta G^{\ddagger}$ of 6.8 kJ mol^{-1}. This analysis suggests that the free energy of activation is independent of the identity of the electrode material and that k° is larger for the platinum electrode because of a larger preexponential factor. However, the quality of the fit shown in Figure 2 is not particularly sensitive to $\Delta G^{\ddagger}$; e.g., increasing $\Delta G^{\ddagger}_{Pt}$ by 25% increases the residual sum of squares between the predicted and experimental peak currents by less than 10%. Therefore, while fitting of the cyclic voltammograms can provide a convenient approach for the determination of k°, for this system it appears to provide only an approximate value for $\Delta G^{\ddagger}$. In contrast, temperature-resolved chronoamperometry can be used to accurately probe both the potential dependence of the heterogeneous electron-transfer rate and the free energy of activation.[17,34]

Chronoamperometry. For an ideal electrochemical reaction involving a surface-bound species, the Faradaic current following a potential step that changes the redox composition of the monolayer exhibits a single-exponential decay in time according to[26,35]

$$i_F(t) = kQ\exp(-kt) \qquad (7)$$

where k is the apparent rate constant for the overall reaction and Q is the total charge passed in the redox transformation.

Figure 3 illustrates typical examples of the current–time transients observed for the $Os^{2+} + e^- \rightarrow Os^{3+}$ redox reaction of $[Os(OMe\text{-}bpy)_2(p3p)Cl]^+$ monolayers on different electrode

(26) Chidsey, C. E. D. *Science* **1991**, *251*, 919.
(27) Weber, K.; Creager, S. E. *Anal. Chem.* **1994**, *66*, 3164.
(28) Tender, L.; Carter, M. T.; Murray, R. W. *Anal. Chem.* **1994**, *66*, 3173.
(29) Marcus, R. A. *J. Chem. Phys.* **1956**, *24*, 966.
(30) Marcus, R. A. *J. Phys. Chem.* **1963**, *67*, 853.
(31) Schmickler, W. *J. Electroanal. Chem.* **1977**, *82*, 65.
(32) Bockris, J. O'M.; Khan, S. U. M. *Quantum Electrochemistry*; Plenum Press: New York, 1979; Chapter 8.
(33) Ebert, K.; Ederer, H.; Isenhour, T. L *Computer Applications in Chemistry: An Introduction for PC Users*; VCH Publishers: New York, 1989.
(34) Forster, R. J. *Anal. Chem.* **1996**, *68*, 3143.
(35) Finklea, H. O.; Hanshew, D. D.*J. Am. Chem. Soc.* **1992**, *114*, 3173.

Table 1. Electrode Response Times, Total Cell Resistances, R, and Area Normalized Interfacial Capacitances for $[Os(OMe\text{-}bpy)_2(p3p)Cl]^{2+}$ Monolayers Assembled on Various Electrode Materials[a]

electrode	RC/ns[b]	R/kΩ	C/μF cm^{-2}
platinum	171 ± 30	8.4 ± 0.3	26 ± 4
mercury	135 ± 20	7.8 ± 0.1	22 ± 3
gold	162 ± 26	8.2 ± 0.3	25 ± 3
silver	180 ± 46	8.1 ± 0.4	28 ± 6
carbon	440 ± 90	3.3 ± 0.1	27 ± 5

[a] Measured using potential step chronoamperometry from −0.150 to −0.100 V. The monolayer is in the 1+ oxidation state. The supporting electrolyte is aqueous 1.0 M $NaClO_4$. [b] The electrode radius is 5 μm except for carbon where it is 12.5 μm.

materials. In these experiments the overpotential η ($\equiv E - E^{o\prime}$) was 0.05 V. To use these data to accurately measure k, the response time of the electrode must be shorter than the time constant for heterogeneous electron transfer. The RC time constants for the different electrodes, where R is the total cell resistance and C is the interfacial capacitance, were obtained by stepping the potential from −0.100 to −0.050 V. The monolayer is not redox active at these potentials, and the current decays follow single-exponential kinetics due to double layer charging. Table 1 contains the resistance, capacitance, and RC time constants for each of the electrodes. Table 1 shows that, irrespective of the electrode material, the 5 μm radius electrodes all have response times that are less than 500 ns. This result means that double layer charging will only contribute to the currents observed in Figure 2 only at time scales shorter than approximately 1.5 μs. Therefore, the heterogeneous electron-transfer rate constant can be measured by analyzing the current−time transients at relatively longer time scales. Beyond the issue of convolution between double-layer charging currents and the Faradaic response, Table 1 also confirms that current−time transients of Figure 2 are not compromised by ohmic effects. For example, the total cell resistance for the 10 μm radius silver electrode is approximately 8 kΩ. Therefore, the iR drop will be less than 10 mV for times longer than approximately 8 μs. The inset of Figure 2 supports this analysis since, in accordance with eq 7, semilog current vs time plots are linear over at least 1.5 lifetimes. Deviations from linearity would be expected if substantial ohmic drop effects were present. Uncompensated resistance causes the applied potential and, hence, the apparent rate to evolve with time. Therefore, iR drop would produce negative deviations in the observed current at short times.[36]

For each electrode material, heterogeneous electron transfer is characterized by a single rate constant indicating that electron transfer is characterized by a single electron-transfer distance, reorganization energy, and microenvironment. Further evidence supporting the predominance of a single rate constant at high concentrations of supporting electrolyte is obtained by examining the intercept of the semilog plot at zero time. As indicated by eq 7, the intercept for a single-exponential decay is $\ln(kQ)$. We find that the charges passed in chronoamperometry agree with those found in slow scan cyclic voltammetry to within 10%. This agreement indicates that all of the surface confined molecules are redox active on a microsecond time scale.

Figure 4 illustrates Tafel plots of ln k vs η for monolayers formed on platinum, gold, and carbon microelectrodes. The dependence of ln k on η is clearly nonlinear at large overpotentials, and the slopes decrease in magnitude with increasing overpotential in both anodic and cathodic directions. This

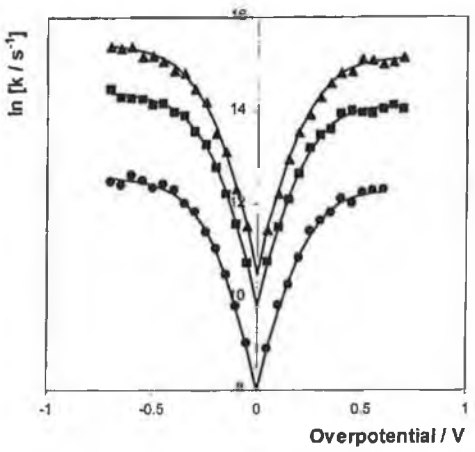

Figure 4. Tafel plot for $[Os(OMe\text{-}bpy)_2(p3p)Cl]^+$ monolayers adsorbed on platinum (▲), gold (■), and carbon (●) microelectrodes. The supporting electrolyte is 1.0 M aqueous $NaClO_4$. The solid curves represent best fits derived from the nonadiabatic electron-transfer model (eqs 2−5). For platinum, gold, and carbon, k^o is 4.0×10^4, 1.8×10^4, and 3×10^3 s^{-1}, respectively, while λ is constant at 27 kJ mol^{-1}. Between monolayer error bars are approximately the same size as the symbols.

behavior contrasts with the predictions of the conventional Butler−Volmer formulation of electrode kinetics[36] which predicts a linear increase in k for all overpotentials. The solid lines of Figure 4 illustrate the best fits obtained from the nonadiabatic tunneling model where k^o is 4.0×10^4, 1.8×10^4, and 3×10^3 s^{-1} for platinum, gold, and carbon, respectively, and λ is constant at 26 kJ mol^{-1}. These values agree with those found on the basis of fitting the scan rate dependent cyclic voltammograms to within 5%. Consistent with this low reorganization energy, the heterogeneous electron-transfer rate constant becomes independent of the electrical driving force for $\eta > 0.35$ V. Table 2 contains the standard heterogeneous electron-transfer rate constants, k^o, obtained by extrapolating the potential dependent rate constants to zero overpotential. These data confirm that k^o depends on the nature of the electrode material. It is important to consider the influence of double layer effects on k^o which occur when the potential at the plane of electron transfer, ϕ_{PET}, is not equal to the potential in solution. For the monolayers considered here, double layer effects do not appear to be important for the following reasons. First, k^o increases by less than 5% on going from 0.1 to 1.0 M supporting electrolyte. If double layer effects were significant, then the compression of the double layer caused by increasing the electrolyte concentration would alter ϕ_{PET} thus changing the apparent heterogeneous electron-transfer rate constant.

Second, the monolayers appear to be solvated and the double layer most likely sets up *within* the monolayer rather than at the monolayer/solution interface. For example, the interfacial capacitance is independent of the bulk electrolyte concentration, C_B, for $C_B > 0.2$ M and a limiting value of 25 ± 5 μF cm^{-2} is observed in 1.0 M $NaClO_4$ at −0.1 V. This value is independent of the electrode material used. This limiting value of the interfacial capacitance is considerably larger than that associated with a solvent-free monolayer.[37] This observation suggests that the electrochemical double layer sets up at the electrode/monolayer interface rather than at the monolayer/solution interface.

(36) Bard, A. J.; Faulkner, L. R. *Electrochemical Methods: Fundamentals and Applications*; Wiley: New York, 1980.

(37) Porter, M. D.; Bright, T. B.; Allara, D. L.; Chidsey, C. E. D. *J. Am. Chem. Soc.* **1987**, *109*, 3559.

Table 2. Standard Heterogeneous Electron-Transfer Rate Constants, k°, Activation Enthalpies, $\Delta H^\ddagger$, Reaction Entropies, ΔS_{RC}°, Free Energies of Activation, $\Delta G^\ddagger$, and Preexponential Factors for the Metal-Based Redox Reaction within $[Os(OMe\text{-}bpy)_2(p3p)Cl]^{+/2+}$ Monolayers on Different Electrode Materials[a]

	$10^{-4}k^o/s^{-1}$	$\Delta H^\ddagger$/kJ mol^{-1}	$\Delta S^\ddagger$/J mol^{-1} K^{-1}	$\Delta G^\ddagger$/kJ mol^{-1}	$10^{-5}\upsilon_{el}/s^{-1}$ [b]	H_{AB}/J mol^{-1}
platinum	4.0 ± 0.2	11.3 ± 0.7	28 ± 4.5	7.3 ± 0.5	7.6 ± 1.7	0.47 ± 0.06
mercury	3.1 ± 0.3	10.6 ± 1.1	26 ± 5	6.9 ± 1.2	5.0 ± 3.1	0.38 ± 0.13
gold	1.8 ± 0.2	11.2 ± 0.5	32 ± 3	6.6 ± 0.3	2.6 ± 0.3	0.27 ± 0.02
silver	1.3 ± 0.2	11.2 ± 0.6	30 ± 4	6.9 ± 0.3	2.1 ± 0.3	0.24 ± 0.02
carbon	0.3 ± 0.03	11.1 ± 0.5	30 ± 4	6.8 ± 0.4	0.5 ± 0.08	0.12 ± 0.01

[a] Standard deviations are for at least three individual monolayers. Supporting electrolyte is aqueous 1.0 M $NaClO_4$. [b] Preexponential factor extracted from the standard heterogeneous electron-transfer rate constant using $\Delta G^\ddagger$.

Third, the potentials of zero charge (PZC) becomes more positive in the order Hg < Au < Pt. In the presence of double layer effects, one would anticipate that these PZCs would lead to k°s in the sequence Hg > Au > Pt. Table 2 clearly demonstrates that this is not the case for these monolayers.

As discussed above, caution must be exercised to ensure that apparent differences in k° are not caused by variations in the free energy of activation, rather than by density of states. Therefore, we have probed the temperature dependence of k in order to extract enthalpies of activation.

Temperature Dependence of *k*. The activation enthalpy extracted from an Arrhenius plot of ln k vs T^{-1} measured at a constant potential has been termed "ideal",[31] and it is labeled here as $\Delta H_I^\ddagger$. For a reduction or cathodic reaction, this electrochemical activation enthalpy can be separated into a "chemical" activation enthalpy term, $\Delta H^\ddagger$, and a contribution from the "electrical" driving force, $\alpha_c F\phi_m$, where ϕ_m is the Galvani potential which corresponds to the formal potential of the reaction under consideration at a given temperature, according to eq 8.

$$\Delta H_{I,c}^{\ddagger} = -R\frac{\partial \ln k}{\partial(T^{-1})}|\phi_m = \Delta H^\ddagger - \alpha_c F\phi_m \qquad (8)$$

The temperature dependence of the heterogeneous electron-transfer rate has been investigated using temperature-resolved chronoamperometry over the range −5 to 40 °C. An overpotential of 50 mV, as determined at 298 K, was used throughout these experiments, and the resulting current−time transients were similar to those illustrated in Figure 2. The corresponding semilog plots were linear over approximately 1.5 lifetimes, and the heterogeneous electron-transfer rate was evaluated from the slopes. In a typical set of experiments, the temperature was systematically varied over a range and then returned to the initial temperature. The same slope, $-k$, and intercept, ln(kQ), were observed within experimental error for the initial and final transients. This consistency indicates that cycling the temperature does not change the heterogeneous kinetics or the quantity of material immobilized on the electrode surface. The heterogeneous electron-transfer rate increases with increasing temperature as anticipated for a thermally activated process. As illustrated in Figure 5, Arrhenius plots of ln k vs T^{-1} are linear (R^2 > 0.995) over the temperature range −5 to 40 °C. The slopes observed for the individual electrode materials are similar indicating that the activation enthalpy is independent of the identity of the electrode material. Table 2 contains the activation enthalpies, $\Delta H^\ddagger$, obtained from the slopes of these plots after using a transfer coefficient of 0.5 to correct for the electrical driving force (50 mV) according to eq 8. These data indicate that the average $\Delta H^\ddagger$ for all of the electrodes investigated is 11.1 ± 0.5 kJ mol^{-1}.

A deficiency in the foregoing analysis is that it fails to take account of the temperature dependence of the density of acceptor states within the electrode. In the Gosavi and Marcus model, this factor appears in the electronic coupling matrix element. Using an approach similar to that taken by Smalley and coworkers,[38] it may be possible to take into account the temperature dependence of both donor/acceptor states *and* the electrode density of states by using a plot of ln[$k^\circ/T^{3/2}$] vs T^{-1} to determine the activation enthalpy. As illustrated in Figure 5, plots of [$k^\circ/T^{3/2}$] vs T^{-1} are linear for each of the electrode materials investigated. Moreover, the slopes for the different electrode materials are identical to within experimental error indicating, as discussed above, that the activation enthalpy is independent of the electrode material. The slopes of these plots yield activation enthalpies that are approximately 30% smaller than those found using the conventional Arrhenius analysis.

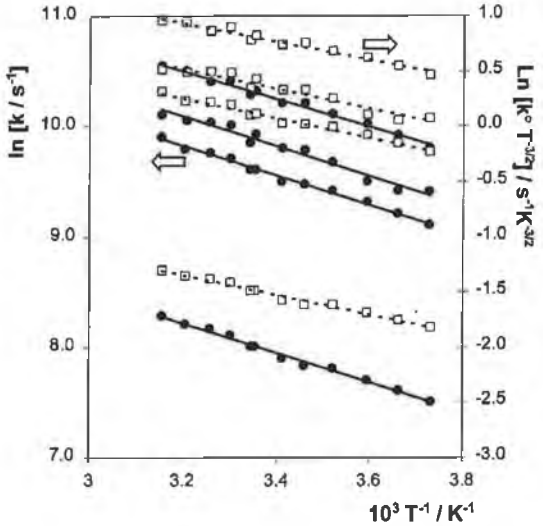

Figure 5. Temperature dependence of the heterogeneous electron-transfer rate constant for $[Os(OMe\text{-}bpy)_2(p3p)Cl]^+$ monolayers on temperature. The overpotential is 50 mV. From top to bottom, the electrodes are mercury, gold, silver, and carbon. The supporting electrolyte is aqueous 1.0 M $NaClO_4$. Filled circles and open squares and denote y-axes of ln(k) and ln[$k/T^{3/2}$], respectively. The error on measurements using three independent monolayers is comparable to the size of the symbol.

To use experimental enthalpies of activation to calculate free energies of activation it is necessary to determine the activation entropy. Comparing these values with the value of $\Delta G^\ddagger$ provided by fitting the high scan rate voltammetric data is an important test of consistency between these two independent approaches.

Reaction Entropies. The reaction entropy, ΔS_{rc}°, quantifies the difference in entropy between the reduced and oxidized forms of the redox couple. The reaction entropy has been determined using a nonisothermal cell by measuring the

(38) Smalley, J. F.; Feldberg, S. W ; Chidsey, C. E. D.; Linford, M. R.; Newton, M. D.; Liu, Y.-P. *J. Phys. Chem.* **1995**, *99*, 13141.

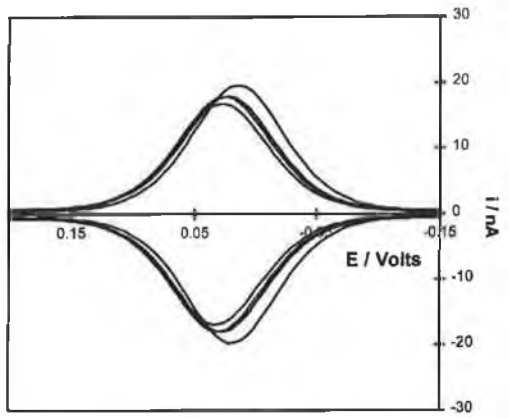

Figure 6. Temperature-dependent voltammetric response for an $[Os(OMe\text{-}bpy)_2(p3p)Cl]^+$ monolayer adsorbed on a 25 μm platinum microelectrode. From right to left the temperatures are −3, 5, 25, and 42 °C. The supporting electrolyte is aqueous 1.0 M $NaClO_4$.

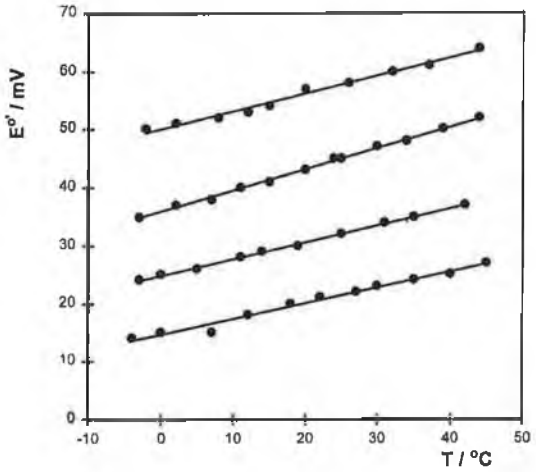

Figure 7. Effect of electrode material on the temperature dependence of the formal potential for the $Os^{2+/3+}$ redox reaction within $[Os(OMe\text{-}bpy)_2(p3p)Cl]^{+/2+}$ monolayers. From top to bottom, the electrodes are carbon, copper, platinum, and mercury. The formal potentials are reproducible to within 5 mV for independent monolayers.

temperature dependence of the $Os^{2+/3+}$ formal potential for monolayers on each of the electrode materials. As discussed by Weaver and co-workers,[14] the temperature dependence of the formal potential can be expressed as

$$\Delta S_{rc}^{\circ} = F(\partial E^{\circ\prime}/\partial T) \tag{9}$$

Figure 6 shows representative temperature-dependent cyclic voltammograms for the metal-based oxidation within $[Os(OMe\text{-}bpy)_2(p3p)Cl]^{+/2+}$ monolayers on a platinum microelectrode. For monolayers assembled on each of the electrode materials investigated, the formal potential shifts in a positive potential direction with increasing temperature. This observation indicates positive reaction entropies and a higher degree of local ordering in the oxidized than in the reduced state. As shown in Figure 7, plots of $E^{\circ\prime}$ vs T are linear over the temperature range −5 to 40 °C, and reaction entropies have been calculated from the slopes according to eq 9. Experimentally, the magnitude of ΔS_{rc}° is independent of the identity of the electrode material with a value of 29.6 ± 2.4 J mol^{-1} K^{-1}. Given that the reaction entropy is sensitive to the local dielectric constant within the monolayer, this result indicates that the microenvironments within the monolayers are all similar. Moreover, the entropy observed is similar to that found for monolayers constructed using related bipyridyl complexes[17,18] suggesting that changes in the structure, e.g., incorporation of methoxy moieties, do not significantly change the extent of solvent ordering within the monolayers.

The entropy of the transition state is assumed to lie between that of the reduced and oxidized forms, and the cathodic free energy of activation is given by

$$\Delta G_c^{\ddagger} = \Delta H_c^{\ddagger} - T\alpha_c \Delta S_{rc}^{\circ} \tag{10}$$

where α_C is the cathodic transfer coefficient. Table 2 shows that the free energy of activation is approximately independent of the type electrode material on which the monolayer is assembled. Taken together, these enthalpy, entropy, and free energy data represent a powerful argument that the activation parameters for the $Os^{2+/3+}$ redox reaction within $[Os(OMe\text{-}bpy)_2(p3p)Cl]^{+/2+}$ are indistinguishable for platinum, mercury, gold, silver, and carbon electrodes.

Preexponential Factor. Table 2 contains values for the electron hopping frequency υ_{el} that have been determined using eq 1 and the experimental values of $\Delta G_c^{\ddagger}$ and k°. Consistent with the modeling of the voltammetric response illustrated in Figure 2, irrespective of the identity of the electrode material, these prefactors are approximately 6 orders of magnitude smaller than those expected for an adiabatic electron-transfer reaction.[39] Table 2 also suggests that υ_{el} is sensitive to the identity of the electrode material. However, in the calculation of υ_{el}, the exponential relationship of eq 1 tends to amplify the small variations observed in $\Delta G^{\ddagger}$. Nevertheless, the large difference in electron hopping frequencies between platinum and carbon might be expected given the known sensitivity of heterogeneous electron transfer to the density of edge-planes in carbon electrodes.[40,41] More significant perhaps, are the differences observed between Pt and Au where the $\Delta G^{\ddagger}$ values are indistinguishable.

The density of states, ρ_F, of platinum is approximately 7.5 times that of gold, which, according to traditional theory, is expected to cause a proportional increase in υ_{el}. However, the Marcus and Gosavi[5] model highlights the importance of considering the identity of the orbitals that are responsible for increasing ρ_F. For example, the d-orbitals found in platinum that lead to an increased density of states are expected to couple less efficiently than the dominant sp-states of gold. Thus, the Marcus model predicts a ratio of $k^{\circ}_{Pt}/k^{\circ}_{Au}$ of 1.8. Superficially, our experimental value of 2.2 ± 0.4 compares favorably with this theoretical prediction. However, it is important to use the experimental data to probe the theoretical prediction that the electronic coupling per state is lower for platinum than for gold.

Electronic interaction of the redox orbitals and the metallic states causes splitting between the product and reactant hypersurfaces which is quantified by H_{AB}, the matrix coupling element. The Landau−Zener treatment[42] of a nonadiabatic reaction yields

$$\upsilon_{el} = (2H_{AB}^2/h)(\pi^3/\lambda RT)^{1/2} \tag{11}$$

where h is Planck's constant. The matrix coupling element has been determined for each of the electrode materials, and the

(39) Weaver, M. J. *Chem. Rev.* **1992**, *92*, 463.
(40) Ray, K. G.; McCreery, R. L. *J. Electroanal. Chem.* **1999**, *469*, 150.
(41) McCreery, R. L.; Cline, K. K.; McDermott, C. A.; McDermott, M. T. *Colloids Surf. A* **1994**, *93*, 211.
(42) Brunschwig, B. S.; Sutin, N. *Coord. Chem. Rev.* **1999**, *187*, 233.

results are presented in Table 2. The fact that H_{AB} is less than 1 kJ mol^{-1} confirms that the system is charge localized and nonadiabatic.[42] These monolayers provide a significant opportunity to compare the extent of electronic communication across the p3p bridge when bound to a metal electrode as opposed to being coupled to a molecular species, e.g., within a dimeric metal complex. For example, Taube and co-workers[43] have used intervalence charge-transfer intensities to probe the extent of electronic coupling across 4,4′-dipyridyl type bridges in which the pyridine rings are separated by a number of methylene spacer groups. Asymmetric dimers linked by related bridging ligands have also been investigated.[44] Dimeric complexes of this type exhibit H_{AB} values between approximately 2 and 10 kJ mol^{-1} and are categorized as class II compounds according to the Robin−Day system.[45] Significantly, the H_{AB} values for the monolayers investigated here are approximately 4 orders of magnitude smaller than those found in dimers. This behavior indicates that the metal center interacts much more weakly with the electrode surface than with another metal center. However, the observation that H_{AB} is approximately 1.8 times larger for platinum than for gold suggests that the higher density of states on platinum relative to gold is not offset by a lower electronic coupling per state as predicted by theory. In this sense, models that assume the heterogeneous electron-transfer rate is proportional to the density of states modulated by the square of the electronic coupling may be incomplete. It is perhaps important to note that probing metal-to-metal charge transfer interactions within mixed valence complexes is an excited-state process as opposed to the thermally activated ground-state process investigated here. Future experiments will probe this issue by measuring rate constants for oxidation of electronically excited monolayers generated using pulsed laser methods.[46]

(43) Taube, H. In *Tunneling in Biological Systems*; Chance, B., Ed.; Academic Press: New York, 1979; p 173.
(44) Fagalde, F.; Katz, N. E. *Polyhedron* **1995**, *14*, 1213.
(45) Brunschwig, B. S.; Creutz, C.; Sutin, N. *Coord. Chem. Rev.* **1998**, *177*, 61.
(46) Forster, R. J.; Keyes, T. E. *J. Phys. Chem. B* **1998**, *102*, 10004.

Conclusions

Adsorbed monolayers of $[Os(OMe\text{-}bpy)_2(p3p)Cl]^+$ have been formed on platinum, mercury, gold, silver, and carbon microelectrodes, where OMe-bpy is 4,4′-2,2′-dimethoxybipyridyl and p3p is 1,4-trimethylenedipyridine. They exhibit nearly ideal electrochemical responses as the potential, temperature, and experimental time scale are varied over a wide range. These monolayers have been used to probe the effect of changing the density of electronic states within the electrode on the heterogeneous electron-transfer rate. Both high scan rate cyclic voltammetry as well as temperature-resolved chronoamperometry and cyclic voltammetry reveal that the free energy of activation is consistent with that expected for a simple outer sphere reaction. The experimental preexponential factors are consistent with those expected for a nonadiabatic reaction in which there is weak electronic coupling between the delocalized metallic states on the electrode and the localized redox states of the osmium complex. The ratio of the prefactors for platinum and gold is 2.9 ± 0.7 compared with a ratio of 7.5 for the density of states. Therefore, our experimental data indicate that the nonadiabatic rate of heterogeneous electron transfer does not depend simply on the density of states within the electrode.

Acknowledgment. The expert advice of Dr. Chris Taylor and Prof. Adam Heller of the University of Texas at Austin on the synthesis of $[Os(OMe\text{-}bpy)_2Cl_2]$ is deeply appreciated. The assistance of Professor Marcus and Dr. Gosavi by providing an advance copy of ref 5 is gratefully acknowledged. We thank Professor Finklea for providing related experimental data on alkanethiol monolayers deposited on gold, silver, and platinum electrodes. We appreciate the ongoing financial support from Enterprise Ireland, the Irish Science and Technology Agency, under Basic Research Grant SC/99/132. The generous loan of potassium hexachloroosmate(IV) by Johnson Matthey under the loan scheme is deeply appreciated. We appreciate the reviewer's suggestion for the alternative analysis of the temperature-dependent rate constant data.

JA002616U

Appendix D

Visual Basic Project for Computer Interface with a Function Generator-Potentiostat used for Chronoamperometry

Introduction

In high speed chronoamperometry, a custom built function generator-potentiostat, with a rise time of less than 10 ns, was used to apply potential steps of variable pulsewidth and amplitude directly to a two-electrode cell. In this appendix, the visual basic form and the code attached to the command buttons on that form are given, for a new interface for computer control of the custom built function generator-potentiostat.

The visual basic form (i.e., the "front end" of the interface) is given in Figure D.1. Communication between the computer and the high speed potentiostat is enabled by the use of the Vbcomm control which is represented by the "Telephone" icon on the form in Figure D.1. There are two command buttons, namely, "Program Waveform Generator" and "Transfer Captured Transient" and the code for these command buttons is listed in the following sections.

The "Program Waveform Generator" command button, when clicked, calls an executable "C" program which controls the settings for the potential step to be used. The "Transfer Captured Transient" command button when clicked, starts the program to capture the resulting data following the application of the potential step.

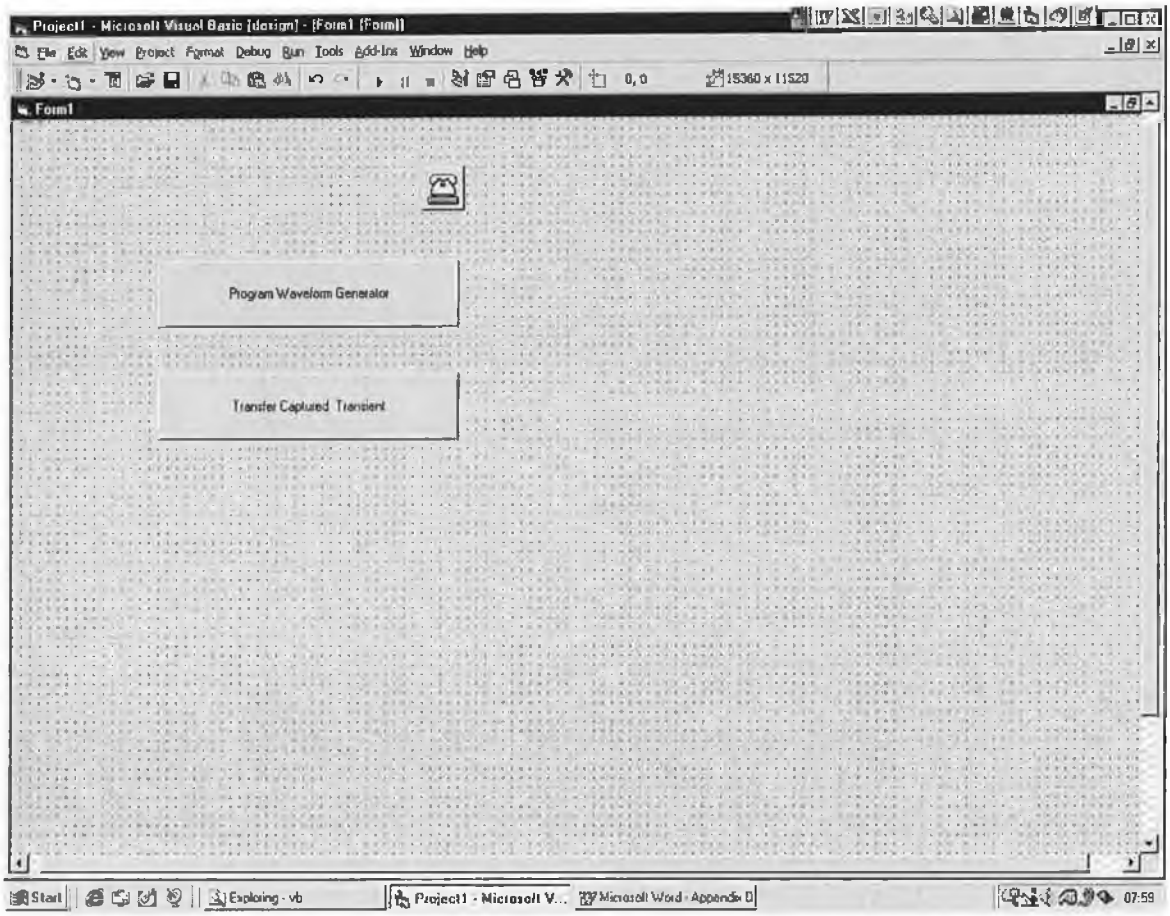

Figure D.1. The visual basic form used for the new computer interface for the high speed potentiostat used in the chronoamperometry experiments.

Code Attached to "Program Waveform Generator" Command Button

```
Private Sub Command1_Click()
Dim X
Message$ = "Please Wait For Waveform Programming"
response = MsgBox(Message$, 0)

X = Shell("c:funcgen.exe", 3)
Form2.Load
Form2.Show


Unload Form1
End Sub
```

Code Attached to "Transfer Captured Transient" Command Button

```
Private Sub Command2_Click()
Dim Char, filename$, Textdata
filename$ = InputBox("Enter filename")

filename$ = filename$ + ".DAT"

cls
Print "Please Wait For Data Transfer"


ReDim pointval%(2004)
MSComm1.CommPort = 1
MSComm1.PortOpen = True

MSComm1.Settings = "9600,N,7,1"
```

```
InputLen = 0
10: MSComm1.Output = "WRT 7" + Chr$(13)
MSComm1.Output = "WAVEFORM PREAMBLE?" + Chr$(13)
MSComm1.Output = "RD 200 7" + Chr$(13)
'destination=source
MSComm1.Handshaking = comRTS

pre$ = MSComm1.Input ' = pre$

MSComm1.Output = "WRT 7" + Chr$(13)
MSComm1.Output = "WAVEFORM; SOURCE CHANNEL 2;FORMAT
WORD;DATA?" + Chr$(13)
MSComm1.Output = "TMO 30" + Chr$(13)
MSComm1.Output = "RD 2 7" + Chr$(13)
headers$ = MSComm1.Input '= headers$

'If Val(headers$) < 102 Then
'cls
'CHECK$ = ""
'Print "Error Detected Check Scope, Press any Key to Retry"
'Do While CHECK$ = ""
'CHECK$ = INKEY$
'Loop
'GoTo 10:
'End If
cls
 Print "Data Transfer in Progress"

For X% = 0 To 2003
MSComm1.Output = "RD 1 7" + Chr$(13)
InputLen = 1
MSComm1.Handshaking = 0
up: hold$ = MSComm1.Input '= hold$
 h = h + 1
```

```
If Val(hold$) = 0 Then MSComm1.Handshaking = h: GoTo up:

hold$ = Right$(hold$, 2)
pointval%(X%) = Asc(hold$)
Next X%

For X% = 0 To 2003 Step 2
pointval%(X% / 2) = pointval%(X% + 1) * 256 + pointval%(X%)
Next X%

'MSComm1.Output = "TMO 30"
Open "Temp" For Output As #2
Write #2, pre$
Close #2

Open "Temp" For Input As #2
discard$ = Input$(1, #2)
Input #2, Format1%
Input #2, TPE%
Input #2, NUMPTS%
Input #2, Count1%
Input #2, xinc
Input #2, xorigin
Input #2, Xref
Input #2, yinc
Input #2, yorigin
Input #2, yref
Input #2, Coupling%
Input #2, Impedance
Close #2

'Shell "C:"
'Shell "cd\qb45\data"
cls:
```

```
Print "Saving Data File"

Open filename$ For Output As #2
Write #2, "Format =", Format1%
Write #2, "Type =", TPE%
Write #2, "Number of Points =", NUMPTS%
Write #2, "X Increment =", xinc
Write #2, "X Origin =", xorigin
Write #2, "X Reference =", Xref
Write #2, "Y Increment =", yinc
Write #2, "Y Origin =", yorigin
Write #2, "Y Reference =", yref
Write #2, "Coupling =", Coupling%
Write #2, "Impedance =", Impedance

For X% = 0 To 1001
Volts = (pointval%(X%) - yref) * yinc + yorigin
Time1 = (X% - Xref) * xinc + xorigin
Write #2, Time1, Volts
Next X%
Close #1
Close #2
'shell "C"
End Sub
```